Al-Hafidh, Maab (2020) *Multi-reflection polarimetry with MEMS-machining and microfluidics.* PhD thesis.

MULTI-REFLECTION POLARIMETRY WITH MEMS-MACHINING AND MICROFLUIDICS

Maab Hafidh Al-Hafidh

Supervisors: Prof. Jonathan Cooper
Dr. Julien Reboud
Prof. Anthony Kelly

A thesis submitted in fulfilment of the requirements for the degree of Doctor of Philosophy

School of Engineering
College of Science and Engineering
The University of Glasgow

This thesis is dedicated to my parents and my husband.

Declaration

“I declare that, except where explicit reference is made to the contribution of others, this dissertation is the result of my own work and has not been submitted for any other degree at the University of Glasgow or any other institution”.

Maab Al-Hafidh

University of Glasgow

Abstract

Polarimetry provides useful insights into the molecular structure of optically active mediums such as chiral molecules in solution, enabling the measurement of the rotation of the polarization of a transverse wave, while also determining the concentration of the analyte present.

The field of microfluidics promises new portable, low-cost, sensing systems, as well as the capabilities to measure the properties of precious samples, for which only small volumes are available. However, when optical sensing methods are involved, using microfluidic channels in millimeter to micrometer range results in a short path length over which the signal can be measured. Polarimetry is an optical sensing modality which would greatly benefit from using small volumes, as it can provide relevant information on the structure of chiral biomarkers in life sciences. However, the small interrogation volumes associated with the minute samples decreases the numbers of molecules in the light path that cause an optical rotation, and, as such, reduces the sensitivity. This thesis is aimed at the development of new methodologies to increase the sensitivity of polarimetry measurements for microfluidics systems. The work focuses on a new geometry whereby an optical beam, passing through a chiral sample, undergoes multiple reflections from suitably aligned and configured external micromirrors. The usual cancelling out of the optical rotation that occurs when the rotated polarized beam is passed back through a solution following reflection at a single mirror can be then negated. This enables the chirality of molecular species present in a microfluidic sample to be measured with increased sensitivity. This approach was validated experimentally using multiple passes of a linearly polarized He-Ne laser and a 403 nm diode laser through solutions of D-(+)-glucose as a chiral molecule, leading to a detection limit enhanced by ~27 times after only 11 passes.

The configuration was also extended in a microscale format by creating mirrored silicon structures for micro-optics. New methods are introduced and characterised to fabricate both 45° and 90° etch-planes from monocrystalline silicon for use as retro-reflective sidewalls in a microfluidic device. Both techniques (to achieve the respective angles) use the same photolithographic pattern orientation, but with two different etchants. Etching on <100> direction in Si(100) with potassium hydroxide gives vertical surfaces, whilst tetramethylammonium hydroxide gives 45° sidewalls. Optical rotations of glucose were measured using an integrated multi-reflections zigzag structure, enabling the use of 20 times smaller sample volumes.

In general, the new method for polarimetry demonstrated in this work, based on multiple reflections across the microchannel, enables to significantly increase the optical path length in optofluidic devices, opening new applications in drug discovery and diagnostics where the sample structure of active molecules is of interest.

Table of Contents

Acknowledgements

I would like to begin by thanking my supervisor, Professor Jon Cooper for his generous assistance, motivation, and immense knowledge. I am very appreciative of the opportunity given to me to work with him. Likewise, I would like to thank my second and third supervisors, Dr. Julien Reboud and Professor Anthony Kelly for constant assistance, advice and support during my PhD.

Similarly, I would like to thank the examiners, Professor Nikolaj Gadegaard, Professor Marc Desmulliez, and Dr. Cristina Gonzalez Garcia, your valuable comments are much appreciated.

A special thanks should go to Dr. Andrew Glidle and Dr. Rab Wilson for their input and guidance on the work. Without their precious support, it would not have been possible to conduct this research. Rab, thank you for being around in the lab and always being up for excellent chat, encouragement and generous help.

To Dr. Qusay Altaai, Dr. Abdullah Al-Khalidi, Dr. Qutaiba Al-Khalidi, Dr. Yang Qian, and Dr. Nada Zain, it was fantastic to work with you all and great to get to know you over the years. Thank you for your invaluable scientific input, resources and time that you put into this project.

I would also like to extend my thanks to Professor Jonathan Weaver for his generous advice, assistance, and resources in my work of micromirrors fabrication.

My grateful thanks should go to all James Watt Nano Centre staff at Glasgow University, especially, Mr. Michael Tormey for his generous in providing the resources for microfabrication and Professor Haiping Zoe and Dr. Mohammed Mirza for valuable advices and immediate help in training. Also, many thanks for Mrs. Hellen Mcllen and Mr. Susan Ferguson, for extensive training on Plassys II, modified evaporator, and SEM microscopy. Likewise, for Mr. Robert Harkins and Mr. Donald Nicolson, for their constant assistance and training on microfabrication work.

Appreciative thanks also go to all my helpful colleagues and staff in Professor Jonathan Cooper's group at level 8, especially Professor Huabing Yin and Dr. Faroha Liaqat, your help is appreciated.

I would also like to acknowledge the International Students Support team at Glasgow University, Mrs. Lisa Milne, Mrs. Avril MacGregor, Mrs. Jill Moore, and Mrs. Jontue Bennett for their valuable support and helpful advice. You all have been my family inside the university campus. Avril MacGregor, your valuable experience and immediate help especially in the visa related problem is much appreciated and unforgotten

In addition, I would like to thank my advisor Mrs. Heather Lambie for immediate help and advice.

I could not, and will never be able to, find words to thank my God, ALLAH, for his great gifts; this is my family and everything in our life. Many thanks should go to a patient and supportive mother and father; sister and two brothers, your love and support are much appreciated. My dad, Dr. Hafidh Tawfeek Al-Hafidh if you had not kept me to a strict timeline and encouragements I may never have reached to this stage. Mum, Mrs. Maha Mahmood Al-Rawi, words cannot describe how amazing you have been throughout my life and especially through my PhD study. My brothers, Mohammed and Ammar, thank you for asking me what I have been doing for the last four years on a regular basis. My lovely sister, Dr. Hafsa Al-Hafidh, without you and your motivations, I may never have thought about the bigger picture.

Nobody has been more important to me in the pursuit of this project than the members of my family. Without doubt, great sincere thanks should go to my patient and supportive husband, Dr. Qusay Altaai, who suffered for a long time, on a daily basis, from a student wife; likewise, my three lovely young sons, Alhasan, Mohammed, and Abdulazeez, who suffered, almost six years now, from a student mum. Again, your patience, love and support are much appreciated. Thanks god for having such a great gifts.

My sincere thanks also go to my parents in law, Mr. Raghib Altaai and Mrs. Jenan Al-Azawi for their motivations and support. Also, my brothers in law, sisters in law, especially Mrs. Huda Altaai, my aunties, my relatives, my neighbours, my friends, especially Embareka and Sara. Thank you all for your valuable support and motivation.

Finally, I would like to thank the Iraqi government for my PhD scholarship funding and to anyone that has tried to help me and make me happy through my PhD study and life.

List of Tables

List of Figures

Publications

Maab H. Al-Hafidh, Andrew Glidle, Rab Wilson, Anthony E. Kelly, Julien Reboud and Jonathan M. Cooper "Multi-Reflection Polarimetry with MEMS-Machining and Microfluidics ", in preparation.

Maab H. Al-Hafidh, Andrew Glidle, Rab Wilson, Anthony E. Kelly, Julien Reboud and Jonathan M. Cooper "Multi-Reflection Polarimetry in Microfluidics" published in IEEE Sensor Letter, Sep 2019.

M. Al-Hafidh, R. Wilson, A. Glidle, J. Reboud, A. Kelly and J. Cooper "Micromirror angle dependence with etchant choice on <100> silicon via wet etching", proceeding paper of oral presentation at IEEE NANO 2018 Conference /Cork, Ireland | 23 – 26 July 2018.

M. Al-Hafidh, A. Glidle, J. Reboud, A. Kelly and J. Cooper "Improved Sensitivity of Optical Polarimetry with MEMS-Machining and Microfluidics", Presented paper in Nanophotonics and Micro/Nano Optics International Conference Barcelona, Spain 13th – 15th Sep 2017.

M. H. Al-Hafidh, A. Glidle, A. E. Kelly, J. Reboud, and J. M. Cooper "High Precision Microfluidic Polarimetry Measurements", Presented poster in a Biomedical away day workshop, Sep 2015.

Abbreviations

Al	Aluminium
Au	Gold
BHF	Buffered Hydrofluoric Acid
BSA	Bovine Serum Albumin
C	Concentration
CPD	Capillary Polarimetric Detector
CRDP	Cavity Ring Down Polarimetry
DOM	Modulation of Depth
GDS	Graphical Data System
HCl	Hydrogen Chloride
HF	Hydrofluoric Acid
HPLC	High-Performance Liquid Chromatography
ICP	Inductively Coupled Plasma
IPA	Isopropanol
KOH	Potassium hydroxide
LOD	Limit Of Detection
LPCVD	Low Pressure Chemical Vapor Deposition
M	Mirror
MEMS	Microelectromechanical systems
MF	MICROPOSIT Metal-Ion-Free DEVELOPER
MOEMS	Micro-Opto-Electro-Mechanical Systems
n	Refractive index
$n_{\pm}$	Refractive index of a chiral medium
n_0	Refractive index of an achiral medium
Na_2HPO_4	Disodium Hydrogen Phosphate
NaH_2PO_4	Sodium Dihydrogen Phosphate
NaOH	Sodium Hydroxide
OH^-	Hydroxyl ions
OR	Optical Rotation
P	Polarizer

PBS	Phosphate-buffered saline
PDMS	Polydimethylsiloxane
PECVD	Plasma-Enhanced Chemical Vapour Deposition
pKa	Dissociation constant
PMMA	Polymethyl methacrylate
PMT	Photomultiplier Tube
PTFE	Polytetrafluoroethylene
R	Reflectivity
$\theta^{(-)}$	Refractive angle of anti-clock wise optical rotation
$\theta^{(+)}$	Refractive angle of clock wise optical rotation
RO	Reverse Osmosis
S/N	Signal-to-noise ratio
SEM	Scanning Electron Microscopy
Si_3N_4	Silicon Nitride
SiO_2	Silicon Oxide
SSP	Single Side Polished
T	Temperature
TMAH	Tetramethylammonium hydroxide
UV	Ultra Violet

Chapter 1 Introduction

1.1 General Introduction

Polarimetry is a technique that measures the rotation of the polarization plane of linearly polarized light that is transmitted through a liquid sample to quantify the optical activities of compounds in solution. The polarized light will either rotate clockwise or counter-clockwise, and the amount it rotates indicates the angle of rotation [1]. Polarimetry is used routinely in quality and process control across a number of sectors, including the pharmaceutical, food and chemical industry, as well as the flavour, fragrance and essential oil industry.

Polarimetry provides useful insights into the molecular structure of an optically active medium, such as chiral molecules in a solution, and measuring the rotation of the polarization of a transverse wave while also determining their concentration [2]. Examples of such chiral compounds include many commonly used medicines whilst observing dynamic changes in chirality can also give insights into protein folding as well as the denaturation of DNA and RNA, [3], [4], [5]. The relative simplicity of polarimetry coupled with its nondestructive nature makes the technique particularly suitable for high value biological [6] [7] and chemical structures [8], [9]. In such circumstances, where the cost of compound production may be high, performing optical rotation measurement in very low, microliter scale volumes using polarimetry is important in order to increase the analytical performance without losing sensitivity.

In a reported study [10], the advantages of using a semiconductor light source for polarimetry have also been demonstrated, specifically by generating high optical power, and less flicker noise. In addition, for a given chiral substance, the wavelength dependence of a specific rotation provides an inversed relation ($1/\lambda^2$) [11]; thus, longer optical rotations require shorter wavelengths.

Here we show that when an optical beam, passing through a chiral sample, undergoes multiple reflections from suitably aligned and configured external micromirrors, the usual cancelling out of the optical rotation that occurs when the rotated polarized beam is passed back through a solution following reflection at a single mirror can be negated. This enables the chirality of molecular species present in a microfluidic sample to be measured with increased sensitivity. This approach was validated experimentally using solutions of D-(+)-glucose as a model system, by investigating the effect of multiple reflections of a linearly polarized He-Ne laser beam and a 403 nm diode laser beam across the microfluidic channel. It was found that there was a 30 fold enhancement in the limit of detection with as few as 11 reflections through the sample.

The layout of the thesis is shown in Figure 1.1.

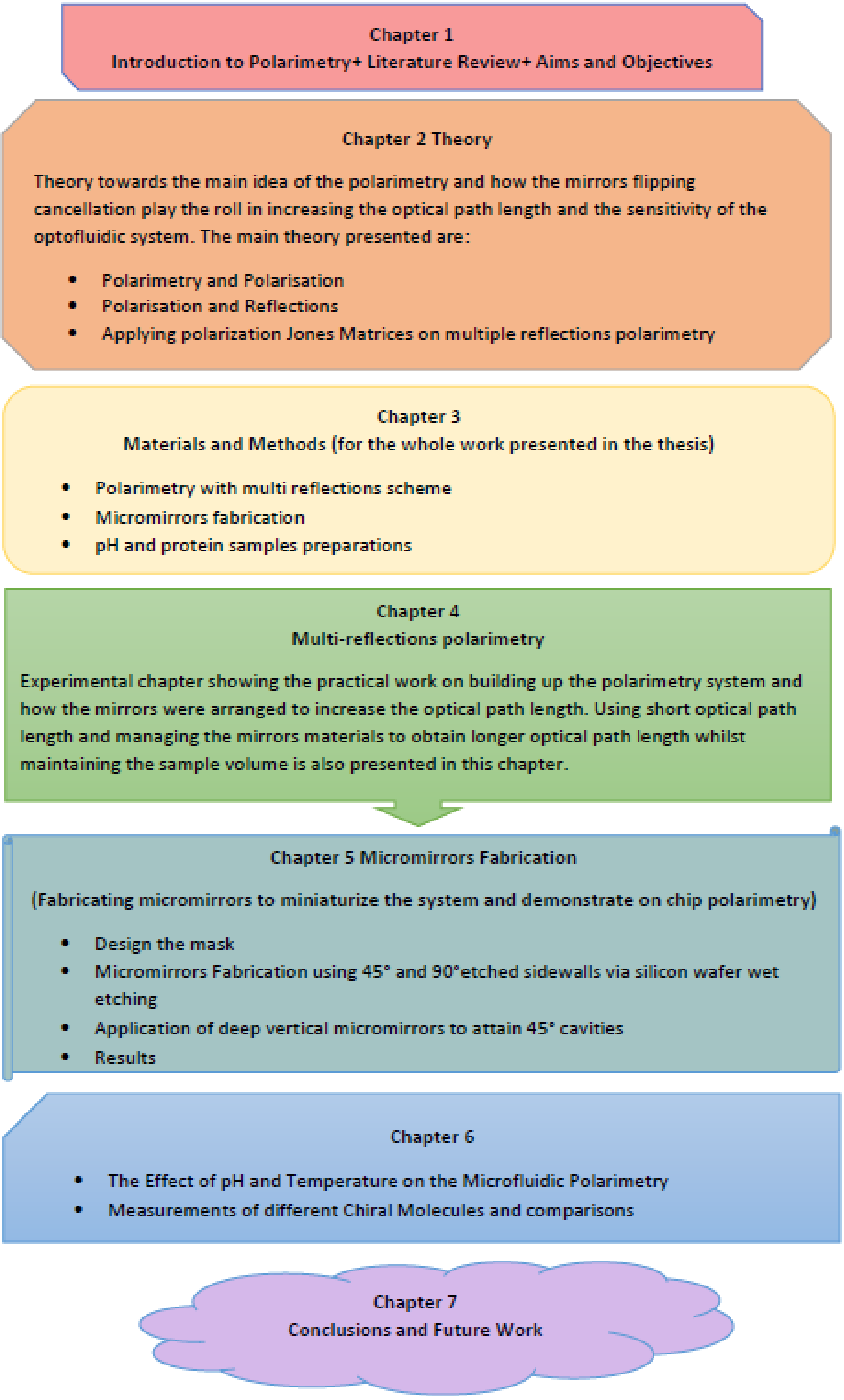

Chapter 1
Introduction to Polarimetry+ Literature Review+ Aims and Objectives

Chapter 2 Theory

Theory towards the main idea of the polarimetry and how the mirrors flipping cancellation play the roll in increasing the optical path length and the sensitivity of the optofluidic system. The main theory presented are:

- Polarimetry and Polarisation
- Polarisation and Reflections
- Applying polarization Jones Matrices on multiple reflections polarimetry

Chapter 3
Materials and Methods (for the whole work presented in the thesis)

- Polarimetry with multi reflections scheme
- Micromirrors fabrication
- pH and protein samples preparations

Chapter 4
Multi-reflections polarimetry

Experimental chapter showing the practical work on building up the polarimetry system and how the mirrors were arranged to increase the optical path length. Using short optical path length and managing the mirrors materials to obtain longer optical path length whilst maintaining the sample volume is also presented in this chapter.

Chapter 5 Micromirrors Fabrication

(Fabricating micromirrors to miniaturize the system and demonstrate on chip polarimetry)

- Design the mask
- Micromirrors Fabrication using 45° and 90°etched sidewalls via silicon wafer wet etching
- Application of deep vertical micromirrors to attain 45° cavities
- Results

Chapter 6

- The Effect of pH and Temperature on the Microfluidic Polarimetry
- Measurements of different Chiral Molecules and comparisons

Chapter 7
Conclusions and Future Work

Figure 1.1 A pictorial form of the thesis layout.

1.2 Milestones of Polarimetry

1.2.1 General polarimetry

Historically, the first studies into polarimetry techniques were recorded in the 16th Century, starting in 1669 when Bartholinus discovered double refraction in calcite. In 1670, Huygens described this resultant wave as a spherical wavefront and discovered extinction through crossed polarizers. Newton, in 1672, first developed the idea that light and crystals have attractive virtues lodged in certain sides and referred to the poles of a magnet as an analogy. This eventually led to the term “polarization”. In the 18th Century, Malus (in 1808) noticed that the intensity of two images in a reflection changed when the crystal rotated, thus “polarization by reflection”. After a few years, Biot, observed the rotation of the plane of polarized light passing through glucose molecules [12]. In 1812, Brewster, established the relationship between the degree of polarization with the angle of reflection and the refractive index [13], while, in 1817, both Fresnel and Young offered a theoretical explanation of Malus’ observation [14], and Faraday, in 1854, investigated the rotation of linear polarization (circular mode) [15].

From the 19th Century to the beginning of the 20th Century, hundreds of researchers studied polarimetry in different fields of application, including astronomy, wireless transmission, and optical polarization. One of the essential applications in optical polarization is the glucose concentration measurements that use a polarimetrical method. In other words, this enables typical monitoring for the level of blood sugar, which is essential for people who have diabetes [16]. In 1996, Darryl J. Bornhop and Joseph Hankins detected the optical rotation of mandelic acid using the capillary tube. In their scheme, the capillary polarimetric detector (CPD) via the capillary tube has two patterns from a laser beam (parallel and perpendicular). Therefore, with the modulation fringe depths, they achieved absolute rotation changes to the order of $1.3\text{x}10^{-4\circ}$ [17].

From the end of the last century until today, researchers have paved the way for noninvasive glucose measurements in a polarimetric setup by using the eye as a perfect optical window to the body, and the skin as an optical medium. In addition, sophisticated research describes the existence of micro-scale polarimetry approaches and how they tackle the barriers to low sensitivity measurement.

1.2.2 Polarimetry and glucose detection

In 1999, a team of researchers led by D. Cameron used two laser wavelengths to reduce the percentage error of the measurements which cause by the cornea birefringence. This was similar to a motion artefact through an interior chamber of the eye (in vivo) of a rabbit, they predicted their rotation effects by adding albumin and chiral protein (in vitro) [18]. Then, in 2001, they compared the glucose level calculations between the aqueous humour and blood. There was a time delay of approximately five minutes in the measurement of the humour and they concluded that this method would develop a way to provide non-invasive glucose predictions as the results were the same as those for blood [19]. By using lock-in amplifiers and a Faraday compensator, the temperature, pH, and birefringence in the eye were demonstrated to study the influence the rotation of polarization; in 2002, the same group studied these again [20]. They concluded that the effect of albumin only becomes vital when using light wavelengths below 600 nm. In 2005, they used combined dual-wavelength in polarimetry to minimize the errors, which came from the birefringence of the cornea; this was achieved by compensating cornea birefringence. These techniques developed a way to calculate non-invasive glucose level measurements with high-efficiency results [21]. The study of polarimetry to determine the glucose percentages of the eye, as a chamber, has been expanded by this group as they have achieved more enhancements in the setup by compensating the birefringent levels that occur in the eye. This was achieved by using real-time and closed-loop feedback, as the reduction of the variant time depended on the artefact motion of the corneal birefringence, which caused high-level sensitivity results [16], [22]. Georgeanne Purvnis worked with the same group to develop a non-invasive polarimetry intervention by measuring the glucose concentrations in the eye of a rabbit. This was subsequently improved for easy use in the home and hospital and without the side effects of invasive measurements [23]. Ansari et al. described a new approach to non-invasively detect optical rotation changes in the aqueous humour of the eye through shifts in the glucose levels. The technique depends on Brewster's reflection concept of circularly polarized light from a lens that enables a simple and comfortable detection method. However, it has low sensitivity and high error due to the motion artefacts and corneal birefringence variation [24].

In 2007, Cameron et al. predicted the glucose concentrations by imaging the scattering of the media which includes the intralipid inside and uses the polarimetry system [25]. Whilst in 2007 and 2008, Pastskovsky et al. made a unique model of surface plasmon resonance polarimetry. They enhanced the work of SPR by using a photo-elastic modulator and achieved an ultra-sensitive, phase-based response to refractive index changes through the mechanism of frequency modulation [26]. Furthermore, they placed spatial modulation by birefringence elements for further enhancement to the latter. The biomolecule interactions are measured by enabling the combination of phase-sensitive modulation with intensity calculations which result in high-level gains when applied to biological interactions [27].

Chi-Fuk So et al. presented the benefits and drawbacks of using the eye as an optical window to the body using polarimetry. Low light absorption and scattering in the aqueous humor of eye encouraged the use of the eye as a detection mechanism for the body. However, the movement of the eye and the resulting motion artefact still represents one of the general sources of error in polarimetry techniques [28].

1.2.3 Micro-scale polarimetry

Different ways of performing polarimetry have already been implemented in microfluidic systems to allow for the measurement of micro-volumes [29]. However, according to Biot's law, the short optical path lengths, in turn, decrease the optical rotation sensitivity [24].

Some microfluidic polarimetry devices have avoided this challenge by improving the sensitivity of measurements without increasing the path length. For example, this involves using back-reflected fringe patterns from the microfluidic channel [17], [30], [31] or measuring the difference between the refraction angle between two circularly polarized beams using microfluidic device chambers in the shape of array prisms [32-34]. These studies are briefly described in this chapter.

In the 1980s, a very limited achievement occurred in the incorporation of polarimetry with microfluidic detection. In the early 1980s, Yeung et al. and Bobbit used a high-performance liquid chromatography detector to expose the optical rotation of microliter-sized samples in flow and gained extinction ratios four orders of magnitude better than the standard instruments [35]. The work of Mayster with Bobbit [36] and Yeung [37] made particular progress upon the earlier work of Yeung et al [35] on the micro-scale ranges in polarimetry building. These gave improved sensitivities down to 10 µM (for a 10 cm path length) by implementing a high-performance liquid chromatography detector (HPLC) in the system. However, the instrument for applying HPLC is expensive. Meanwhile, in an effort to expand the capability of polarimetric detection in micro-volumes, Lloyd et al. improved the sensitivity of the measurement by using a semiconductor diode laser, which has low flicker noise, along with the coupling of HPLC and UV detectors to reach 8 µL of 1 cm length of sample cell [38].

The miniaturization trends in polarimetric setups were continuous up to the 1990s. Mayster and a team of researchers configured a 'two in one' detector system by introducing a refractive index detector in addition to polarimetry for 'equalization, refractive index compensation'. This eliminated the false pseudo rotation leading to increases in sensitivity to a 3 µL sample using a 10 cm length path cell. In this method, the additional management of the refractive index helped to avoid interactions with the sample [36].

Despite these many attempts to implement polarimetry in a small volume range, the detection was challenging since the signal to noise ratio was low. It involved a large volume flow cell and, therefore, the optical arrangement was complicated. Bornhop achieved picolitre volumes by using micro interferometric backscattering. The positional shifts between the maximum and minimum fringes correspond to refractive index variations; these were measured and facilitated the detection of flowing streams in a capillary tube with a 350 pL volume. The sample solution in this capillary cell was illuminated at its central side axis; the scattered light was collected at 360° with the concentration detection depending on the observation results of the interference fringes [17], [39]. Furthermore, in 1996, Bornhop worked with Hankins to develop a sensitive technique based on the modulation depth (DOM) of the high-frequency component, which is sensitive to the plane of polarization of incident light (10^{-4} °). Furthermore, it enabled the determination of optical rotation in nanoliter samples by a Capillary Polarimetric Detector (CPD) [17], (see Figure 1.2).

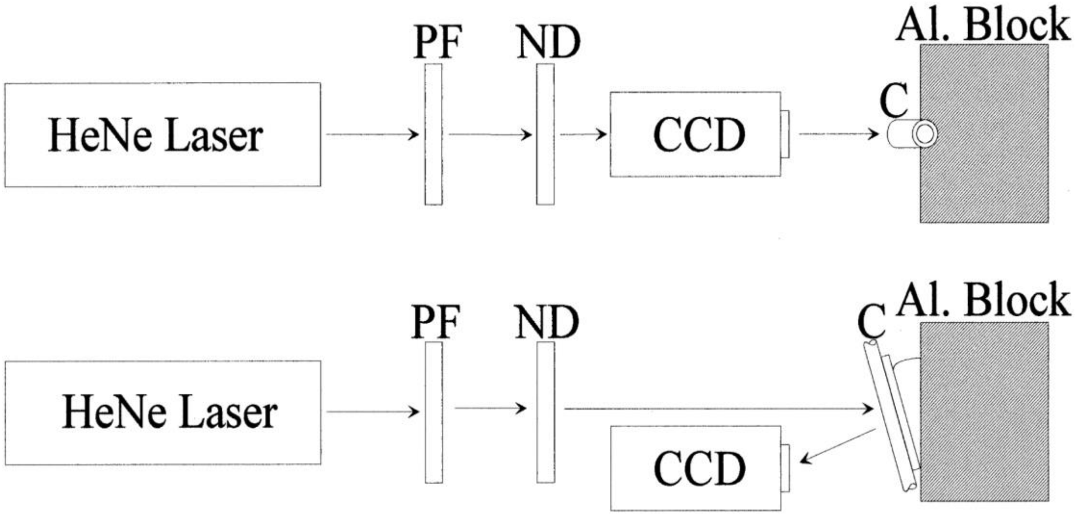

Figure 1.2 Block diagram for the capillary polarimeter (sideview). The He−Ne laser is linearly polarized, PF is a 10 000:1 glass polarizing filter, ND is a neutral density filter, C is a fused silica capillary, Al block is a mounting block made of aluminium, and CCD is a camera. The output (fringes) of the CCD is sent to an LBA (laser beam analyzer, not shown), which in turn sends a signal to a personal computer (also not shown) [17].

Recently, various optical approaches have been implemented to enhance polarimetry measurements in small volumes. Gibbs et al. established parallel detection by the synchronized imaging of the optical activity of several channels with a 12 cm path length that opened up multiplexed imaging polarimetry. Although the well has a small volume of 10 µL, it has a long optical pathlength and a low resolution of 0.5° [30]. Swinney et al. developed their work along with a Capillary Polarimetric Detector (CPD) to measure the absolute optical rotation power, [40]. They minimized the perturbation of the refractive index using the scope-configured detector, and achieved a 10^{-6o} resolution of solutions with 66×10^{-6} M R-mandelic acid [41].

Although the fringes method, which depends on the calculation of the depth of modulation, was simple to implement in nanoliter polarimetric measurements, DOM is time-consuming (10 minutes per data point) due to the fact that fringes are usually obtained manually then transferred to a computer for analysis. In addition, the calculations only consider two data points (I_{max} and I_{min}), omitting the rest of the trace, which depends on the CCD chip size and therefore yields large percentage errors and low signal to noise (S/N) ratios. To tackle this, Markove et al. interrogated a Fourier transform of the data to dramatically increase the speed (microsecond time scale) and S/N, and reduced the error, as this method can analyze several fringes simultaneously [42].

In 2012, Bornhop et al. described a polarimetry on-chip set-up that used micro interferometric backscattering from a 90 µm microfluidic channel on the chip, and imaged the fringes to determine the optical rotation to 1.8 nL [31], (see Figure 1.3).

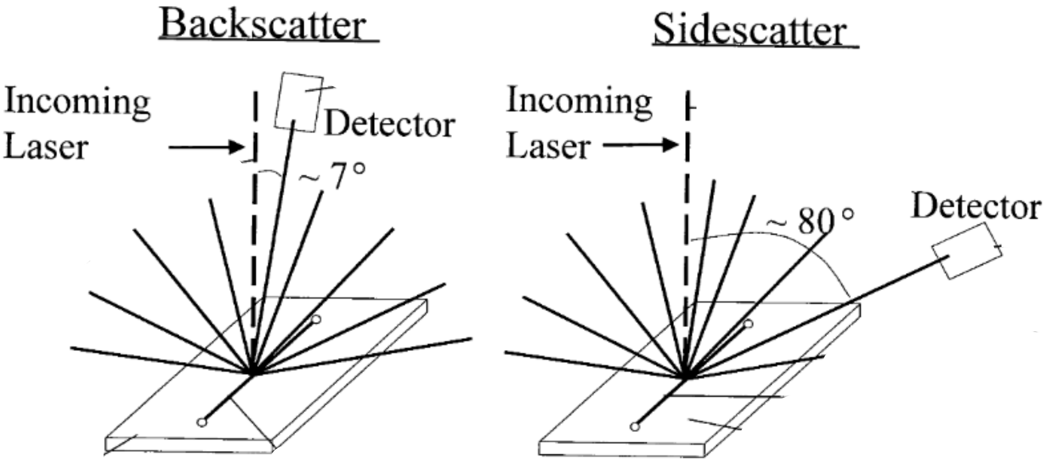

Figure 1.3 Schematic illustrations showing the relative positioning of a photodetector element in direct backscatter and side scatter detection configurations, respectively [31].

In the trend for enhancing polarimetry detection in lab-on-chip devices, Rajan et al. measured the differences between the refracted angles between two circularly polarized beams using microfluidic device chambers in the shape of array prisms to reach a 5.5×10^{-2} mM (10 mg/ml) glucose limit of detection [32-34], (see Figure 1.4).

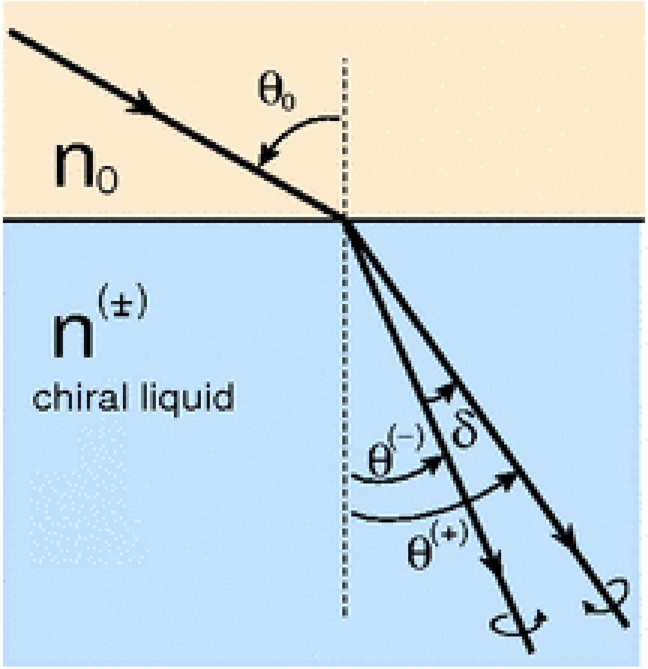

Figure 1.4 Splitting of a linearly polarized light beam when it is incident on a chiral medium from an achiral medium [32].

1.2.4 Reflection polarimetry

Cavity-ring-down spectroscopy, classically using a two-mirror cavity without intra-cavity optics, was used to increase the optical path length. This strategy can be applied to polarimetry but requires additional intra-cavity optics to avoid the light rotation of forward and backward reflections through the cavity, which cancel out each other. To overcome this, Rakitzis et al. [43], [44], [45], [46] used an intra-cavity Faraday rotator as a nonreciprocal signal reversing method; this enabled an increase in the optical path length of up to 100 km, (see Figure 1.5). Although Muller et al. used the same cavity, they also incorporated an intracavity λ/4 retarder to make the ring down sensitive to the effects of optical rotation and to overcome the back and forth polarization cancellation through a chiral medium [47]. However, this method requires high-cost equipment and large set-ups (>1 m path length) (see Figure 1.6).

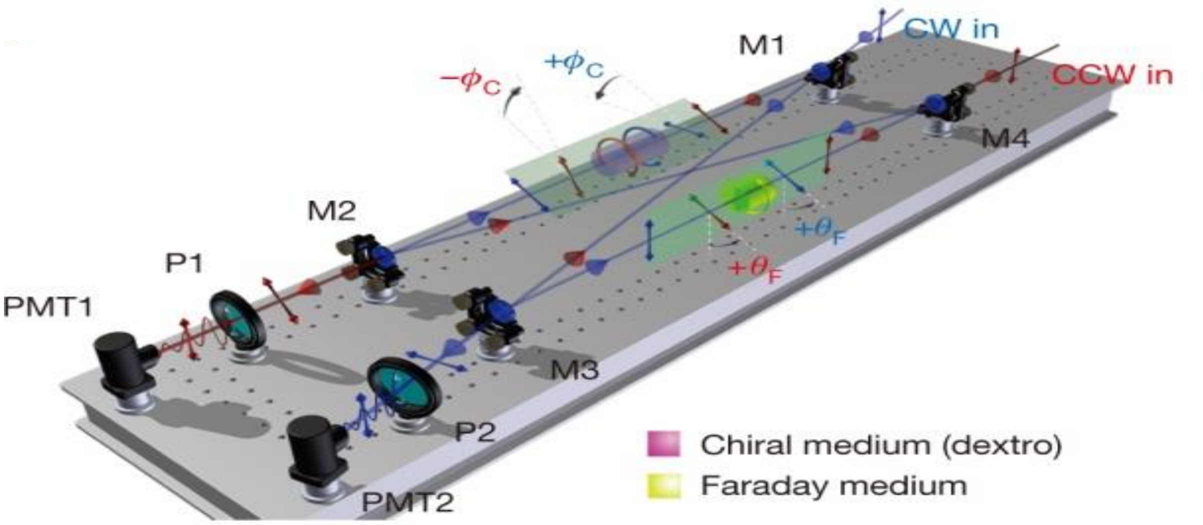

Figure 1.5 The layout of four mirrors (M1–M4), polarizers (P1, P2), photomultiplier tubes (PMT1, PMT2), the chiral sample, the Faraday medium and the counter-propagating laser beams (CW and CCW), [45].

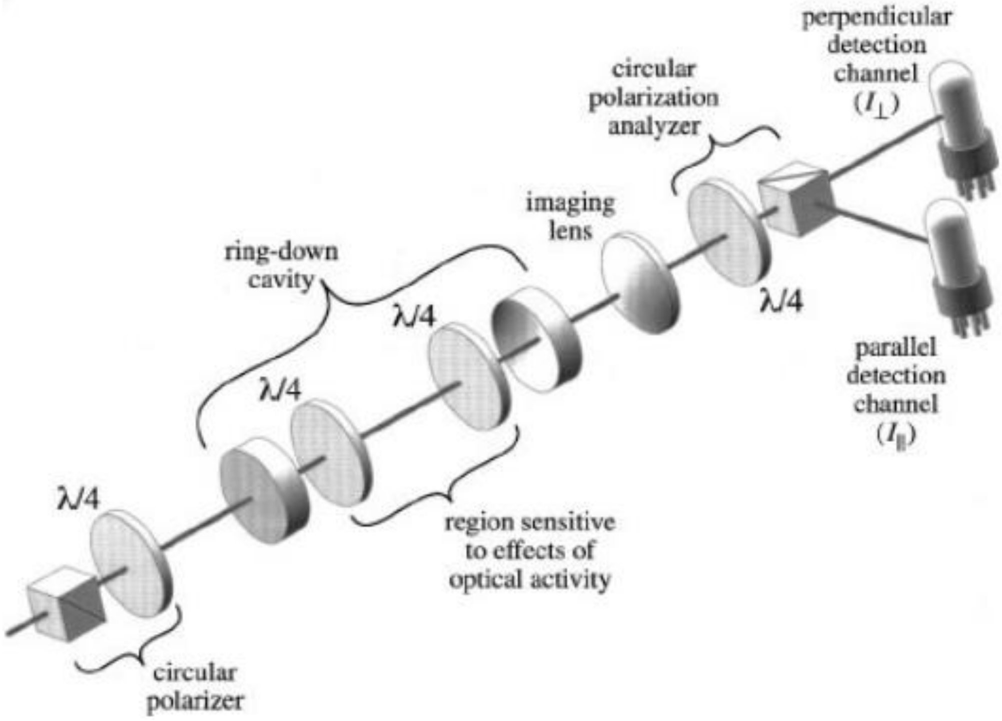

Figure 1.6 Schematic diagram of the CRDP apparatus. The pulsed radiation at 355 nm or 633 nm is spatially filtered and the mode-matched for the CRDP resonator before a circular polarizer is traversed. This consists of a tandem calcite prism (linear polarizer) and a quarter-wave plate. The resulting beam is coupled with a stable linear cavity by passing through the planar rear surface of the input mirror. Intracavity l/4 retarders are aligned to produce a linearly polarized internal field. Light emerging from the output mirror is imaged onto identical photodetectors that monitor the two mutually orthogonal components of linear polarization generated via a second circular polarization analyzer [47].

Zhou et al conducted the only investigation into polarimetry by reflection without a cavity ring down. The beam was internally reflected at an angle slightly greater than the Brewster angle (from dielectric material) of the sample container. A sizeable optical rotation of the reflected light was obtained from a small change in the polarization of the incident light (polarization differential detector); this delivered a sensitive system for the low sample optical rotation. However, the optical path length was more than 1 cm (the cuvette) with high volume, the system was slightly complicated, and the massive intensity losses for the second or higher order reflections generated impractical measurements [10].

1.2.5 Other studies

Protasov et al. used an infrared laser to detect the light optical rotation when passes through biological tissues by utilizing the hand's fingers as a biological object chamber. They converted the analyzer rotation to an optical signal to attain a 0.18°/cm resolution [48]. Gevorgyan et al. hypothesised a way to amplify the optical rotation signal by using different materials that suited linear and elliptical polarisation; however, these are yet to be used in reflection polarimetry [49]. Although this work was undertaken for a non-microfluidic sample, it can be helpful to amplify the signal to compensate for the micro-sample's weak optical rotation.

1.3 Aims and Objectives

The primary aim of this project was to investigate a way to amplify the weak polarisation rotation inherited within microfluidic samples in a polarimetry system. Due to the non-reciprocal nature of chiral molecule-polarised light interactions, it was postulated that, by adding double reflections before each sample pass, the polarisation could be reverted to a native state after a proceeding pass. As such, the research objectives were categorised into three sections:

1. The utility of two reflections before the laser interrogates the sample in order to overcome the cancellation of the polarisation rotation using two regular parallel mirror reflections.

2. The fabrication of 45° and 90° micromirrors using silicon micromachining to build on-chip polarimetry using multiple reflections.

3. The use of acid and base-chiral molecule interactions to increase the plane-polarised optical rotation.

Each of these objectives forms a results chapter containing an introduction that provides an explanation as to why the project objectives align with prominent issues identified in the literature.

Therefore, this introductory chapter provides a broader sense of the field of polarimetric measurement technologies and the various ways to cancel the reversible manner of chiral molecules on reflections.

Chapter 2 Theory

2.1 Polarimetry

The biomedical research field is expanding as rapidly as creativity and scientific resolves allow. One of the main aims of biomedical research is to elucidate the molecular world, which still remains uncertain but is becoming ever clearer. Micro-scale polarimetry is one of the critical measurements requiring highly sensitive techniques to achieve accurate information about chiral molecules. Polarimetry measures the rotation of the polarization of the transverse wave when it passes through an optically active medium, such as chiral molecules [2].

The basis of polarimetry is the interaction between polarized light and an optically active sample, as shown in Figure 2.1 [50]. This interaction is related to the nature of the molecular structure of the sample and the electron cloud of the molecule. The optical rotation depends on the concentration of the solute and the path length. The specific rotation takes these factors into account. In addition, the optical rotation is also dependent on the wavelength and temperature, but usually not as much as the path length and concentration.

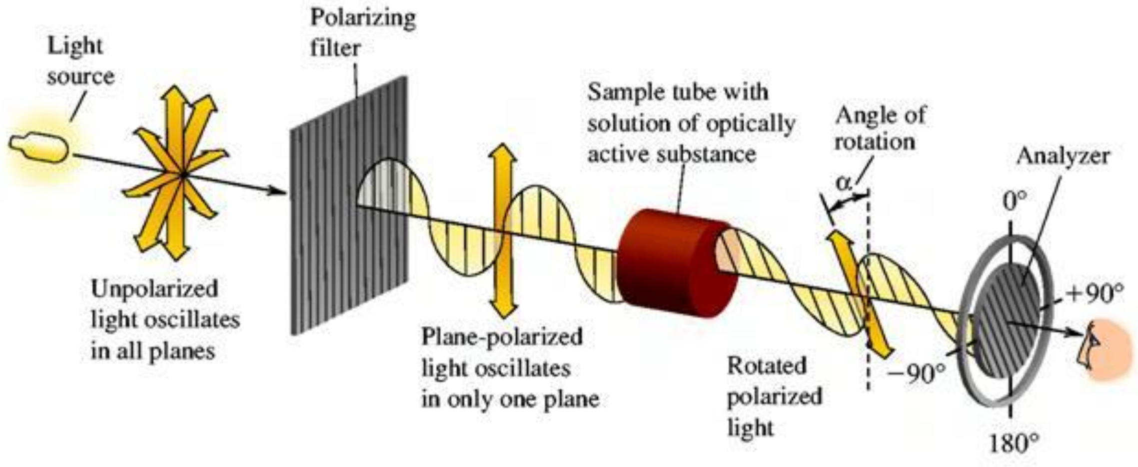

Figure 2.1 Polarimetry system to measure the polarization rotation of polarized light in the optically active sample [51].

$$\left[\alpha\right]_{\lambda,pH}^{T} = \frac{\alpha}{cl} , \tag{2.1}$$

The specific rotation $\left[\alpha\right]_{\lambda,pH}^{T}$, Equation (2.1), is a physical property and defined as the optical rotation where α is a path length, l is 10 cm, concentration c is 1g/mL, T is solution temperature (usually 20 °C), and λ is a wavelength of the light source, pH is the power of the hydrogen of the sample [11]. This equation was necessary for my work because I increased the optical path length through managing the factors which the optical rotation rely on upon via this equation.

However, the fabrication of micro-polarimetry devices needs to implement different techniques and approaches. The synchronization of instruments operations in polarimetry plays an important role, as the power corresponding to each polarizer angle is different from the others and the measurement of shift (rotation angle) depends on this value of power (real time) for each angle. Advances in polarization modulation, detector and computational technologies alongside novel polarimetry provide the capability of measuring in nano-litre samples with a high degree of spatial and temporal resolution.

2.2 Polarization

The basis of polarimetry work is the polarization of transverse mechanical waves, which are polarised when the propagation direction line of the wave, and the line along which the vibrating particles are both on the same plane (the displacement of the particles). This is because these waves usually oscillate in any orientation that is perpendicular to the direction of travel - from side to side or up and down, etc.

Electromagnetic waves comprise of perpendicular oscillating electric and magnetic fields, perpendicular to the propagation direction, which make these waves transverse. This means that Electromagnetic waves can be polarised. The plane containing the oscillating electric field vector and the direction of propagation is the vibration plane of the Electromagnetic wave. The perpendicular plane to that containing the electric vector is the plane of polarisation. Transverse waves can oscillate in any plane, while linear polarisation is the process by which the oscillations are located on one plane only (see Figure 2.2).

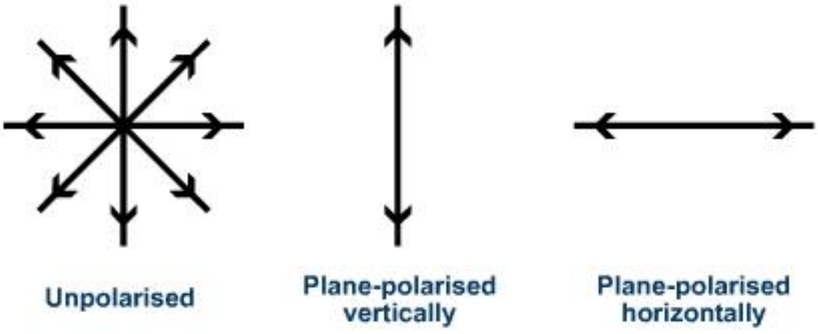

Figure 2.2 Illustration of the type of polarizations [52].

In some cases, the polarization occurs by passing the waves through a 'grid, like the polarizer' so that only the waves that can fit through the slits pass through (Figure 2.3). Also it can be by reflections or creating waves in one plane (for example, a laser) [52].

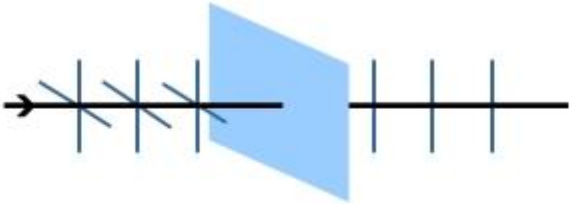

Figure 2.3 Polarizer to convert the unpolarized laser to a polarized one [52].

As indicated, the light wave whose electric vectors move in perpendicular directions is linearly polarized light. Otherwise, it is either circularly polarized light (when their electric vectors have equal amplitude but are out of phase (π/2)), or elliptically polarized light (unequal in amplitude and phase shifted) [52].

2.3 Maintaining linear polarization

When the light passes through several components in the experiment, this will result in several changes to its power and polarization. The problems that one might encounter are as follows [53, 54]:

- **Depolarization on reflection:** If the light is linearly p-polarized (Its vector precisely perpendicular to the plane of the incident), the polarization state will not be changed. Nevertheless, the difference in the phase shift between reflected s (The light vector precisely perpendicular to the plane of the incident) and p components of the light will happen when this polarized light encounters a material interface leading to elliptical polarized light if the initial polarized light is not aligned.

- **Geometrical effect:** In such a sensitive polarimetry experiment, the light should be kept in a plane of polarisation vector or perpendicular to the polarization vector.

- **Elements to manipulate the polarization (waveplates, polarizers)**: These elements depend mostly on the wavelength of the light.

2.4 Birefringence and chiral molecules

The rotation of the plane of polarization of linearly polarized light as it travels through certain materials is called optical activity or rotation. Optical activity only occurs in chiral materials, or those lacking in microscopic mirror symmetry. Unlike other sources of birefringence, which alter the beam's state of polarization, the optical activity can be observed in fluids. There are some specific changes that happen to the substances which are illuminated by polarized light. These could include rearranging the absorbing centre, damaging the absorbing molecules, or other variations according to the light polarization. The effect of molecules changes on the polarization state of the light leads to changes in the absorption coefficient (named dichroism) and/or in the refractive index of the material (named birefringence), namely, an optical anisotropy [55].

Chiral molecules are like pairs of mirror-image isomers (two mirror images of a chiral molecule are called enantiomers or optical isomers). A pair of enantiomers have identical physical and chemical properties, but also have two exceptions: the way that they interact with polarized light and the way that they interact with other chiral molecules [56]. Pairs of enantiomers are often designated as "right-"

and "left-handed", as shown in Figure 2.4, for the generic amino acid, for example, of a chiral molecule.

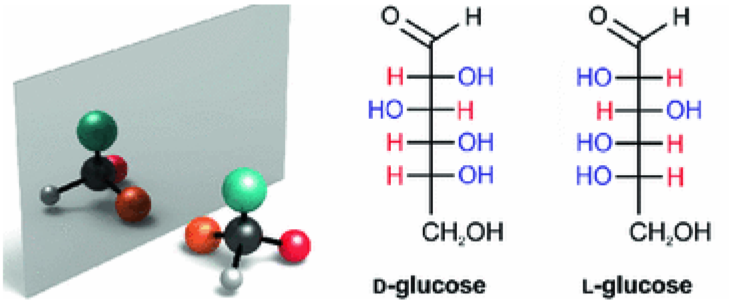

Figure 2.4 An example of a chiral molecule (glucose) [57].

In some applications that require interactions between the polarized light with the molecule possessing chirality properties, it can be clearly seen that the plane of the output polarized light is rotated by an angle toward the right or left according to the original orientation and depending on different parameters. This type of molecule is known as an optically active molecule. Depending on the direction of rotation, the compound that rotates the plane of polarized light counterclockwise is called levorotary (-), while that which rotates in a clockwise direction is called dextrorotatory (+) [58].

The following sections provide a set of equations designed to keep track of any change in the polarization of light when it passes through the optical elements. In addition, these changes in the polarisation of polarimetry system arise as a result of the introduction of reflection arrangement in the polarimetry system to increase the optical path length.

2.5 Jones Vectors

Jones presented a two-dimensional matrix algebra which offers a useful way to represent polarized light for optical components in order to study their polarization effect [54]. For the electric field, Maxwell's plane wave solution is considered in Equation (2.2) [59].

$$E(z,t) = \left(E_x \mathbf{x} + E_y \mathbf{y}\right) e^{i(kz-\omega t)} \tag{2.2}$$

Where E_x and E_y are the instantaneous scalar components of the electric field (light) in X and Y directions, respectively ($E_x = E_o \cos\varnothing_x$, $E_y = E_o \sin(\theta + \varnothing_y)$), E_o is the amplitude of the electric field, k is the wave number, z is the wave propagation direction, ω is the light angular frequency, t is the time. The coordinate system is depicted in Figure 2.5.

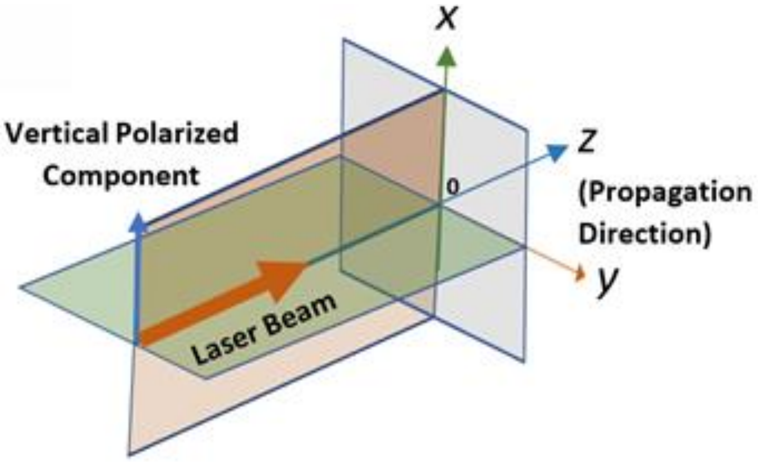

Figure 2.5 Coordinate system for wave propagation, with the laser beam polarized on the *xz* plane.

By adding the complex phases of the field components, which are required in Jones vectors, in order to know the polarization state, the electric field becomes as shown in Equation (2.3):

$$E(z,t) = \left(|E_x| e^{i\varnothing_x} \mathbf{x} + |E_y| e^{i\varnothing_y} \mathbf{y}\right) e^{i(kz-\omega t)} \tag{2.3}$$

Where $\varnothing_x$ and $\varnothing_y$ are a phase of $\mathbf{x}$ and $\mathbf{y}$ components, respectively. Equation (2.3) can be written in a general form that is very simple to put in the matrix form:

$$E(z,t) = E_{eff}\left(Ax + Be^{i\Delta}\, y\right) e^{i(kx-\omega t)} \tag{2.4}$$

where:

$$E_{eff} = \sqrt{|E_x|^2 + |E_y|^2}\, e^{i\varnothing_x} \tag{2.5}$$

$$A = \frac{|E_x|}{\sqrt{|E_x|^2 + |E_y|^2}} \quad , \quad B = \frac{|E_y|}{\sqrt{|E_x|^2 + |E_y|^2}} \quad , \quad \Delta = \varnothing_y - \varnothing_x \qquad \textbf{(2.6)}$$

Now we can represent the general form of the Jones vector as Equation (2.7), and the special case for the linearly polarized light as Equation (2.8).

$$E = \begin{bmatrix} A \\ Be^{i\Delta} \end{bmatrix} \qquad \textbf{(2.7)}$$

$$E = \begin{bmatrix} E_x \\ E_y \end{bmatrix} = \begin{bmatrix} \cos\vartheta \\ \sin\vartheta \end{bmatrix} \qquad \textbf{(2.8)}$$

Where, ϑ is the direction of E (electric field of the light) with respect to the x-axis. An operation on the polarization state will perform if this light will encounter the optical components.

The Jones matrix for one of the most essential elements, namely the polarizer, in its general form, is shown in Equation (2.9), where β is the angle of the polariser direction with respect to the y-axis.

$$M_p = \begin{bmatrix} \cos^2\beta & \cos\beta\sin\beta \\ \sin\beta\cos\beta & \cos^2\beta \end{bmatrix} \qquad \textbf{(2.9)}$$

For the optically active medium sample, the Jones matrix is written as [24]:

$$M_{OAR} = \begin{bmatrix} \cos\alpha & -\sin\alpha \\ \sin\alpha & \cos\alpha \end{bmatrix} \qquad \textbf{(2.10)}$$

Where α is the angle of optically active rotation given in Equation (2.1).

2.6 Polarization and reflection

The Fresnel coefficients in the perpendicular and parallel components of the light (r_s and r_p), Equations (2.11)-(2.12) respectively [50], identify the quantity of transmitted and reflected light and pursue the phase shift between s and p of the electric component of the light, which ultimately gives the polarisation state after reflection [60].

$$r_s \equiv \frac{E_r^{(s)}}{E_i^{(s)}} = \frac{n_i \cos\vartheta_i - n_t \cos\vartheta_t}{n_i \cos\vartheta_i + n_t \cos\vartheta_t} = \frac{\sin(\vartheta_t - \vartheta_i)}{\sin(\vartheta_t + \vartheta_i)} \quad \textbf{(2.11)}$$

$$r_p \equiv \frac{E_r^{(p)}}{E_i^{(p)}} = \frac{n_i \cos\vartheta_t - n_t \cos\vartheta_i}{n_i \cos\vartheta_t + n_t \cos\vartheta_i} = \frac{\tan(\vartheta_t - \vartheta_i)}{\tan(\vartheta_t + \vartheta_i)} \quad \textbf{(2.12)}$$

Where E_i and E_r are the incident and reflected electric fields, n_i and n_t are the refractive indices of the incident and transmitted mediums respectively. ϑ_i and ϑ_t are the incident and transmitted angles respectively, $\boldsymbol{i} = \sqrt{-1}$.

For instance, linearly polarised light might become elliptically polarised after reflection from metal [61]. Similarly, right-circularly polarised light may change to left-circularly polarised light since the beam reflects at a normal incidence [59, 62]. This is the reason why the right-hand of a person appears to be the left hand when observed in a mirror [59].

For example, Figure 2.6 illustrates the relationship of the Fresnel coefficients to the incident angle in the case of an air-glass (dielectric) interface. It can be noted that there is a negative reflection coefficient for the perpendicular components and a part of parallel components, which correspond to a phase shift of π upon reflection. These coefficients are encountered in the case of absorbing materials because the complex index of refraction with more complicated phase shifts can arise due to this complex index [61].

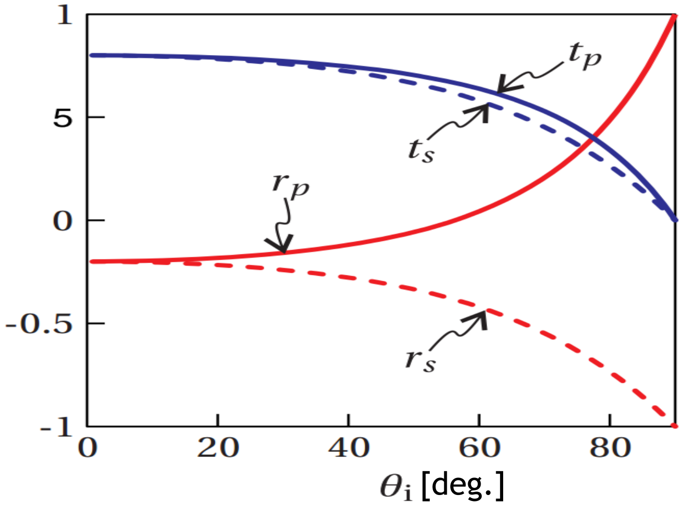

Figure 2.6 Fresnel coefficients at dielectric boundary. r_p and r_s (solid and dashed red respectively) are reflactance Fresnel coefficients in the parallel and perpendicular components of the light respectively. t_p and t_s (solid and dashed blue respectively) are transmitance Fresnel coefficients in the parallel and perpendicular components of the light respectively [59].

To represent the reflection of polarized light, the Jones matrices are useful for keeping track of any change in the polarization of light when passing through the optical elements. The Jones matrix of the reflection M_r from the surface is shown in Equation (2.13) [59].

$$M_r = \begin{bmatrix} -r_p & 0 \\ 0 & r_s \end{bmatrix} \quad \textbf{(2.13)}$$

The negative sign of r_p refers to the handedness or chirality of the inversion, r_s and r_p (Fresnel coefficients); determine the final relative properties of the s and p field components and the phase shift between them as they define the ratios between the existing fields to the incident fields. When Equation (2.13) operates on an arbitrary Jones vector, such as in Equation (2.7), $-r_p$ multiplies the horizontal component of the field and r_s multiplies the vertical component of the field.

In the case of multiple reflections within two or more mirrors, which lie in the same plane, the polarisation result is the multiplication of the sequence of appropriate Jones matrices in Equation (2.13) with the initial polarisation state. However, the coordinate system will be reoriented before each mirror, if these mirrors are vertically tilted in order to have a new vertical and horizontal of s- and p- polarised dimension, respectively [59]. The rotations of a coordinate system through an angle (ϑ_c) is shown in Equations (2.14) and (2.15).

$$E_1 \equiv E_x \cos\vartheta_c + E_y \sin\vartheta_c \tag{2.14}$$

$$E_2 \equiv -E_x \sin\vartheta_c + E_y \cos\vartheta_c \tag{2.15}$$

This rotation can be accomplished by multiplying the incident Jones vector with the matrix M_{rco} as in Equation (2.16) [59, 63].

$$M_{rco} = \begin{bmatrix} \cos\vartheta & \sin\vartheta \\ -\sin\vartheta & \cos\vartheta \end{bmatrix} \tag{2.16}$$

In the case of the coordinate's reorientation, the new field components are obviously the result of the combined formation of two orthogonal initial components. These quantify the orientation of the minor and major axis of the resultant elliptically polarised light, but do not change the elliptical properties of the polarisation.

As it is known, the detected power can be expressed as intensity (I_r and I_i) (i.e. power (P) per area), where the intensity is proportional to the square of the field amplitude. So the fraction of reflected power, called reflectance, can be written in terms of the previously defined Fresnel coefficients [59].

$$R_s \equiv \frac{P_r^{(s)}}{PI_i^{(s)}} = \frac{I_r^{(s)}}{I_i^{(s)}} = \frac{\left|E_r^{(s)}\right|^2}{\left|E_i^{(s)}\right|^2} = \left|r_s\right|^2 \tag{2.17}$$

$$R_p \equiv \frac{P_r^{(p)}}{P_i^{(p)}} = \frac{I_r^{(p)}}{I_i^{(p)}} = \frac{\left|E_r^{(p)}\right|^2}{\left|E_i^{(p)}\right|^2} = \left|r_p\right|^2 \tag{2.18}$$

From Equations (2.17) and (2.18), the total reflected intensity can be calculated according to Equation (2.19).

$$\boldsymbol{I}_r = I_r^{(s)} + I_r^{(p)} = R_s I_i^{(s)} + R_p I_i^{(p)} \tag{2.19}$$

Where the total incident intensity, according to the Poynting vector for a plane wave, can be written as Equation (2.20).

$$\boldsymbol{I}_i = I_i^{(s)} + I_i^{(p)} = \frac{1}{2} n_i \varepsilon_o c \left[\left| E_i^{(s)} \right|^2 + \left| E_i^{(p)} \right|^2 \right] \tag{2.20}$$

For an air-glass interface, for example, Figure 2.7 shows the typical reflectance and transmittance values plotted versus ϑ_i with n_i = 1 and n_t = 1.5.

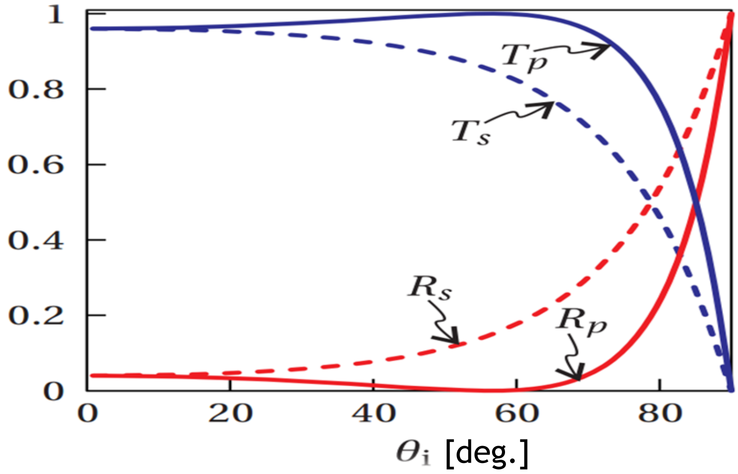

Figure 2.7 The reflectivity and transmissivity plotted versus incident angle ϑ_i. R_p and R_s (solid and dashed red respectively) are reflactivity Fresnel coefficients in the parallel and perpendicular components of the light respectively. T_p and T_s (solid and dashed blue respectively) are transmissivity Fresnel coefficients in the parallel and perpendicular components of the light respectively [59].

In most cases, the Fresnel coefficients can be calculated from the angle of incident and the index of reflection for both the metallic and dielectric mediums. According to Snell's law, Equations (2.11) and (2.12) can be rewritten as Equations (2.21) and (2.22) [59].

$$r_s = \frac{n_i \cos\vartheta_i - n_t\sqrt{\frac{n_i^2}{n_t^2}sin^2\vartheta_i - 1}}{n_i \cos\vartheta_i + n_t\sqrt{\frac{n_i^2}{n_t^2}sin^2\vartheta_i - 1}} \quad \textbf{(2.21)}$$

$$r_p = \frac{n_t\sqrt{\frac{n_i^2}{n_t^2}sin^2\vartheta_i - 1} - n_i \cos\vartheta_i}{n_t\sqrt{\frac{n_i^2}{n_t^2}sin^2\vartheta_i - 1} + n_i \cos\vartheta_i} \quad \textbf{(2.22)}$$

As mentioned above, the reflected surfaces are either dielectric or metallic materials. The Fresnel forms in Equations (2.21) and (2.22) can be applied with the first type. However, these coefficients are not directly applicable to metal reflections where more complicated phase shifts can arise. Therefore, in the case of a metal with a complex refractive index, $N = n + i$ k (n is the material refractive index and k is the extinction coefficient), the Fresnel forms can be written as [59]:

$$r_s = \frac{\cos\vartheta_i - \sqrt{N^2 - sin^2\vartheta_i}}{\cos\vartheta_i + \sqrt{N^2 - sin^2\vartheta_i}} \quad \textbf{(2.23)}$$

$$r_p = \frac{\sqrt{N^2 - sin^2\vartheta_i} - N^2\cos\vartheta_i}{\sqrt{N^2 - sin^2\vartheta_i} + N^2\cos\vartheta_i} \quad \textbf{(2.24)}$$

After calculating these reflectivities, it is useful to write them as an expression of the quantity of the output orthogonal components and the phase shift (polarization), $\Delta = \varphi_p - \varphi_s$, between them, thus:

$$r_s = |r_s| e^{i\varphi_s} \quad \textbf{(2.25)}$$

$$r_p = |r_p| e^{i\varphi_p} \quad \textbf{(2.26)}$$

Where φ_s and φ_p are the phases between the Fresnel coefficients, r_s and r_p, on reflection. Figure 2.8 shows both components with their corresponding shift versus the angle of the incident [52].

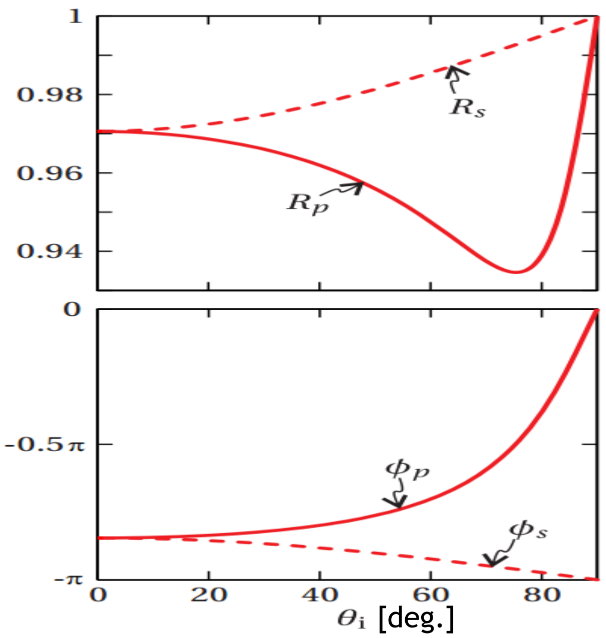

Figure 2.8 The reflectance (top) with the associated phases (bottom) for silver, which has index n = 0.13 and k = 4.05. Note the minimum of r_p corresponding to a kind of Brewster's angle [59].

The phase shift behaviour upon the reflection from the metal and dielectric surfaces related to the angle of the incident wave is illustrated in Figure 2.9 [64].

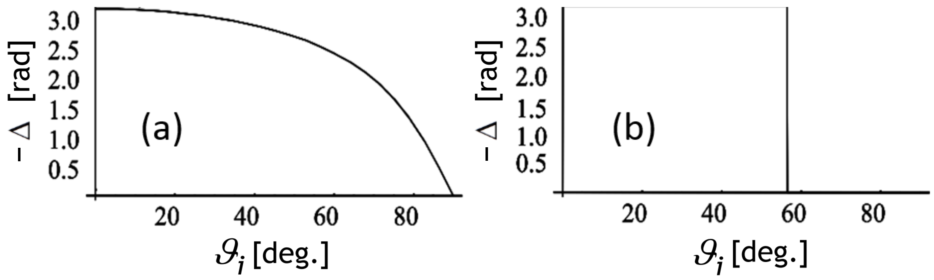

Figure 2.9 a) $-\Delta$ versus ϑ_i for a typical metal; b) $-\Delta$ versus ϑ_i for a typical glass [64].

The phase shift behaviour upon reflection is related to the angle of incidence. The phase shift between s and p components at ($\pi/2$) incident angle is zero, so the reflected light remains linearly polarized. However, at an incident angle (<20°), the polarization is inverted, i.e. $\Delta \sim \pi$ (180°). This value is different for other metal materials, although all metals exhibit this same behaviour [64].

2.7 Advantages of two external reflections from mirrors out of the chiral molecules

To understand the effect of the optical path length on the polarimetry systems in a microfluidic scheme, one must first understand that the asymmetric structure of the chiral molecules rotate the azimuthal angle of the polarization vector of a propagating linear polarized beam by an amount (α) that depends both on the concentration (c) of the sample and the optical path length (l) (Equation (2.1)),[65].

Thus, for a given concentration of a specific chiral substance, the optical rotation is proportional to the optical path length. In microfluidic samples, the small critical dimension of many of the channels induces a small optical path length, and accurate measurements are difficult to obtain. In our study, several iterations of mirror configurations were performed to increase the optical path length using a different spatial arrangement of mirrors (Section 4.4) – the best of which involved a zigzag arrangement of offset sandwich mirrors. To understand this zigzag multiple-reflections approach, the change of polarization upon reflection from such surfaces is described as follows. The 180° polarization rotation at the mirror, before interrogating the sample plays a vital role in this multi-reflection setup, as the basic concept depends on nullifying the 180° flipping of the polarization at each mirror before interrogating the sample through the subsequent pass, as shown in Figure 2.10.

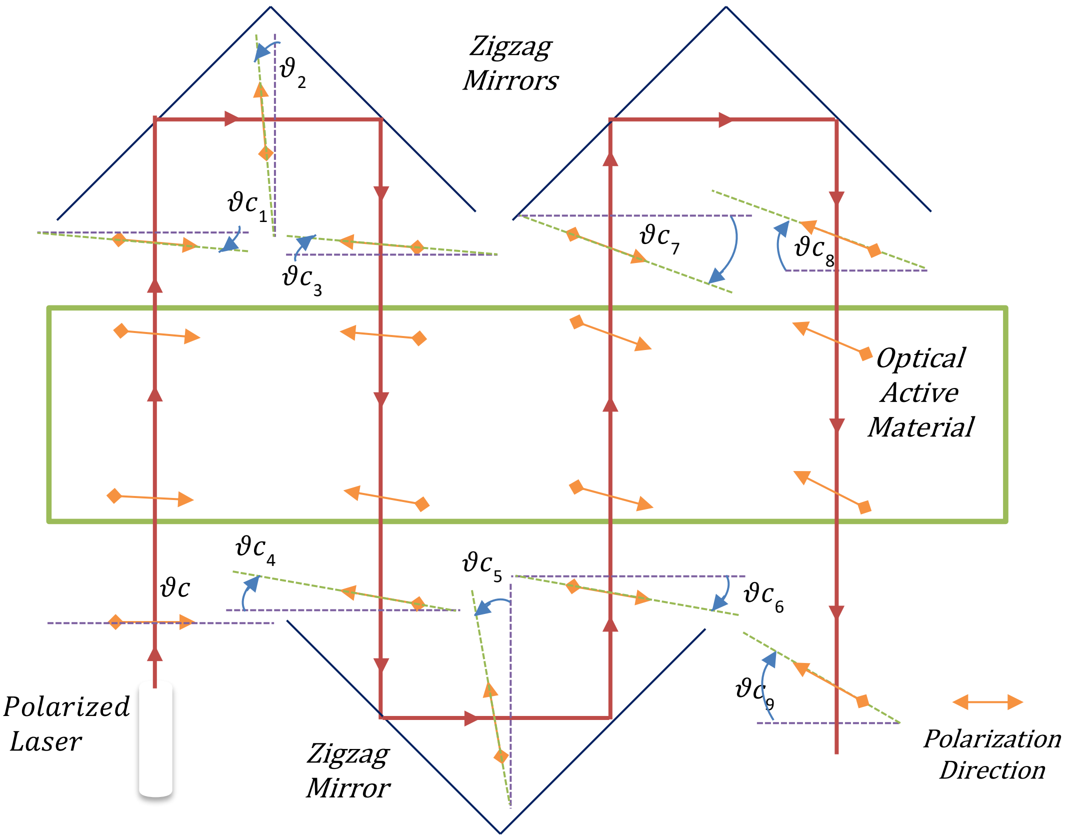

Figure 2.10 A schematic diagram of the operation of the polarization rotation, which increases upon the multi-reflection approach around the capillary of the chiral molecules. The polarized beam of the laser of the polarization angle ϑ_c passes through a liquid of the chiral molecules, which rotates the beam by an arbitrary angle, which is α (optical rotation). This is flipped at the first 45° tilted mirror and then reversibly flipped by the second mirror, passing another time through the same capillary of the chiral molecules. This angle of polarization rotation will increase by another angle of α with each passage.

As illustrated in Figure 2.10, the polarized beam of the laser of the polarization angle ϑ_c passes through a liquid of the chiral molecules, which rotates the beam by an arbitrary angle, which is α (optical rotation). This is flipped at the first 45° tilted mirror and then reversibly flipped by the second mirror, passing another time through the same capillary of the chiral molecules. This angle of polarization rotation will increase by another angle of α with each passage.

In our work, aluminium mirrors were used instead of silver mirrors in order to make this flipping as close to 180° as possible and to achieve less polarization noise at the mirrors, as aluminium has relatively better polarization flipping at a 45° incident angle than silver, as shown in Figure 2.11 [66] [67].

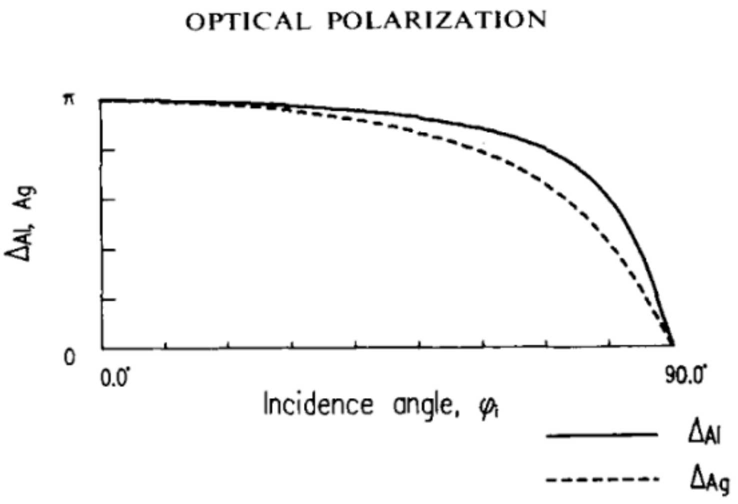

Figure 2.11: Phase shift (Δ) as a function of incidence for aluminium and silver [66].

In this study, if the laser reflects from a metal surface, there will not be a linear polarization change to a circular or elliptical polarization so long as the laser polarization is either exactly in, or perpendicular to, the plane yz (and the normal vectors of the mirror surfaces are in the plane yz). In other words, if the linear polarization angle is 0 or 90° and the beam path is in the plane of yz (i.e. the mirrors do not introduce any changes in height to the laser), then the polarization will remain linear.

If the height of the beam is changed by the mirrors, then it will alter the polarization of the beam. A single component of the vertically polarized laser will experience a phase shift after passing the optically active medium (relative to the phase of the input field). However, there is still no second or orthogonal polarization component after the interaction with the surface. In this way, there is still only one non-zero field component (phase-shifted), which by definition is linear polarization. Regardless of the angle of incidence, as long as the laser enters with only one polarization component, it will exit with only that polarization component; there is no field in the orthogonal direction. It does not matter how many bounces take place: if there is no field in that direction, there will never be any field in that direction.

2.8 Applying polarization Jones Matrices on multiple reflections polarimetry

Polarization is determined by the relative magnitude between the s and p-polarized components (given by R_s and R_p, respectively) - see Equations (2.25) and (2.26), and the relative phase Δ between the s and p- polarized components (given by φ_s and φ_p, respectively). Therefore, this phase difference (along with the magnitude difference) gives the polarization difference. If $\varphi_s - \varphi_p$ =0, then the wave is linearly polarized (the polarization angle is determined by R_s and R_p). If $\varphi_s - \varphi_p$ = +/- (π/2) and $R_s = R_p$, then the wave is circularly polarized. In any other case, the wave is elliptically polarized. For multiple reflections, this should still work after accumulating the phase and magnitude differences between the two components. To state the procedure explicitly, the following steps are implemented:

- The incident field is written in the form given by Equation (2.2). By calculating how each polarization component changes upon reflection, the Fresnel coefficients in Equations (2.23) and (2.24) are then given; thus the new field in the form of Equation (2.4) can be written. After this, the polarization state upon reflection can be realized. In all likelihood, the polarization will be elliptical unless there is only one polarization component, (for example: $E_x = E_o$ and E_y = 0); in which case, it does not matter what the phase is as the polarization is linear.

- The absolute value squared of r_s and r_p (i.e. $R_s = |r_s|^2$ or $R_p = |r_p|^2$) gives the total reflectance of the wave. The complex phase of r_s and r_p gives the phase shift of each component, as in Equation (2.27). The relative phase shift between the s and p-polarized waves is known by subtracting φ_s and φ_p (Δ).

$$\varphi_s = \tan^{-1}\frac{\mathrm{Im}(r_s)}{\mathrm{Re}(r_s)}, \varphi_p = \tan^{-1}\frac{\mathrm{Im}(r_p)}{\mathrm{Re}(r_p)} \qquad \textbf{(2.27)}$$

Where $\mathrm{Im}(r_{s,p})$ and $\mathrm{Im}(r_{s,p})$ are the imaginary and real parts of the perpendicular and parallel light components (r_s and r_p), respectively.

- The second step is independent of the electric field, but the refractive indices n_i and n_t depend on the wavelength of the laser. Consequently, the Fresnel coefficients are still subject to the parameters of the light source.

For a continuous wave, monochromatic laser beam, such as a He-Ne laser, it is usually correct to assume an electric field in the form of a plane wave, as in Equations (2.2) and (2.3). If polarized light is in, or perpendicular to, the plane of the optical table (yz), then the initial field is as simple as Equation (2.28). In this case, there would be no y component.

$$E = E_o e^{i(kz-\omega t)}\ x \qquad \textbf{(2.28)}$$

The value of E_o is not significant in finding the ellipticity and/or polarization, as it cancels out in the calculation.

If the polarization angle is 0, then the magnitude of $E_x = E_o$ and the magnitude of E_y = 0. If the polarization angle is 90 °, then the magnitude of E_x =0 and the magnitude of $E_y = E_o$. If the polarization angle is ϑ, then the magnitudes of E_x and E_y are $E_x = E_o \cos J$ and $E_y = E_o \sin J$; thus, it is a simple projection of the vector onto each direction.

The single component will experience a phase shift (relative to the phase of the input field), but there is still no second/orthogonal polarization component after the interaction with the surface. In this way, it still has only one non-zero field component (phase-shifted), which by definition is linear polarization.

- To determine the polarization state of the light through the whole system, the following is applied: matrices multiplications of light, reflections, (Equations. (2.8) and (2.13) respectively), with the polarizer, analyzer and the optical rotation of the chiral molecules (the following Equations. (2.9) and (2.10) respectively).

To implement and interpret all the steps above, the present system design was simulated from a simple model using Matlab to demonstrate different schemes that increase the optical path length of the polarimetry system. The model was applied to both metal and dielectric mirrors with different designs and mirror arrangements, and a variety of polarization states and light incident angles that used several terms of Jones' vectors (section 2.5) to account for any change in the polarization state of light when passing through the optical elements. The model indicated that, if the dielectric mirrors are used in a multi-pass scheme (two-reflections before each pass), the polarization orientation will change only once regardless of the number of passes. In contrast, it is changed linearly for subsequent passes when using metal mirrors. Therefore, metal mirrors are used to implement the function to increase the optical path length, as shown in Appendix A.

2.9 Optical Rotatory Dispersion (ORD) effect on the polarization rotation

For a specified chiral solution, the specific rotation depends on the wavelength which gives the ORD characteristics of the constituent molecule. The relation is an inverse proportion; therefore, the shorter the wavelength the greater the optical rotation of the chiral molecules achieved and vice versa. This is illustrated by the approximation of Drude's Equation, [68]:

$$\left[\alpha\right]_{\lambda,pH}^{T} = \frac{K_0}{\lambda - \lambda_0} \tag{2.29}$$

Where λ is the source wavelength, λ_0 is the maximum absorption for a given compound, and K_0 is the proportionality constant at that wavelength.

2.10 Conclusions

Our approach to the absolute measurement of chirality makes use of the polarization reversal of the mirror, with two 45° faced mirrors positioned before passing the beam through the chiral molecules. Unlike the two-mirror cavity, the zigzag cavity mirrors break the symmetry between the beams by applying two reflections to these two mirrors, which cancels the 180° flipping upon each mirror. A chiral sample is introduced between this sandwich cavity. Each mirror flips the polarization by the same magnitude as the previous rotation of that passed through chiral molecules but in the opposite sign. The same chiral molecules sign for all beams remain. Therefore, the total number of single-pass optical rotations for the forward and backward beams are given by their sum, which is subject to the number passing, the optical path length, the type and concentration of the chiral molecules, and the wavelength of the light.

The polarization state does not change to elliptical polarization upon reflection from the mirror when the laser beam is linearly polarized. The laser is aligned carefully so that the polarization is entirely vertical or entirely horizontal, and the mirror is also oriented in such a way that its interface can be described entirely in either the horizontal or vertical plane (regardless of the incident angle). However, the polarization will change upon reflection when the laser is non-linearly polarized, or the polarization is not exactly parallel or perpendicular to the plane defined by the mirror's interface.

Although in this study we considered laser measurements that were reflected 20 times from the zigzag sandwich mirrors, an optical rotation measurement that uses more multiple passes of light is also possible. Our preliminary theoretical predictions show that the sensitivity to small optical rotations can be enhanced using multiple reflections of light at the expense of the total detected intensity. However, in practice, we found that the measurement of the second - or higher - order reflected light with the relatively weak source used in our studies was not practical because of significant losses. Further studies that use an intense, collimated beam need to be realized before the advantages and disadvantages of using multiply reflected light for the measurement of optical activity can be identified.

Chapter 3 Materials and Methods

3.1 Polarimetry with multi-reflections scheme

The system was designed and constructed to measure the optical rotation using a multi-reflection scheme, as depicted in Figure 3.1. The system employs a He-Ne laser of 632.8 nm (Melles-Griot, 20 mW, polarization 500:1) and a laser diode of 403 nm (TOPTICA Photonics, ibeam-smart, tunable power 1-150 mW, polarization 100:1), as linearly polarized sources. The laser beam passed through a Glan-Thompson 100 000:1 polarizer (Thorlabs) oriented at 90° to further purify the polarization state of the beam before passing through the sample.

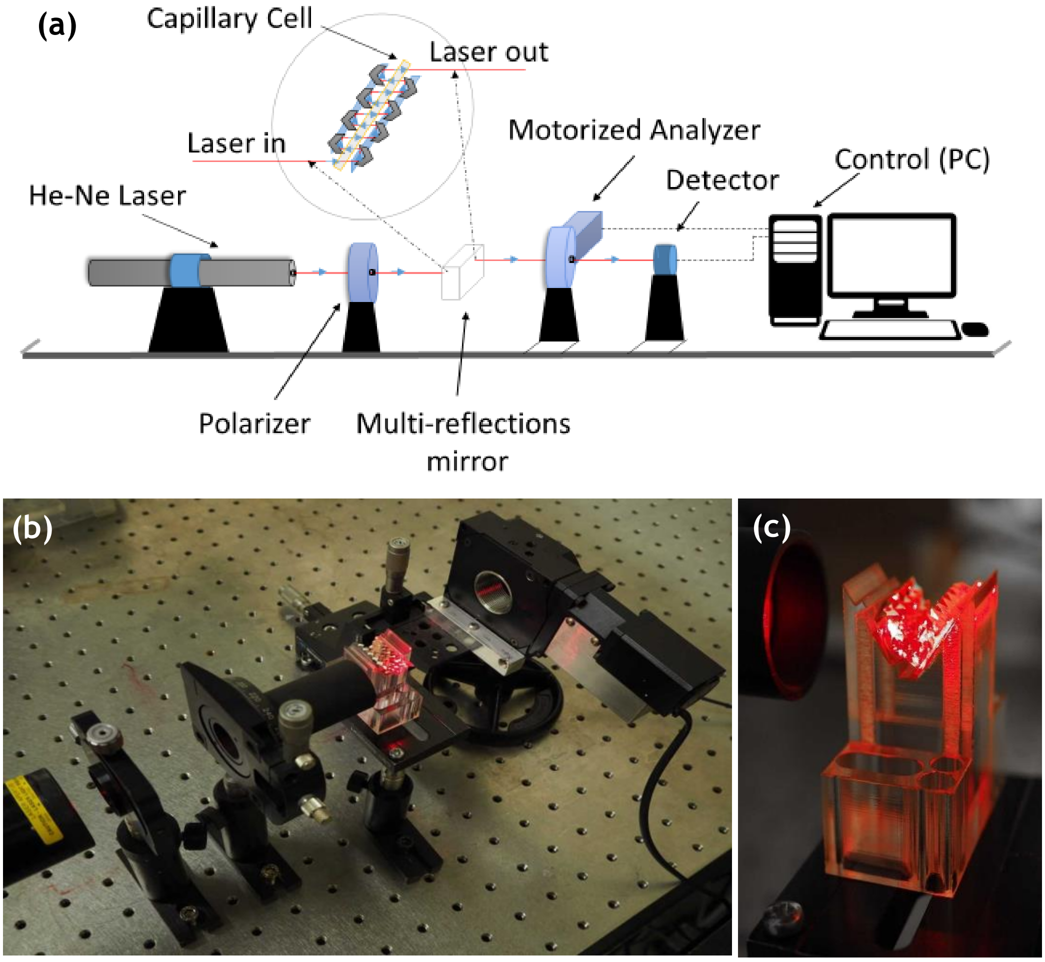

Figure 3.1 a) Experimental set-up of polarimetry applying mirrors that were used around the 1 mm path length capillary. Light from the linearly polarized He-Ne laser (632.8 nm) or diode laser (403 nm) passes through the Glan-Thompson polarizer, then multiple times through the sample, escalating the optical rotation. The polarization angle of the light was measured through a computer controlled rotating analyzer, by the power meter (using LabVIEW). The angle of rotation was extracted using the curve fitting in Matlab. b) Cube mirror arrangement along with the polarimetry setup.

In a bulk-reflective polarimetry system, a microscopic cell (1 mm width) was used as a sample cuvette. The laser passed through that cuvette and was reflected by mirrors (silver, d=1 cm, Newport or aluminium, d=1 cm, Newport), as shown in Figure 3.2.

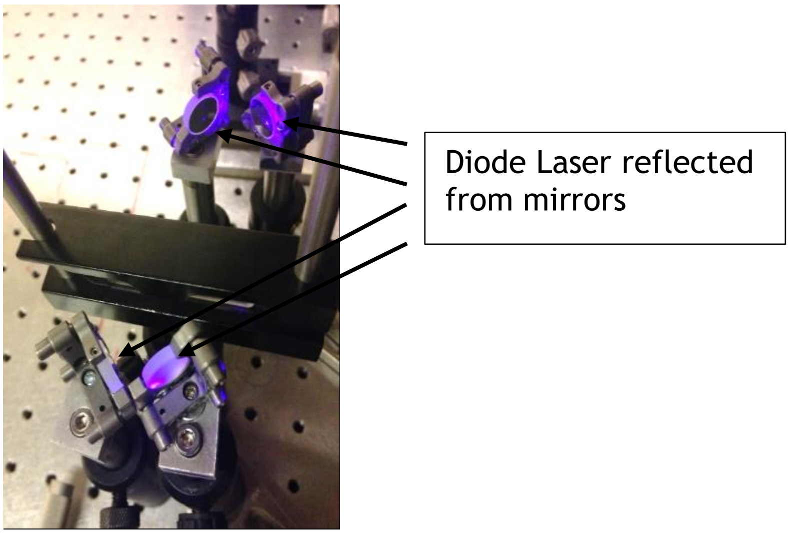

Figure 3.2 Photo of the reflection scheme inside the polarimetry system showing the diode laser (403 nm) passing through mirrors of the system.

In the further minimised system, the sample was contained in a 1 mm capillary channel sandwiched by two zigzag mirrors (Figure 3.1 b and c), comprising an array of 2.5 mm cubes of PMMA (Polymethyl methacrylate) mirrors (Edmunds) held at 55° and translated on a custom fabricated mount. A thick layer of 1000 nm aluminium was evaporated on the cubes by metal evaporation using Plassys4 (MEB 4005). In order to align the laser to achieve two reflections before the light passed through the sample for each passage, the cube mirrors were arranged to be linearly shifted by 2.5 mm (the width of each mirror) to each other. Therefore, the laser was reflected twice before passing through the sample volume to nullify the 180° flipping of the polarization state of each mirror before interrogating the sample through the subsequent pass and thus adding up the polarization rotation through multiple passes. In most cases, the laser passed through a pinhole (400 µm or 100 µm), which lay in front of the laser to decrease its beam size.

The total number of passes should be odd, as it needs at least four reflections and three passes. The output light from the final pass of the sample passed through an analyzer (Edmund), which was placed on a motorized mount (Newport) to rotate the polarizer before its detection by a power meter (COHERENT). The power meter can be adjusted for different wavelengths.

The motorized analyzer and power meter were controlled via a serial cable to the computer, and were programmed using a LabVIEW™ (13.0.1) to detect the signal for each angle of rotation. The program was written to synchronize the operation of the power meter and analyzer rotation and then to export the data to a PC for further analysis to calculate the optical rotation using Matlab.

All power values were acquired by averaging ten readings for each analyzer step via the Matlab code (see Appendices A.1 and A.3). The averaged data were then imported to the fitting tools and compared with the measured water as a reference. All sample solutions were prepared with D-(+)-Glucose, which is a safe chiral molecule; research-grade chemicals (SIGMA-ALDRICH), and were dissolved in the distilled water. To evaluate the design of a real system in detail, the experimental set-up was modelled by applying Jones' matrices (see Appendix A.3) of the optical components and using simulations in a Matlab environment, confirming the functionality.

3.2 Fabrication of micromirrors

3.2.1 Cleaning of substrates

Substrates were cleaned thoroughly in order to remove any organic contaminants and particles. First, the substrates were cleaned using an ultrasonic bath where they were placed in acetone for 10 minutes, rinsed with isopropanol (IPA) and dried using a nitrogen gun. They were then transferred to a Gala Plasma Prep 5 oxygen plasma asher and ashed for 2 minutes at 100 W.

3.2.2 Photolithography

Lithography is a process used to transfer a pattern onto the surface of the substrate. It allows for a resist image to be created on a surface. Light from an illumination source passes through a predesigned mask; acetate and chrome masks were used in this work, which defines the resist pattern. There are two complementary regions on a mask; one is opaque and the other transparent, allowing light to pass through. As the wafer is coated with a photosensitive resist, this process of area-specific illumination enables the transferral of the pattern to the wafer. There are two types of photosensitive resist - positive and negative - although both undergo a chemical reaction upon exposure to light, following illumination from the light source. The positive resist becomes more soluble in the developer, whereas the negative resist becomes cross-linked/polymerised and is not soluble in the developer (as shown in Figure 3.3) [69],[70].

Substrates were spin-coated with either S1818 photoresist (Shiply, USA) at 4000 rpm for 30 seconds to produce a ~1.8 μm thick layer and baked at 95°C for 3 minutes, or SU8 photoresist. However, SU8 was replaced by the S1818 photoresist to avoid using Piranha to strip the prior layer. This was intended to avoid the danger of using Piranha; also, S1818 can be removed easily by soaking the sample in a warm Acetone bath (50°C) for two hours, then rinsing it with the IPA, drying it with Nitrogen, and then cleaning it with a plasma Gala Prep5 oxygen barrel at 150 W for three minutes.

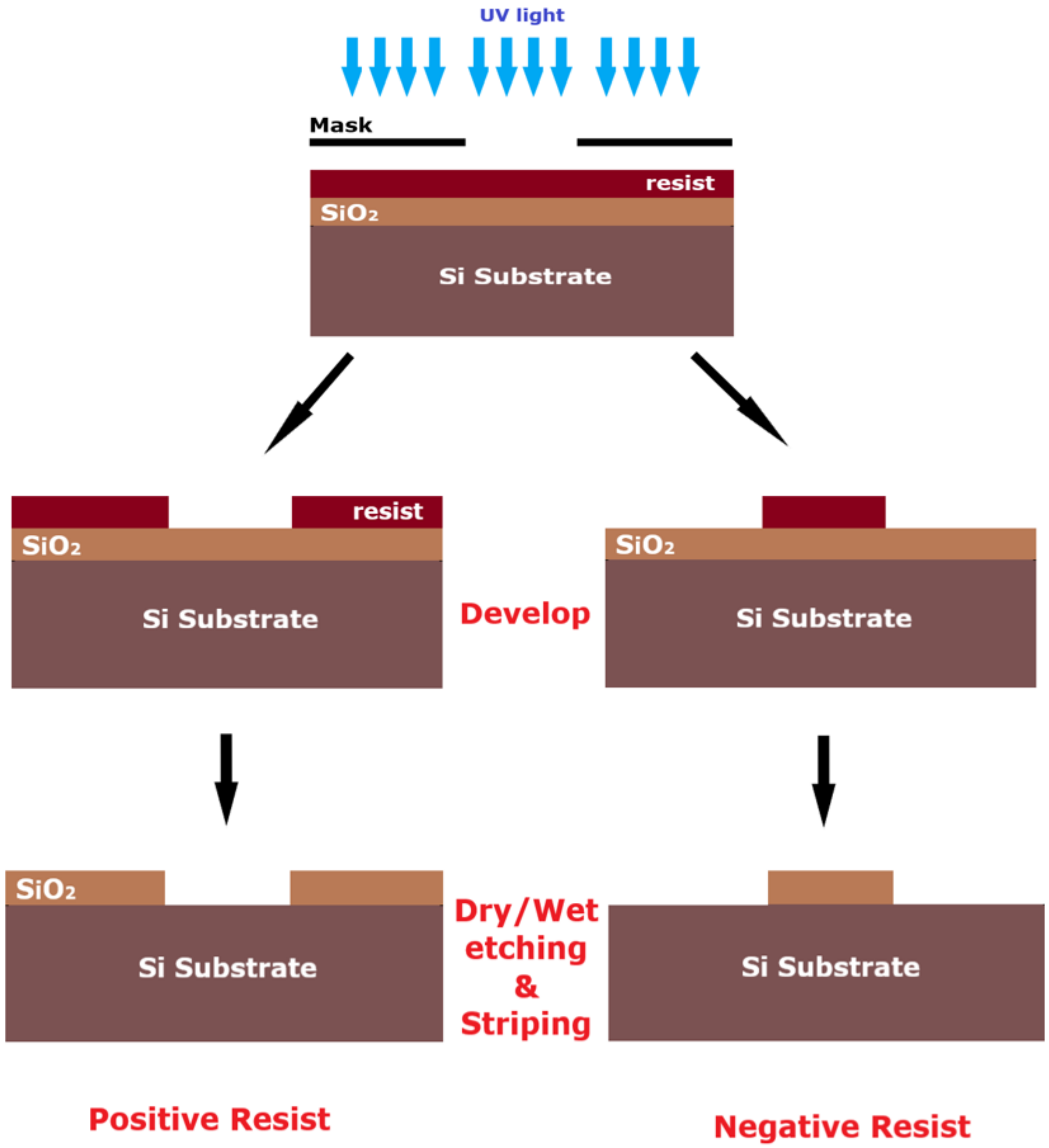

Figure 3.3 The photolithography process with negative and positive photoresist [70].

Micropatterns were transferred onto the wafer by exposure to UV radiation (SUSS Microtec MA6, Germany) for 4.5 seconds through a chrome or acetate mask. The development of the S1818 resist was performed using a 1:1 ratio of Microposit developer (Shipley, USA) and reverse osmosis (RO) water for 1 minute. Samples were then dried under nitrogen and patterns checked for over/under exposure using an inverted microscope. This was followed by dry etching to remove the Si_3N_4 layer of the desired pattern using a BP80 RIE dry etch tool with 100 W and under the pressure of 23 mT using C_2F_6 gas at different times depending on the Si_3N_4 layer thickness. Samples were subsequently ashed for 2 minutes at 100W to remove the residual photoresist. This was followed by a cleaning step in order to remove the photoresist: substrates were rinsed in acetone and IPA and dried under nitrogen (as illustrated in Figure 3.6).

3.2.3 Design of patterns

Patterns were designed using L-Edit CAD software (Tanner Research Inc.) and exported as a graphical data system file (GDS) containing a multilayer pattern. Layout Beamer (GenlSys Gmbh) was then used to extract each layer in the GDS file and to generate a corresponding file which was transferred to the VB6 machine for writing the pattern on the substrate.

3.2.4 SU8 zigzag micromirrors fabrication

SU8 photoresist layers were deposited to form a thick (100-150 µm) layer, which was patterned to fabricate zigzag mirrors as shown in the design in Figure 3.4.

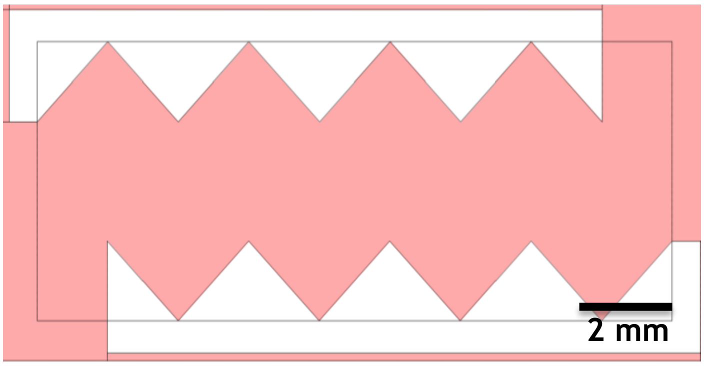

Figure 3.4 Photo-mask of fabricating a multi-reflection mirror using SU8 photoresist.

Substrates were spin-coated with SU8 3050 photoresist at 500 rpm for 30 seconds to spread the resist, and then at 2000 rpm for 30 seconds to produce a ~40 µm thick layer. After this, they were baked at 95°C for 3 minutes and at 120°C for 5 minutes in the oven. The same process was repeated three times to produce a ~120 µm layer. Micropatterns were transferred onto the wafer by exposure to UV radiation for 5 seconds through a chrome or acetate mask. The development of the SU8 resist was performed using an EC solvent (2-methoxy-1-methylethyl acetate) developer then rinsed reverse osmosis (RO) water for 45 seconds. Samples were then dried using a nitrogen gun and patterns were checked for over/under exposure using an inverted microscope. To harden the resist, the substrate was hard baked within a 190°C oven for up to six hours. The resultant zigzag SU8 layers were not smooth and tilted, so the mirrors metallisation process was not implemented (see Chapter 5).

3.2.5 Metal deposition

Different layers of aluminium and gold were deposited onto the surfaces of the substrates through an electron beam evaporator using a Plassys MEB 4005. Aluminium layers were evaporated as a targeted layer on the fabricated micromirrors. In order to evaporate aluminium or gold on the surface of the substrate, it is essential to apply first an adhesive layer. This is necessary to improve the adhesion of the metal layers to the surface. Titanium was used as the adhesive layer; 10 nm of titanium was evaporated to improve the adhesion to a range of gold and aluminium layers with thicknesses between 50 – 1500 nm.

3.2.6 Dry etching

In this work, a reactive ion etching (BP80-RIE) tool was used to perform the anisotropic dry-etching of the Si_3N_4 and SiO_2 thin layers. Table 3.1 summarizes the parameters of the etching recipe utilized.

Table 3.1 BP80-RIE process parameters for the anisotropic Si_3N_4 and SiO_2 dry-etching.

Parameter	Value
Gas	C_2F_6
Flow (sccm)	20
Platen Power (W)	100
Pressure (mT)	23
Etch Rate (nm/min)	50

All the dry-etching processes were performed on the BP80-RIE tool (Oxford Plasma Instruments) in the JWNC facilities.

3.2.7 Si_3N_4 deposition

The Si_3N_4 layer was created in-house. The tools used for the Si_3N_4 deposition were Oxford Instruments PECVD 80+ (Plasma-Enhanced Chemical Vapour Deposition), and ICP Deposition (Alcatel Vacuum Technology, Adixen, France) in the JWNC facilities. Semco Tube 3 LPCVD can deposit a high-quality Si_3N_4 layer on a silicon wafer. Hence, it was used in our work for most of the wet etching processes.

3.2.8 SiO_2 growing

The Semco Tube 2 WetOx instrument can grow SiO_2 on the silicon wafer. SiO_2 was grown and applied to smoothen the fabricated micromirrors by developing the oxide layer and then etching it using HF wet etching for about one hour (depending on the thickness of the grown SiO_2 layer).

3.2.9 Dektak

Dektak is surface profiler used to measure the height of the SU8 layer. DEKTAK XT Vision64® and ContourGT® Bruker machines were used at the JWNC facilities. This was used to test the suitable spinning speed and related SU8 layer depths.

3.2.10 Optical Profiler

Optical profiler Vision64™ ContourGT-X™ (Bruker Nano) was used to measure the roughness of the fabricated mirror surface after the SiO_2 layer was grown and etched by HF (Hydrofluoric acid).

3.2.11 Scanning Electron Microscopy

Scanning Electron Microscopy (SEM) images are generated by probing the specimen with a focused high-energy beam of electrons. The electrons interact with the sample surface, specifically the atoms, which generate a signal that contains information about the specimen surface topography and characteristic features [71]. SEM images were obtained using a Hitachi S-4700 SEM and a Bruker SU8240 SEM; both were operated at 10 kV.

3.2.12 Micromachining processes and recipes

The etching experiments with KOH and TMAH solutions were conducted using 3”, 4”, and 6” (100) silicon wafers of 380, 500, and 659 µm thickness respectively. These were supplied by CHALMERS Nanofabrication Laboratory, University Wafer, and James Watt Nanofabrication Centre /UK respectively. The 3” wafer is double-sided, polished and has a nitride layer over the thermal oxide layer on both sides at 60/40 nm in order to obtain a masking window. The 4” and 6” wafers have a 100 nm LPCVD-nitride masking layer. The wafers were patterned in photolithography on one side - using mainly different sizes and spaces at a 45° tilted pattern (see Figure 3.5). The dry etching of the nitride and/or thermal oxide layer was followed, which gave the desired pattern. Subsequently, after removal of the photoresist from the hard mask, selective etching in a BHF (10:1 buffered hydrofluoric acid) solution was used for one minute to remove the native oxide before the etching process. Finally, the sample was rinsed thoroughly with deionised water and dried with N_2. The experimental processes are illustrated in Figure 3.6.

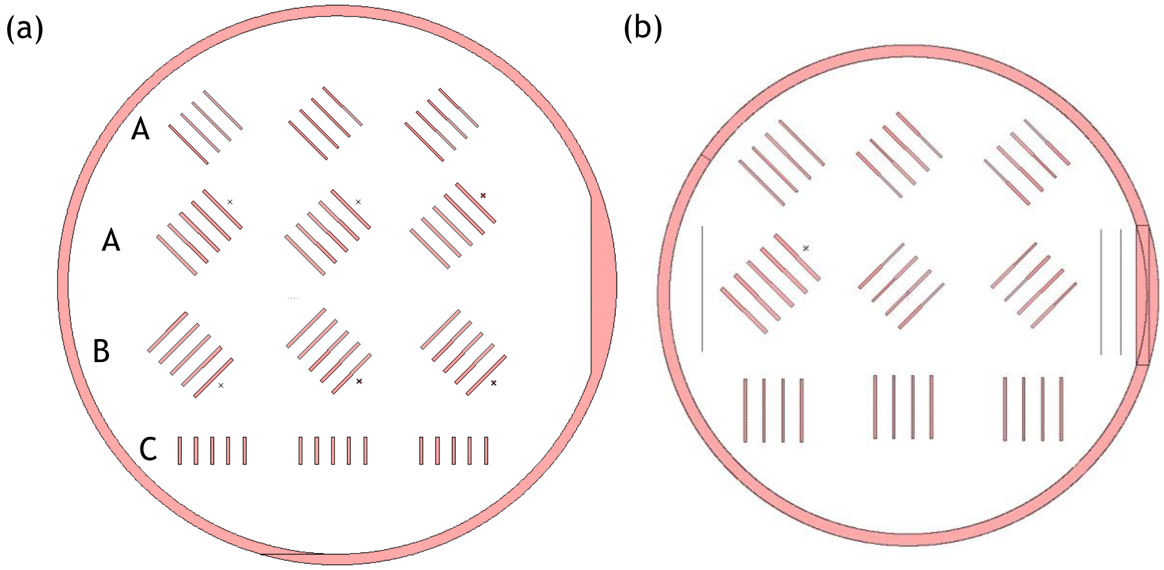

Figure 3.5 Mask designs for a photolithography process, (a) for the 4-inch wafer, (b) for the 3-inch wafer. A are the 45° slanted stripes, B are the -45° slanted stripes, and C are the straight stripes with respect to the primary flat edge of the wafer. The lines enable wafer alignment with the mask purposes during the patterning processes.

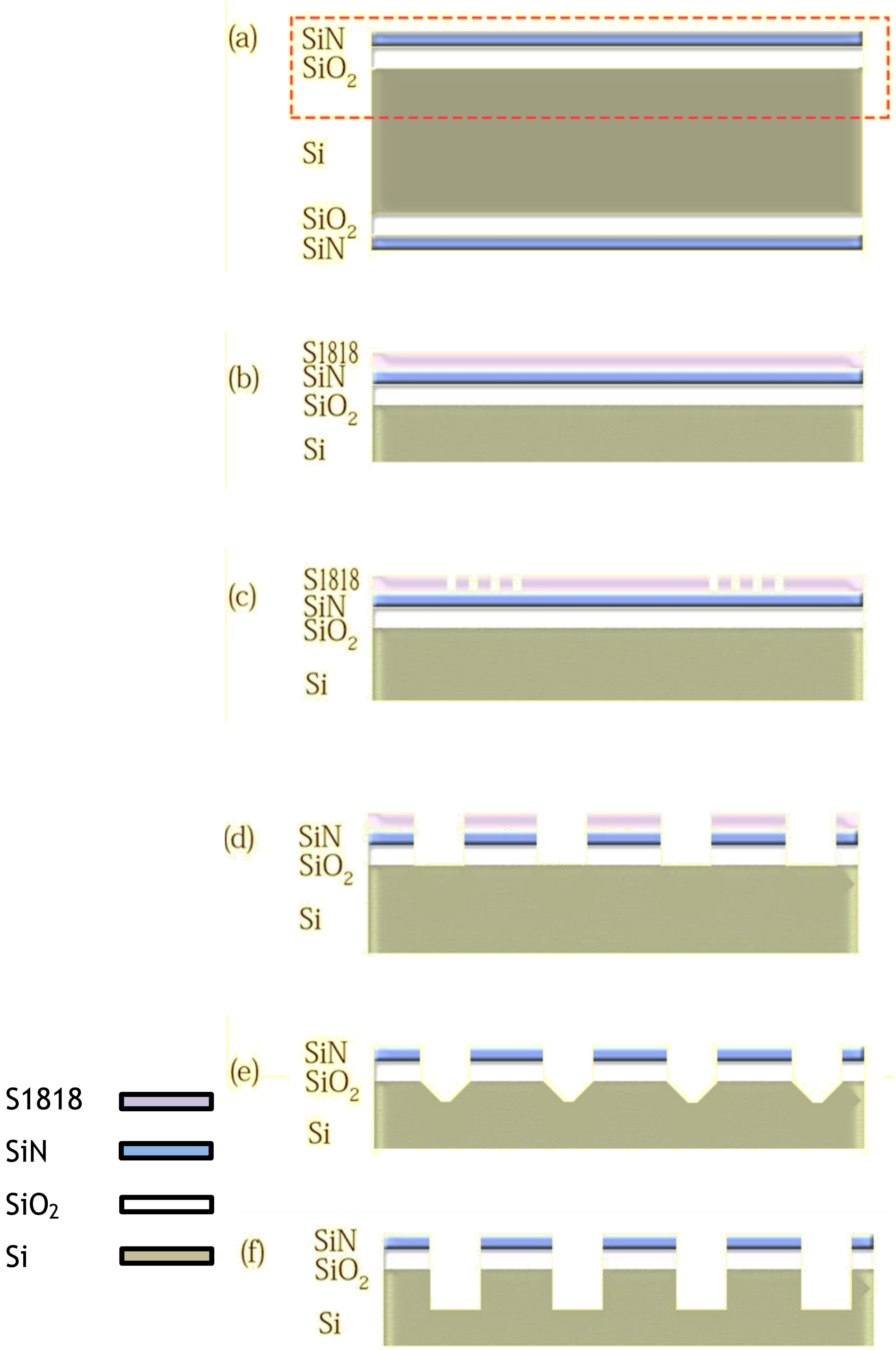

Figure 3.6 Photolithography processes on (a) 3-inch Si(100) wafer, which has Si_3N_4 and SiO_2 layers at 40 and 60nm respectively on the front and back sides. These function as a mask to protect the back side and the undesired area from wet etching, (b) Positive photoresist, S1818, layer on the Si wafer after spinning and baking, (c) The designed mask in Figure 3.5 was carefully aligned with the flat edge of the wafer and exposed to UV light using MA6. It was then developed using MF (MICROPOSIT® MF® -319) developer after a post-exposure bake. The windows of the desired pattern were then developed through exposure to UV light, (d) Si_3N_4 and SiO_2 were etched using a dry etch process with an appropriate recipe. This used BP80 to open the windows of the design to wet etch the silicon, (e) and (f) show etched trenches after the wet etching process produced vertical and 45° sidewalls using KOH and TMAH respectively.

KOH was made freshly from potassium hydroxide pallets, supplied by Sigma-Aldrich. Pyrex glassware was used to avoid KOH etching the glass. Mixing KOH with water is very exothermic, so it was handled with extreme caution. Different weighted pellets, depending on the KOH recipe, were placed in a suitably sized beaker. Water was poured slowly into the beaker at room temperature (first 200 ml), and then the solution was stirred gently (using a paddle). More water was added until the desired volume was reached and the mixture was then gently shaken. The specific volume of the additives, like *tert*-butanol alcohol or Triton X-100 (Sigma-Aldrich), was added slowly while continuously mixing the solution. After finishing the mixing, the desired temperature was reached through the use of a water bath.

For TMAH etching, 25% TMAH (supplied by KMG ULTRA PURE CHEMICALS) was used with Triton X-100 surfactant (Sigma-Aldrich). A mercury thermometer (0-100°C) was used to monitor the desired temperature. A substrate on a holder was then carefully added to the mixture using PTFE or polypropylene tweezers. During etching, the samples were held vertically to promote the detachment of the hydrogen bubbles during etching. This was achieved by a Teflon holder, which was immersed in the 1500 ml etching solution and contained in a Pyrex vessel, (shown in Figure 3.7).

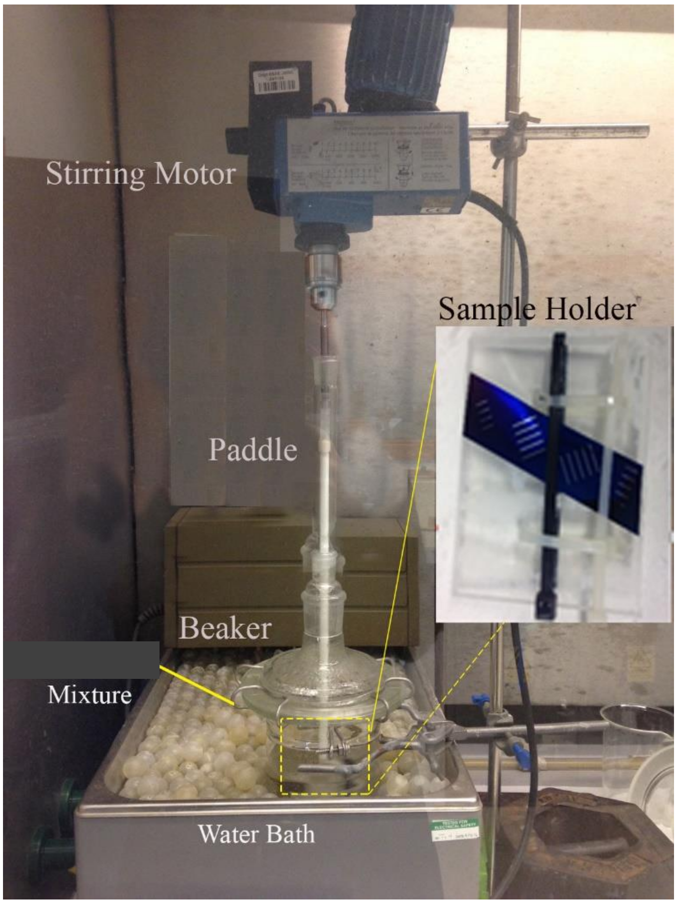

Figure 3.7 Setup of a wet etch process. Inset is the holder and substrate to be etched in the KOH solution in the beaker.

The etching process was carried out under atmospheric pressure and at different stabilized temperatures (75-85 °C). The etching solution was stirred mechanically at variable rotation speeds using an IKA laboratechnik stirrer equipped with a motor and Teflon paddle. The Teflon paddle was fully immersed in the solution during the etching, although it was located markedly above the sample holder with some contact to allow the sample holder to stir during the etching process; this strengthened the stirring. The process was performed in a condenser to control the evaporation over time. While the substrate was soaking, the sink was filled with water (using over 100 times water for dilution). After cleaning the substrate with RO water, the resulting alkaline solution was disposed down the sink by flushing it away with plenty of water. All the work was carried out under an extracted fume hood using a constructed kit (shown in Figure 3.7) and/or a kit in the clean room at the James Watt Nano Fabrication Centre (see Figure 3.8).

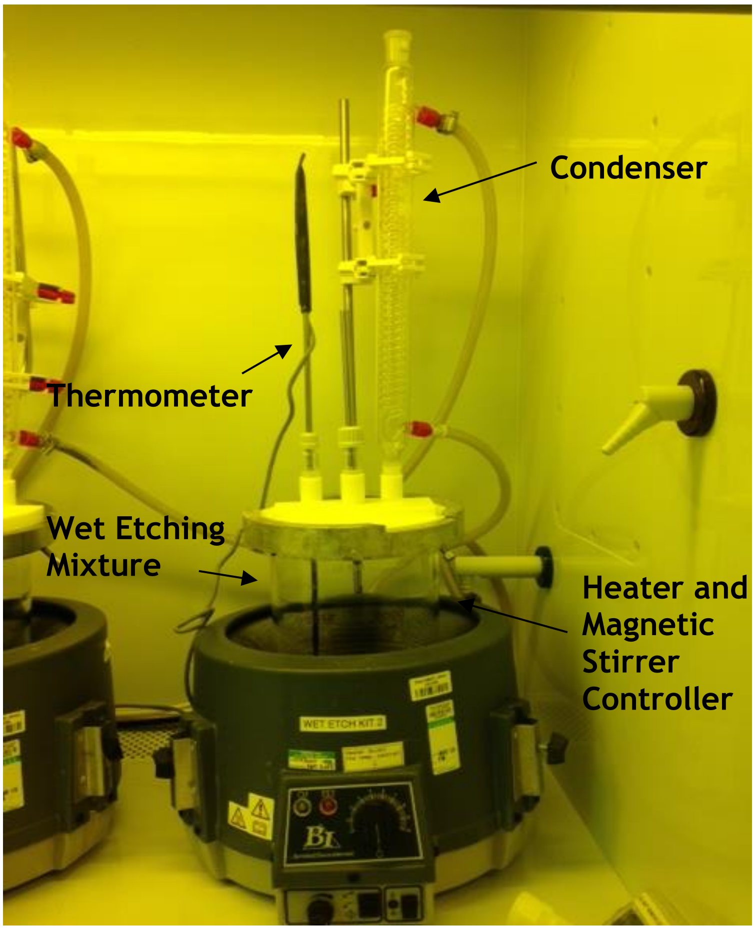

Figure 3.8 Wet etching kit at the James Watt Nano Fabrication Centre.

The etching time during the fabrication of the micromirror structures was selected individually for each structure so that the etching rate was varied. The surface morphology, sidewall angle, and etch depth of the etched spatial microstructure were investigated using the SEM.

3.2.13 Cleaving the fabricated device

After the fabrication of the micromirrors, different sets and dimensions were fabricated on the same substrate. In order to use them in the polarimetry setup, one set was cleaved from the others to avoid misalignment. The Si(100) substrate cut allowed for the cleaving of the substrate that was parallel and perpendicular to the wafer flat edge. However, the design of the mirrors requires a 45° cleave along with the pattern direction. Therefore, for silicon wafers, the pattern was cut using a saw tool. Before cutting the mirrors, S1818 photoresist was used to protect the device during the sawing process. The substrate, after cleaving, was cleaned by soaking it in a warm acetone (50°C) for approximately three hours, after which it was rinsed with IPA and dried using a nitrogen gun.

3.2.14 Fabrication of the microfluidic channel

The channel was designed using the L-Edit tool. The design was patterned to fit the dimensions of a multi-reflection mirror device, as shown in Figure 3.9 (a).

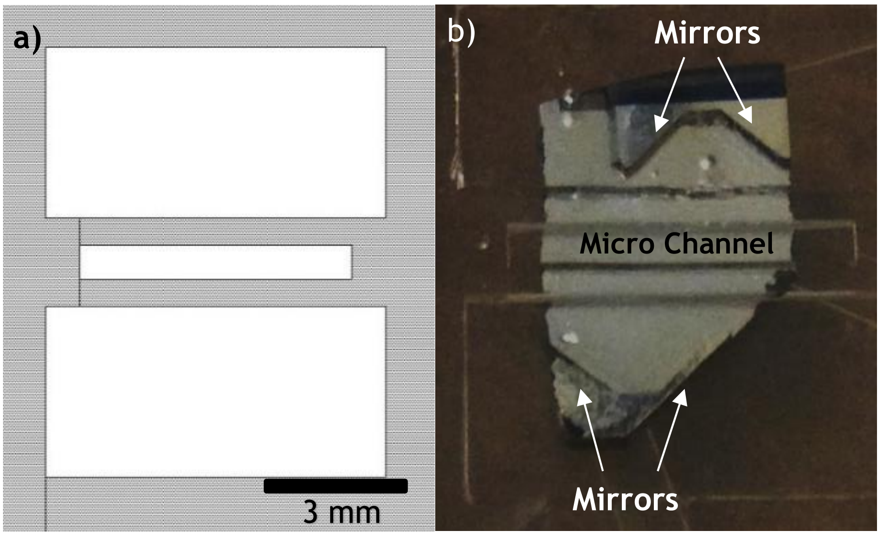

Figure 3.9 a) Microfluidic channel design using L-Edit. The fabricated channel is the middle rectangle while the other two rectangles are rooms for fabricated mirrors. b) Photo of the fabricated device – four fabricated zigzag mirrors with a microfluidic channel between them.

In order to fabricate the crests, the designed pattern was printed on the chromium plate as a mask in the photolithography processes. This used electron beam lithography VB6 based at JWNC. The mask was then used to pattern the design on a glass substrate.

Firstly, the substrates were cleaned. A layer of SU8 3050 photoresist was deposited onto the substrate to cover the whole substrate. These were then spun at 2000 rpm for 30 seconds resulting in a resist layer thickness of 50 µm. The glass substrate was then soft baked at 95°C on a hotplate for 30 minutes with one minute on a 65°C hotplate beforehand and afterwards to evaporate the solvent. This process was repeated for many times allowing for the production of a thicker layer for deeper microchannel purposes. The mask aligner tool was then used to align the mask with the substrate and to pattern the substrate through UV exposure for 15 seconds. After patterning, the substrate was post-exposure baked by a 95°C hotplate for five minutes with one minute on a 65°C hotplate beforehand and afterwards. The exposed SU8 photoresist was then developed for two minutes using the EC solvent (2-methoxy-1-methylethyl acetate) developer. After development, the pattern appeared; therefore, the substrate was hard baked to harden the resist. This used a 190°C oven for up to six hours and worked as a hard physical mask.

The mask then was ready to pour the PDMS on it and get the desired design. If the channel needs to be thicker and deeper, to firm the sample with the multi-reflections device and manage the sample volume purposes, a thicker SU8 layer should be deposited at the beginning by either spinning multilayers or using a slower spinning speed. In the case of using a thicker SU8 layer, the baking, exposure, and development times should be increased accordingly.

The channel was fabricated using three layers of SU8 photoresist mask to fabricate a ~1 mm deep channel pattern using PDMS. The PDMS was prepared by mixing 184 silicone elastomer (SYLGARD^{TM}) and its curing agent with at a 10:1 ratio respectively. The mixture was then poured on the mask, which was already placed in a Petri dish, and then placed in a vacuum for at least 30 minutes in order to draw the bubbles out, which were created during the PDMS mixing process. After that, it was placed in the 120°C oven for six hours to cure the PDMS. The PDMS was then dry enough; it was released from the mask mould and used as a channel on the multi-reflection scheme in the polarimetry system. Optical rotation with different pH, temperature, and another chiral molecule were then measured.

3.2.15 Buffered pH solutions preparation:

Phosphate buffered preparations of 50 mM sodium dihydrogen phosphate (NaH_2PO_4) acid and 50 mM disodium hydrogen phosphate (Na_2HPO_4) with deionized water were prepared. The buffered solution from mixing these solutions was prepared to tune the pH to the desired values of between 2 and 12. The specific weight of the glucose powder related to a particular concentration that was mixed with a suitable volume of the buffered solutions. The pH result depends on the pH of the prepared buffered solution.

3.2.16 Non-buffered pH solutions preparation:

2 M of both HCl and NaOH were prepared from diluting 37% hydrochloric acid and mixing the specific weight of sodium hydroxide with deionized water respectively. Specific glucose and BSA protein concentrations were made up (1 litre at a time) and refrigerated for 12 hours to allow for the complete equilibration of the glucose. Upon removing the stock solution from the fridge, the sample was left until it reached room temperature before measuring out aliquots in 10 ml centrifuge tubes. The pH was then checked and drops of HCl and NaOH were added to the glucose and BSA protein solutions to adjust and tune the pH as needed. It is necessary to provide sufficient time for the solutions to equilibrate after making the pH changes. Therefore, the sample was left for at least 2 hours after the pH changes and the pH was then rechecked before the sample was run in a cuvette. A fresh cuvette was used for each sample measurement.

3.2.17 Measurement method

The optical rotation was measured for the mixture in our custom-built polarimetry system; this used 1 cm and 10 cm path length cuvettes with one pass. To manage the temperature, the cell was placed on the hot plate where a thermometer and an IR camera were used to monitor the temperature of the hot plate and the solution inside the cell, respectively. The calculated optical rotation represented the mean of three and five readings.

The optical rotations were also measured with a commercial polarimeter (Autopol VI, Rudolph Research Analytical), with a resolution of 0.0001° and tunable six wavelengths. This used a 10cm glass cell, which has an electronic heating and cooling temperature control. The pH of the solutions were measured by a Henna Edge-pH meter, equipped with standard calomel electrode and two glass electrodes, one of which was for high pH use.

3.2.18 BSA preparations and measuring method

Concentrations of the protein solutions were prepared. BSA (protein serum albumin) and albumin from bovine serum (SIGMA. Life Science) were used. A stirrer bar with a heater was used to dissolve the BSA powder in either water or PBS solution by placing the stirring bar inside the sample after cleaning and setting the temperature to reach up to 37°C (normal human temperature). A phosphate buffer saline, PBS, (SIGMA. Life Science) were used as a buffered solution in the range of 7.1-7.5 pH, with BSA. For non-buffered protein solutions, deionized water and NaOH and HCl were used to manage the pH of the solution using a pH meter. In some cases, the protein solution was filtered using a syringe filter of 0.2 µm, (CORNING), to filter the protein from impurities and avoid scattering and errors in the measurement.

After fabricating the reflection’s device, the measurements with glucose and BSA with different pH values were then implemented using three reflections and a 1mm path length (integrated fabricated microchannel) (Section.3.4.12 and Chapter 5).

Both He-Ne (632 nm) and a diode laser (403 nm) were used as light sources in the measurements to indicate the difference in the optical rotation when using diverse wavelengths and changed pH and/or sample temperatures.

Chapter 4 Multi-Reflection Polarimetry

4.1 Introduction

One major limitation when reducing sample volumes within microfluidic systems that are interrogated optically is the resulting short path lengths over which the signal is generated. In polarimetry, small interrogation volumes decrease the opportunity for optical rotation and therefore, reduce the sensitivity. In this study, a multi-reflection technique is used to increase this optical length. Different setup arrangements were designed to avoid any change in the polarization state of the laser and to achieve a preferable longer path length.

Reflections depend on the consideration of several parameters; the mirror material type, angle of incident, number of reflections, and polarization change upon reflection. In the optically active sample, an even number passes through should be taken into account as the polarized light is completely unaffected [50].

In addition, this research aims to investigate the use of various techniques to minimize the size of the system by demonstrating a capability of measuring micro samples (concentration and volume), such as using shorter optical path length lasers, manipulating the mirror's material, and enhancing the data acquisition system. The chapter addresses the following:

Firstly, LabVIEW was used to run the components of the system in real time. The LabVIEW codes for the motorized analyzer mount and power-meter detectors were combined in one code to resolve the time delay in operation and the effect of laser fluctuations. This was achieved by averaging several power readings in one step of the analyzer mount.

Secondly, this research focused on the parameters, which affect the measurement of the optical rotation as the extent of this rotation is subject to the nature of the substance, the optical path length of the solution and any environmental factors, such as external noise (temperature, mechanical noise) in the microfluidic scheme. An investigation into the source of the system errors was realised and studied. This aimed to rectify errors and quantify the ability of the system to measure the microfluidic scheme. Minimising noise influence was the goal of achieving accurate polarimetry detection on the chip.

Thirdly, the research presents a novel technique to increase the optical path length in the sample. This is demonstrated by making multiple reflections through the sample cell from the mirrors' surfaces and measuring any influence on the polarization of the light and power losses.

Finally, the research illustrates the optical rotation measurements using cube mirrors as an integrated multi-reflection scheme in a polarimetry system. The cube mirrors enhanced the elongation of optical path length and sample volume. This allowed, in general, for the detection of samples with reduced concentrations and in smaller volumes.

The calculated date represents the optical rotation calculated from Biot's law (eq.2.1), ($\left[\alpha\right]_{\lambda,pH}^{T}=\frac{\alpha}{cl}$).

4.2 Polarimetry Construction (Bulk Setup)

A polarimetry setup was built up using a He-Ne laser, optical elements (pinhole, polarizer), a sample cuvette system (building cell 5 and 10 cm), a commercial cell (5 and 10 cm), a syringe pump controller, and a power meter, as shown in Figure 4.1. The system was aligned and the power meter was calibrated using an alignment tool like a portable hanged metal needle. An optically active molecule can be detected using this system whose signal increases in a concentrated and optical path length-dependent manner.

Different cells were constructed at 10 cm and 5 cm lengths, as shown in Figure 4.2.

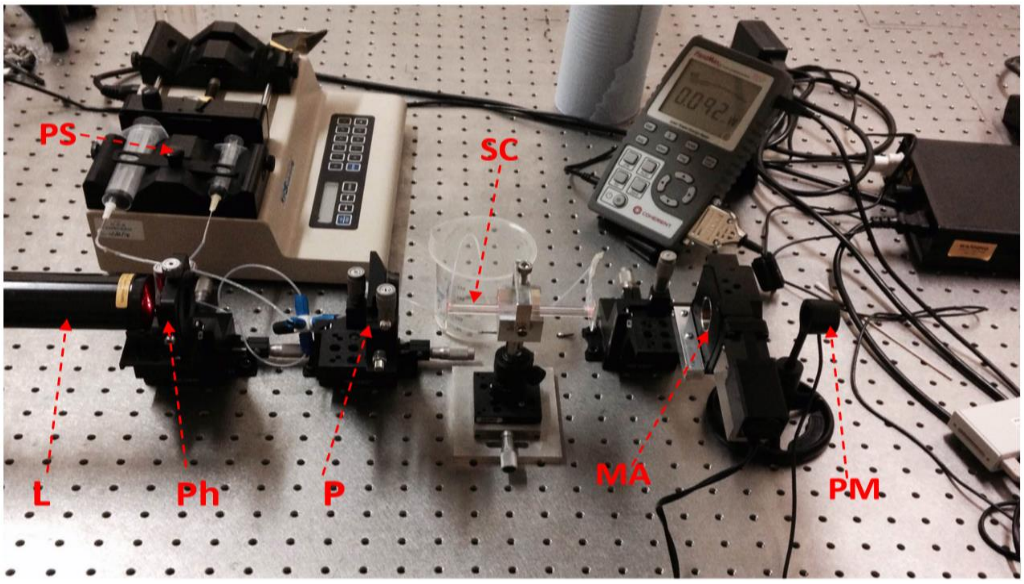

Figure 4.1 Image of the bulk polarimetry setup. L is the He-Ne laser; Ph is the pinhole; PS is the pumping of the syringe system; P is the polarizer; SC is the sample chamber; MA is the mount of the analyzer; PM is the power meter.

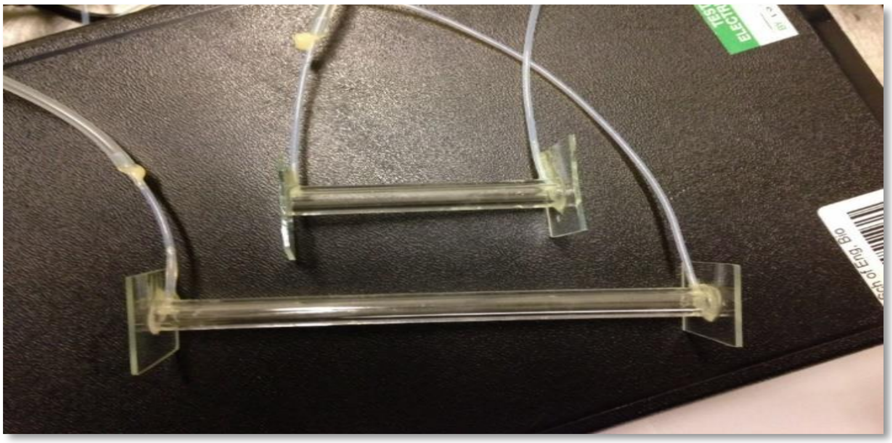

Figure 4.2 Image of 5 and 10 cm long constructed cells comprising, acrylic tubes and microscopic slides on the edges. The laser goes through the tubes.

A set of glucose concentrations was prepared, and the corresponding rotated angles of polarized light for these samples (0.75 ml and 1.5 ml for 5 and 10 cm cells respectively) were measured manually, as shown in Figure 4.3.

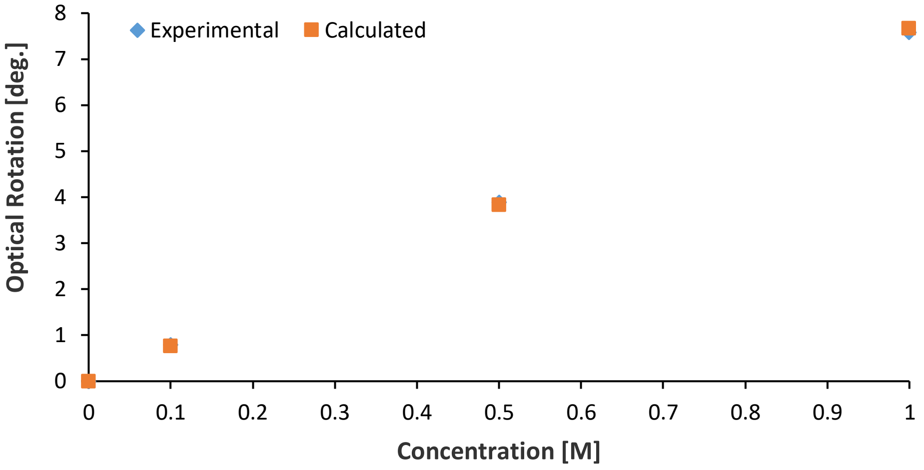

Figure 4.3 Manual measurements of the optical rotation for 0.1, 0.5, and 1 M glucose compared with their theoretical values (Biot's low). As a test, no error bars are represented because the measurement was done once for each concentration.

The measurements were then repeated for different glucose concentrations and compared with constructed set up, as shown in Figure 4.4. The results of the constructed setup were calibrated with a commercial setup. The tests were undertaken in the Chemistry Department Polarimetry located in Glasgow University (RUDOLPH RESEARCH ANALYTICAL, 354 Rout 206 Flanders, NJ 07836).

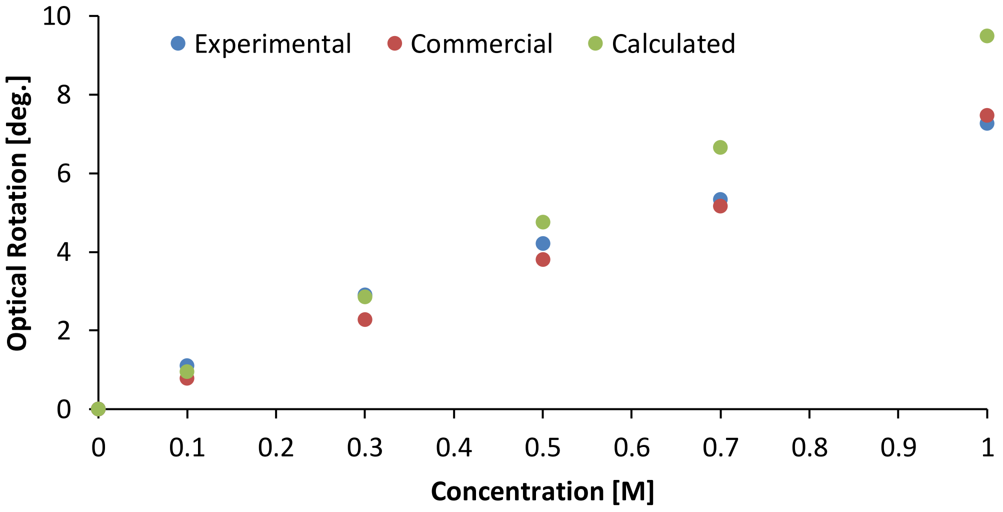

Figure 4.4 The rotation angles of the 0.1, 0.3, 0.5, 0.7, and 1 M glucose measured values compared with their theoretical values and the measurements of the Chemistry Department Polarimetry. As a test, the measurement was undertaken once for each concentration.

A standard microscopic cell of (10×1) cm size was used (as shown in Figure 4.5) to compare with the constructed cell and minimise the cell's length error, or parallelism of two sides of window error. The optical rotation for the same concentrations was measured at the Chemistry Department at the University of Glasgow, as shown in Figure 4.6.

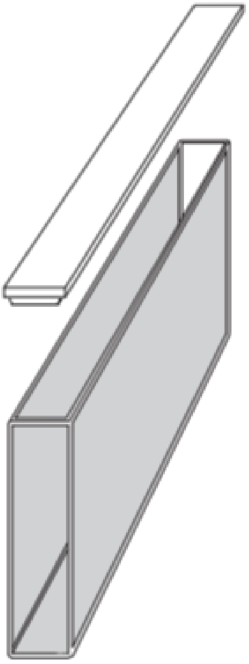

Figure 4.5 Image of 10 cm microscopic cell.

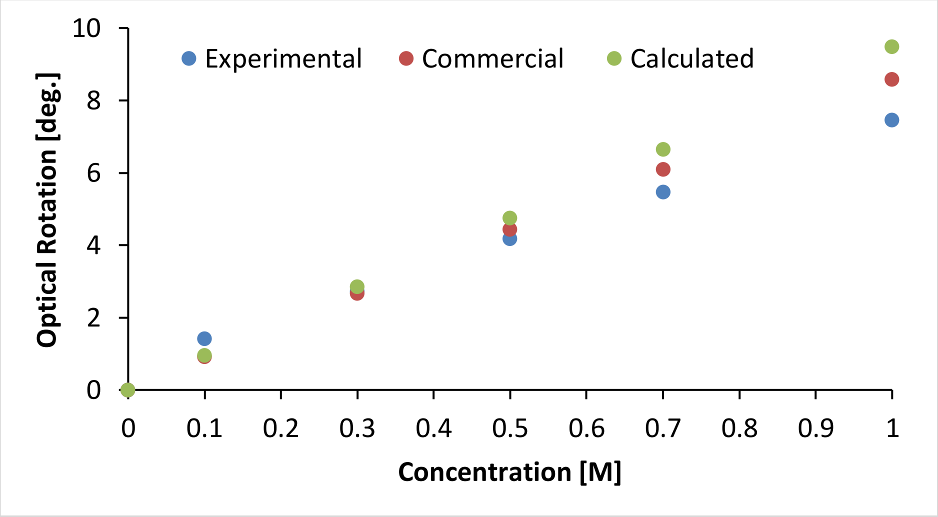

Figure 4.6 The rotated angles of 0.1, 0.3, 0.5, 0.7, and 1 M glucose using new microscopic cells; these are compared with their theoretical values and the measurements of the Chemistry Department Polarimetry. As a test, the measurement was undertaken once for each concentration.

Commercial polarimetry is a device in the Chemistry Department. There was a slightly difference in the results between the constructed and standard sample cells. The system was developed to enable measurement in real time. In other words, it can automatically measure the optical rotation for each analyser angle using LabVIEW and accurately calculate a phase shift (optical rotation) for each measurement using a Matlab code, as shown in Appendix A.

4.3 Real-time measurement results

Different samples with different glucose concentrations were measured by applying a system enhancement - running the components at the same time and calculating the optical rotation using the customised curve fitting (see Appendix A) at the Matlab code, as shown in Figure 4.7. The same concentrations were repeated using a 1 cm sample cell (see Figure 4.8), in order to minimize the optical pathlength.

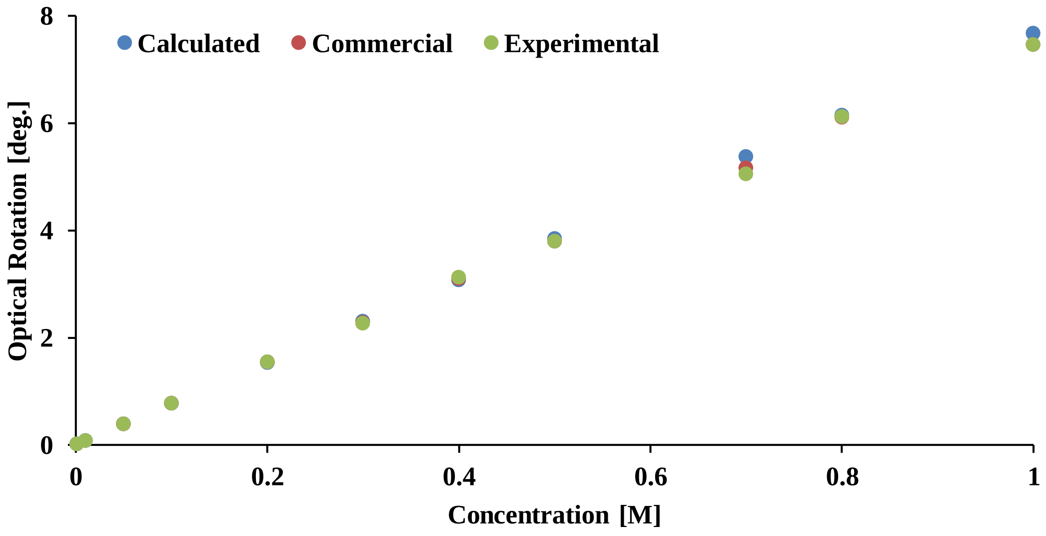

Figure 4.7 Rotated angles for the polarisation measurements with their theoretical values for different glucose concentrations using the fitting tool and measurement in real time enhancements (10 cm sample cell). The vertical error bars show the standard deviation (n=3), which was always <4%.

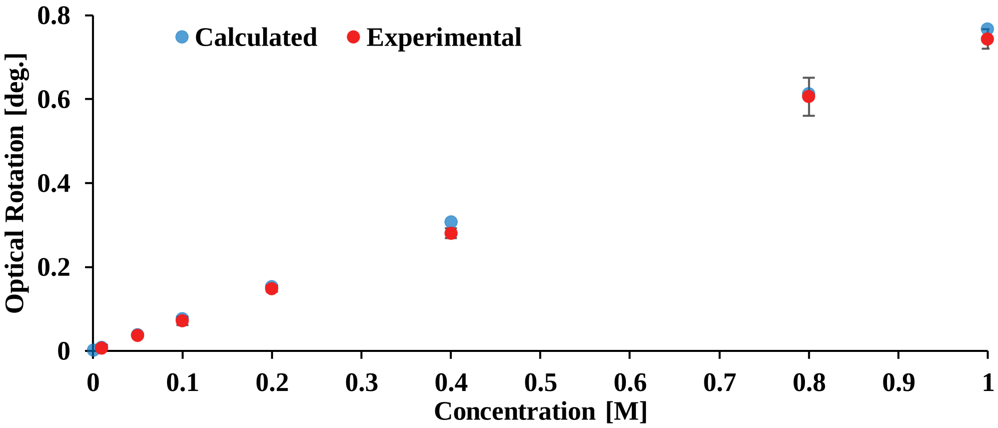

Figure 4.8 Rotated angles for polarisation measurements with their theoretical values for different glucose concentrations using the fitting tool and measurement in real time enhancements (1 cm cell). The vertical error bars show the standard deviation (n=3), which was always <4%.

Another comparison was made by repeating the same measurements without using a pinhole to determine whether the pinhole would influence the rotation angle, as shown in Appendix B2. Comparisons between the measurements errors were studied and discussed in Appendices B2.2 and C. The influence of different parameters (pinhole size and low signal detection) on the measurements sensitivity were studied and discussed, as shown in Appendices B and C. Several studies were performed in detail to diagnose the noise that influences the accuracy of experimental results in different parts of the polarimetry setup (see Appendix C).

4.4 Advantages of two external reflections from mirrors out of the chiral molecules

One of the obstacles when transferring to a microchip cuvette is the very short optical path length (100-500 µm), which is the main parameter regarding the influence on the detection of the rotation angle of a polarised light plane in a chiral molecule sample. In this study, a multi-reflection technique was used to increase this optical length, and various setup arrangements were designed to avoid changes in the polarization and to attain a longer path length.

4.4.1 Results and discussions

In the reflections' setup design, two mirrors of 25.4 mm diameter at R>96% reflectivity were added. In order to reduce the chamber dimensions of the polarimetric system, two mirrors were introduced around the cell, which increased the laser optical path length and allowed for several reflections (as shown in Figure 4.9).

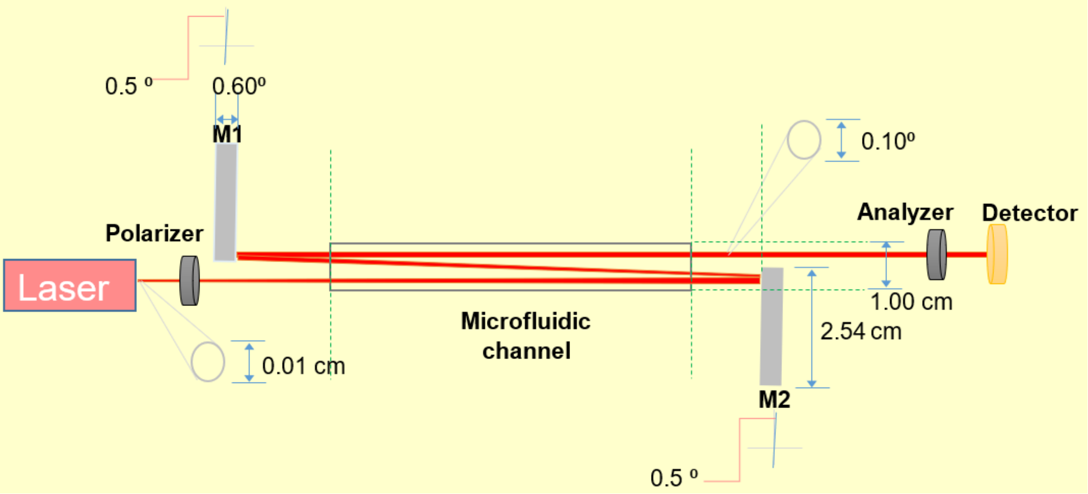

Figure 4.9 First enhancement in the polarimetry system (increasing the optical path length by introducing multi-reflections through the sample by mirrors M1 and M2).

The polarisation rotations and power were measured every two reflections. Despite several measurement trials, there was no apparent indication of a relationship between the increased reflections and the polarisation angle (see Figure 4.10).

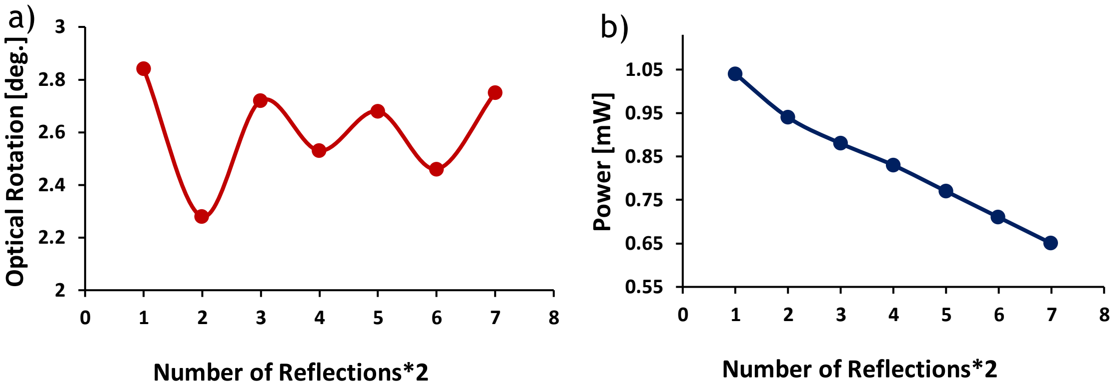

Figure 4.10 a) Polarisation angles related to the number of reflections (parallel mirrors), b) The power related to the number of reflections (parallel mirrors).

The output power declined as the number of reflections increase due to the mirror’s losses in reflectivity.

This was experimentally proven since the polarisation angle of the vertically polarised light without mirrors (and even without sample cell) was measured. The two parallel mirrors were fixed around the sample cell with a small angle of incidence (5°). The polarization angle did not have a regular change and was the same without any reflection, as shown in Figure 4.9. Following this, another new setup was arranged; a 1 cm cell was placed after the first polarizer, encountering the mirror at a 45° angle of incidence. Then the laser beam passed through another 1 cm sample cell, as shown in Figure 4.11.

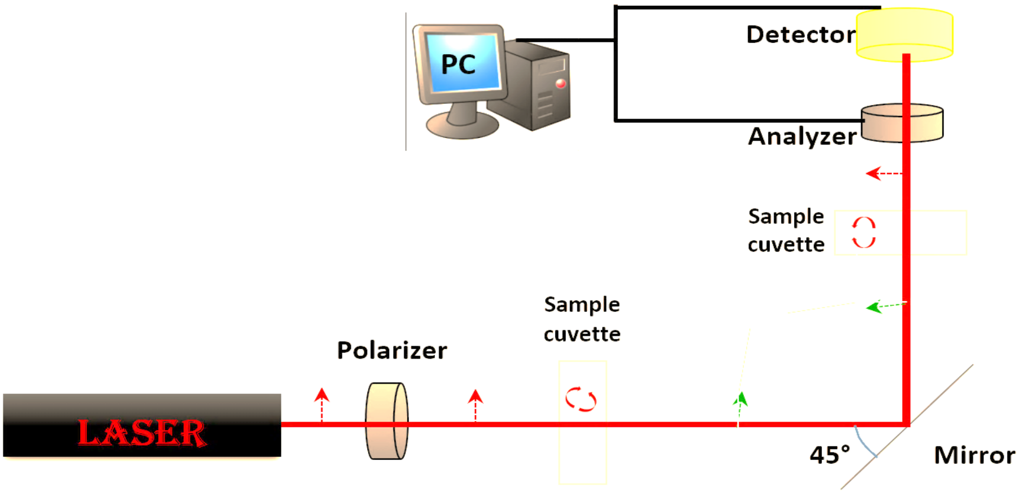

Figure 4.11 One mirror setup, arrows indicate the polarisation rotation of a linearly polarised laser.

Three cases were studied and the polarization rotations were measured under three conditions: a) when both cells were filled with water (as a reference); b) when water was in the first cell and glucose (1 M) in the second; and c) when glucose was in both cells. The results show that the polarization rotation cancelled each other under condition C and rotated about 0.81° (theoretically 0.766°) under condition B.

The setup was then modified for two arrangements; this was achieved by placing another mirror in front of the first one, with the light reflected at a 45° angle, as shown in Figure 4.12 (a and b).

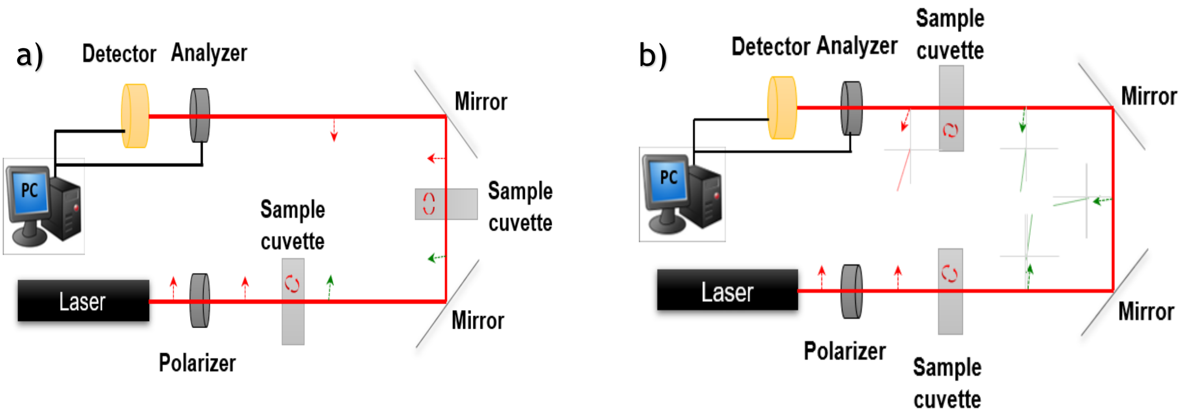

Figure 4.12 Two mirror setup a) cuvette between mirrors, b) without cuvette between mirrors. Arrows indicate the polarisation rotation of the linearly polarised laser.

The measurement showed that the glucose also rotated the plane of polarized light when both cells were filled with glucose, as shown in the setup in Figure 4.12 (b). In comparison, the polarization angles of two glucose cells nullified each other in the setup, shown in Figure 4.12 (a). This inspired us to make two reflections outside the chiral molecules to attain a long optical pathlength, as shown in Figure 4.13.

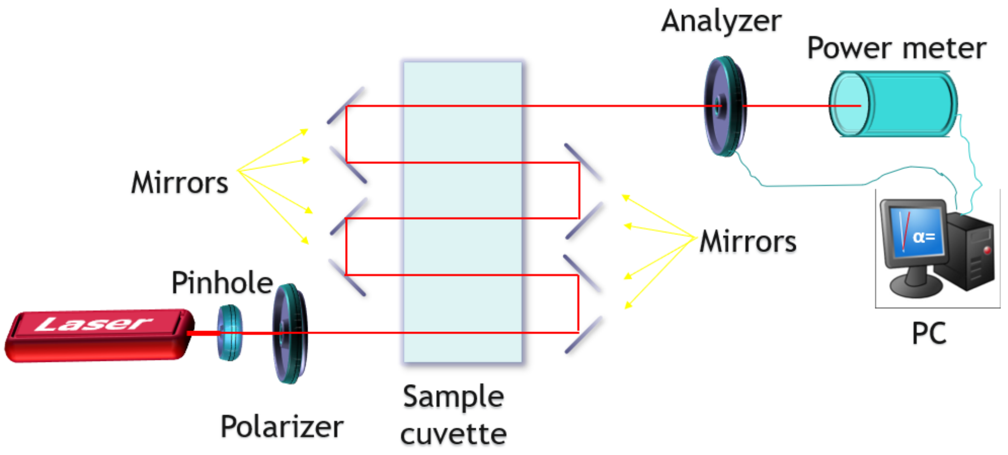

Figure 4.13 Multi-reflection setup in the polarimetry system (two reflections from the chiral molecules).

4.5 Miniaturizing the polarimetry

With the aim of miniaturizing the system, a 2 mm path length cell was constructed using microscopic slides (see Figure 4.14 (b)). A sample of 1 M solution was measured for a direct pass, and then for three passes arranged in a set of four smaller mirrors (12.7 mm), as shown in Figure 4.14. The corresponding results were recorded and compared with that of a direct pass. The results indicated that the increased percentage error and variance when using multi-reflection schemes were 2% and 0.1° respectively. The reason for this could be the path length error (when the cell was constructed); as such, the measurement of the path length has been tried using blue dye and Beer-Lambert Law, but it could not be recognized because of the laser fluctuation. It was then noted that the error did not relate to the path length as the standard microscopic cell was used.

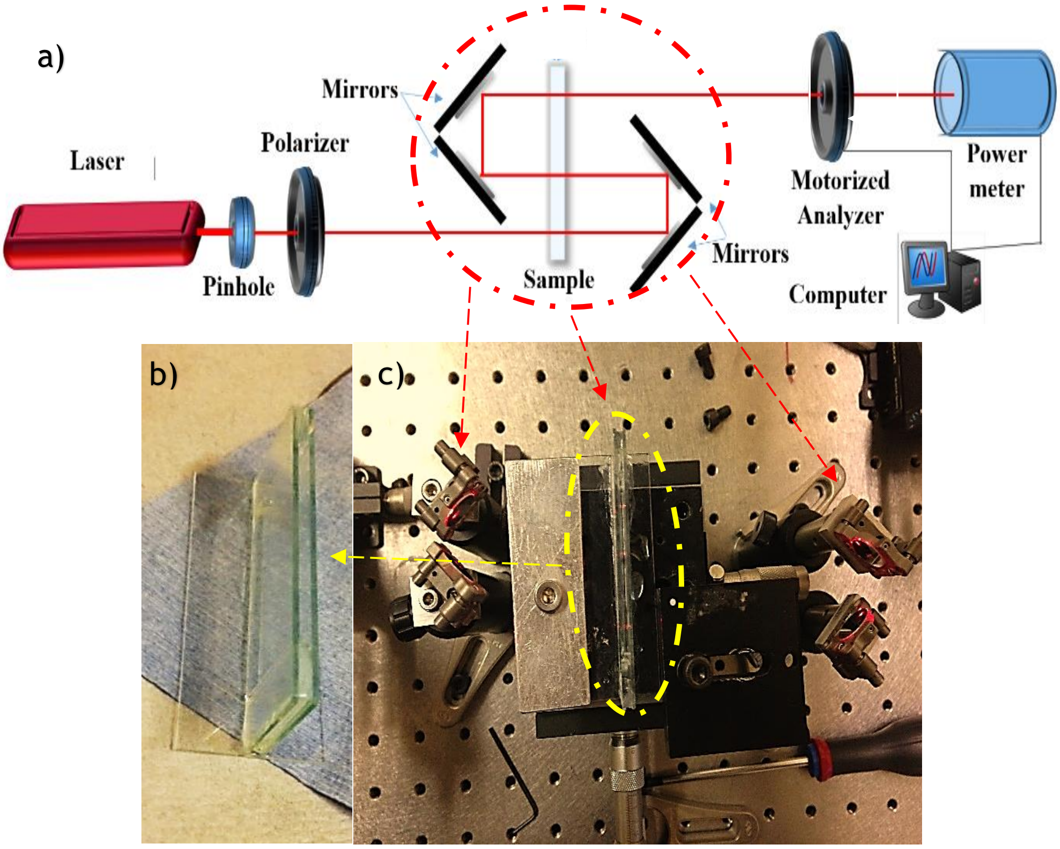

Figure 4.14 a) Block diagram of a multi-reflection polarimetry setup using: b) A 2 mm path length cell construction (two stacked microscopic slides perpendicular on the third one); c) An image of a multi-reflection scheme.

4.6 Metal and dielectric mirrors

To implement and interpret Jone's matrices for the experiment [54], a Matlab code was written using several Jone's vector terms to determine the polarization results of different designs on multiple reflections upon metal and dielectric mirrors in a polarimetry system, as shown in Appendix A.3 (3.1 and 3.2).

The analysis proved that, when using dielectric mirrors, the polarisation would not change through a multiple reflection scheme, although it changes if the mirrors are metal coated. This is because of the complex refractive index part that appears when the light reflects from metals, as indicated in Chapter 2.

Experimentally, the initial measurements were made for two glucose concentrations (0.5 and 1 M) with a water reference when a laser beam passes three times through the sample. When metal mirrors (silver) were used, the percentage error and variance between the analysis and experimental results were about 5% and $1.2X10^{-3\circ}$respectively. While in the case of dielectric mirrors, the polarisation angle rotated once (namely, one pass) regardless the number of passes. The percentage error and variance were much smaller than in the metal one, 1.2% and $3X10^{-5\circ}$ respectively. This demonstrated a polarisation stability of dielectric materials in comparison with the elliptic change of metal mirrors (as shown in Figure 4.15).

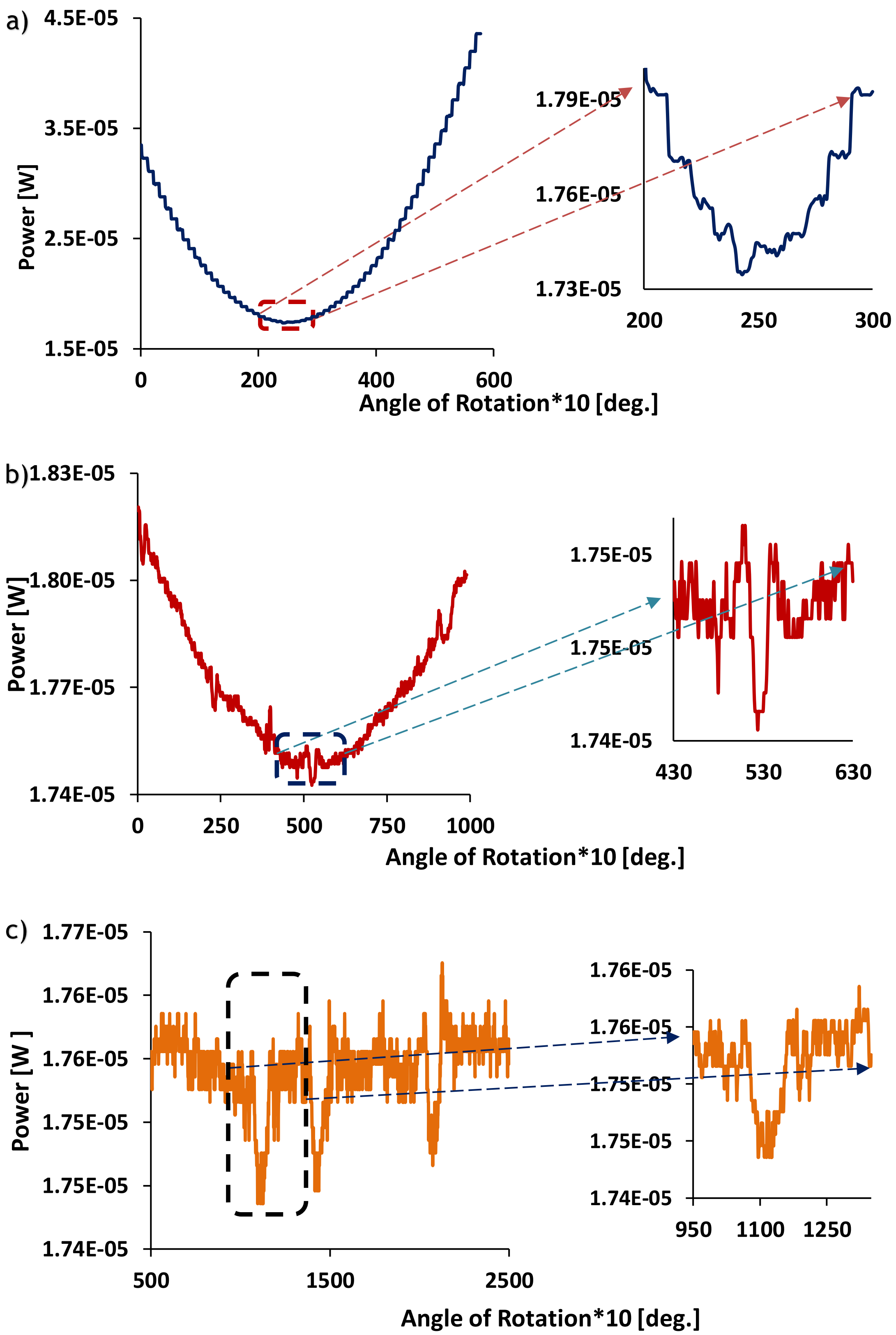

Figure 4.15 Laser fluctuation in the trough of a multi-reflection polarimetry scheme (without sample cell) for (a) 0.1°, (b) 0.01°, (c) 0.001°. steps of the analyser (Glan-Thompson) mount using dielectric mirrors. Here the date is multiplied by ten as each degree of rotation has 10 readings.

Therefore, metal mirrors were used in the multi-reflection scheme despite the stability results when using dielectric mirrors. This was due to the cancellation of the polarisation state for even reflections of light when passing through chiral molecules; this did not happen in silver mirrors due to their elliptical polarisation change.

4.7 Improvements of Polarimetry System

4.7.1 Using Shorter Laser Wavelength

Working in a micro-dimension required improvements to some of the parameters and tools that were used in a bulk dimension; this helped to decrease the disadvantages of a short optical path length. One of these parameters is the laser's wavelength; shorter wavelengths make a larger angle of rotation [35].

Here, a short wavelength diode laser (403 nm) was used instead of the He-Ne laser 632 nm, previously used laser, in order to increase the specific rotation and the optical activity of the chiral molecules. This wavelength increases the optical activity of chiral molecules by a factor of three, which improves the percentage error and allows for the limit of detection to decrease to a value less than half of that when using the He-Ne laser. According to the specific rotation values for both the He-Ne and diode lasers (42.6 and 120.08 ($\text{deg}\cdot\text{mL}\cdot\text{g}^{-1}\cdot\text{dm}^{-1}$) respectively [68]), the angle of rotation when using the diode laser is greater than for the He-Ne laser by 2.8 with the same glucose concentration and cavity length.

The previously constructed polarimetry setup was improved to also include: the diode laser (BEAM-SMART- 405-s_13667; tunable power, 403 nm); optical elements, including: pinhole (400 µm,100 µm); beam splitter; aluminium mirrors (Newport; 05D20AL.2), a data acquisition system; and a power to voltage converter (National Instrument: NI USB-6343) (see Figure 4.16). These were added to the previous system, aligned and calibrated.

The diode laser (of 403 nm) was used as a polarised laser source for the polarimetry setup, as the glucose-specific angle of rotation increased with short wavelengths [68]. A set of different sample concentrations of glucose (0.05, 0.1, 0.3, 0.5, 0.7, and 1 M) were prepared. The corresponding angles of rotation for these samples were measured for both lasers (see Figure 4.17).

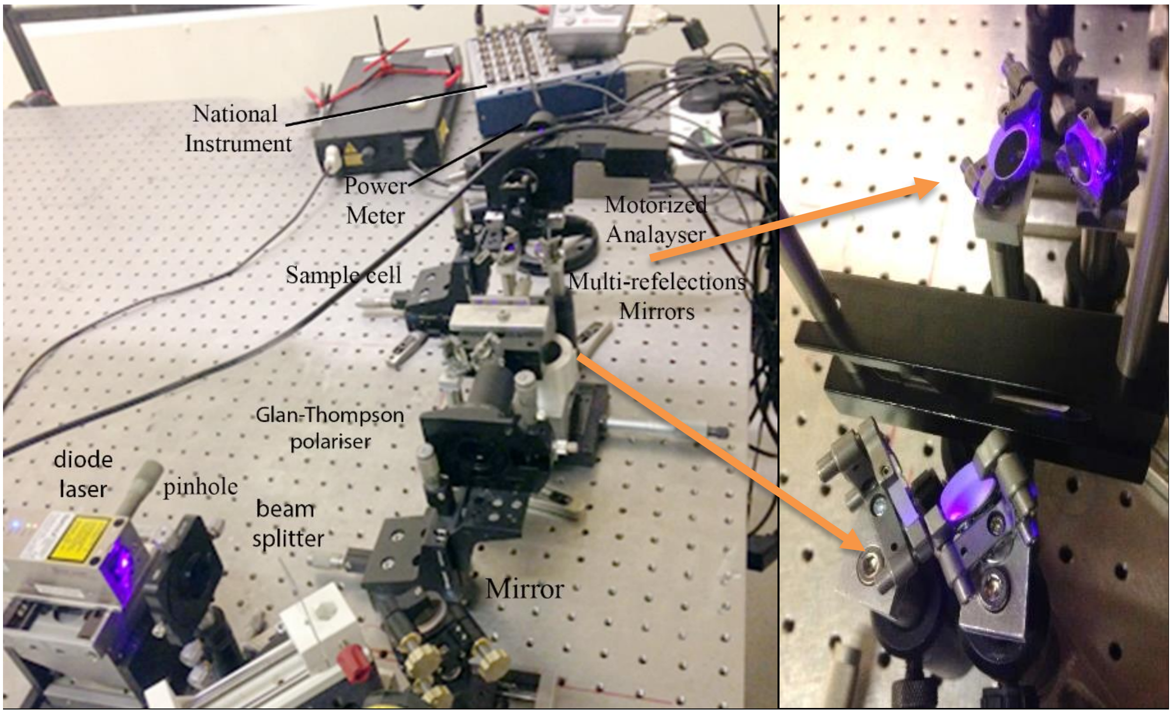

Figure 4.16 Photograph of the polarimetry setup showing the diode laser (403 nm) passing through the optical elements of the system, which includes the multi-reflections scheme.

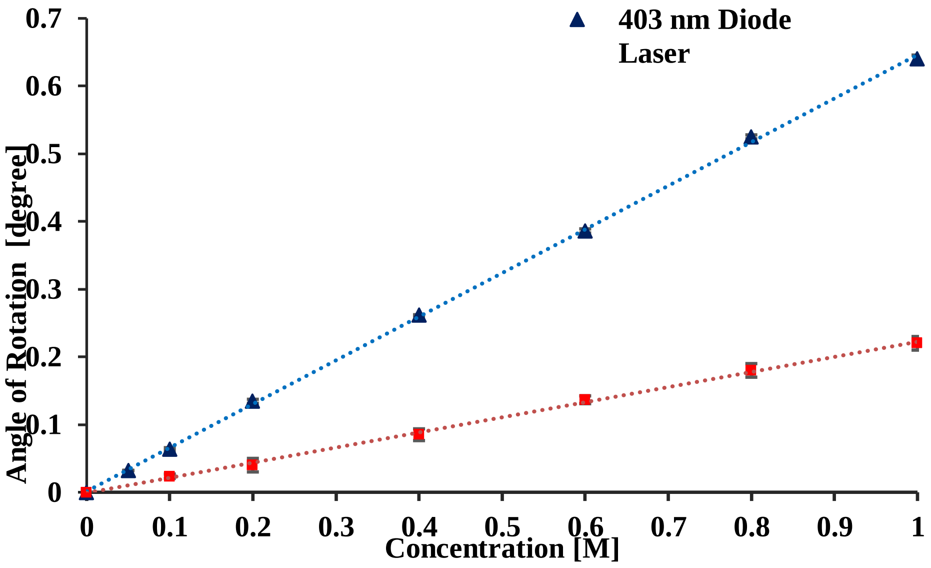

Figure 4.17 Polarisation rotation of different glucose concentrations using the He-Ne laser (red line) and a diode laser (blue line). The vertical error bars show the standard deviation (n=3), which was always <4%.

Comparisons were made for two sets of laser measurements by considering the percentage error, variance, and the limit of detection for each measurement (the optical rotation of the water plus the triplet of the standard deviation). The results confirmed the theoretical calculations of this factor of three increase, and the detection limit was enhanced approximately two times when using a blue laser. The variance in the optical rotation when using a diode laser was less by more than four times compared with the use of a He-Ne laser (1.66 $X10^{-3}$° and $7.21X10^{-3}$°, respectively).

4.7.2 Aluminium mirrors

The 180° polarisation flipping of the mirror before interrogating the sample, plays an essential role in this multi-reflection setup. This is because the basic concept depends on nullifying the 180° flipping of the polarisation at each mirror before interrogating the sample through the subsequent pass, and thus adding rotation through multiple passes. Aluminium mirrors were used instead of silver mirrors in order to make this flip as close to 180° as possible and with less polarisation noise at the mirrors. The aluminium mirror has better polarisation flipping at a 45° incident angle than the silver, as shown in Figure 4.18 [66].

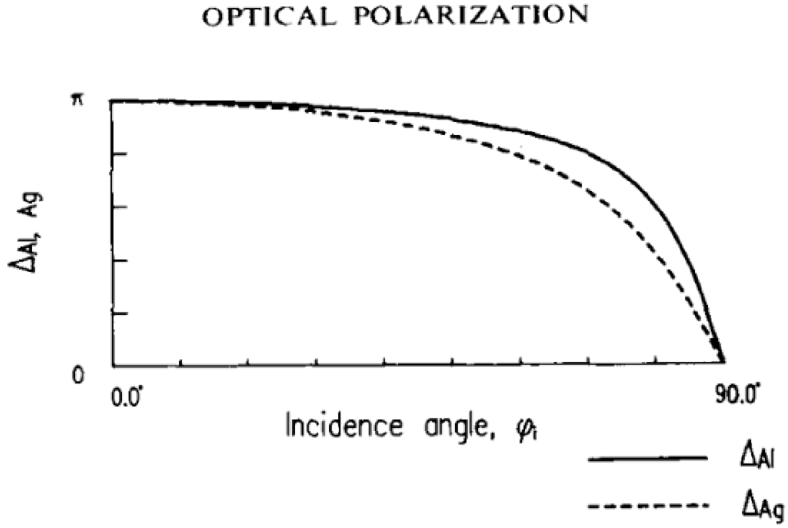

Figure 4.18 Phase shift (Δ) as a function of incidence for the aluminium and silver surfaces [66].

Experimentally, the comparison was made in the multi-reflection polarimetry system using both types of mirrors, as shown in Figure 4.19.

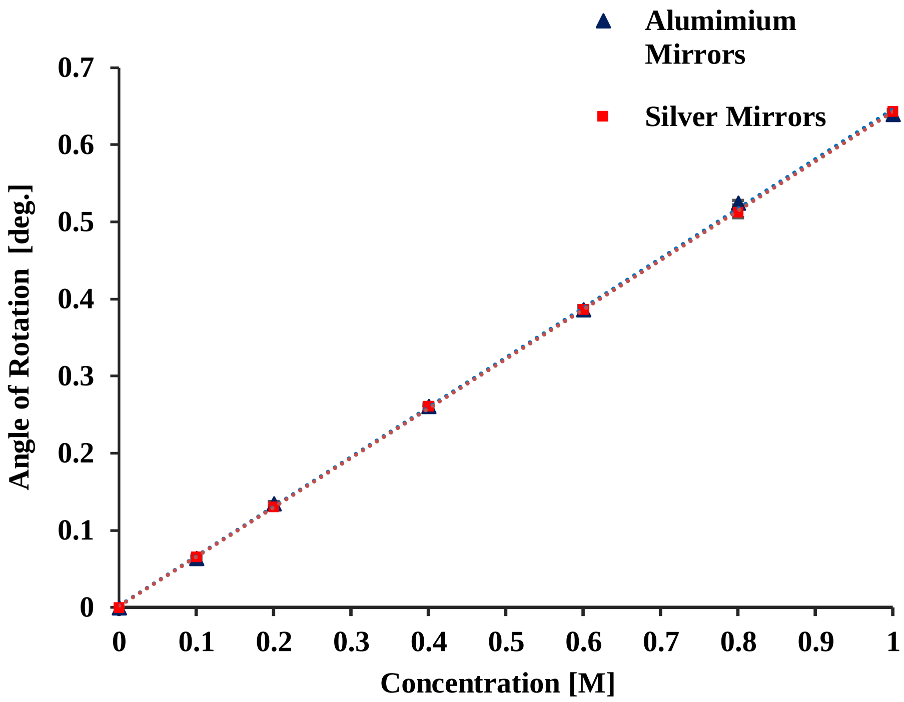

Figure 4.19 Optical rotation for different glucose concentrations using silver and aluminium mirrors. The vertical error bars show the standard deviation (n=3), which was always <4%.

The results showed that the use of aluminium mirrors reduced the average standard deviation of an optical rotation for glucose reducing it to $2.86X10^{-3\circ}$ compared to $3.79X10^{-3\circ}$ for the silver mirror. The average percentage error for this measurement was below 1% when using aluminium mirrors compared to silver.

The Matlab code was established (shown in Appendix A.6) to specify the measured polarisation angle in the region between the peak and trough of the output power. It is a sensitive region in which to indicate the optical rotation's deference between water (as a reference) and glucose [72].

4.7.3 Improvement of data acquisition speed

One of the obstacles facing the experiment was the slow data acquisition from the power meter (10 Hz). A National Instrument device was used along with the power meter to acquire a voltage of the output laser instead of power; the process showed a very fast data acquisition (about four minutes for 360 data points) compared to the power data acquisition (about 12 minutes). This long time has an adverse effect as the measurement depends on the output laser power and any drift in the power will affect the value of the resultant optical rotation. A Matlab code (shown in Appendix A.7) was created to compensate for the fluctuations in the voltage due to the auto scale in the power meter; this effects the scale factor of the analogue voltage. The detection limit was enhanced 10 times when using only three passes with the mirrors (10 mM D-Glucose (with blue line) and 100 mM without reflections (red line) - see Figure 4.20), while achieving an excellent linear correlation (linear correlation R^2>0.99). The system achieved a resolution angle of 0.001°, demonstrating the potential impact of our approach to increased sensitivity and thus opening up microfluidic applications.

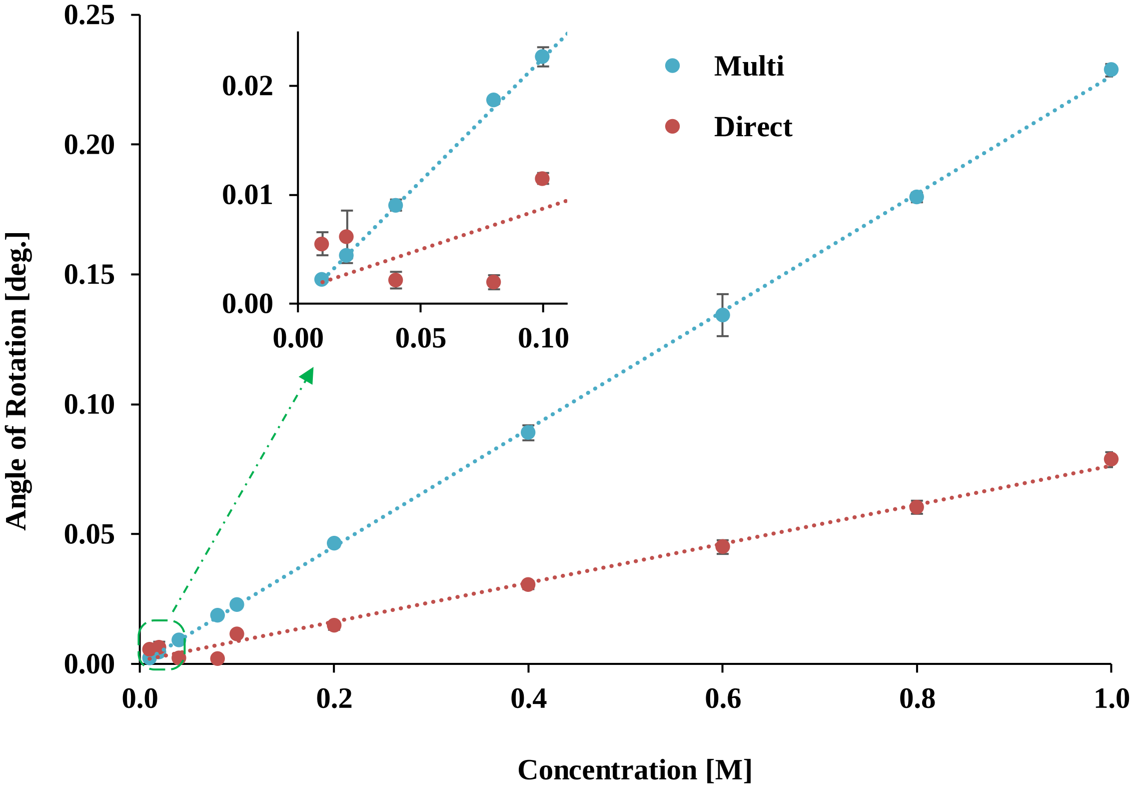

Figure 4.20 Optical rotation for different glucose concentrations using the multi-reflection (three passes) setup (blue line) and without it (red line). The vertical error bars show the standard deviation (n=3), which was always <4%. The linear correlation is R^2>0.99. The inset is a zoom on the low concentrations showing the limit of detection for both approaches.

4.8 Multi-reflections scheme using cube mirrors

To demonstrate micromirrors in a multireflection scheme, PMMA (Polymethyl methacrylate) commercial 2.5 mm cube mirrors were used – see Figure 4.21.

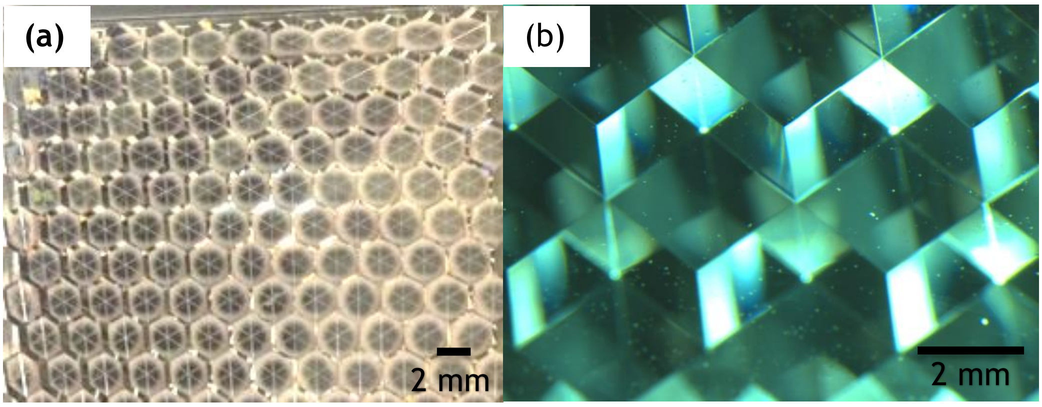

Figure 4.21 Image of PMMA cube mirrors.

4.8.1 Enhancement of the mirror’s reflectance

The aluminium layer was evaporated using an electron beam evaporation tool (Plassys 2) at the JWNC. However, the PMMA mirrors were partially transparent even after evaporating 1500 nm thick aluminium layers. This is due to the non-uniformity of the evaporated aluminium resulting from the tilted PMMA cubes on the substrate. Therefore, the laser signal was lost after several reflections. The maximum reflectivity achieved was around 60 % (see Figure 4.22).

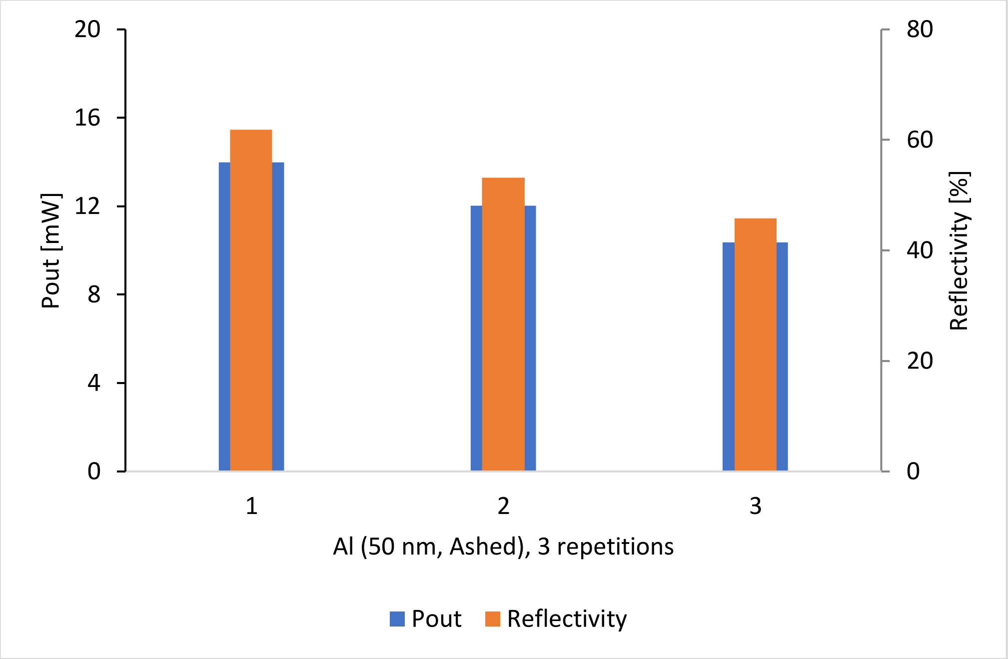

Figure 4.22 Reflectivity and output power from the cube mirrors, which were evaporated with an aluminium layer of 50 nm with tilted 45° substrate at three repetitions.

Different layers of titanium with aluminium, and gold were evaporated on these mirrors, but the mirrors were still transparent, and the laser beam was lost (going through the material) after the fourth reflection (Figure 4.23). The maximum reflectivity was achieved (up to 68%) using gold-coated structures, while the reflectivity of aluminium was around 40%. The silicon wafer was evaporated with a 100 nm aluminium layer to compare it with the PMMA substrate. The reflectivity was above 70%, which is about double the aluminium coated PMMA cube mirrors (40 %), as shown in Figure 4.23.

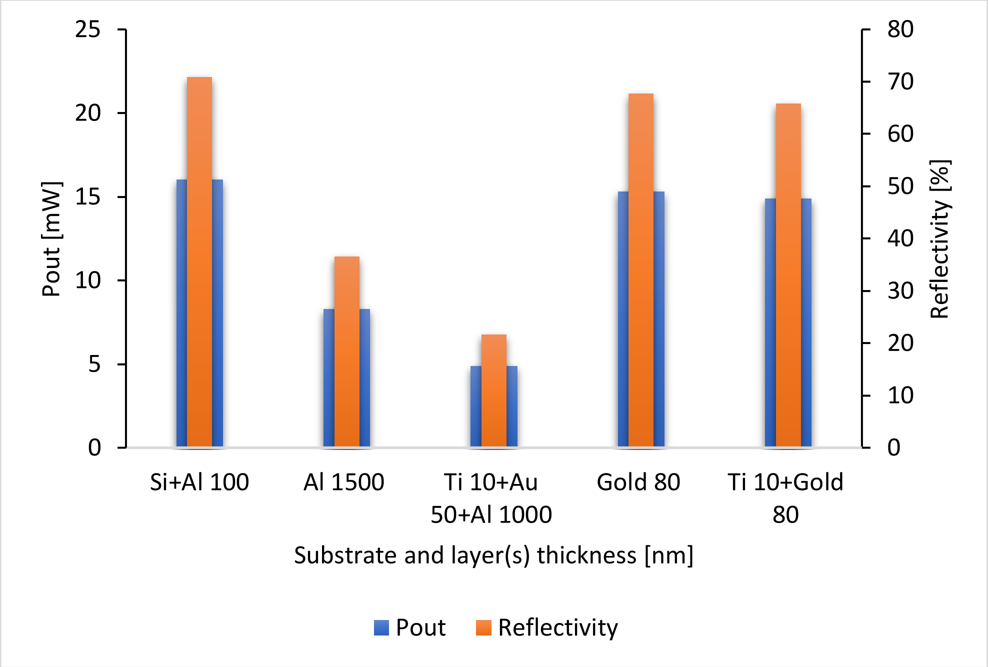

Figure 4.23 Reflectivity and output power from cube mirrors and a silicon substrate, which was evaporated with different metal layers and with just aluminium respectively.

One of the other solutions was to stick portions of silicon on the facets of the PMMA mirrors. The aluminium layer was first evaporated on the silicon then the silicon substrate was cleaved into about 1 mm square to suit the size of the cube mirrors. This approach did not result in an enhanced signal, as the signal was misaligned due to the tiny portions of cleaved silicon sticking out of the substrate. Therefore, the silicon substrate did not sit flat. Other enhancements to the reflectivity were applied including the evaporation of a thick aluminium layer (1500 nm) on tilting and rotating the silicon substrate during the evaporation process of the aluminium layer by 14.4°. The substrate was first cleaned by the plasma asher and, consequently, the reflectivity was raised to 63% - see Figure 4.24 - and 20 reflections were achieved to enable 11 passes through the arrangement of the mirrors.

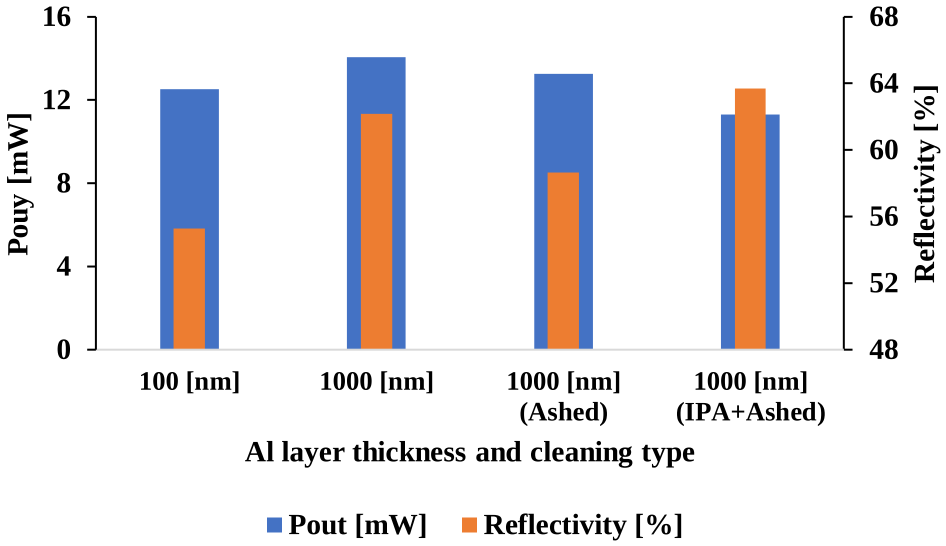

Figure 4.24 Reflectivity and output power from the cube mirrors, which were evaporated with a different thickness of aluminium layer, using a 14.4° tilted and rotated holder during the evaporation process.

4.8.2 3-D printing the mirror mount

In order to align the micromirrors to get two reflections before interrogating the sample for several reflections, the 3-D mount was designed using SolidWorks. The design took into account the tilting of the PMMA cube mirrors – see Figure 4.21(a). It enabled both sides of the micromirror’s cavity to be held in the same holder with a 55° tilt to each to achieve the aligned and parallel beam reflections - see Figure 4.25. In addition, it had the flexibility of screwing it to different sizes and distances on plates or to an optical bench, as shown in Figure 4.25 (b and c). After 3-D printing the design, it was soaked in a chemical mixture of 2% sodium hydroxide, 1% sodium sodicate and water for two hours in order to clean the residual wax around it.

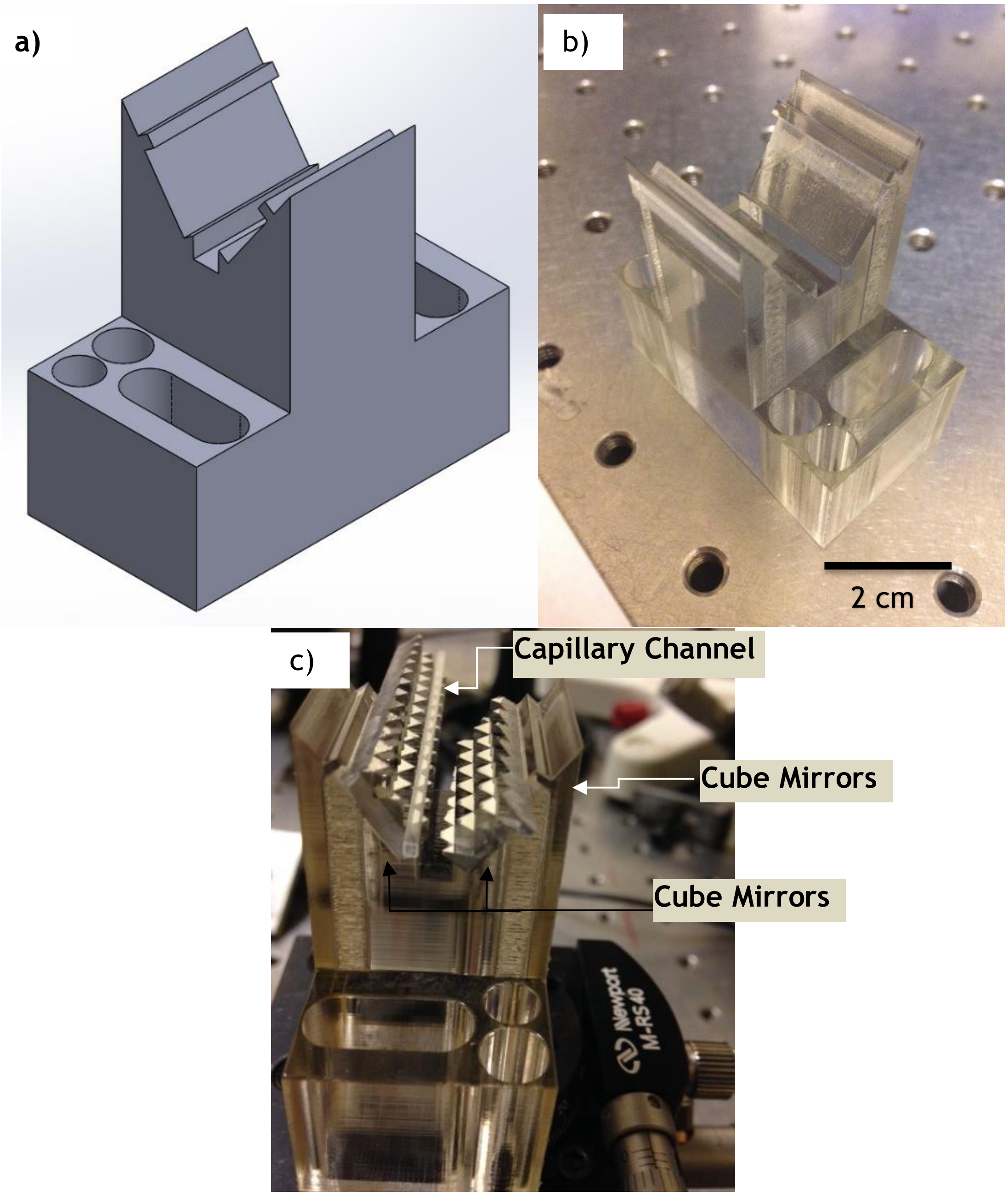

Figure 4.25 3-D micromirror holder: a) the 3-D design in SolidWorks software, b) the 3-D printed mount, and c) the 3-D printed mount with the cube mirrors and capillary channel.

4.8.3 Multi-reflection results and discussions using cube mirrors

We analysed the increase in the optical rotation performance of the system by studying the rotation produced by different concentrations of glucose. As illustrated in Figure 4.26, the optical rotation curves are for different glucose concentrations at a different number of passes (up to 11 passes). Although 13 pass measurements were attempted, the laser spot was lost due to the low reflectivity of the evaporated aluminium layer (R= 63%, He-Ne power is 19.5 mW). This results in high losses of the beam on four times for every three passes (four reflections).

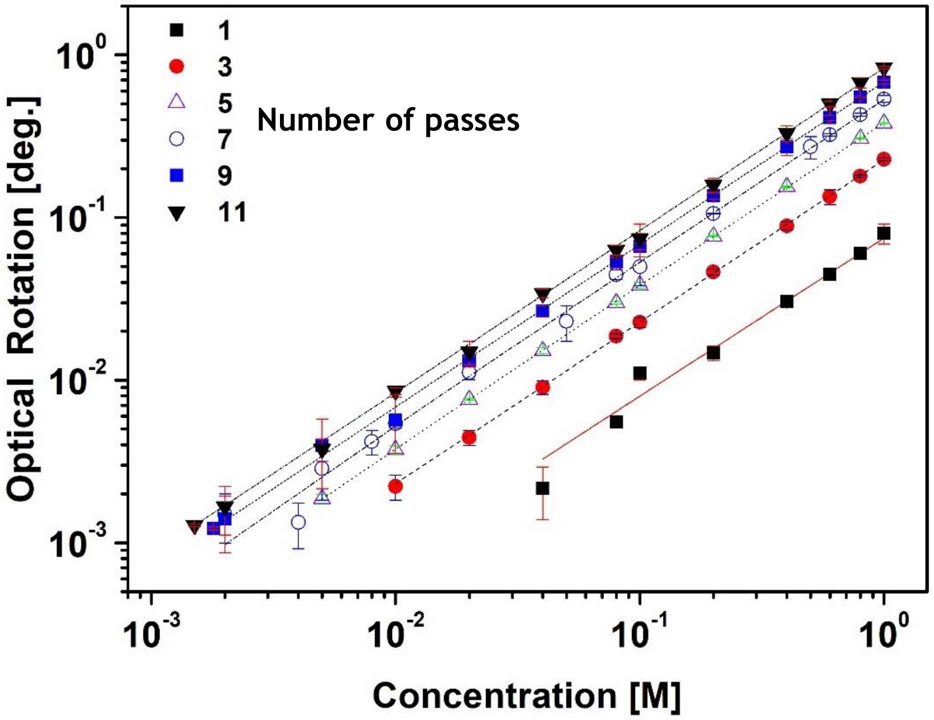

Figure 4.26 Optical rotation for the different glucose concentrations using a multi-reflection setup and a He-Ne laser (632 nm) (one pass is without using the multi-reflection). The vertical error bars show the standard deviation (n=3), which was always <4%. The linear correlation is at least R^2>0.997 for all different passes.

The power was calculated and measured for each number of passes; the reduction in the power within the number of passes shows a regular and uniform decrease. This observation translates into a uniform evaporation layer of aluminium, as shown in Figure 4.27 (a). Each curve of the polarization rotation shows a linear increase in the optical rotation by the same number of passes through the optical rotation. This confirms the theory in the preceding section, as shown in Figure 4.27(b).

The limit of detection for each pass shows an improvement compared to the one pass, thus decreasing linearly by increasing the number passing through the sample by 1/(number of passes)^2. The detection limit was enhanced 4 times when using only 3 passes with the reflections (10 mM D-Glucose and 40 mM without reflections, as shown in Figure 4.27(c)). In comparison, it improved by up to 27 times for lower concentrations (1.5 mM) when using the 11 passes scheme, which is about 750 times higher than the limit for the best commercial instrument but was accomplished in 30 times smaller volume and overcame the diffraction losses associated with directly shining the laser at the channel.

For a given concentration, for example 100 mM, the optical rotation was increased about seven times; the 11 passes scheme was introduced to polarimetry compared to the one pass optical rotation (see Figure 4.27(d)).

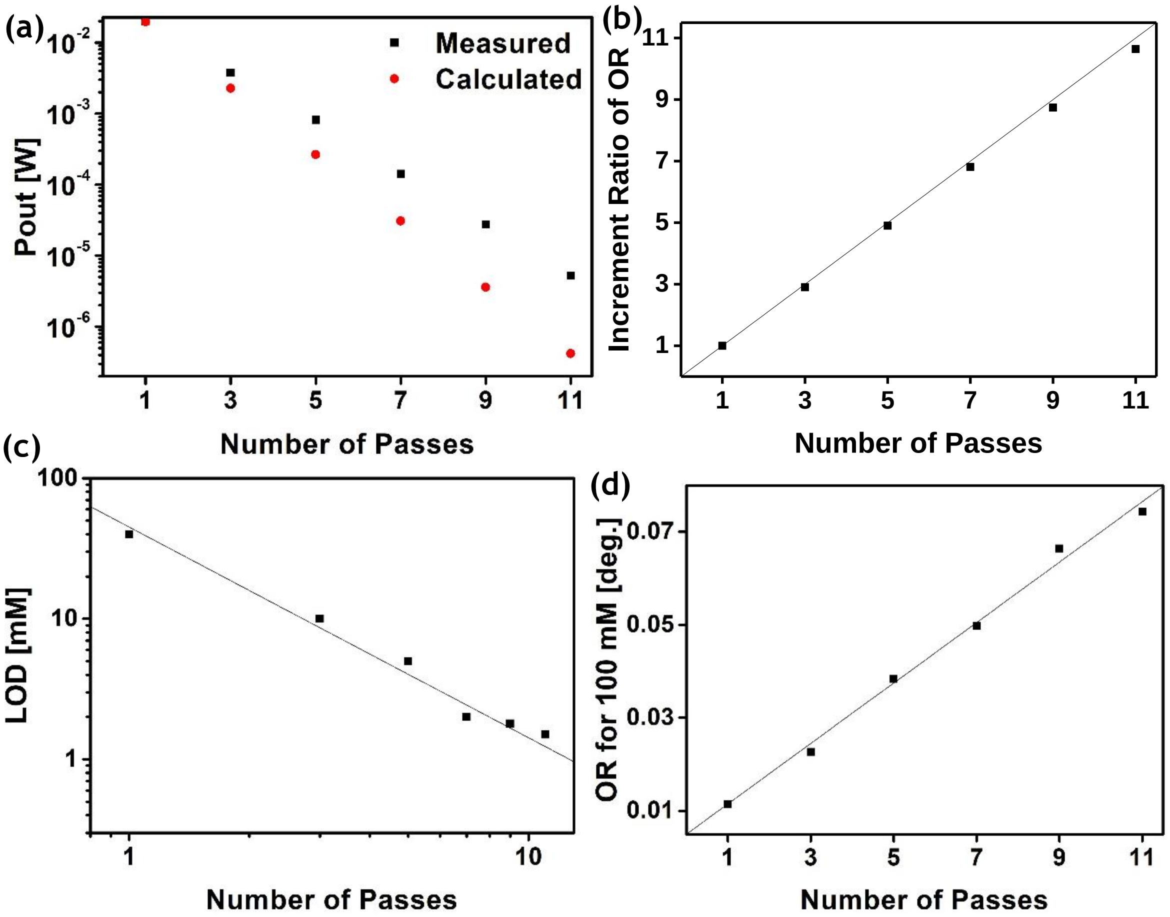

Figure 4.27 a) Output power (Pout) from the cube mirrors: theoretical and measured. The reflectivity of the mirrors (depending on the measurement of the input and output power of the coated aluminium layer) is 63%, and the input power of the He-Ne laser is 19.6 mW. b) Increment ratio comparison for the optical rotation (OR) between each set of measurements at each number of passes (in Figure 4.26) with one pass (without reflection). c) Limit of detection (concentration) (LOD) of each measurement at each number of passes. d) Optical rotation (OR) of the glucose of 100 mM at a different number of passes.

The system saturated at concentrations ranging above 2 M (Figure 4.28 (a)), while there was a sharp divergence of optical rotation in 2 M and its following concentrations when measuring in the seven passes scheme (see Figure 4.28(b)).

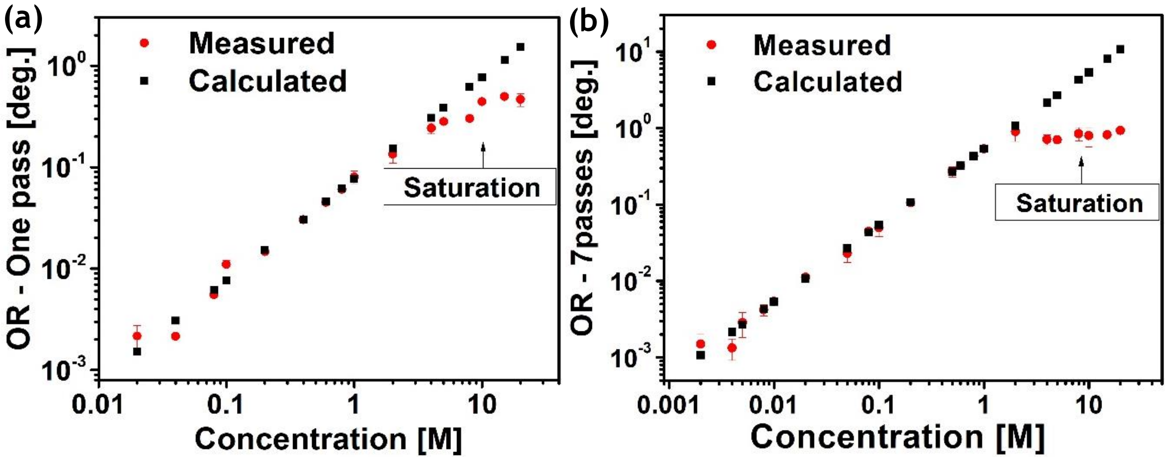

Figure 4.28 Optical rotation (OR) of a) One pass, and b) Seven passes, showing the optical rotation saturation point of the system without and with the reflection scheme, respectively. The vertical error bars show the standard deviation (n=3), which was always <4%.

4.8.4 Using shorter wavelength along with the multi-reflection scheme results

As presented in Section 4.7, in order to increase the rotation of the polarization for a given chiral substance, and provided that the pH and temperature are constant, the 403 nm laser was used instead of the He-Ne laser. This provides a higher optical rotation by a factor of three. The multi-reflection scheme was applied using this diode laser by the same maximum number of passes (11), despite the fact it exhibits a far higher power than He-Ne laser (up to 100 mW), as shown in Figure 4.29 and Figure 4.30.

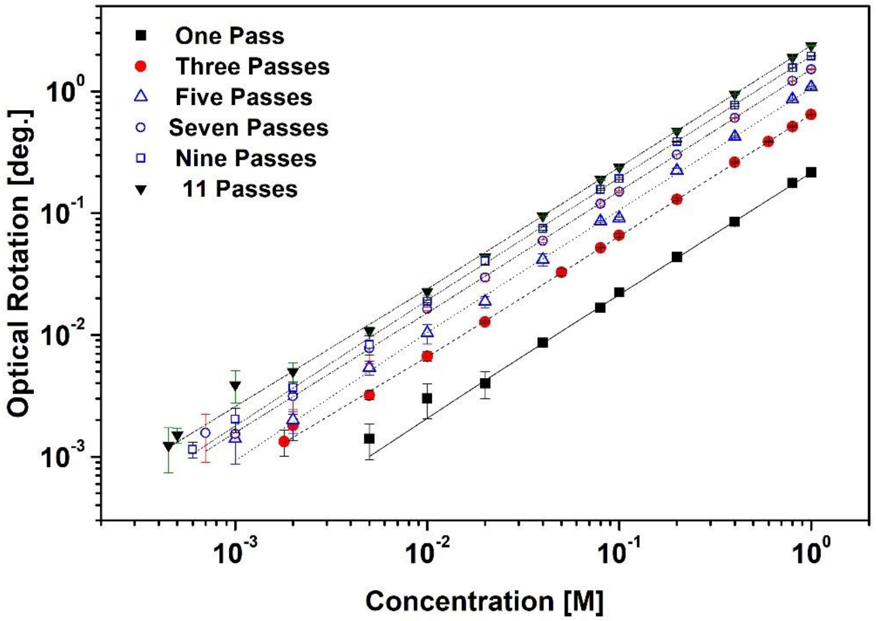

Figure 4.29 Optical rotation for different glucose concentrations using the multi-reflection setup and applying a diode laser (403 nm) (one pass does not use the multi-reflection setup). The vertical error bars show the standard deviation (n=3), which was always <4%. The linear correlation is at least R^2>0.997 for all different passes.

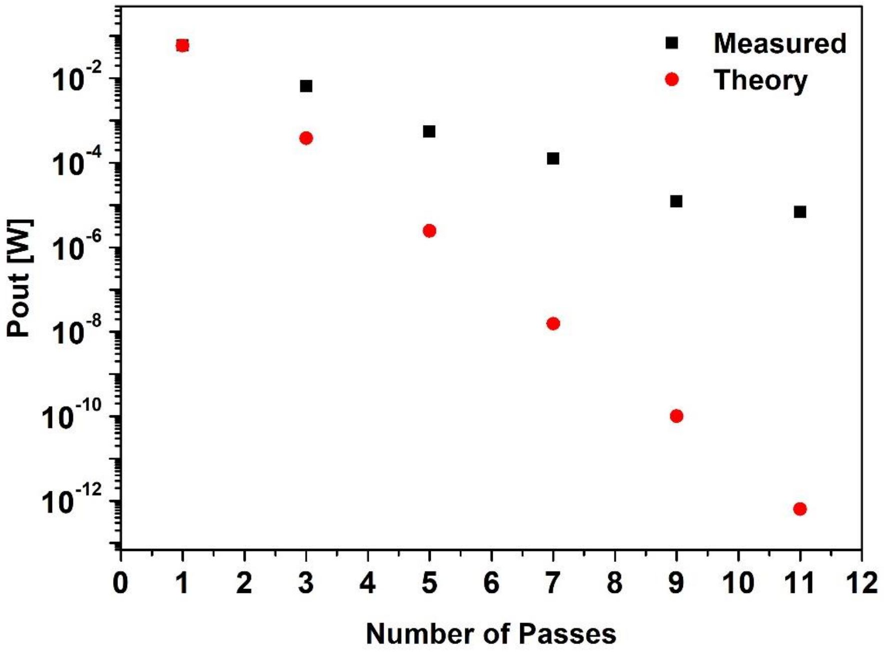

Figure 4.30 Output power from the cube mirrors: theoretical and measured. The reflectivity of the mirrors (depending on the measurement of the input and output power of the coated aluminium layer) is 32%, and the input power of the diode laser is 59.5 mW.

The increment ratio for each number of passes related to one pass is increased as with the He-Ne laser, and with a same number of passes. Meanwhile, the detection limit is reduced by more than three times (4.5 ×10^{-4} M) compared with the lowest concentration detected in 11 passes when the He-Ne laser was used (see Figure 4.31).

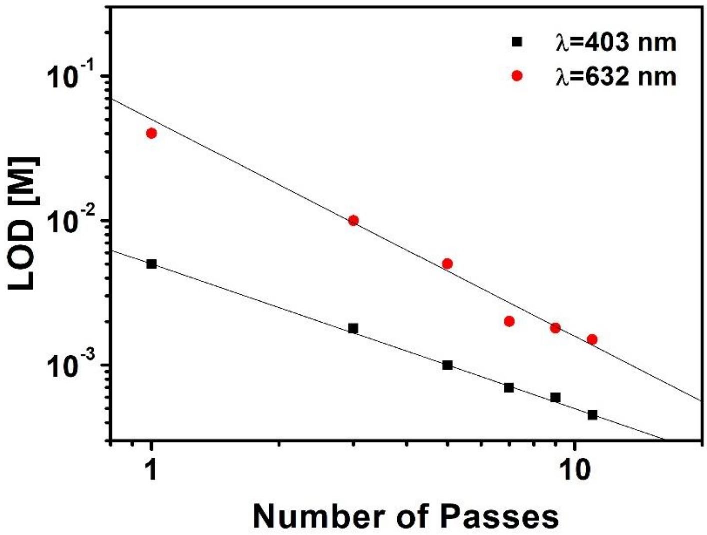

Figure 4.31 Comparison between the limit of detection of the He-Ne laser and diode laser for a different number of laser passes in the polarimetry system.

This is about 225 times higher (more than three times less than the limit of detection of the He-Ne laser results) than the limit for the best commercial instrument but was accomplished in three decades smaller volume.

4.9 Comparison between direct and multiple passes schemes of polarimetry

In the present system, the maximum number of passes achieved was 11, which increased the optical path length to 11 mm instead of 1 mm in the one pass case. When the laser directly shines at the channel's side, and not from the channel's side, the optical path length is roughly 21 mm (the path length of the channel used to obtain 11 passes (higher passes attained) in the multi-reflection arrangement). Therefore, it is nearly twice the optical path length between the direct and multi-pass schemes, while achieving less distortion and noise compared to the one pass direct shine. However, it is a channel and mirror width dependent. If the width of the channel is 1.9 mm, the multi-passes' optical path length is almost 21 mm, which is equal to the direct optical path length. If the width of a single mirror in the row is less, less channel path length will be used, and an equal optical path length in the multi-reflection will be used. The smaller the mirrors, the more reflections and the longer the optical pathlength acquired. Furthermore, the advantage of multi-reflections can be more worthy when overcoming the obstacles of direct shining the laser into the microfluidic channel, as it will create numerous challenging laser diffractions on the input side of the channel which effects the polarization calculations of the laser. We can alter the results by enhancing the reflectivity of the aluminium layer and making it close to commercial versions, as the reflectivities of the evaporated aluminium layer are just 63% and 32% using the He-Ne and diode lasers respectively.

4.10 Conclusions

An optical bench based setup and data fitting method were established to benchmark, and tune the system in order to give highly reproducible measurements. The setup was characterized using a glucose concentration (as a model of chiral molecules) in millilitre and micro volumes, which was the first step in paving the way towards the qualification of the microfluidic scheme. Polarimetry measurements using mirrors to simulate the setup in a microfluidic channel were performed prior to the design and fabrication of the microsystem.

Arranging the mirrors to obtain two reflections before passing through the sample volume nullifies the 180° flipping of the polarisation at each mirror before interrogating the sample through the subsequent pass, thus increasing rotation through multiple passes and enhancing the functionality of the polarimetry system.

In general, there will not be any polarization change as long as the laser polarization is either exactly on the plane of the optical bench or perpendicular to this plane, and the normal vectors of the mirror surfaces are also on the plane of this bench. In other words, if the linear polarization angle is 0° or 90° and the beam path stays on the plane of the bench (i.e. the mirrors do not introduce any changes in height to the laser), then the polarization will remain linear. If the mirrors change the height of the beam, then it will begin to alter the polarization of the beam. A single component of the vertically polarised laser will experience a phase shift (relative to the phase of the input field), but there is still no second/orthogonal polarization component after interaction with the surface.

The multi-reflection scheme enables a reduction in the volume of a sample (from 1.5 mL to 20 μL), which was accomplished in a three times smaller volume capillary of the best commercial instrument while decreasing the LOD for each number of passes and increasing the polarization rotation by using shorter wavelength to reach to 1.5 mM and 0.45 mM for the He-Ne (632 nm) and diode (403 nm) lasers, respectively.

Chapter 5 Micromirrors Fabrication

5.1 Introduction

The multi-reflection mirrors around the microfluidic channel have an essential role in increasing the optical path length in a polarimetry system, as discussed in Chapter 4. In this chapter, the development of this unique apparatus has been motivated by the MEMS-machining of micromirrors which affords an optical 90° reflection of light [73]. In particular, the fabrication of micromirrors was described using different silicon cut substrates, masks, and KOH recipes and TMAH etchants with different surfactants and alcohol to achieve smooth, 45° sidewall mirrors. These were put, sandwich-like, around the microfluidic channel as a cavity around the sample in the polarimetry system, as shown in Figure 5.1.

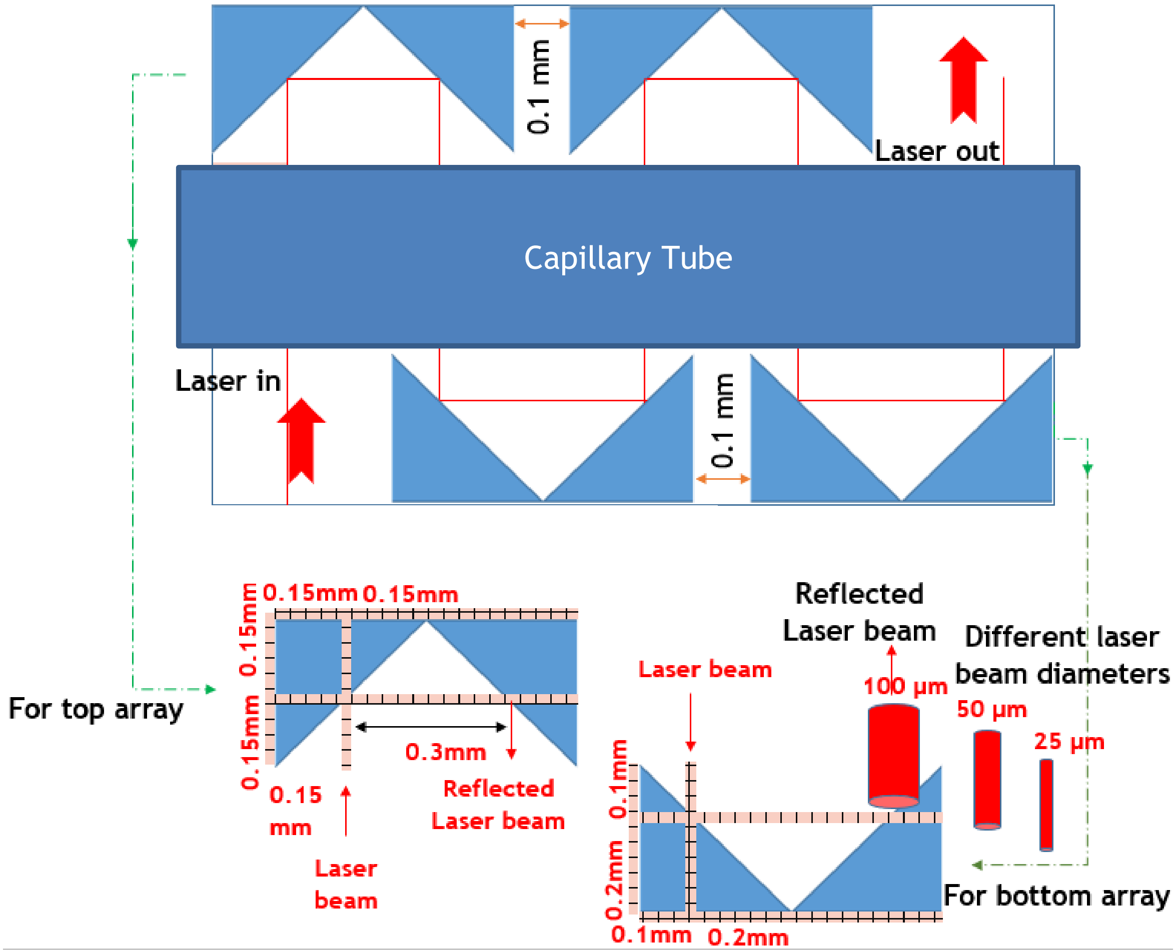

Figure 5.1 Schematic diagram shows the dimensions of the micromirror cavity in the multi-reflection scheme for different suitable beam sizes.

However, the fabrication of such deep, 45° mirrors which were closely related to the angle of the {110} plane of the silicon, [74], was a tedious task as it required sophisticated equipment and methodology. To address these shortcomings, alternative techniques were proposed and executed which did not require a slow etch recipe (TMAH with Triton X-100 (iso-octylphenoxy polyetoxyethanol)) of any kind. One utilised structures (pattern) whose corners already merged at 45° before etching, then selected the recipe to achieve 90° etched sidewalls (KOH with *tert*- butanol). While these techniques are alignment-free, they suffered from an associated error due to a varying undercut rate at different places on the pattern. This overcame the shortcomings of all the previous techniques in terms of being self-aligned, with the high etch rate of {100} plane; moreover, it was simple to implement, and reduced efforts to identify the direction.

Silicon bulk micromachining technology has been developed and is commonly carried out using a wide variety of different etches. It depends on several processes, for which the main one is the wet anisotropic etch of crystalline wafers for the fabrication of different kinds of microstructures (including microcavities, cantilevers, diaphragms, and so forth) [75-79]. In addition, these same etches are integral to the manufacture of various integrated devices, such as accelerometers [80], beam splitters [81], transistors [82] and comb structures [83]. The development of some optical apparatus has recently been stimulated by the ability to use MEMS-Machining to produce an array of micromirrors which afford an optical 90° reflection of light [73]. This is a scalable, low-cost technique and is therefore suitable for large batch processing. Potassium hydroxide (KOH) and tetramethylammonium hydroxide (TMAH) are the main etchants commonly used for such bulk silicon micromachining [84], [85], [86]. KOH is often desired to attain a higher etch selectivity at between {111} and {110}/{100} planes than for TMAH [87]. KOH has a high etch rate, which is suitable for the application of high throughput micromirror devices. Different parameters influence the surface morphology and etch rates, such as etchant concentrations, additive types, solution temperatures, and mass transfer/convection (stirring) speeds [88]. In order to enhance the surface morphology, surfactants and alcohols are combined in the etching process [74], [89], [90], [91], [92], [93].

Anisotropic silicon wet etching using a Si(100) wafer has previously been reported to achieve vertical sidewalls at {100} using KOH [94], [95]. However, the surface was not smooth enough to produce mirrors. Similarly, a 45° slanted smooth sidewall at {110} on Si(100) has been created [96], [97], [98], using TMAH with a variety of different additives, concentrations, and stirring speeds. Gosalvez, et al. presented an extensive study and results on etching in TMAH + Triton solutions [99-102]. They attempted to interpret the phenomena occurring during the etching in TMAH with the addition of the surfactant to achieve a highly improved Si(110) finish on a 45° tilted plane.

The angle between the etched sidewall and the wafer surface depends on the wafer crystal structures and the photo pattern orientation. However, the formation of a preferential different sidewall plane relies on the surface tension (which mainly varies with both the concentration and temperature of the etchant mixture) [103]. The results of the wet etch fabrication showed a smooth and handy etched sidewall; thus, 45° and 90° sidewalls have been achieved. High surface tension has an adverse effect on the 45° slanted wall but is preferable in attaining the vertical etched wall from the same window direction.

Preceding the wet etching, and in order to fabricate the mirrors in a safe, simple, and alignment-free way, another method was used to achieve the two zigzag mirrors on one substrate. This was achieved by spinning different SU8 photoresist layers on a substrate to act as a mirror's walls.

5.2 Mirror fabrication using patterned photoresist

In this approach, single and double layers of SU8 3050 and SU8 3025 photoresists were used to make a thick layer (around 100 μm) on any silicon substrate in order to develop it with a zigzag mask (see Figure 5.2) and to achieve 45° mirrors immediately after evaporating the suitable metal (e.g. aluminium) on the resultant sidewalls.

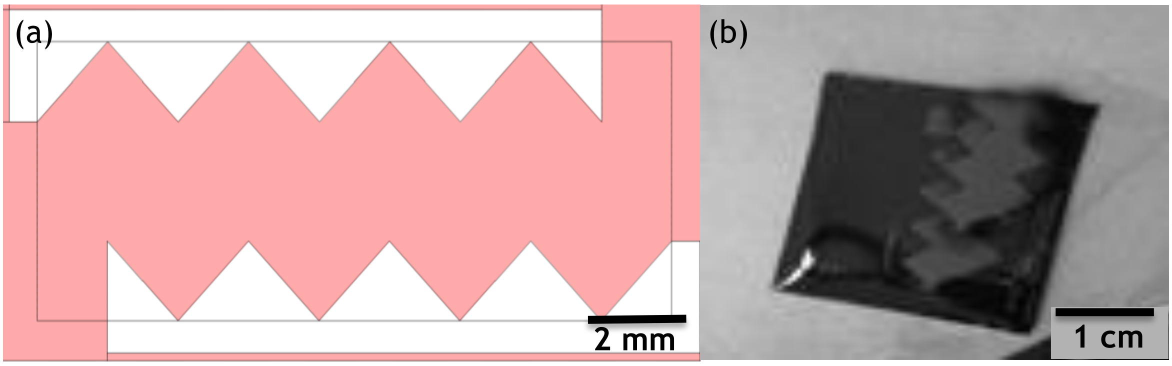

Figure 5.2 a) Photo-mask fabricating a multi-reflection mirror (vertical etching), b) SU8 layer on the silicon substrate after the photolithography process and using the photo-mask in (a).

This approach is simple as it does not require etching and mirror alignment as it depends on the mask orientations. However, it did not result in a vertical sidewall in the two ways to create one layer and dual layers, as shown in Figure 5.3 and Figure 5.4, respectively. This is because the resultant walls depend on the developing and baking of the SU8 photoresist, and these final processes melt the resist in an irregular shape (randomly tilted and rough).

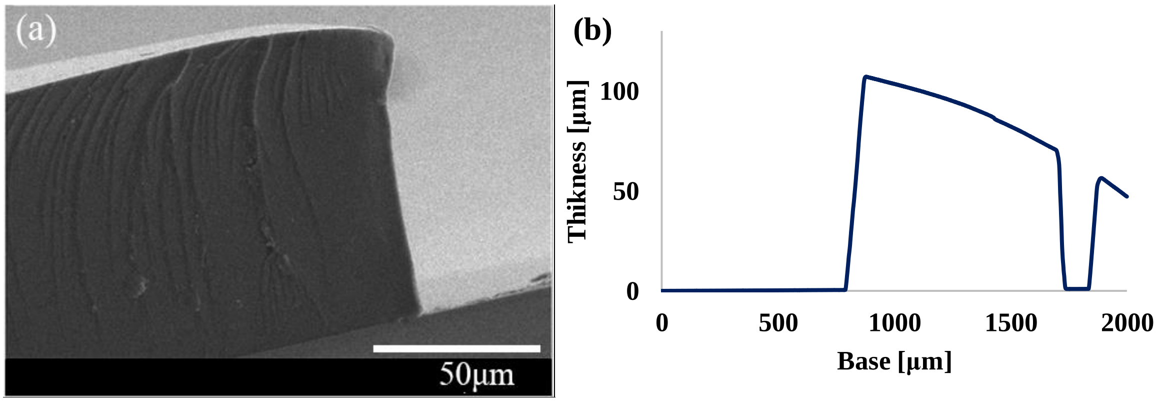

Figure 5.3 (a) SEM images of single SU8 3050 photoresist layer after lithography using the photo-mask in Figure 5.2 (a). (b) Dektak measurement of the sidewall depth; the depth of the sidewall is 100±15 µm.

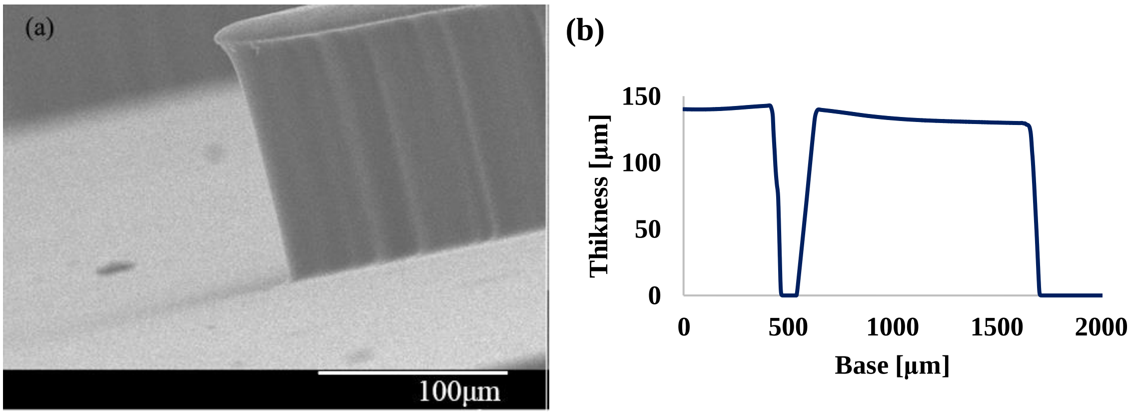

Figure 5.4 (a) SEM image of dual SU8 3050 and 3025 photoresist layers after lithography and using the photo-mask in Figure 5.2 (a). (b) Dektak measurement of the sidewall depth; the depth of the sidewall is 125±25 µm.

5.3 Silicon micromachining to achieve 45° and 90° etched sidewalls

5.3.1 Introduction

The resultant 45° and 90° sidewalls of the etching process of monocrystalline silicon were obtained using the same pattern orientation with different etchants. Etching experiments on <100> direction in Si(100) were conducted with 10 M KOH and 0.1 M *tert*-butanol to give vertical sidewalls. They were also conducted with 25%wt TMAH with the addition of 0.1% Triton X-100 to give 45° sidewalls for the fabrication of integrated micromirrors for optofluidic applications.

The high surface tension influences the etching of the crystallographic silicon planes with the aim of achieving vertical sidewalls [103]. The smoothness of the surface and etch rate are crucial parameters for the fabricated structures, because the etch rate can influence the wall's smoothness, and smoothness is a key parameter in the fabrication of a mirror. Triton X-100 surfactant was used with TMAH to smooth the 45° etched slanted walls. The low concentrate of tert-butanol did not much affect the lowering of the surface tension with high concentrated KOH for mirrored vertical {100} achieved planes. At the end of the chapter, the structure to enable the optical beam's reflection parallel back and forth from a 45° and -45° tilted vertical mirror cavity is illustrated, described, and used as an integrated device in the polarimetry system.

5.3.2 Silicon wafer properties and orientations

Silicon (Si) is the most common semiconductor material used in microelectromechanical systems (MEMS) [104]. It is an anisotropic crystalline material, and single crystal Si can be manipulated into wafers with diameters of up to 300 mm cut from a single crystal semiconductor ingot. Wafers are a thin, circular slice of single-crystal semiconductor material (their thickness depends on a wafer's diameter but they are typically equal to or less than 1 mm). A fundamental shape can be achieved by dividing the silicon crystal with a characteristic shape, volume, and content.

Miller Indices describe all lattice planes and lattice directions. The cubic lattice system is shown in Figure 5.5.

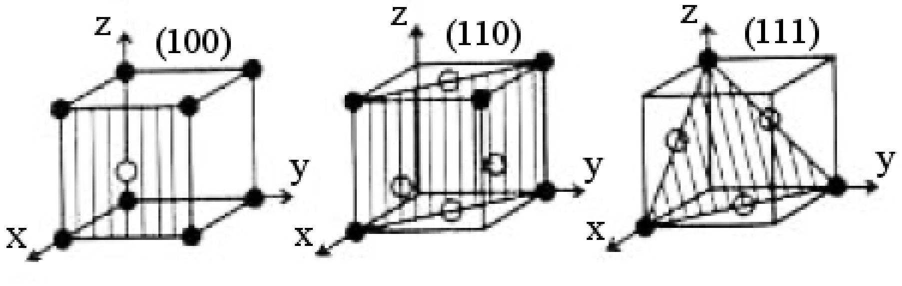

Figure 5.5 Miller indices of silicon crystal planes [105].

The fabrication of a 45° sidewall can be achieved using either Si(100) cut or Si(110) cut. Plane configurations for (100) and (110) wafers are shown in Figure 5.6 [105].

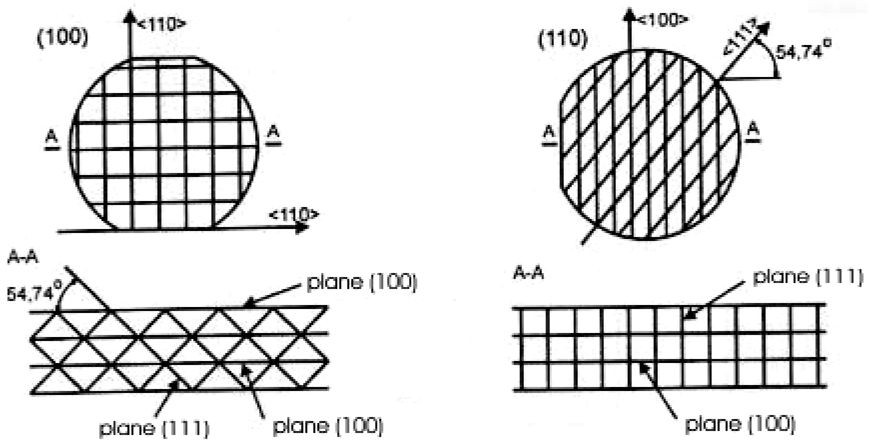

Figure 5.6 Orientations of silicon (100) and (110) wafers [33].

5.3.3 Mask orientations to achieve 45° and 90° using wet etching

In order to achieve 45° slanted sidewalls, a Si(100) wafer should be used and the mask patterns should be aligned in the <100> direction, which is essentially at 45° (or -45°) to the <110> wafer flat, as shown in Figure 5.7 [74]. A basic technique to align the mask edges along the crystal directions was used with the flat wafer as a reference. The crystallographic property of silicon comprises a {110} wall at a <100> direction and this {110} wall is inclined at 45° to the wafer surface (basically the {100} surface).

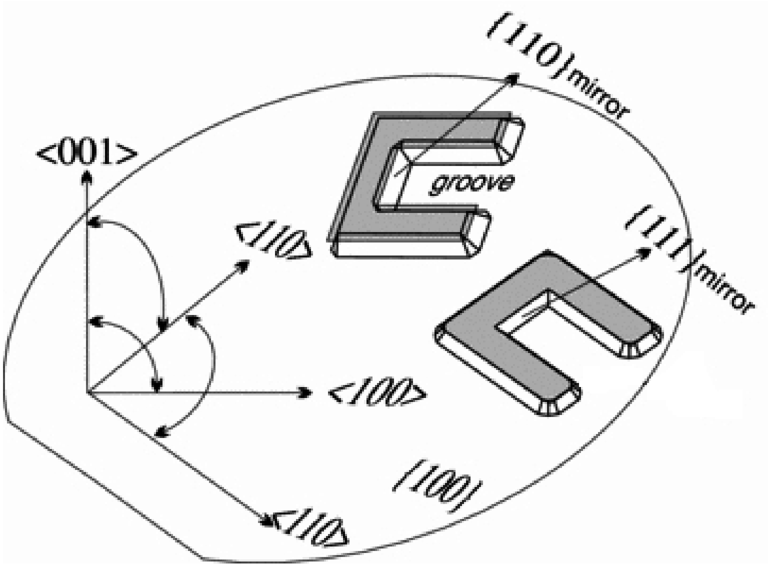

Figure 5.7 Mask orientation to achieve {110} etched sidewall (45° slanted wall), [74].

In this way, the strips of the mask will be aligned to a <100> direction and will yield the {110} plane, which will be inclined at 45° to the wafer surface. When the silicon is wet etched, it will achieve {111} sidewalls owing to its slow etch rate (the etch rate of {100} and {110} is very high). However, this property can be altered and tuned to the etching rate of the planes to make sure that the {110} plane is the slowest etching plane and not {100}. For this, adding Triton to KOH or adopting a TMAH based etchant should use a surfactant. This will reduce the etch rate of {110} planes, and since there are no {111} planes on the <100> direction, the etching process will end up with 45° walls. Alternatively, Si(110) can be used to achieve a 45° sidewall by orienting the trenches parallel to the flat edge of the wafer [106].

In order to achieve vertical sidewalls using Si(100), a high surface tension (>74 mN/m) should be used in the etching process [103]. This allows the etching of a {110} plane until the vertical plane {100} is reached, as depicted in Figure 5.8.

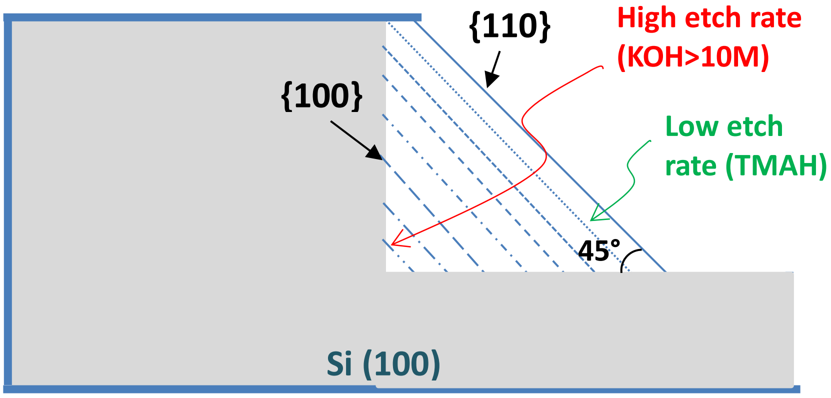

Figure 5.8 Dependences of the solution's surface tension and etch rate on the preferential formatted plane of Si(100) in aqueous TMAH and KOH etchants.

Adding *tert*-butanol alcohol decreases the surface tension [107], and results in smoother sidewalls as it decreases the etch rate of both {100} and {110} planes [108]. Thus, a low percentage of *tert*-butanol (0.1%) was added to achieve smooth sidewalls, and surface tension was kept high to attain 90° sidewalls using a high hydroxide concentration KOH (10 M). Both the 90° and 45° smooth sidewalls were attained from the same silicon cut and pattern orientation (with the mask aligned 45° to <110> direction).

5.3.4 Results and discussion of 45° slanted wall's fabrication

To form a 45° slanted wall using the anisotropic wet etching process, it is essential to ensure anisotropic etching behaviour so that the {110} plane's etch rate remains the lowest for planes between {100} and {110}. The desired strips of the mask should be aligned to the <100> direction and will yield the {110} plane, which will be inclined at 45° to the wafer surface (see Figure 5.9).

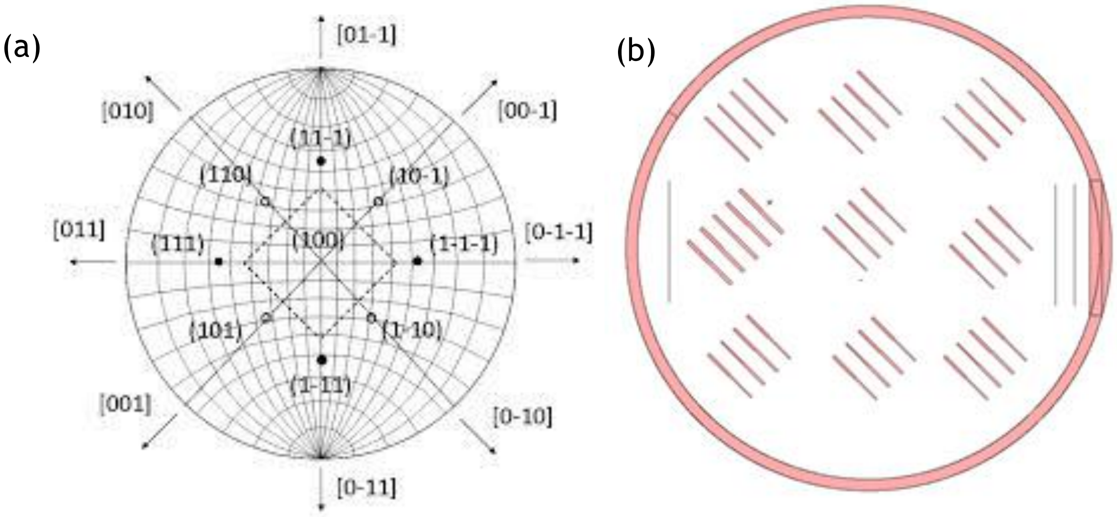

Figure 5.9 (a) Stereographic projection on {100} plane. The arrangement of the etching masks in relation to crystallographic directions is marked with a dashed line [109]. (b) Mask design for a photolithography process; the trenches are 45° slanted, <100> direction with respect to the primary flat edge of the Si(100) wafer (<110> direction).

Different recipes have been prepared and applied to etch different silicon orientation wafers depending on their previously applied recipes [73], [106], [107], [110]. A variety of silicon cuts, hard mask designs, etchant types and concentrations, additive types and quantities, mixture temperatures, and stirring speeds were also implemented. These factors resulted in a variation of the etch rate of the different silicon substrates.

- **KOH and Si(100)**

The KOH etchant composition is potentially appropriate for the fabrication of 45° micromirrors. KOH is cheaper than TMAH, which can be significant in the mass production of MOEMS devices [73]. In addition, it can produce smooth etched sidewalls [111]. Therefore, the initial trials to achieve 45° sidewalls were conducted using Si(100) wafer and KOH etchants with different additives, mixture temperatures, and etching times (see Table 5.1).

Table 5.1 Wet etching recipes on Si(100) with different hard masks, temperatures, etchants and additives.

Mask layers for Si(100)	KOH [M]	T [°C]	Additives	Duration [hours]	Results
SU8 mask	2	75	Triton X-100 (60 μL)	5	Random etching, Figure 5.10
Si_3N_4/SiO_2 mask (commercial)	2	75	Triton X-100 (30 μL)	7	45° sidewalls, Figure 5.11
SiO_2 mask	3	75	*tert* -butanol (0.1 M)	1	45° sidewalls, Figure 5.12
Si_3N_4/SiO2 mask (commercial)	3	75	Triton X-100 (30 μL)	5	45° sidewalls, Figure 5.13
Si3N4/SiO_2 mask (commercial)	10	80	*tert* -butanol (0.1 M)	5	Smooth 90° sidewalls, Figure 5.14 and Figure 5.15
Si_3N_4/SiO_2 mask (commercial)	8	75	IPA (0.1 M)	6	90 and 45° sidewalls, Figure 5.16

The first recipe was repeated several times for the Si(100) substrate (500 μm thickness, single side polished (SSP)). On the first occasion, the etching was random as the SU8 photoresist had been used. This allowed the etchants to go between the substrate and SU8 layer, which resulted in random etching. In addition, the SU8 did contaminate the KOH solution resulting in a non-uniform etching, as shown in Figure 5.10.

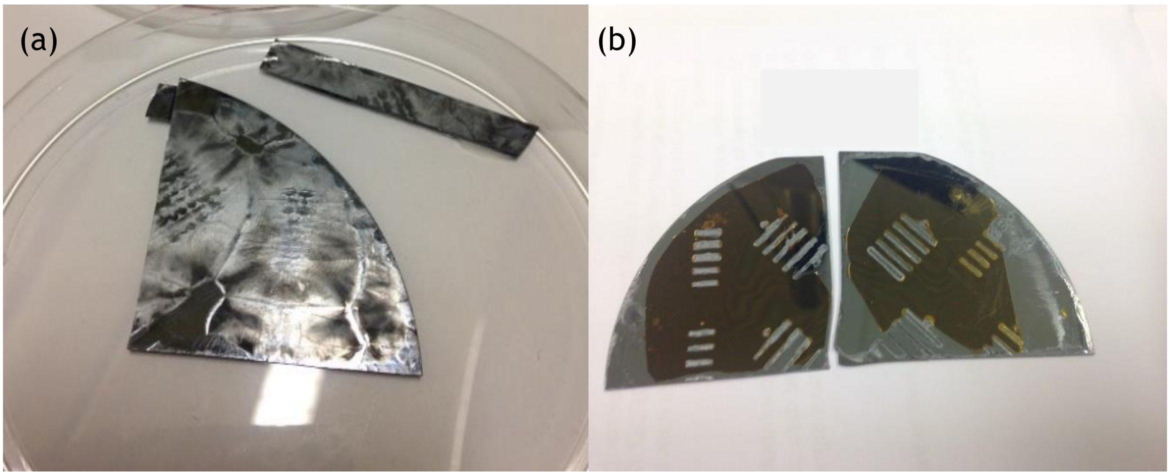

Figure 5.10 Etched Si (100) substrates for different etching processes showing the non-uniform etching due to the SU8 mask that comes out through the etching process.

Then, a 3-inch wafer (380±50 µm thickness, DSP) with Si_3N_4 (40 nm) and SiO_2 (60 nm) layers was used. These layers were used as a mask instead of the SU8 photoresist to prevent the KOH etching of the desired silicon area - hard (etching) mask. Si_3N_4 and SiO2 have a slow etch rate when using the KOH etchant. The etch rate of silicon nitride, if it etches at all, is under 1 nm/hour. While the KOH etching of silicon dioxide is observable, but the etch rates are much slower than that of silicon (1-2 orders of magnitude), so should be considered as a mask for deep etching processes [112].

Therefore, the previous recipe was applied using this silicon substrate with SiO_2 and Si_3N_4 layers for seven hours; 45° slanted walls were achieved, as shown in Figure 5.11.

The SEM images show that the resultant walls were rough but nearly 45° tilted on the {110} plane, as discussed in Sec. 5.3.4. This might be the reason for using an acetate photomask. It is insufficient to provide a sharp edge hard mask when the photoresist on the silicon substrate is exposed to UV light. The light will wavily expose it and consequently produce non-straight lines on the photoresist mask for the dry etching processes. The dry etching then will be wavy as it depends on the mask written on the photoresist (which is not straight). The last windows after etching the SiO_2 and/or the Si_3N_4 layers will be curvy; moreover, the wet etching will etch these curvy windows and will not yield a smooth sidewall.

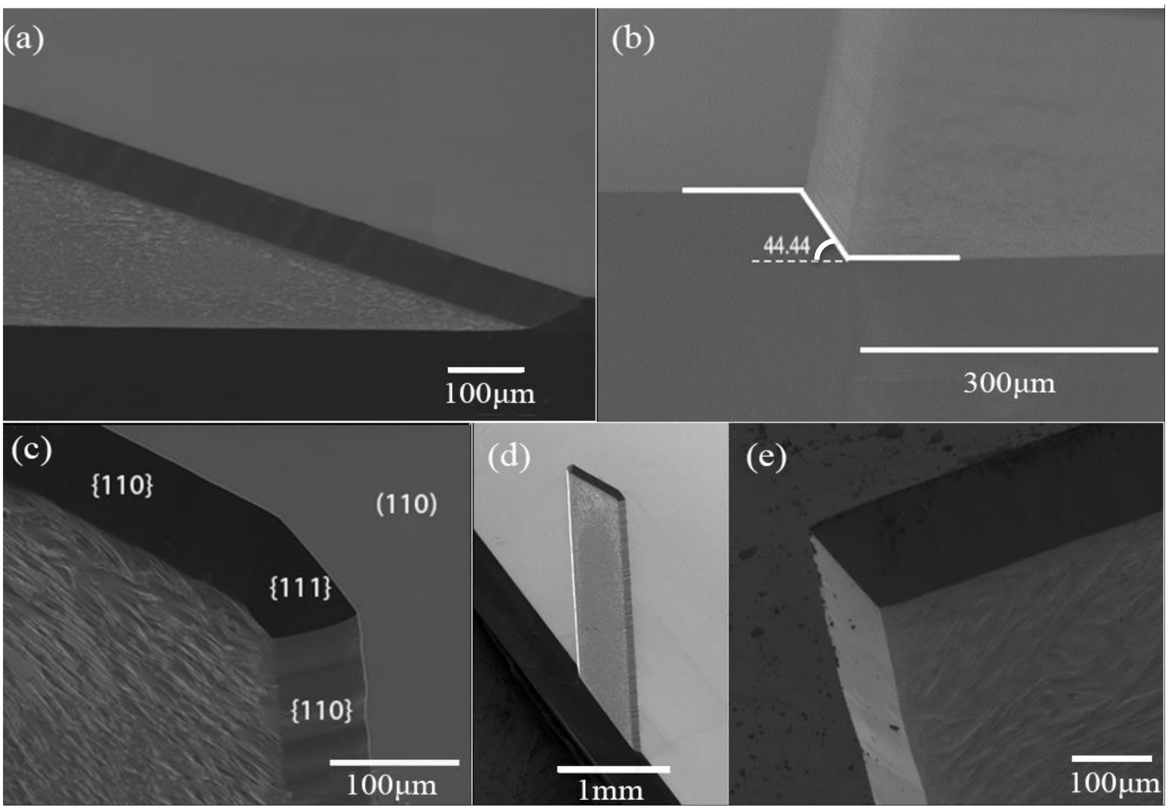

Figure 5.11 SEM images of etched grooves ending by (a-d) 45° sidewalls of 45° tilted trenches mask, and (e) 54.6° sidewalls of straight trenches mask with respect to the wafer flat edge, fabricated with the 2 M KOH and Triton (groove depth 63 μm) of Si(100) substrate which has SiO_2 and Si_3N_4 mask layers.

The micromirror's reflectivity indicates that replacing the Triton surfactant with alcohol in the KOH solution reduces the optical power loss caused by the reflection. The achieved reflectivity is comparable with that obtained by etching in the TMAH solution with a surfactant [73]. In addition, the low etch rate of the {100} plane in the KOH solutions with Triton is a certain drawback of this etching mixture because it slows down the fabrication process [73]. Hence, for two hour the third recipe, 3 M KOH with 0.1 M *tert* -butanol, was applied to Si(100), which has a SiO_2 layer (120 μm). Rough 45°sidewalls were also achieved, as shown in Figure 5.12.

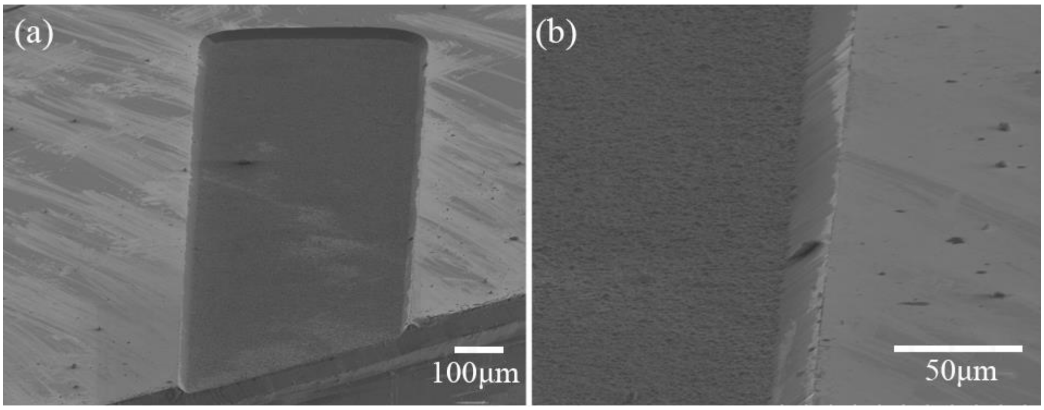

Figure 5.12 SEM images of etched grooves ending with ~45° sidewalls fabricated with 3 M KOH and 0.1 M *tert*-butanol for 2 hours (groove depth 34 μm); Si(100) substrate has a SiO_2 mask layer and the trench is tilted 45° with respect to the wafer flat edge.

The results of using a different additive (*tert*-butanol) were roughly similar to the previous results when using Triton X-100; the etched walls were rough. This might relate to a stirring issue. For this, the previous recipe was repeated for five hours but with Triton X-100 (30 μL) surfactant and a 200 rpm stirring speed for Si(100), which has Si_3N_4 and SiO_2 layers. A 45° sidewall was achieved but also rough, as shown in Figure 5.13.

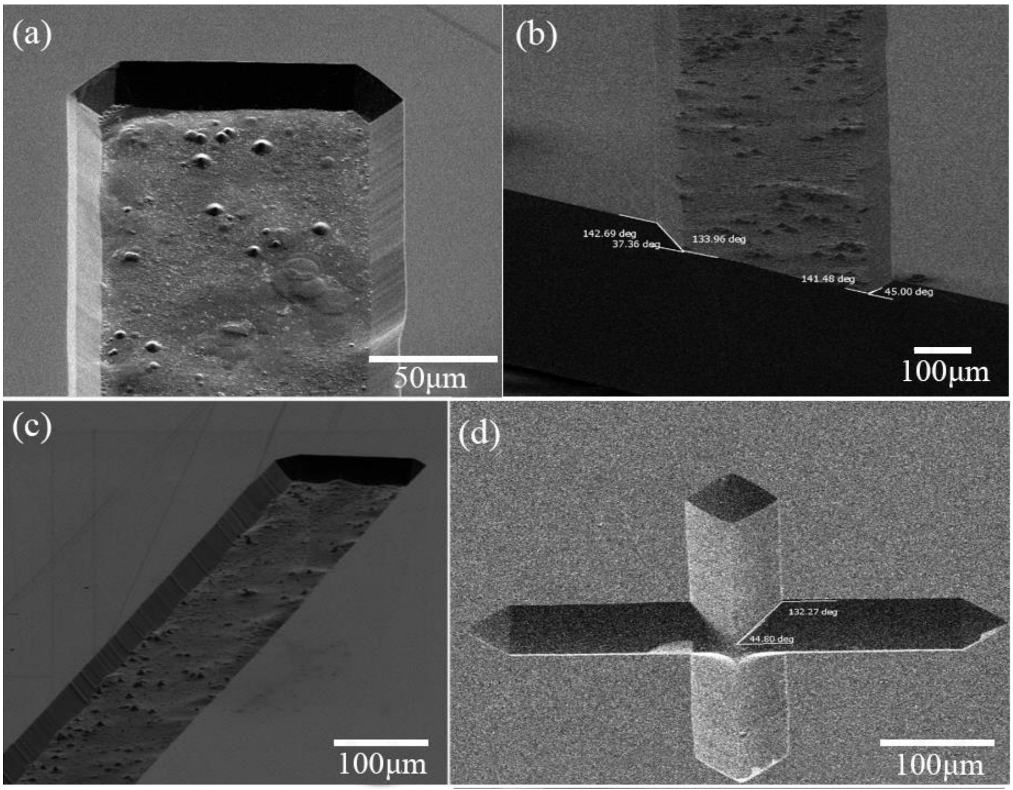

Figure 5.13 SEM images of etched grooves ending with (a-d) 45° sidewalls of 45° tilted trenches mask (groove depth ~46 μm), fabricated with 3 M KOH of Si(100) substrate, which has SiO_2/Si_3N_4 mask layers.

These rough sidewalls might be due to the low etch rate (9 µm/hour) resulting from the use of a low concentration of KOH (2 and 3 M). Consequently, a higher KOH concentration (10 M) with *tert*-butanol (a fifth recipe), adopted from a previous work's recipe [109], was used for 5 hours to etch the Si(100) substrate, which has oxide and nitride layers. The results showed very shiny and smooth sidewalls; however, it had a 90° ending, shown in Figure 5.14.

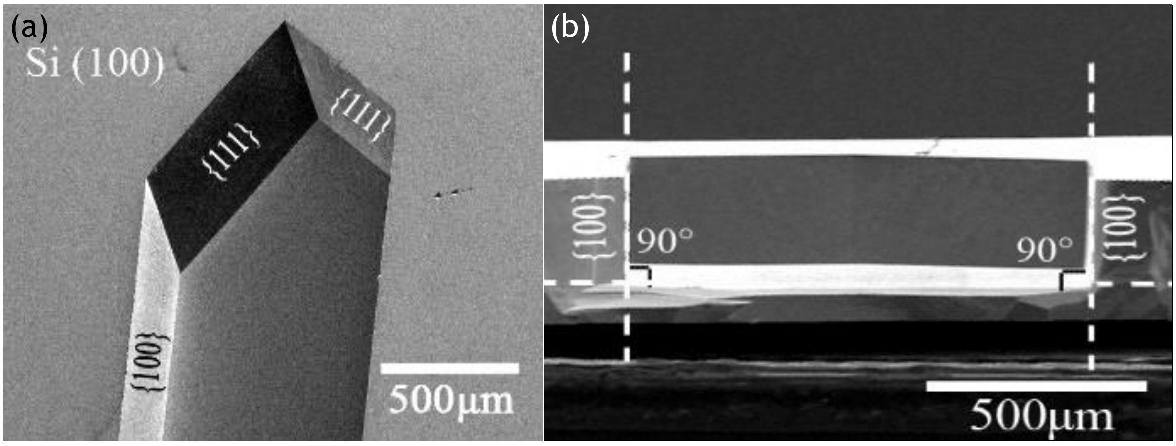

Figure 5.14 (a) Top view, (b) Sideview, of SEM images of etched grooves ending with vertical sidewalls of 45° tilted mask trenches with respect to the flat edge. The groove depth is ~250 µm, fabricated in 10 M KOH and 0.1 M *tert*-butanol on Si(100) substrate, which has SiO_2/Si_3N_4 mask layers.

The angle between the etched sidewall and the wafer surface depends on the wafer and pattern orientations. However, the formation of the preferential different sidewall planes relies on the surface tension (which mainly varies with the concentration and temperature of the etchant mixture) in the case of a high alkaline concentration (e.g. KOH,>5 M) [103]. A vertical sidewall would be attained by using Si(100), and high surface tension (>74 mN/m) should be achieved through the etching process [103]. This will allow the etching of {110} plane until the vertical plane {100} is reached, as depicted in Figure 5.8.

Adding *tert*-butanol alcohol decreases the surface tension [107], but results in smoother sidewalls as it decreases the etch rate of both the {100} and {110} planes [108]. The recipe comprising 10 M KOH and 0.1 M *tert*-butanol has been repeated for 5 hours. The results showed that the 90° sidewall that was achieved was reproducible, as shown in Figure 5.15.

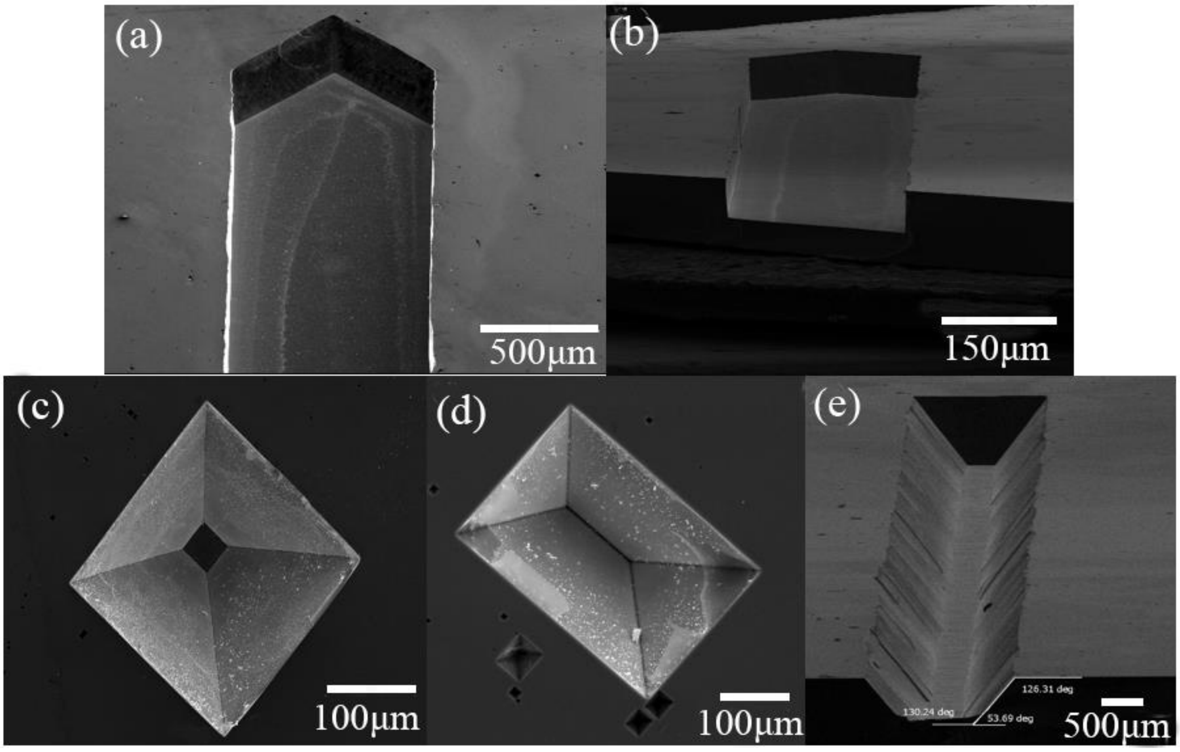

Figure 5.15 SEM images of etched grooves ending with (a-e) 45° sidewalls of 45° tilted trenches mask (groove depth ~257 µm) and (f) 53.69° sidewalls of straight trenches mask with respect to the wafer flat edge, fabricated with the 10 M KOH and *tert*-butanol of Si(100) substrate, which has SiO_2/Si_3N_4 mask layers (2nd time).

The etch rate order of the KOH standard solution in H_2O for different crystal planes is {110} > {100} > {111} [87]. However, for the etch rate of different crystal planes in KOH, the *tert*-butanol mixture is {100}>{110}>{111} [108]. Hence, with the addition of tert-butanol to high concentrated KOH (10 M), the {110} planes tend to be etched and reach {100} plane (90° sidewall), for a long each time (up to five hours).

A lower concentration of KOH (0.8 M) with 0.1 M of the *tert*-butanol recipe was used to etch the same Si(100) substrate for 6 hours, which has SiO_2 and Si_3N_4 layers. The results (illustrated in Figure 5.16) show that the etching process tends to produce a 90° sidewall; however, the plane that was not etched to reach 90° is 45° as the concentration is less.

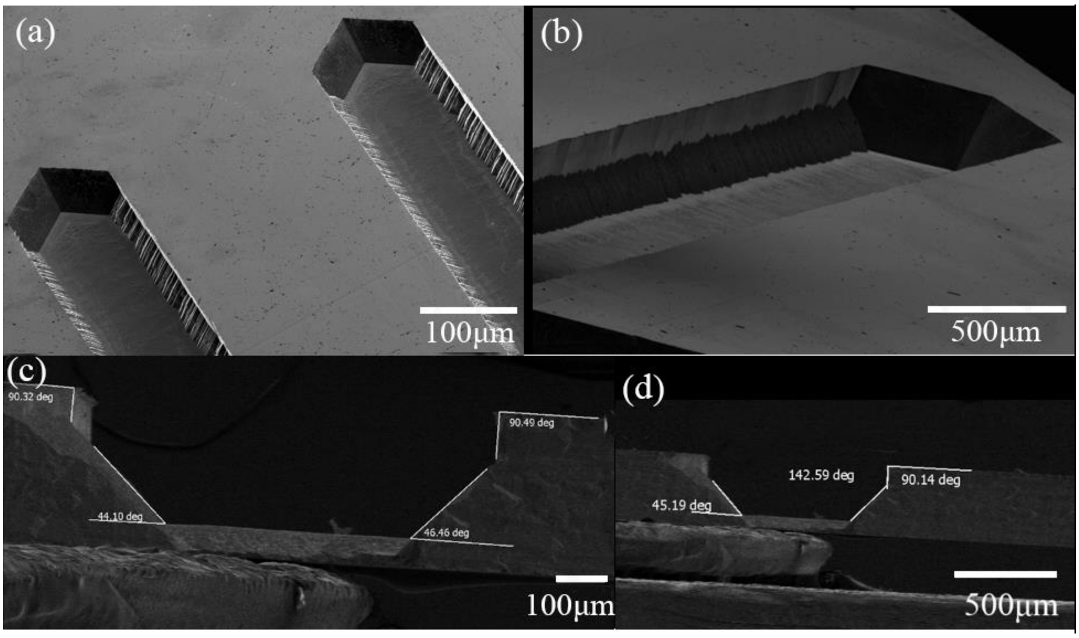

Figure 5.16 SEM images of etched grooves ending with ~45° and 90° sidewalls, fabricating 45° tilted trenches mask with respect to the wafer flat edge, using 8 M KOH and 0.1 M *tert*-butanol on Si(100) substrate, which has SiO_2/Si_3N_4 mask layers.

For lower KOH concentrations (low surface tension), i.e. when using 8 M with the same concentration of *tert*-butanol, there is a remaining artefact of {110} planes along with {111} planes.

From this, it can be concluded that the KOH is not suitable to attain smooth, 45° etched walls with different additives, temperatures, and stirring speeds. Even when the etchant's concentration is varied, it leads to different angle sidewalls because of the surface tension, which effects the resultant sidewalls of the etching process. The smoothness has a relationship to the etch rate; a slow etch rate is preferable to achieve smooth walls. Therefore, a TMAH etchant was used instead of KOH as it has a slower etch rate, as described in the following section.

- **KOH and Si(110)**

In the case of the Si(110) substrates, the sidewalls inclined towards the substrate at 45° can be formed by {100} planes. These {100} sidewall planes are attainable in pure, highly concentrated KOH water solutions in which the edges of the etching mask are set perpendicularly to the <110> direction. Therefore, the mask was aligned, in this case using Si(110), and achieved 45° etched sidewalls, parallel to the flat wafer edge, i.e. perpendicular to <110> direction (see Figure 5.17) [109].

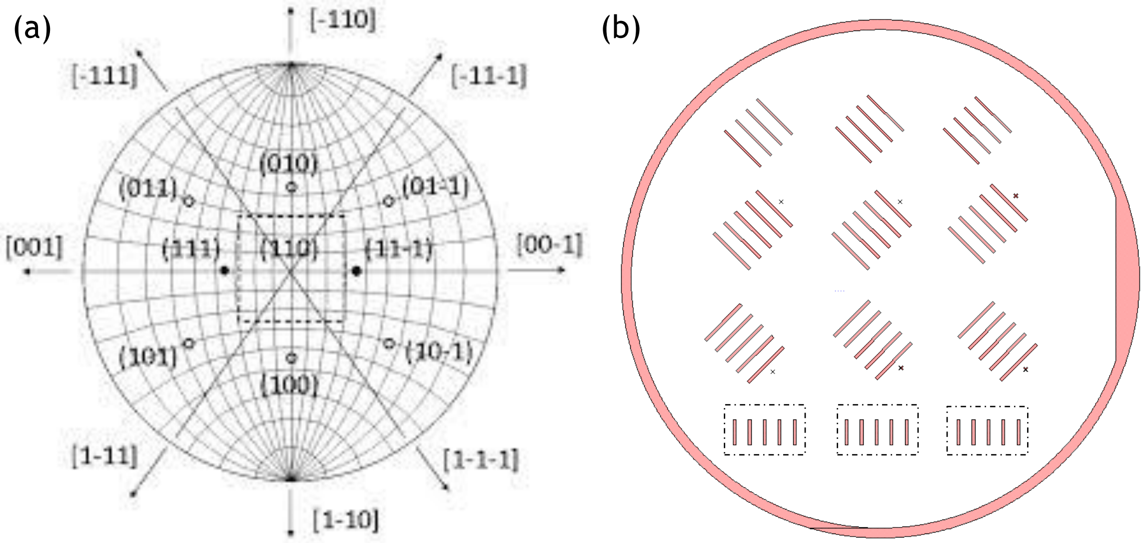

Figure 5.17 (a) Stereographic projection on Si(110) plane. The arrangement of the etching masks in relation to the crystallographic directions is marked with a dashed line [109]. (b) Mask design for a photolithography process. The trenches that are 90° slanted, <100> direction with respect to the primary flat edge of the Si(110) wafer are marked with the dashed line at the bottom; these are the targeted straight stripes with respect to the primary flat edge of the wafer.

The {100} plane is the slowest etched plane for <110> direction in the aforementioned solution and forms a sidewall of the etched structure, as per the result of setting the mask [106], [107], [109]. Several recipes were used for this (see Table 5.2).

Table 5.2 Wet etching of KOH recipes on Si(110) substrate with different temperatures and additives.

Mask layers for Si(110)	**KOH [M]**	**T** [°C]	**Additives**	**Duration** [hours]	**Results**
SU8	10	80	---	1	Random
Si$_3$N$_4$(100 nm)	10	80	---	1	Random
Si$_3$N$_4$(500 nm)	10	75	*tert*-butanol (0.1 M)	2	90 and 45° sidewalls, Figure 5.18
Si$_3$N$_4$(500 nm)	3	90	IPA (60 g)	2:15	Etched the whole sample

The first experiment was conducted in 10 M KOH solution without surfactant or alcohol at a temperature of 80°C with 250 rpm stirring for one hour using SU8 as a mask during the etching process. The result was random because the SU8 layer is etched resulting in an undercut, as indicated in section 5.3.5.

A Si_3N_4 layer of 100 nm thickness has been deposited on both sides of the Si(110) substrate using an inductively coupled plasma (ICP) deposition tool in order to use it as an etch mask. However, this layer came out through one minute of HF(10:1) etching (when it is required to remove the native oxide). Despite the reduction of HF etching time to 10 seconds, the Si_3N_4 layer came off another time through KOH etching. This is because of the hydrogen contamination of the Si_3N_4 layer during the deposition process in the JWNC.

Another deposition has been applied, but for 500 nm thickness, when the layer survived in 30 seconds of HF etching and two hours of the 10 M KOH with 0.1 M *tert*-butanol alcohol etching mixture. However, the results showed that there is an undercut etching and some of the layers on the edge have been taken off through the KOH etching. In addition, the attained sidewalls are rough and tilted ~90° and 40°, as shown in Figure 5.18.

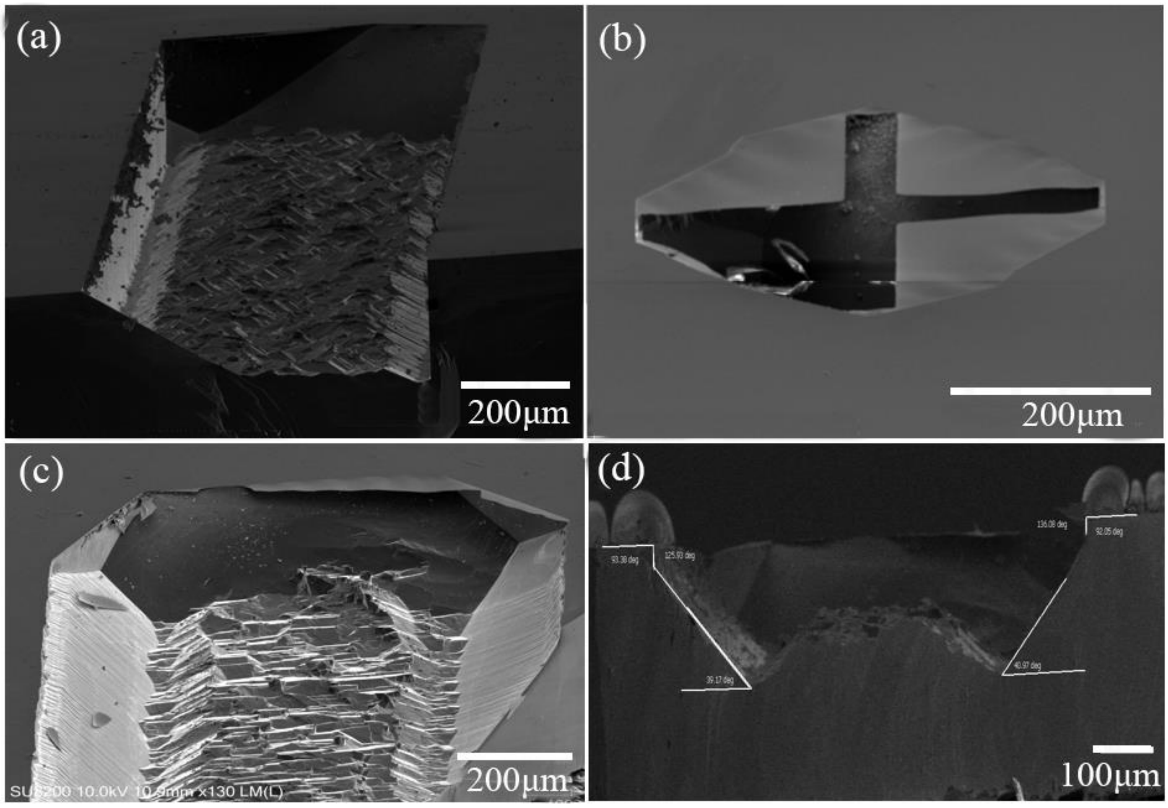

Figure 5.18 SEM images of etched grooves of (a and b)~ 90° sidewalls of straight trenches mask and (c and d) 45° sidewalls of 45° tilted trenches mask with respect to the wafer flat edge, fabricated with the 10 M KOH and 0.1 M *tert*-butanol on Si(110) substrate, which has a 500 nm Si_3N_4 mask layer.

From the shapes of the etched structures, it was evident that the trenches, which are perpendicular to <110> (45° tilted trenches widows with respect to the wafer flat edge), were 45°slanted walls - {110} plane as predicted [109], but not smooth due to the poor quality of the Si_3N_4 layer.

With the aim of achieving a 45°etched wall using Si(110), the substrate was conducted by carrying out some recipes from previous studies by Rola and Zubel, [109], [107] respectively. It was etched with a lower KOH concentration (3 M) with IPA (60 g) additive but at higher temperatures (90°C). During the etching process, the silicon wafer and its holder were etched aggressively due to the high temperature. Therefore, these recipes were not used again due to the aggressive etching for the whole substrate whilst less time was not preferable as a deep sidewall is required to suit the laser spot size.

In conclusion, Si(110) was not suitable to achieve the mirrored 45° in the experiment. This was due to the surface tension and high etch rate of the KOH etchant. A further review of the reported work found that TMAH was able to accomplish a mirrored 45° slanted side wall rather than use other etchants [109], as shown in the following section.

- **Achieving a 45° slanted wall using a TMAH etchant:**

The results of the investigations concerning anisotropic etchings that aimed to achieve a 45° sidewall were modified by another etchant, namely TMAH. The etching anisotropy was assessed on the basis of smoothness and the direction of the resultant walls using SEM. The morphologies of the etched surfaces are highly improved. IPA and Triton X-100 were used as additives in order to enhance the roughness (see Table 5.3).

Table 5.3 Wet etching of TMAH etchant's recipes on different silicon cut substrates with different additives at 80°C for two hours.

Silicon type & mask layers	Additives	Results
Si(100) with Si_3N_4/SiO_2 mask (commercial)	350 ml IPA	90° and 45° non-uniform walls, Figure 5.19
Si(110) with Si_3N_4(500 nm) mask	Triton X-100 (0.1%)	45° rough walls, Figure 5.20
Si(100) with Si_3N_4/SiO_2 mask (commercial)	Triton X-100 (0.1%)	45° rough walls, Figure 5.21

Several additives to TMAH solutions have been employed to improve the etching results from the previous research [98]. The first was isopropyl alcohol (IPA). It requires a significantly long etching time to achieve the same etching depth as pure TMAH. However, the morphologies of the etched surfaces are highly improved. The first attempt of the TMAH etching was on -45° tilted trenches to the flat edge of Si(100), which has Si_3N_4 over SiO_2(60/40 nm). The results were not expected as the walls were not 45° and not uniform, as depicted in Figure 5.19.

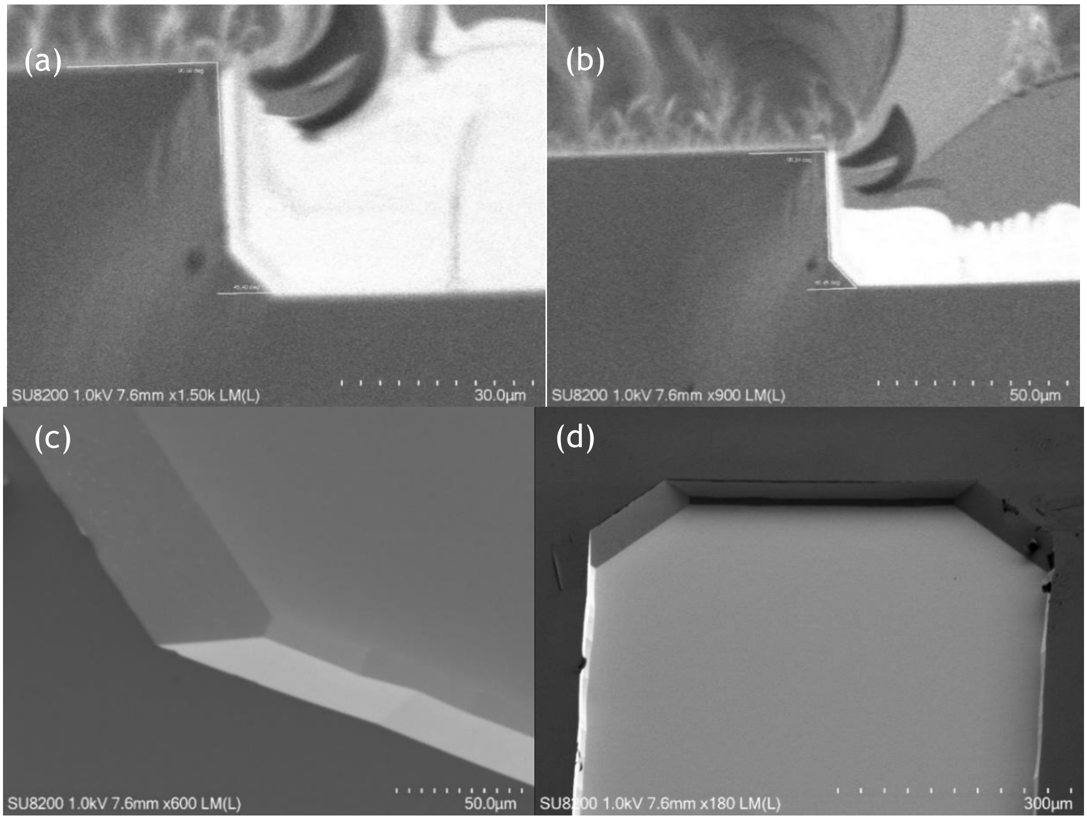

Figure 5.19 (a) and (b) are top view, (c) and (d) are to view of SEM images of etched grooves ending with ~45° and ~90° sidewalls fabricated on 45° tilted trenches mask with respect to the wafer's flat edge and using 25% TMAH and IPA on Si(100) substrate, which has SiO_2/Si_3N_4 mask layers.

The problem might arise from the acetate mask, which is not accurate under UV exposure and results in a wavy shaped hard mask after developing the Si_3N_4 and SiO_2 layers, and consequently rough sidewalls.

The beneficial effect of IPA led to the search for other additives, which would improve the etching results. Over the last few years, many studies have been dedicated to the examination of Triton X-100 as an addition to the TMAH solution. Triton (iso-octylphenoxy polyetoxyethanol) is a non-ionic surfactant and reduces the etching of V(100) by about 15% at the optimal composition of the etching solution of 25% TMAH and 50 ppm Triton. The roughness of (110) surface was reduced to a value of Ra = 5.2 nm, while Ra = 180 nm, when etched in TMAH+IPA solution [98]. When the silicon is wet etched, it would achieve {111} sidewalls owing to its slow etch rate (the etch rate of {100} and {110} is very high). However, this property can be altered and tuned to the etching rate of the planes to make sure that the {110} plane is the slowest and not {100}. For this, a surfactant was used, through adding Triton to a KOH or TMAH based etchant. This will reduce the etch rate of {110} planes, and since there are no {111} planes in the <100> direction, the etching process will achieve 45° walls.

Therefore, a mixture of 25% TMAH with 0.1% Triton was used on Si(110). The etched walls are approximately 45° but rough due to some scratches that occurred in the processing of the sample before the wet etching, as shown in Figure 5.20.

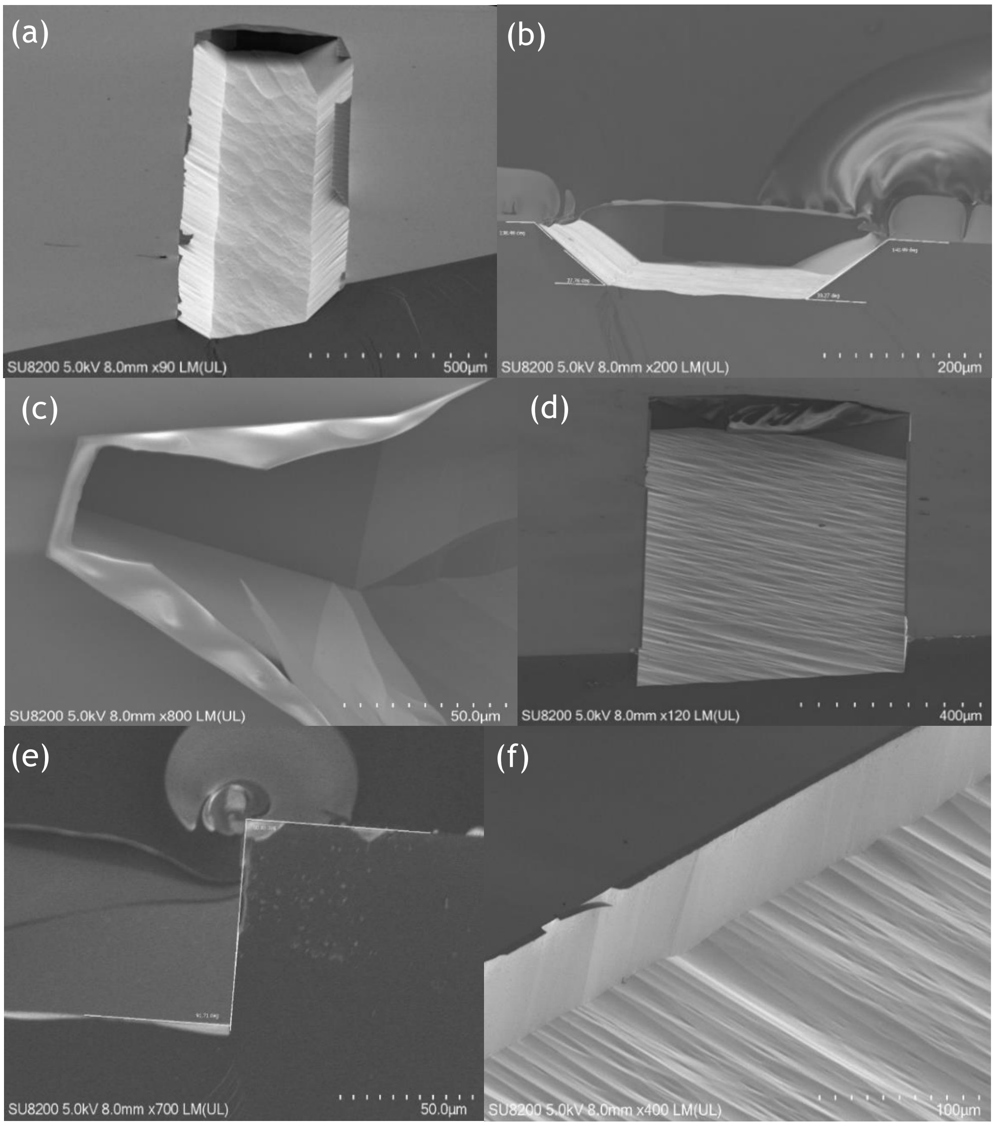

Figure 5.20 SEM images of etched grooves of (a-c) 45° sidewalls of 45° tilted trenches mask with respect to the wafer flat edge and (d and f) ~ 90° sidewalls of straight trenches mask, fabricated using 25% TMAH and 0.1%Triton X-100 on Si(100) substrate, which has 500 nm Si_3N_4 mask layer.

In addition, the Si_3N_4 layer has deteriorated etching due to the poor quality of the layer fabricated. The same recipe was then applied to the -45° trenches of Si(100).

The images in Figure 5.21 show promising results for some un-patterned parts using the same mixture and etching condition, as shown in Figure 5.21 (c).

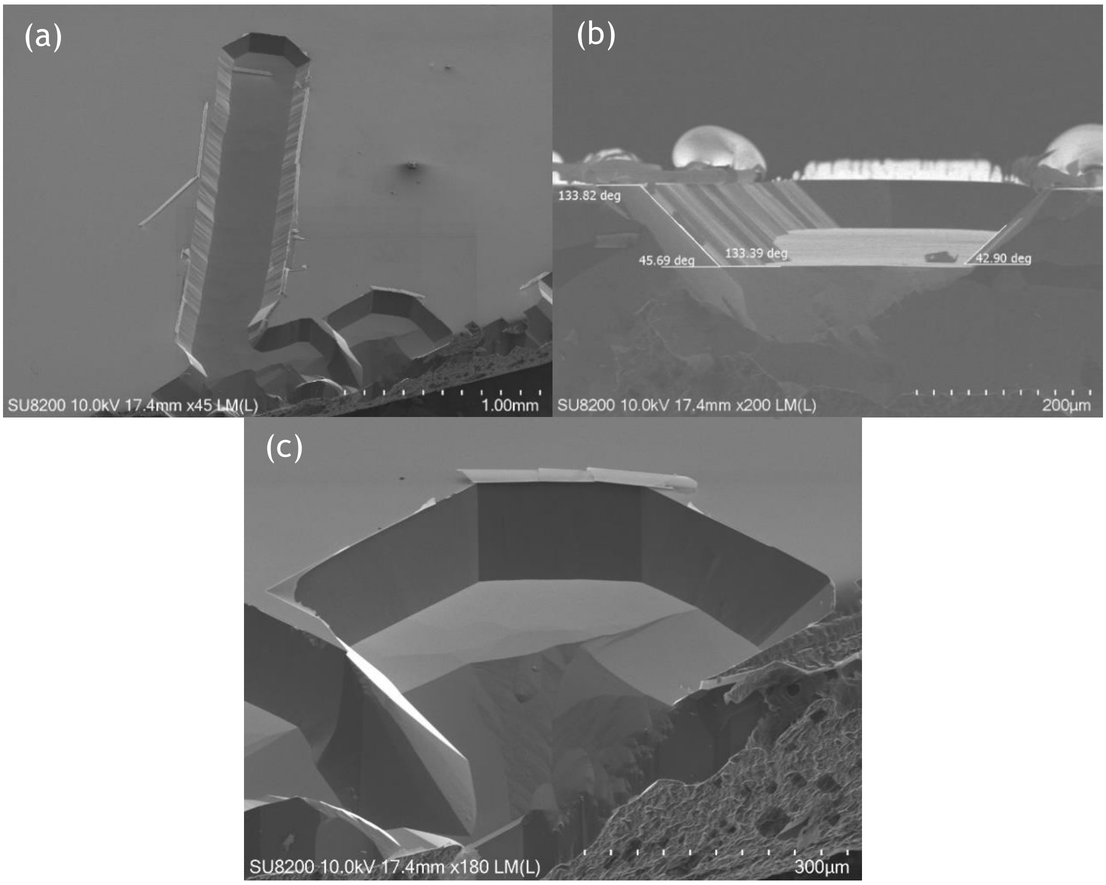

Figure 5.21 SEM images of etched grooves ending with ~45° sidewalls fabricated from (a) -45° and (b) +45° tilted trenches mask with respect to the wafer flat edge using 25% TMAH and Triton X-100 on Si(100) substrate, which has SiO2/Si_3N_4 mask layers.

It can be concluded that the etching mixture is efficient in producing a smooth 45° etched wall. The reasons for roughness are the photomask, hard mask, and prior mixtures, i.e. the KOH etchant recipes that have been used.

- **Enhancements in Protocol and Photomask**

- Chromium mask and different protocols before wet etching:

As indicated in the previous section, the problem with all rough and non-uniform etched trenches is mainly the use of acetate photomasks and poor-quality hard masks (Si_3N_4 layer). The accidently broken etched feature (Figure 5.21 (c)) showed smooth sidewalls. To overcome this, a chromium photomask was designed and fabricated at JWNC using different trenches, directions, sizes, and spacing sizes with a 3-inch wafer size, as shown in Figure 5.22.

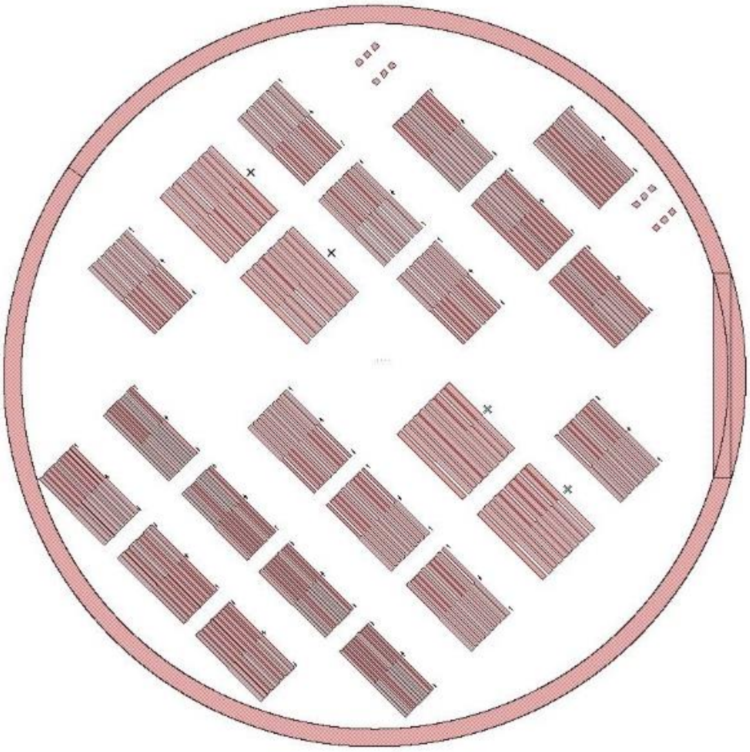

Figure 5.22 Mask design for the photolithography process; the trenches are 45° slanted, <100> direction with respect to the primary flat edge

In addition, a different photoresist (S1818) replaced the SU8 photoresist to avoid using Piranha resist stripper. S1818 can be taken simply by soaking the sample in a warm acetone bath (50°C) for two hours, then rinsing it with IPA and drying it with Nitrogen. They were then transferred to an oxygen plasma asher (Gala Plasma Prep 5) and ashed for three minutes at 150 W. The process flow for preparing the sample for wet etching is illustrated in Figure 5.23.

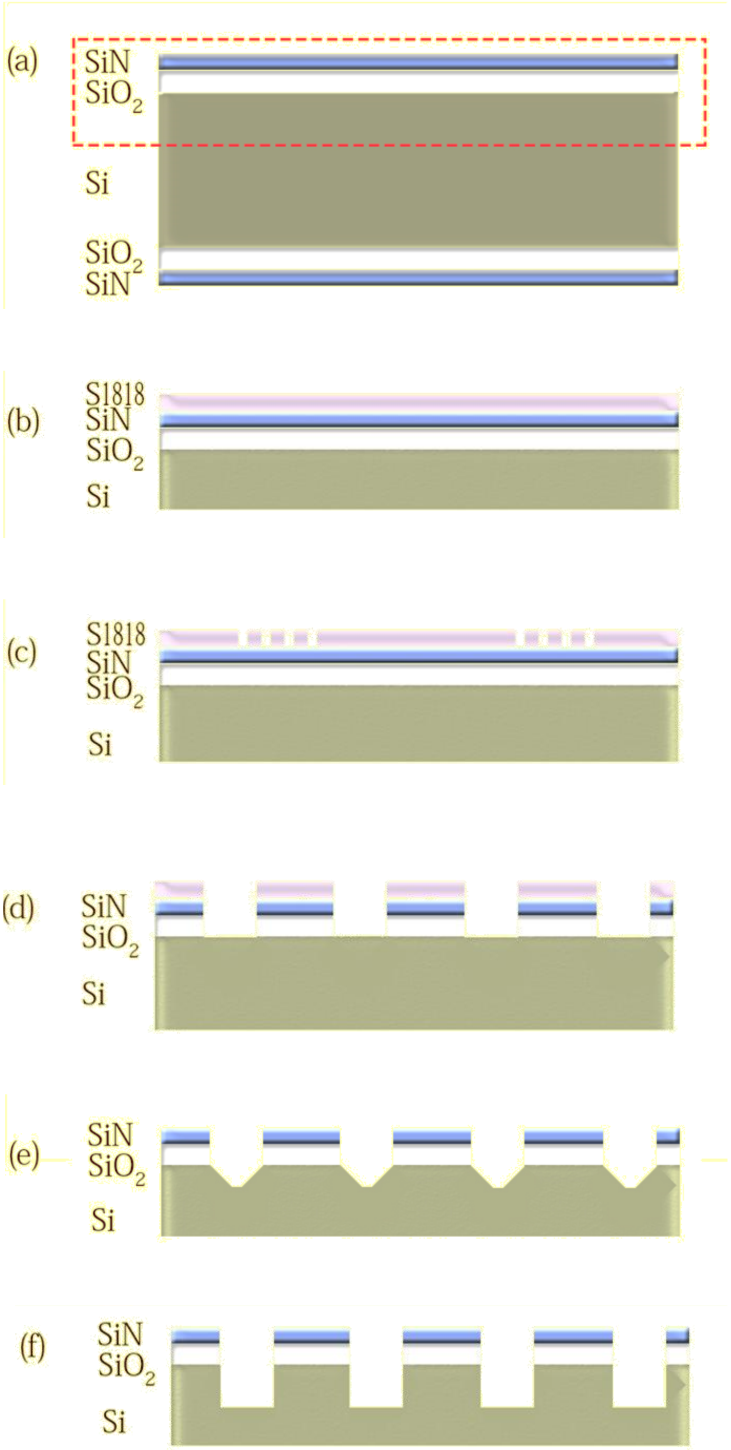

Figure 5.23 Photolithography processes on (a) 3-inch Si(100) wafer which has Si_3N_4 and SiO_2 layers of 40 and 60 nm respectively on the front and back sides as a mask to protect the back side and undesired areas from wet etching. The wafer was cleaved for the desired pattern size and then cleaned, (b) A positive photoresist (S1818) layer on the Si wafer after spinning and baking, (c) The designed mask in Figure 5.22 is aligned carefully with the flat edge of the wafer and exposed to UV light using a mask aligner, then it is developed using MF(MICROPOSIT® MF® -319 Metal-Ion-Free DEVELOPER) developer after a post-exposure bake. The windows of the desired pattern have now developed as it was exposed to UV light, (d) Si_3N_4 and SiO_2 have been etched using the dry etch process of an appropriate recipe using BP80 to open the windows of the design to the wet etching of the silicon, (e) and (f) Etched trenches after a wet etching process producing vertical and 45° using KOH and TMAH respectively.

- **Applying the new protocol on Si(100) using the 25% TMAH and Triton recipe**

The previous etching recipe, 25% TMAH and 0.1% Triton X-100, was used on the same cut silicon orientation wafer, Si(100), by using the new stated protocol above and a new (chromium) mask (see Table 5.4).

Table 5.4 Wet etching of TMAH and Triton X-100 recipes on Si(100) substrate at a different temperature.

Mask layers for Si(100)	T [°C]	Duration [hours]	Results
Si_3N_4/SiO_2 mask (commercial)	75	4	45° less rough walls, Figure 5.24
Si_3N_4/SiO_2 mask (Commercial)	80	2	45° rough walls (without stirring), Figure 5.25
Si_3N_4 mask (JWNC 6-inch wafer)	80	3:30	45° smooth walls, Figure 5.26

The first recipe was applied for four hours at 75°C. The SEM images show a more enhanced sidewall angle direction and smoothness (Figure 5.24). However, the walls were not very smooth but were 45° slanted.

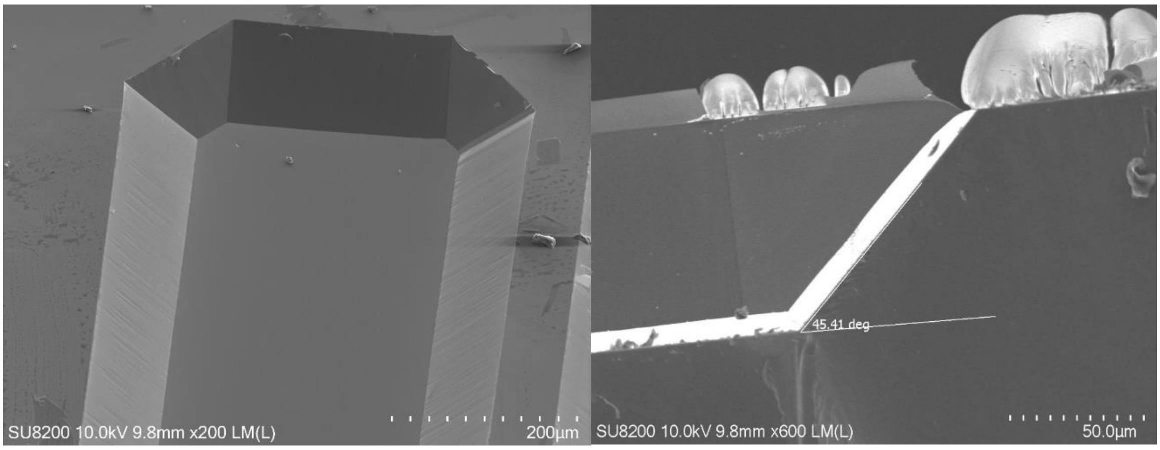

Figure 5.24 SEM images of etched grooves ended with ~45° sidewalls fabricated from 45° tilted trenches mask with respect to the wafer flat edge using a new photoresist, chromium photomask, 25% TMAH and Triton X-100 on Si(100) substrate, which has SiO_2/Si_3N_4 mask layers.

The roughness now is not a result of the hard mask and/or silicon and layer issues. The temperature has mainly an effect on each rate, but it also influences the surface morphology [113]. Therefore, the same pattern of the same silicon wafer was etched using the previous mixture but at 80°C. Rough, 45° slanted walls were obtained – see Figure 5.25.

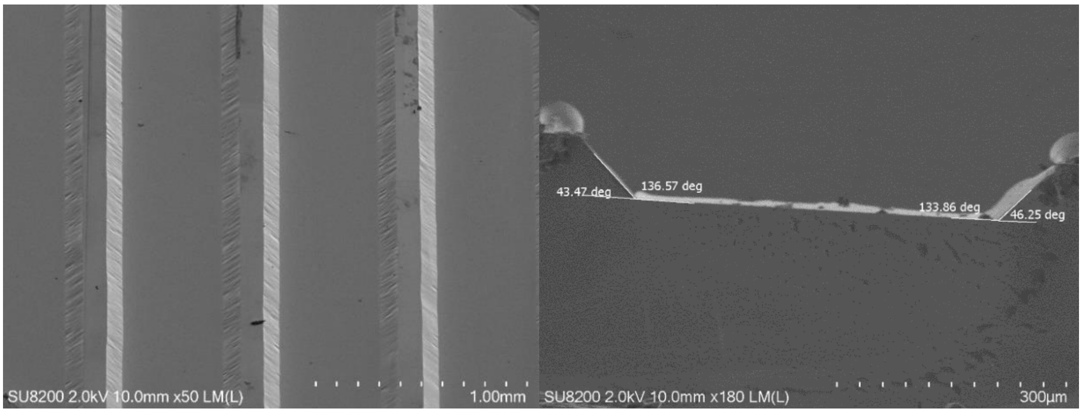

Figure 5.25 SEM images of etched grooves ending with ~45° sidewalls fabricated from 45° tilted trenches mask with respect to the wafer flat edge using a new photoresist, chromium photomask: 25% TMAH and Triton X-100 on Si(100) substrate which has SiO_2/Si_3N_4 mask layer.

The reason for roughness is that the process happened without stirring and the sample was, by accident, not held vertically. Hence, the walls are extremely rough, as it faced the bubbles of the mixture, and the detachment of the hydrogen bubbles did not happen during the etching process. The procedure is carefully repeated by monitoring every step under the microscope to realise if there is an error throughout the preparation of the wafer before the wet etching process. A 6-inch Si(100) wafer was used with a 500 nm thick Si_3N_4 layer deposited using a low-pressure chemical vapour deposition (LPCVD) tool at JWNC. Smooth and 45° slanted walls are achieved using the same recipe of 25% TMAH with 0.1% Tritons at 80°C in temperature (see Figure 5.26). The groove depth is ~92 μm with an etching rate of 0.43 μm/min.

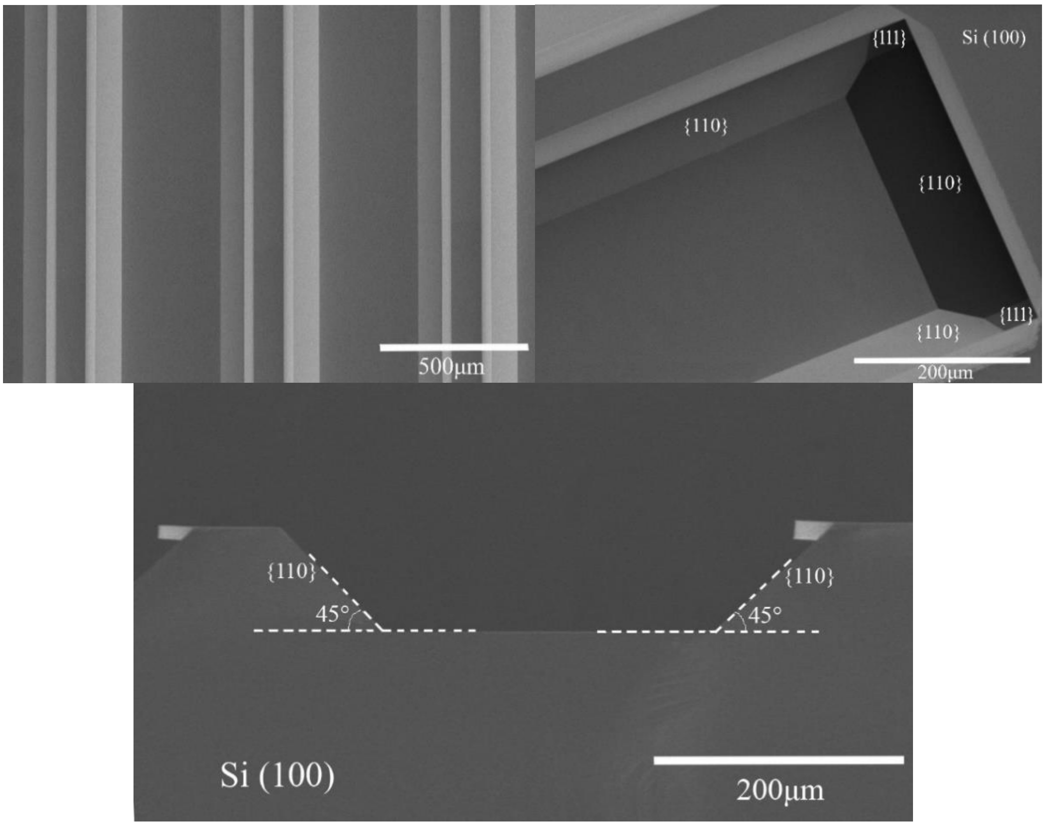

Figure 5.26 SEM images of etched grooves ending with 45° sidewalls of 45° tilted trenches mask fabricated with the 25% TMAH and 0.1% Triton (groove depth ~92 μm) of Si(100) substrate, which has SiO_2 and Si_3N_4 mask layers.

In the case of both TMAH with Triton solutions, the sidewalls formed by {110} planes as well as the surfaces of the (100) substrates are very smooth. However, the (111) plane is widely developed, due to the high value of the V(110)/V(100) etch rate ratio and the low etch rate of (100) plane. This would lead to the decline of the {110} planes in favour of the {111} planes if the structure is etched several times deeper [109].

5.3.5 Micromirror alignment

The fabricated micromirrors were coated with a 50 nm aluminium thick layer using electron beam evaporation in a Plassys MEB 4005 at JWNC. This is to increase the reflectivity of the micromirrors and gain more reflection in the polarimetry setup as micromirrors in the multi-reflection scheme. The layer was flat, as shown in Figure 5.27 (b). However, the alignment was complicated due to the large spot size.

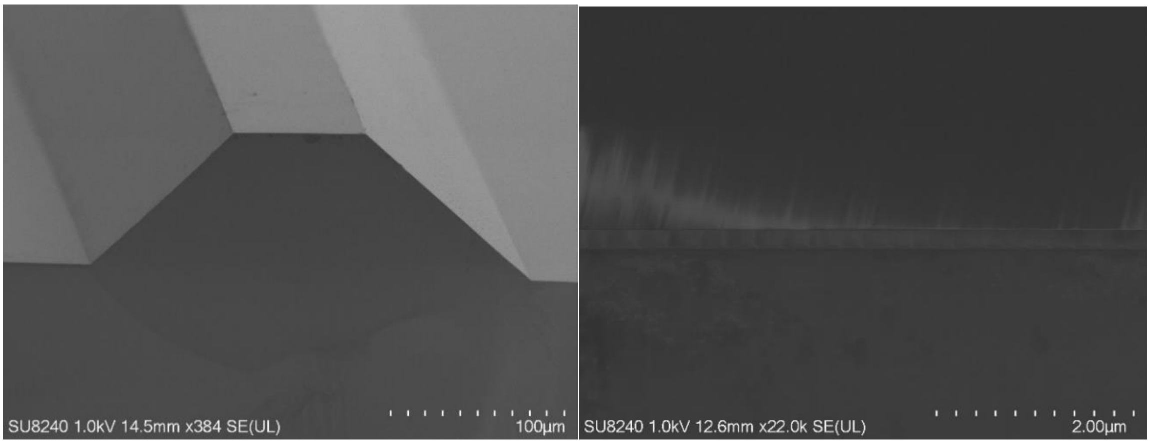

Figure 5.27 SEM images of the aluminium layer on 45° slanted fabricated micromirrors.

Different ways have been used to align the micromirrors with the polarimetry setup; the alignment occurred under the microscope (shown in Figure 5.28). A beam expander (at the opposite side) was used, but it could not shrink the beam size of 1 mm. The beam size became even broader because of the divergence. Lenses were used but the divergence also had an adverse effect. An attempt was made to use the pinhole, but the diffraction was an obstacle for the micromirror size.

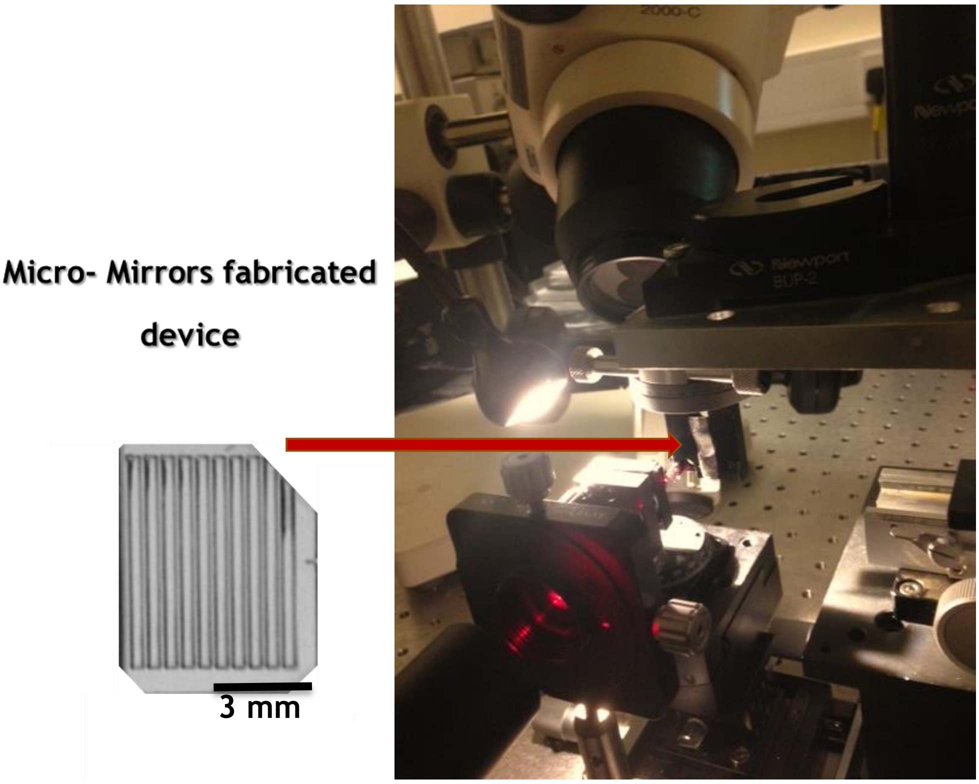

Figure 5.28 Alignment of micromirrors under the microscope.

The big spot size remained the obstacle of the alignment with micro size mirrors. Therefore, the fabrication of deeper micromirrors was attempted in order to develop wider micromirrors and an easier alignment, as shown in the following section.

1.1.1 Achieving deeper smooth 45° sidewalls

After getting smooth, 45° slanted micromirrors with 92 µm depth, wider (deeper etched) micromirrors are desired to suit the laser beam size and ease the alignment process in the multi-reflection scheme (see Table 5.5).

Table 5.5 Wet etching of TMAH and Triton X-100 recipes on Si(100) substrate at 80°C for a longer wet etching time to achieve deeper etched sidewalls.

Mask layers for Si(100)	Duration [hours]	Results
Si_3N_4 mask (500 nm) (JWNC 6-inch wafer)	3:50	45° smooth walls but cracked Si_3N_4, Figure 5.29
Si_3N_4 mask (100 nm) (JWNC 6-inch wafer)	5	45° walls but scribed Si_3N_4, Figure 5.30
Si_3N_4 mask (100 nm) (JWNC 6-inch wafer)	9	45° walls (ruined or some good) but scribed Si_3N_4, Figure 5.31
Si_3N_4/SiO_2 mask (Commercial)	9	45° ruined or not smooth walls Figure 5.32
Si_3N_4/SiO_2 mask (Commercial)	5	45° smooth walls, Figure 5.33
Si_3N_4 mask (500 nm) (JWNC 6-inch wafer)	3:50	45° smooth walls but cracked Si_3N_4, Figure 5.29

The same procedure and recipe were repeated on the same silicon wafer for a longer wet etching time. However, the Si_3N_4 layer cracked through the wet etching process (Figure 5.29), especially if the wafer cleaves several times before the process, to obtain a desirable silicon substrate size for the targeted pattern.

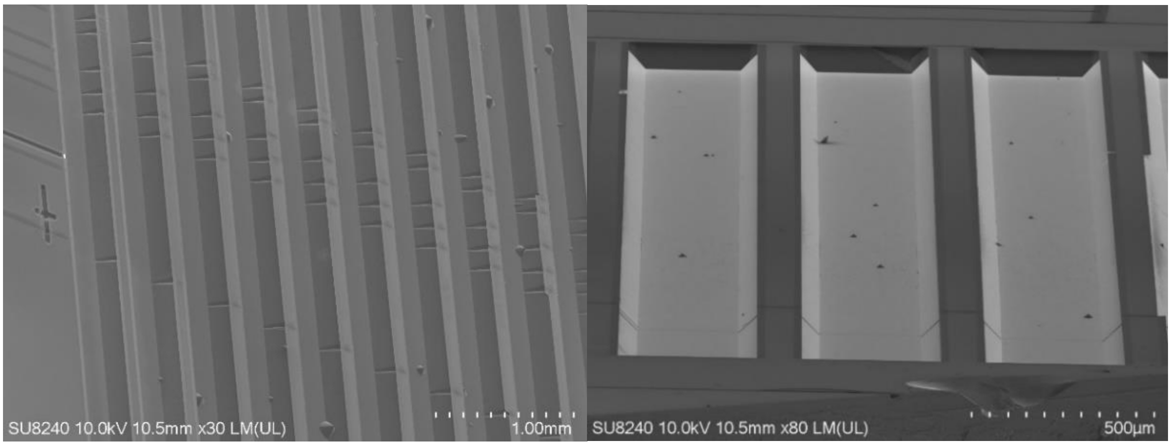

Figure 5.29 SEM images of etched grooves ending with fabricated ~45° sidewalls showing a cracked Si_3N_4 layer on Si(100), which has 500 nm Si_3N_4, during the wet etching process of 25% TMAH and Triton etchant mixture for 3.5 hours.

Reducing the wet etching time did not solve the problem of the cracked Si_3N_4 layer (Figure 5.29), and it is not preferable because a long etching time is desired to ensure deeper etched walls. The cracking occurred due to the surface stress of the Si_3N_4 layer. The solution for this is to deposit a thinner Si_3N_4 layer, <300 nm, to decrease the surface tension throughout the preparation of the wafer and to prevent cracking.

For the thinner Si_3N_4, 100 nm, the layer was deposited in order to overcome the cracking of the mask during the wet etching processes and to place less stress on Si(100). The same protocol and recipe were applied; the Si_3N_4 layer did not crack, but some were torn off through the wet etching, see Figure 5.30.

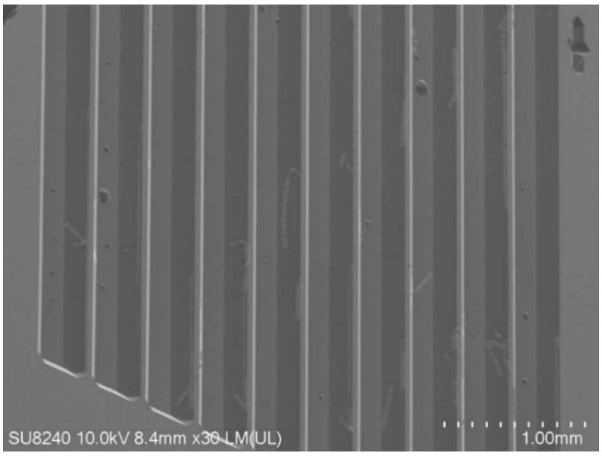

Figure 5.30 SEM images of etched grooves ending with fabricated ~45° sidewalls showing the torn Si_3N_4 layer on Si(100), which has the occurrence of 100 nm Si_3N_4 during the wet etching process of the 25% TMAH and Triton etchant mixture, and took 5 hours.

Longer wet etching of 9 hours was performed using the same recipe. The narrow-patterned trenches (130 μm) were damaged through the process while the mirrors of the broader trenches (200 μm) were intact, as shown in Figure 5.31 (a) and (b), respectively.

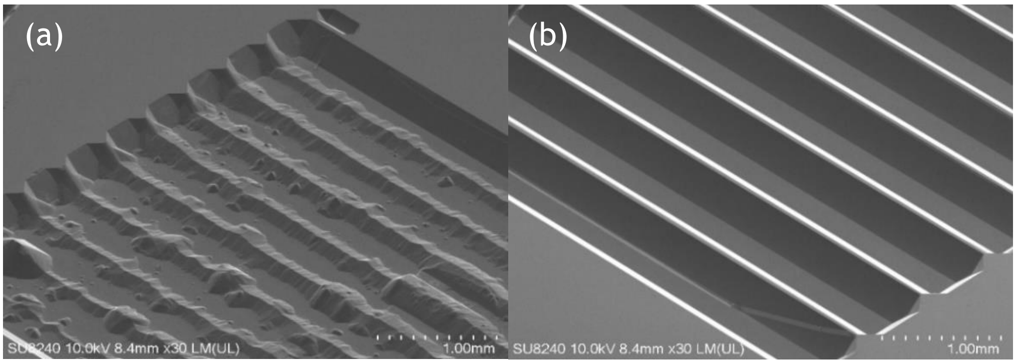

Figure 5.31 SEM images of etched grooves on Si(100), which has 100 nm Si_3N_4 showing (a) ruined narrow-patterned trenches,130 μm, and (b) surviving wider trenches, 200 μm, occurring within the wet etching process of a 25% TMAH and Triton etchant mixture and taking 9 hours.

The width of the trenches was around 100 μm; however, it was not suitable for the width of the laser spot size (960 μm). The reason for the etching of the spacing between the trenches is the poor quality of the Si_3N_4 layer. Hence, commercial Si(100) with high-quality Si_3N_4 and SiO_2 layers were used instead. The wafer was then etched for the same period as the previous wafer, namely for 9 hours. The narrow-spacing trenches, at 130 μm, were also damaged whilst the wider trenches, at 200 μm, were intact (shown in Figure 5.32). It also depends on the spacing between the trenches in the pattern before the wet etching process.

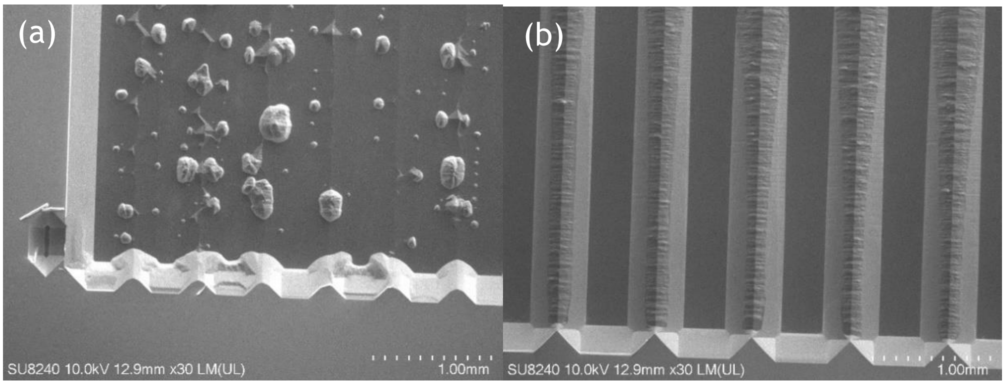

Figure 5.32 SEM images of (a) ruined narrow-patterned trenches,130 μm, and (b) survived wider trenches, 200 μm, during the wet etching process of a 25% TMAH and 0.1% Triton etchant mixture which took 9 hours on a commercial Si(100) wafer and has 60/40 nm of Si_3N_4 and SiO_2 layers respectively.

A reduced wet etching time of 5 hours for the same wafer and recipe were repeated to verify if the reduced duration would not stripe the spacing between the trenches. The 600 µm and 400 µm wide trenches lasted (shown in Figure 5.33 (a) and (b) respectively), as they have a wider spacing (200 µm). The 200 µm trenches were intact, but the etching reached the edges between each trench, as showed in Figure 5.33 (c).

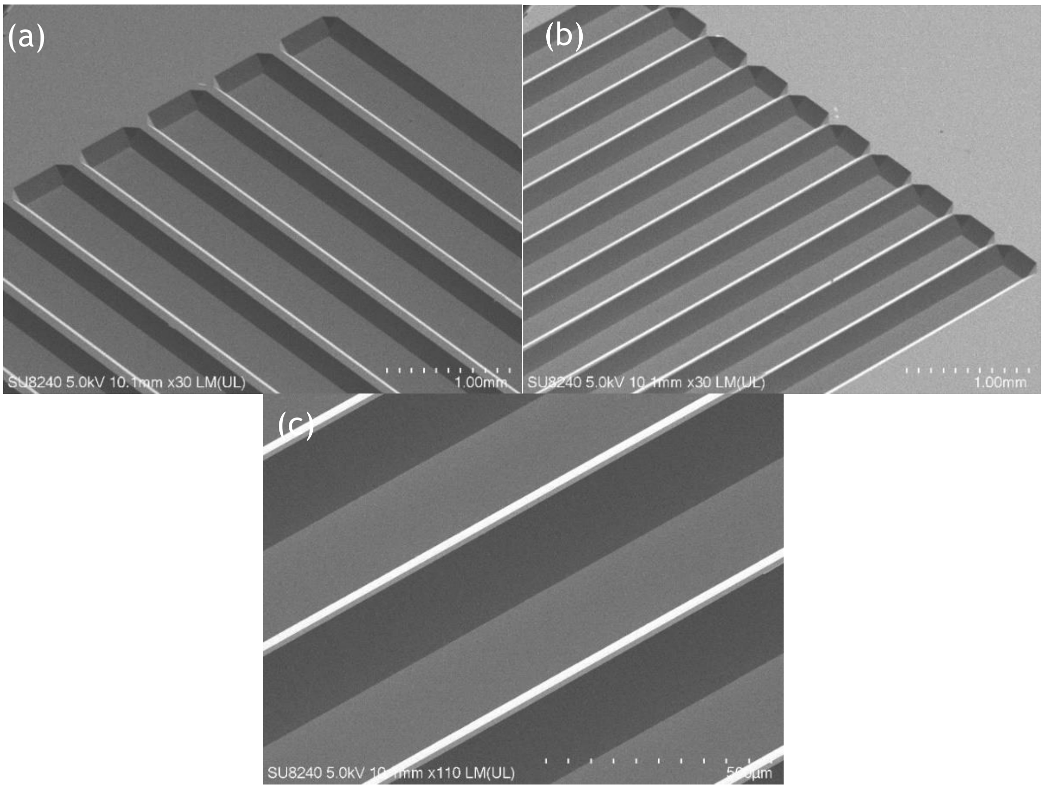

Figure 5.33 SEM images of a) and b) surviving wide, 600 µm and 400 µm, patterned trenches of 130 µm spacing respectively, and c) surviving 200 µm trenches during the wet etching process of a 25% TMAH and 0.1% Triton etchant mixture which took 5 hours on a commercial Si(100) wafer with 60/40 nm of Si_3N_4 and SiO_2 layers. The sidewalls were 170 µm depth.

The etching of the Si_3N_4 layer caused roughness throughout the wet etching process. The sidewalls were 170 µm deep with adequate smoothness. An aluminium layer of 50 nm was evaporated to use these micromirror devices in the multi-reflection scheme in the polarimetry system. However, the alignment also complicated the achievement of an output signal from these micromirrors due to the big laser spot size.

The sidewall width of the endured walls was around 170 µm, and the remaining spacing was very narrow and, so not enough to make a longer etching time to attain wider trenches. In addition, the wider spacing could not withstand the longer time required to accomplish the targeted width (~400 μm etched wall). Even if the spacing was wider, the surface morphology deteriorated when the duration of the etching process was more than 6 hours due to mask layer corrosion through the etching process.

Therefore, a longer etching process is required to reach deeper sidewalls and perform the alignment. In addition, smoothness is crucial to achieving the mirrored walls. The misalignment of the pattern, with 45° tilted trenches to the flat edge of Si(100) wafer before wet etching, might be the reason for the undercut etching.

5.3.6 Enhancement of the alignment of the photomask

Etching characteristics are orientation dependent. In order to fabricate microstructures with high dimensional accuracy, it is vital to align the mask edges along with the crystal directions comprising the slowest etching planes [114]. As a result, the determination of accurate crystal directions is of utmost importance to ensure dimensionally accurate microstructures for an improved performance. The perfect alignment also prevents the undercut etching and roughness. A unique alignment was applied using two masks [114]. The first mask, which has circles in different angle directions of the silicon wafer size (Figure 5.34), was first aligned in the corner of the expected 45° to the wafer's flat edge (Si(100)).

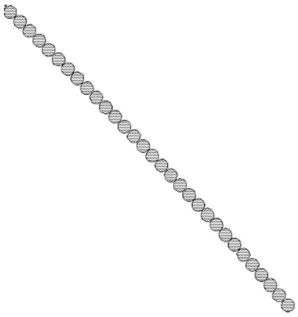

Figure 5.34 Pre-etched pattern of the circular openings' arc technique proposed by Sajal et al. [114], for identifying the ⟨100⟩ direction on Si(100), each square is 100 μm.

After patterning, the circles were then etched for two hours. The resultant etched squares, mainly from the circles, were monitored under the microscope to select the right angle from the centred angled square for <100> direction, as shown in Figure 5.35.

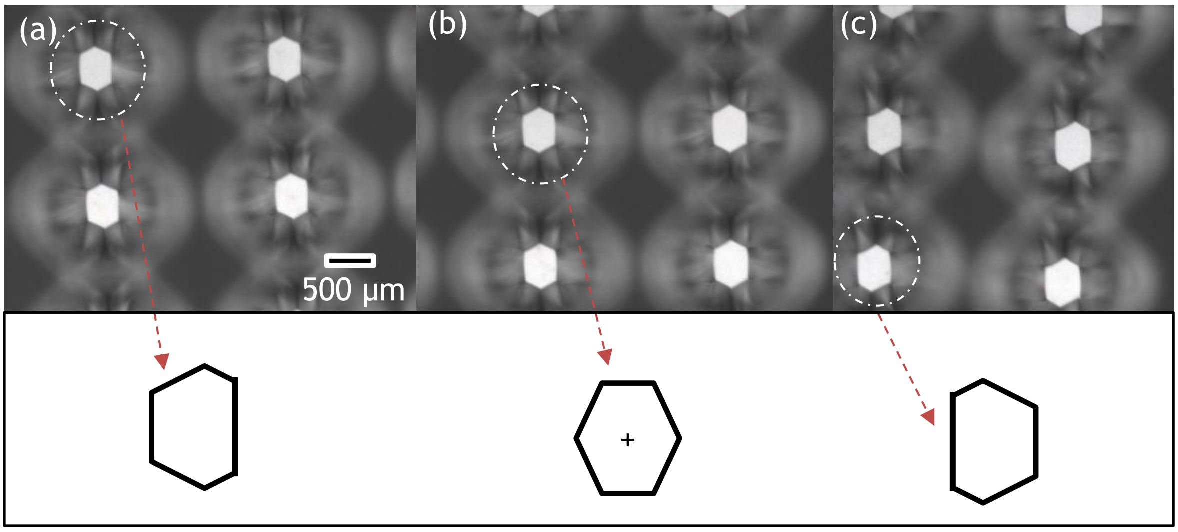

Figure 5.35 Optical images of the etched profile corresponding to multiple arrays of the patterns shown in Figure 5.34. Circles take the form of hexagonal grooves. The etched profile showed the deviation of the corners of adjacent hexagons when there is a) right-hand side deviation, b) no deviation, c) left-hand side deviation in the opposite direction. In case of no deviation, the ⟨100⟩ direction passes through the centre of the corners of the hexagons.

The right 45° squares to the wafer flat edge are shown in Figure 5.35 (b), because all the hexagons have similar distance lines. Unlike in Figure 5.35 (a) and (c), the lines of the hexagons are not regular leading to the unequal distances of the parallel lines in each square. After selecting the 45° angle direction of the centred etched square, the lines in the mask (shown in Figure 5.36) aligned along the selected angle and the whole desired design was then patterned.

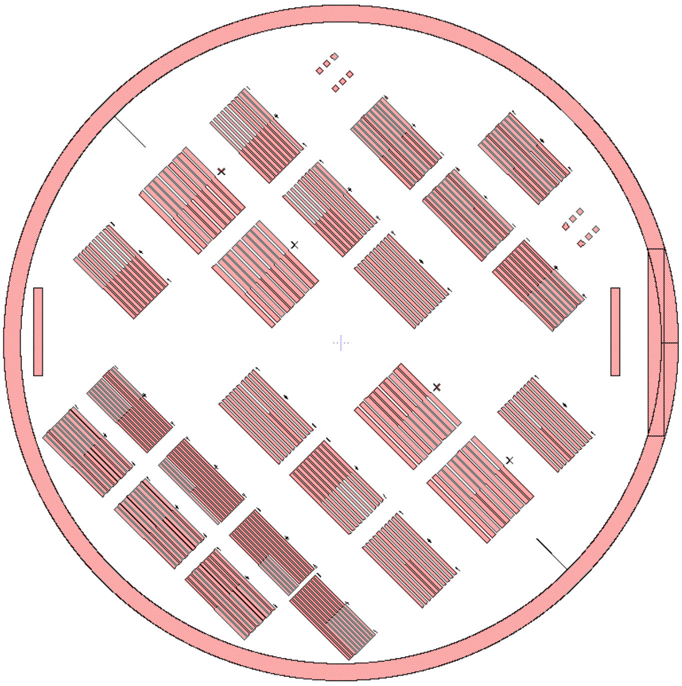

Figure 5.36 Photo mask of different windows and spacing widths to implement the second step of the alignment to ensure the desired windows were aligned to the correct 45° direction, namely, <100> direction on Si(100), to the wafer flat edge to get 45° slanted etched planes.

A previous wet etching process (25% TMAH and 0.1% Triton) were then repeated for the aligned mask (see Table 5.6).

Table 5.6 Wet etching of TMAH etchant with 0.1 % Triton X-100 recipes on Si(100) substrate at 80°C using the new photomask alignment way.

Mask layers for Si(100)	**Duration [hours]**	**Results**
Si_3N_4 mask (500nm) (JWNC 6-inch wafer)	6:30	45° ruined or not smooth walls
Si_3N_4 mask (100nm) (JWNC 6-inch wafer)	7:15	45° ruined or not smooth walls

The first etching trial was performed by using an efficient quality Si_3N_4 layer (see Figure 5.37).

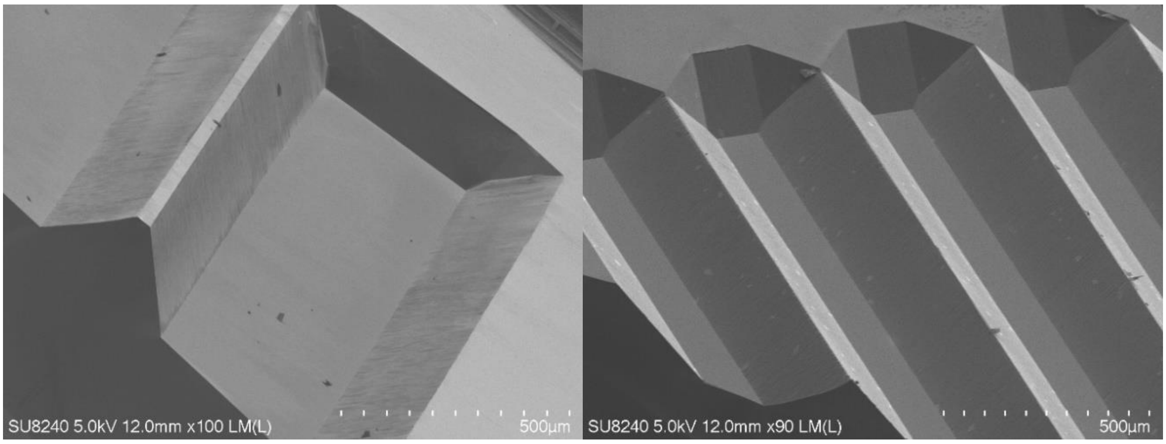

Figure 5.37 SEM images of a) survived wide, 600 µm and b) 400 µm, patterned trenches of 130 µm spacing respectively, during the wet etching process of 25% TMAH and 0.1% Triton etchant mixture for 6:30 hours on Si(100) using the new photomask alignment way.

The plane's angle for the intact patterns (of the wide spacing) was 45° slanted with 230 µm depth for six and a half hours. However, the facets were rough. Although the resultant etched planes were 45° tilted and the alignment was satisfactory; however, these were already attained. This alignment is more helpful for the alignment of small features.

A longer wet etching time, seven and a half hours, was implemented in the broader spacing pattern using commercial Si(100) in order to make deeper etching and achieve wider mirror facets. The same recipe (25% TMAH and 0.1% Triton) was applied for 7 hours and 15 minutes. The patterned trenches were intact, but they were also rough (Figure 5.38) despite the high-quality Si_3N_4 commercial layer.

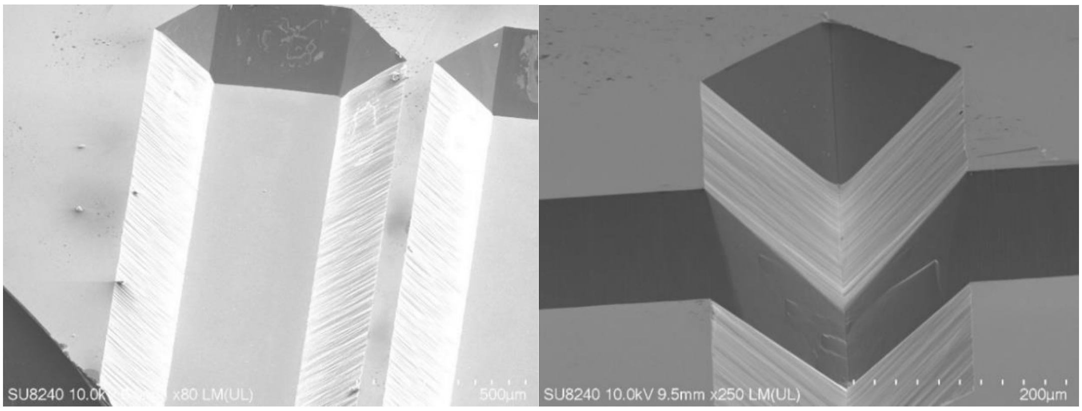

Figure 5.38 SEM images of survived wide, 600 µm, patterned trenches during the wet etching process of a 25% TMAH and 0.1% Triton etchant mixture for 7 hours 15 minutes on commercial Si(100) using the new photomask alignment.

With anisotropic etching, the lateral undercut etching rate increases rapidly with orientation, particularly over the first one or two degrees with respect to the <110> direction [115], [116]. Generally, the surface roughness deteriorates with increasing temperature or decreasing etchant concentration because the etching rate increases. In addition, the average surface roughness worsens by increasing the etching duration; this is because the TMAH does etch to the Si_3N_4 and/or SiO_2 layers over a long etching time, even it has a low etch rate of 1 nm/hour and 0.18 nm/min respectively [93], [117].

5.4 Vertical wet etch to achieve 45° zigzag slanted walls

Different techniques were discussed, including the use of different etchants, additives, hard mask layers and the use of pre-etched patterns to indicate the crystal directions. Different geometric patterns were analysed based on their applicability to either the Si(100) or Si(110) wafer. The basic technique to attain the 45°slanted micromirrors along with the wet etching on the crystallographic structure is to achieve a <110> plane as it is tilted 45° to the wafer surface. However, given the large laser spot size and rough etched <110> planes, the technique was not enough to achieve the deep, wide mirrors desired for laser alignment. As a result, alternative methodologies were developed; one was achieved by fabricating structures using the same wafer cut and structure and employing the KOH recipe to achieve a vertical, deep, smooth etched wall. From this, a zigzag pattern, which already had the structure, was developed, with a 45° tilted pattern that faced each other and accomplished an accurate self-aligned mirror device (see Figure 5.39).

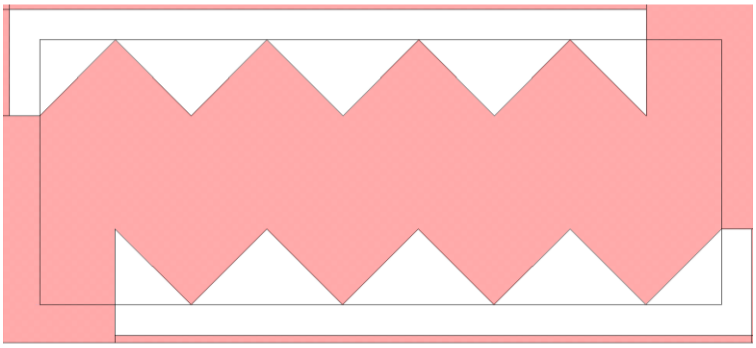

Figure 5.39 Photo mask fabricating a multiple retro-reflections cavity which makes parallel beam reflections via 45° tilted vertical etched mirrors.

Consequently, vertical sidewalls with patterns inclined to 45° and -45° (Figure 5.39) were fabricated for applications in multipass micro mirrored cavities.

Smooth 45° micromirrors can be obtained with a high etching rate by taking advantage of the resulting smooth vertical sidewalls due to the high surface tension micromachining processes of the <100> direction in Si(100) (Figure 5.14). The advantage of this process is evident in its ability to achieve deep, smooth 45° micromirrors with high etch rates compared to those fabricated using TMAH.

Hence, several trials, see Table 5.7, were performed to conduct the same recipes that achieved vertical wet etching walls (10 M KOH and 0.1 M *tert*-butanol etchant mixture) on the photomask (illustrated in Figure 5.39) and attain the 45° tilted vertical etched mirrors.

Table 5.7 Wet etching processes fabricating a multiple retro-reflection cavity, which makes parallel beam reflections via 45° tilted vertical etched mirrors using 10 M KOH with 0.1 M *tert*-butanol etchant recipes on a Si(100) substrate, which has a Si_3N_4 mask of 100 nm at 80°C using the photomask at different directions to realize the 90° etched walls.

Duration [hours]	Results
6	Smooth 53° zigzag sidewalls, Figure 5.40
4:35	90° zigzag sidewalls, Figure 5.41
5:45	90° zigzag sidewalls, Figure 5.42
5	90° zigzag rough sidewalls, Figure 5.47
3:30 + 2hours different stirring and sample holder	90° zigzag smooth sidewalls, Figure 5.48
5	90° zigzag smooth sidewalls, Figure 5.49
5:30	90° zigzag smooth sidewalls, Figure 5.50

The first attempt was made to align the whole photomask (Figure 5.39) at 45° to the Si(100) flat edge in order to repeat the same alignment of the vertical walls (Figure 5.14). The resultant walls, however, were approximately 53° tilted ({111} plane), shown in Figure 5.40. This is because the features are already 45° tilted and were patterned parallel to the flat edge when the whole mask was patterned 45° tilted to the flat edge (<110> direction).

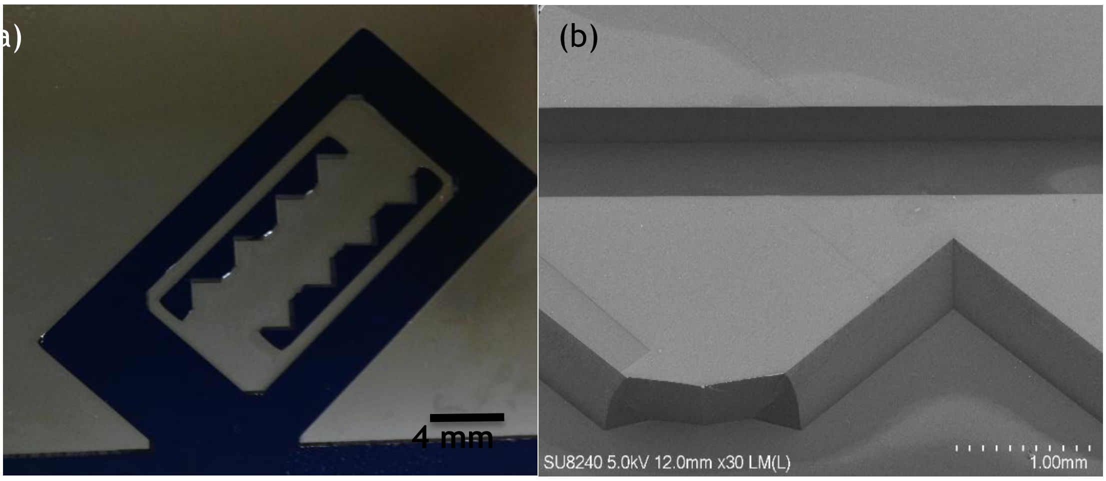

Figure 5.40 a) Photograph of the whole micromirror device. b) SEM micrograph of etched walls ending with 53° tilted ({111} plane) etched sidewalls with 45° tilted whole structure pattern with respect to the wafer flat edge of Si(100) substrate, which has SiO_2/Si_3N_4 mask layers using 10 M KOH and 0.1 M *tert*-butanol etchant mixture.

Hence, the whole pattern was then aligned parallel to the Si(100) flat edge (the features were aligned in <100> direction) – shown in Figure 5.41.

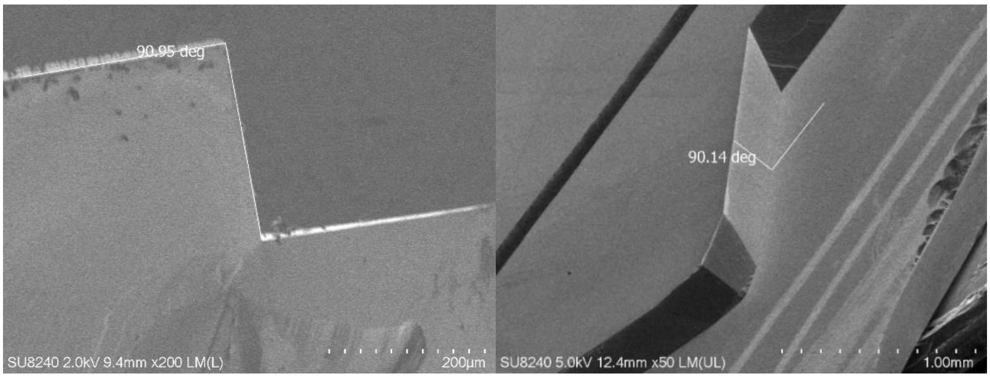

Figure 5.41 SEM micrograph of etched walls ending with 90° ({111} plane) etched sidewalls with 45° tilted desired pattern of the structure with respect to the wafer flat edge of Si(100) substrate, which has SiO_2/Si_3N_4 mask layers using 10 M KOH and 0.1 M *tert*-butanol etchant mixture.

The etched planes then were vertical, at {100} plane, but not sufficiently smooth for mirrors.

The same procedures were repeated using the same recipe and photomask alignment in order to accomplish the full zigzag cavity as the previous one was cleaved for SEM purposes. The vertical sidewalls were not smooth enough for mirrors, as shown in Figure 5.42.

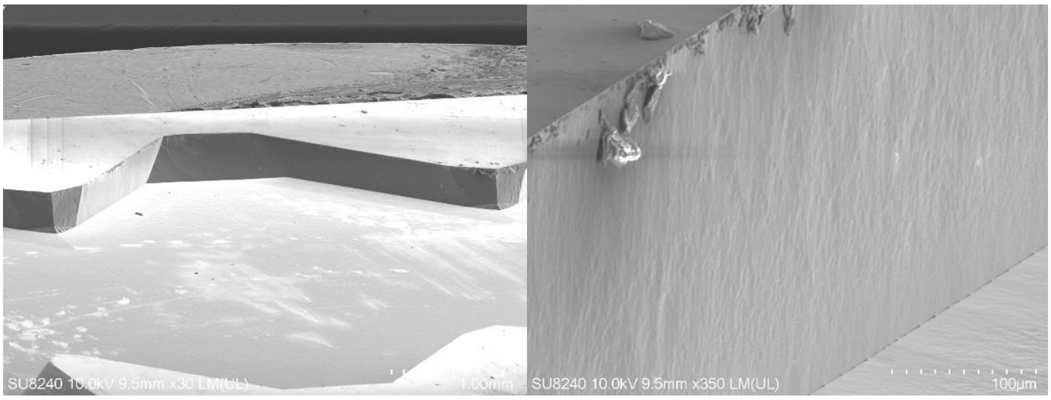

Figure 5.42 SEM micrograph of etched walls ending with 90° ({111} plane) etched sidewalls with a 45° tilted desired pattern of the structure with respect to the wafer flat edge of Si(100) substrate, which has SiO_2/Si_3N_4 mask layers using a 10 M KOH and 0.1 M *tert*-butanol etchant mixture.

The sample's roughness was tested using an optical profiler (Bruker) at JWNC. The roughness was approximately 170 nm, as shown in Figure 5.44.

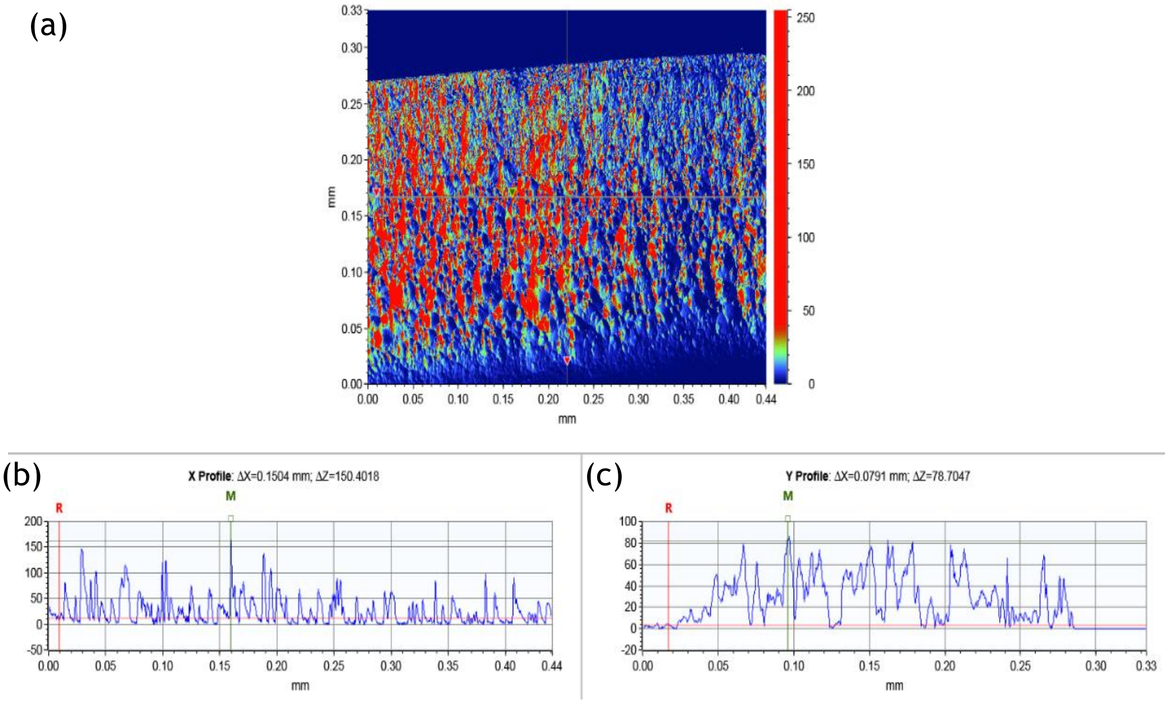

Figure 5.43 (a) and (b) Optical profiler image of an etched vertical sidewall using 10 M KOH and 0.1 M *tert*-butanol etchant mixture. (c) The measurements of roughness which is around 150 nm.

Thermal oxidization of 1 µm thickness was then grown in order to oxidize and remove the silicon top grooves and smooth the walls. The thermally oxidized samples were then etched by HF (10:1) for 10 minutes and (5:1) for four minutes to remove the grew SiO_2 layer. The roughness decreased to 110 nm, as shown in Figure 5.44.

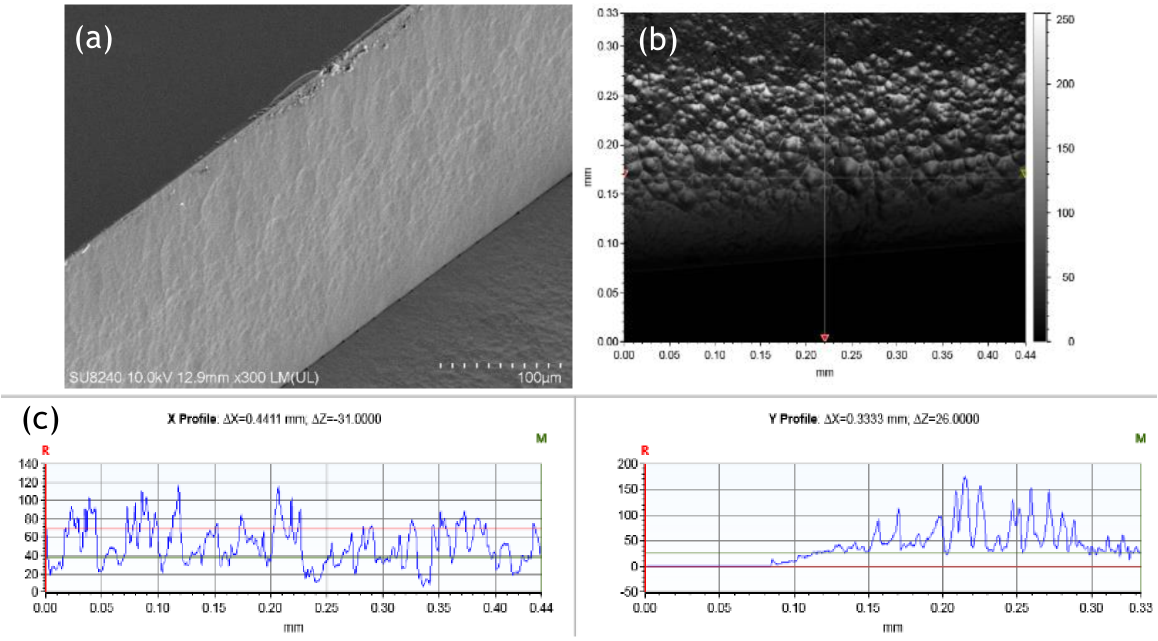

Figure 5.44 (a) SEM micrograph of the vertical etched wall showing the roughness after 1 µm thick oxidization processes. (b and c) An optical profiler image of an etched vertical sidewall using 10 M KOH and 0.1 M *tert*-butanol etchant mixture after etching the thermal oxide layer with 10:1 HF for 10 minutes and 5:1 HF for 4 minutes.

With the aim of measuring if the angle of the pattern retained 45° after the wet etching process, measurements were made using SEM picture tools, as depicted in Figure 5.45.

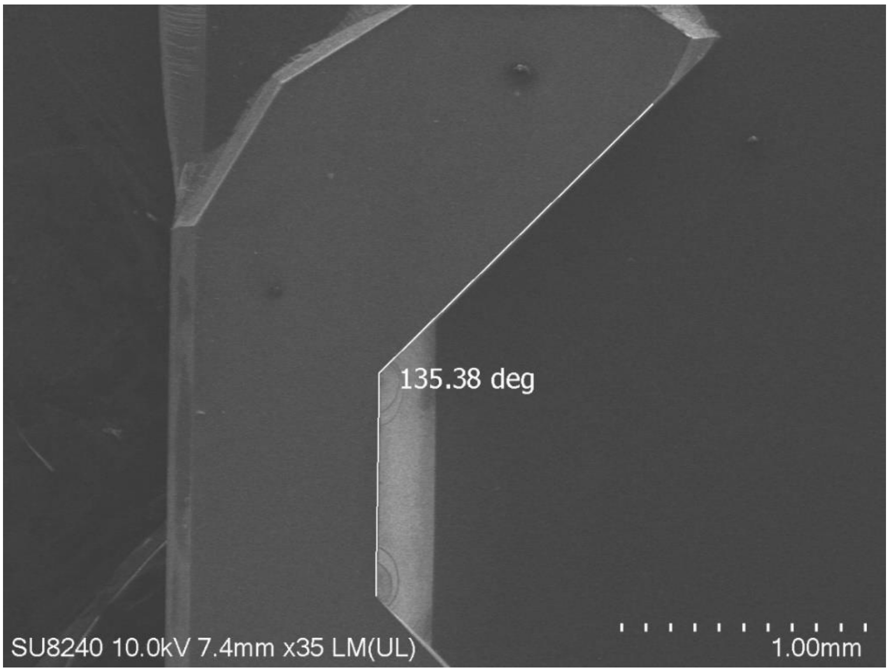

Figure 5.45 SEM micrograph testing the etched pattern angles after the wet etching processes.

The angle is approximately 45° and proved that this way of using a zigzag photomask to secure 45° mirrors is functional.

A chromium mask was then designed and printed in e-beam (Figure 5.46) at JWNC to overcome the roughness that might result from an acetate mask.

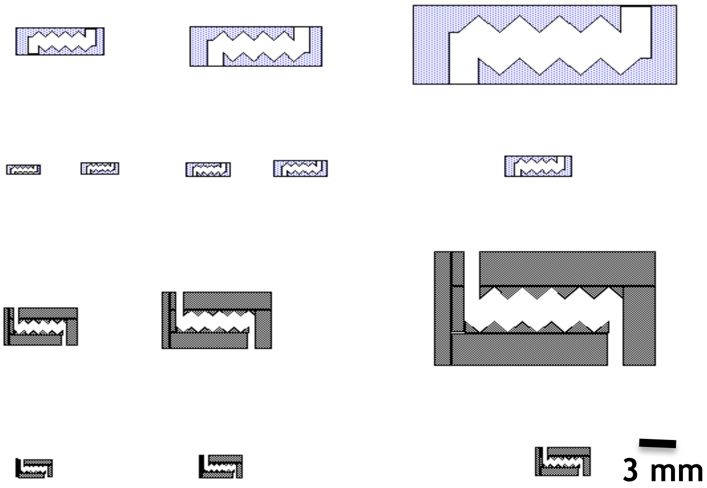

Figure 5.46 Chromium photomask design for a variety of different dimensions and number of mirrors.

The designed mask provides different sizes and a number of mirrors and cavity dimensions (zigzag pattern) in order to test whether the small size can be etched efficiently, i.e. less etching time with deep vertical walls. Moreover, the smaller mirror size affords more reflections and less sample volume.

Hence, the new chromium designed mask, shown in Figure 5.46, was then used in the photolithography process to decrease the roughness that might come from the acetate mask. The recipe of 10 M KOH with 0.1 M *tert*-butanol was repeated. The walls were rough - see Figure 5.47 - because the stirring speed of the clean room kit is random and relatively slow.

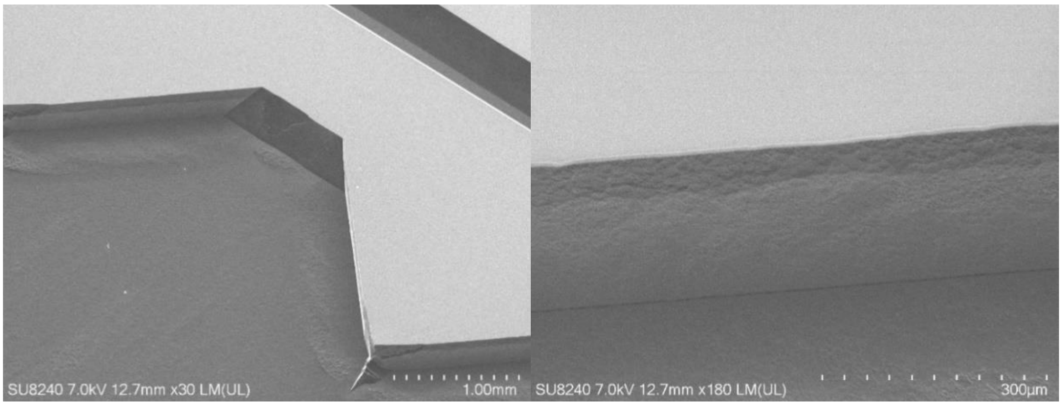

Figure 5.47 SEM micrograph of etched walls ending with 90° tilted ({111} plane) etched sidewalls with 45° tilted desired pattern of the structure with respect to the wafer flat edge of Si(100) substrate. This has SiO_2/Si_3N_4 mask layers using 10 M KOH and 0.1 M *tert*-butanol etchant mixture and chromium mask.

To avoid the decline of the surface morphology due to a stirring defect of the etchant mixture, the kit in the lab (constructed one – see Chapter Three) was used instead of that at the JWNC. This kit allows for control of the stirring speed of the solution. The same mask and recipe were used and repeated, respectively. The sample holder was also stirred at 120 rpm. The sample was first etched for 3 hours 30 minutes when the walls were 90° but rough. The smoothness of the walls, however, improved, after two hours further etching, as shown in Figure 5.48.

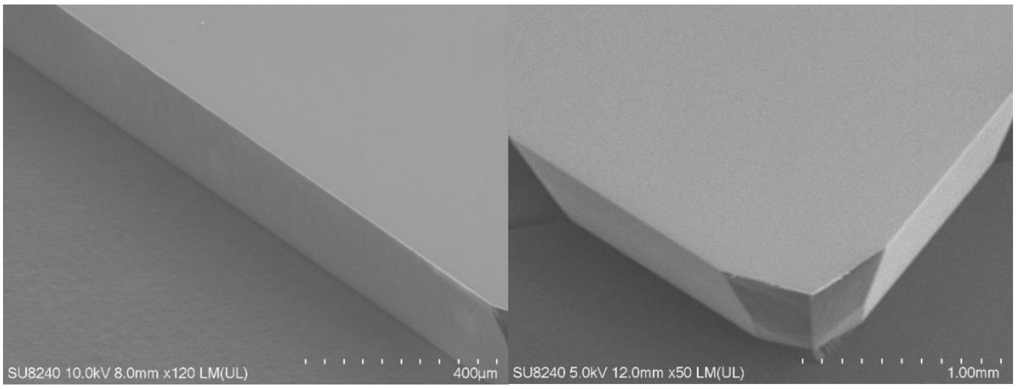

Figure 5.48 SEM micrograph of etched walls ending with a 90° tilted ({111} plane) etched sidewalls with 45° tilted desired pattern of the structure with respect to the wafer flat edge of Si(100) substrate, which has SiO_2/Si_3N_4 mask layers using a 10 M KOH and 0.1 M *tert*-butanol etchant mixture, chromium mask, and controlled stirring speed. a) 3:30 hours etching duration and b) 2 hours etching duration, with 400 µm depth (total etching is 5:30 hours).

It can be concluded that the stirring speed has a crucial impact on the surface morphology in the wet etching process. Smooth 90° walls were attained; however, the sample was cleaved for SEM purposes. Hence, the recipe was repeated for the same conditions for five hours, shown in Figure 5.49.

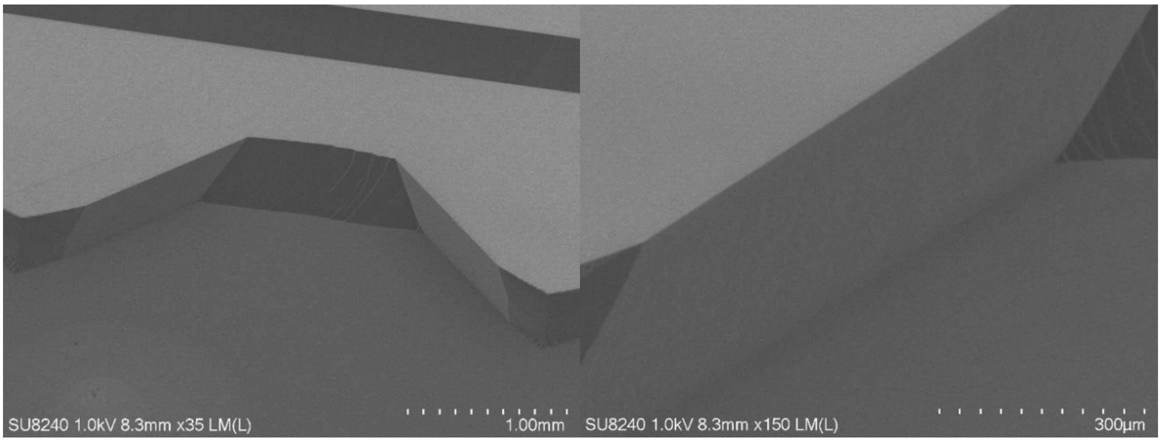

Figure 5.49 SEM micrograph of etched walls ending with 90° tilted ({111} plane) etched sidewalls with a 45° tilted desired pattern of the structure with respect to the wafer flat edge of Si(100) substrate, which has SiO_2/Si_3N_4 mask layers using 10 M KOH and 0.1 M *tert*-butanol etchant mixture, chromium mask and controlled stirring speed with 320 µm depth.

The recipe was repeated for the same conditions but for five and a half hours (Figure 5.50) to accomplish 400 µm depth walls, which were cleaved for SEM purposes (Figure 5.48).

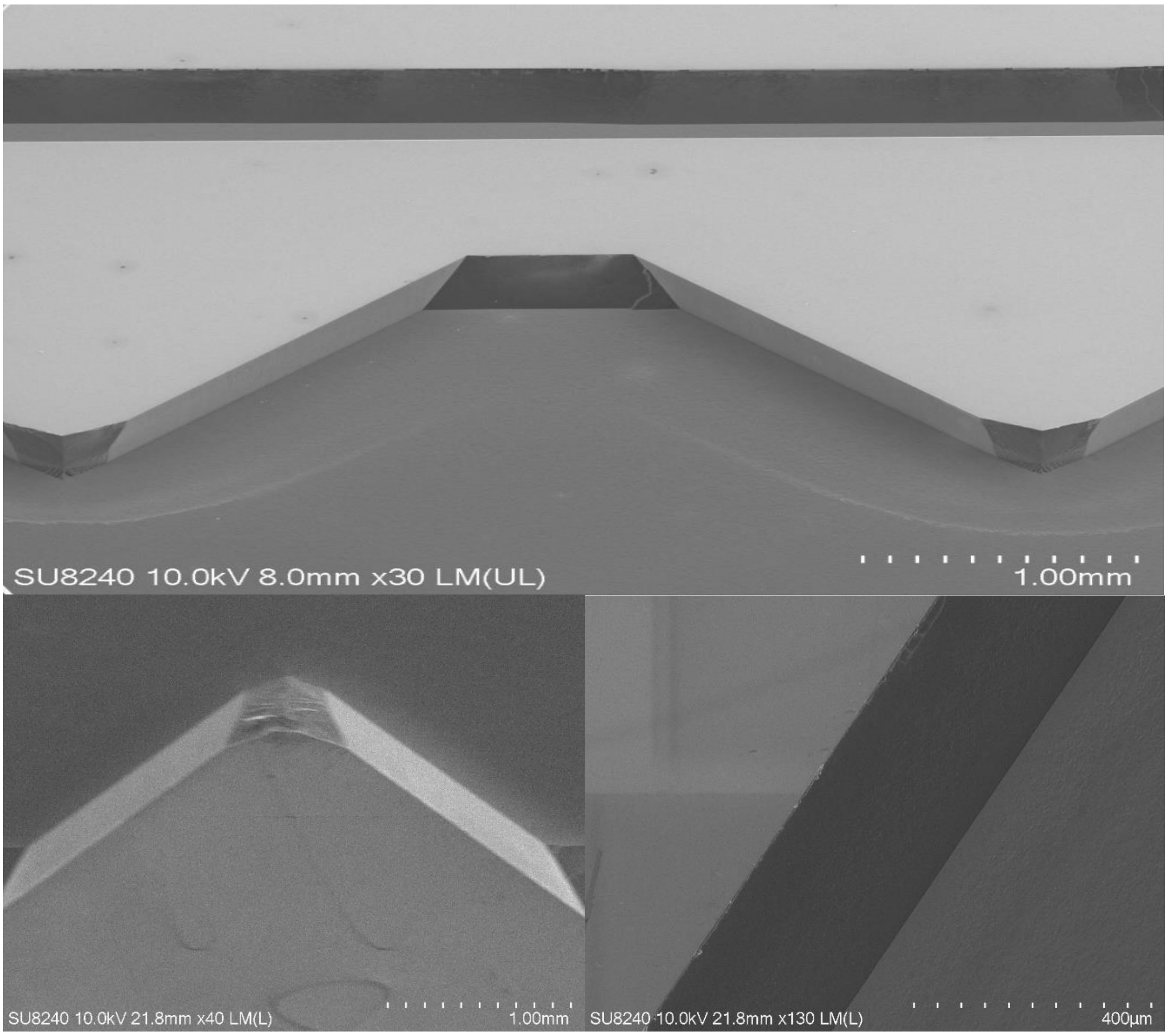

Figure 5.50 SEM micrograph of etched walls ending by 90° tilted ({111} plane) etched sidewalls with 45° tilted desired pattern of the structure with respect to the wafer flat edge of Si(100) substrate which has SiO_2/Si_3N_4 mask layers using a 10 M KOH and 0.1 M *tert*- butanol etchant mixture, chromium mask and controlled stirring speed with 400 μm depth.

In general, when *tert*-butanol was added to high concentrated KOH (10 M), {110} plane was etched and reached {100} plane (90° sidewall), due to the effect of the surface tension (as indicated in section 5.3.4). This was achieved with a stirring speed of 130 rpm and at 80°C to enhance the surface morphology. The etch rate was 0.96 μm/min.

5.5 Application of deep vertical micromirrors to attain 45° cavities

Structures were designed, where the sidewalls form multiple mirrors to bring parallel optical beams through a cavity. The structure in the Si(100) substrate was etched in 10 M KOH mixed with 0.1 M *tert*-butanol. The fabricated micromirror cavity is presented in Figure 5.51 (a). The edges between the two {110} planes forming the mirrors were not sharp after the etching process due to the formation of {111} during the etch process. The structure can serve as a cavity or waveguide via retroreflection at an angle 90° parallel to the substrate (Figure 5.51 (b)).

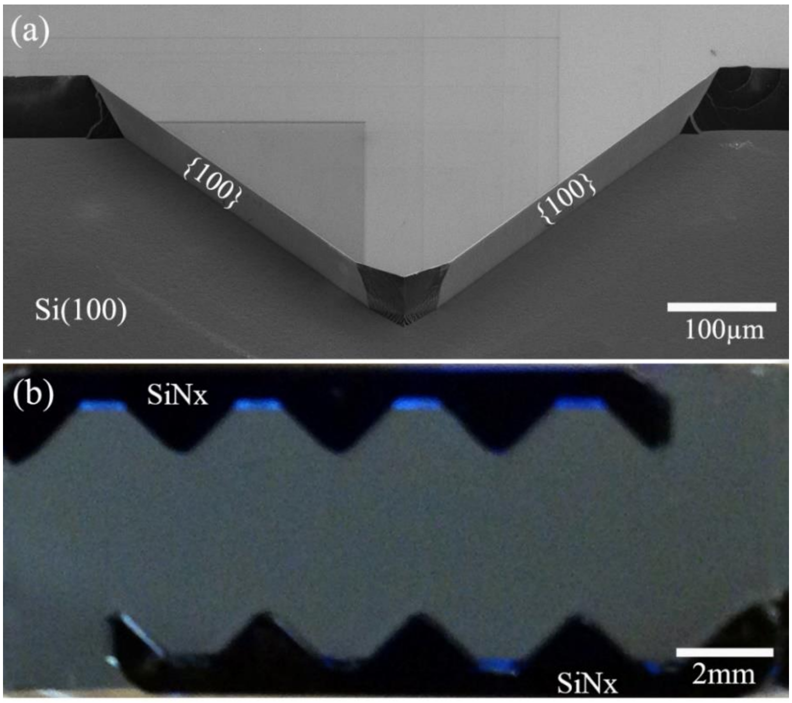

Figure 5.51 SEM micrograph of etched walls terminated by 90° sidewalls with a 45° and -45° tilted pattern with respect to the wafer flat edge of Si(100) substrate, which has SiO_2/Si_3N_4 mask layers using a 10 M KOH and 0.1 M *tert*-butanol etchant mixture (depth ~200 μm). (b) Photograph of multiple retro-reflection cavity which makes parallel beam reflections via 45° tilted vertical mirrors.

The structure shown in Figure 5.50 (b) demonstrates the possibility of providing a large number of optical passes through a given sample, which may, for example, be within a microfluidic device, where the sample being probed could either be part of a medical (e.g. serum or urine) or environmental (e.g. waste-water) study. By providing a significantly increased path length using this method, we can produce an integrated, self-aligned retroreflective topology, which can potentially increase the performance of instruments. The sensitivity of the measurement will be proportional to the effective optical path length, and can, therefore, increase this without a concomitant increase in form factor.

The vertical sidewalls of the pattern inclined 45° and -45° towards the wafer's flat edge were conducted due to the possible application for micromirrors. Thus, smooth 45° micromirrors can be obtained with a high etching rate by taking advantage of the resultant smooth vertical sidewall via high surface tension micromachining processes of <100> direction on Si(100) (Figure 5.14). The merit of this process is the attainment of deep, smooth, and fast 45° micromirrors rather than obtaining mirrors with a trench of shallow and slower etch rates with other etchants, like TMAH. The structure has been designed with the sidewalls forming multiple mirrors to bring parallel optical beams via a cavity. The structure, shown in Figure 5.51, can serve as a cavity or waveguide by reflecting at a 90° angle parallel to the substrate.

5.6 Multi-reflections device in polarimetry system

The device was already fabricated with the desired design by creating arrays of micromirrors that enable the reflection of an optical beam parallel back and forth, from 45° and -45° tilted vertical structures. Hence, the mirrors were then used for these reflections in the polarimetry system in order to increase the optical path length, as mentioned in Chapter 4. The 1000 nm aluminium layer was evaporated using the metal evaporation machine at JWNC. The laser beam with mirrors was aligned; nonetheless, it could not achieve an output uniform beam due to scattering. Therefore, the device was cleaved to reduce the number of mirrors to avoid loss of the laser beam spot due to weak reflectivity. Three passes were attained using a four-mirror cavity, as shown in Figure 5.52.

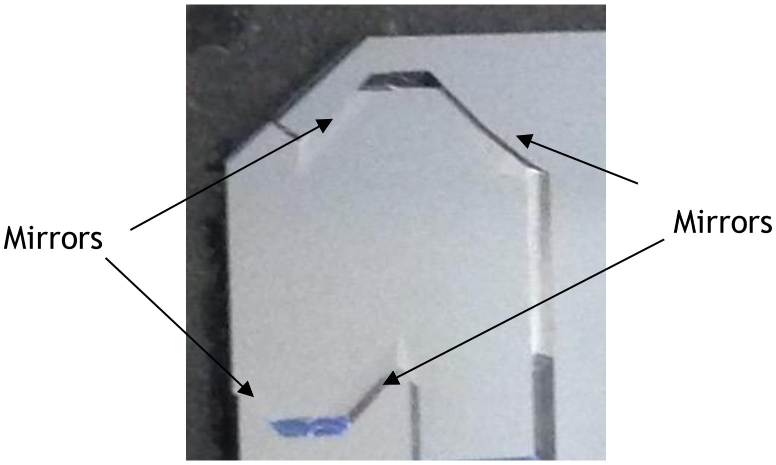

Figure 5.52 Cleaved fabricated cavity device of three reflections.

In addition, the microfluidic channel was designed for placement between the two symmetric mirrors as a sample channel in the polarimetry system.

5.6.1 Microfluidic channel design

Several trials were attempted to place a microfluidic channel between the cavities of the multi-reflection scheme in the polarimetry system. One was achieved by using a rectangular 1 mm glass capillary channel; however, it has thick edges that blocked the beam. Putting a coverslip on the device meant it performed different, but did not precisely determine the optical path length or the volume of the sample. Therefore, the PDMS microfluidic channel was designed and fabricated to fit with a dimension of the device, as shown in Figure 5.53.

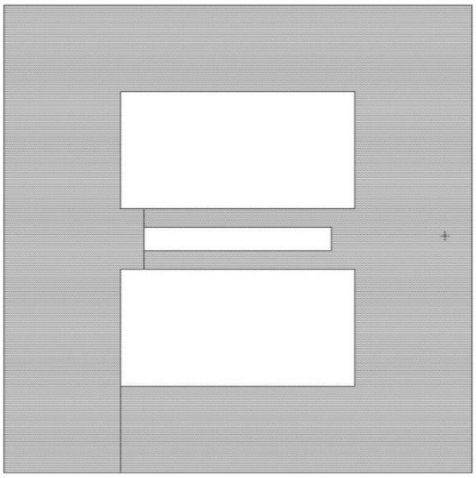

Figure 5.53 Mask design for the photolithography process; the upper and lower rectangles are fit with a mirror cavity, while the middle rectangle is for the microfluidic channel.

A 1 mm thick channel was fabricated and placed in the middle of the four-mirror cavity. A different set of glucose concentrations were prepared, and the optical rotation was measured for each – see Figure 5.54.

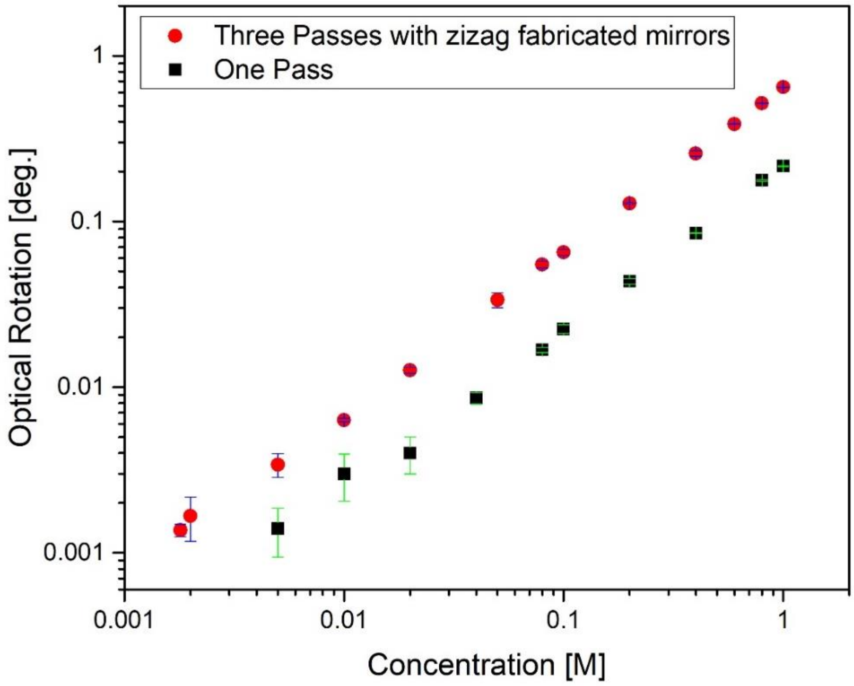

Figure 5.54 Optical rotation for different glucose concentrations using the multi-reflection setup (three passes) and a diode laser (403 nm). One pass is without using the multi-reflection scheme. The vertical error bars show the standard deviation (n=3). Linear correlation is at least R^2>0.997 for all different passes.

The limit of detection for three passes was 1.8 mM, which is about three times less than for the one pass arrangement results. This is approximately the same comparison for the 2 mm cube mirror results for three passes (Chapter 4) but achieved with 10 times less sample volume (20 µL in a capillary tube when using cube mirrors and 2 µL when using the fabricated multi-reflections device).

5.8 Conclusions

Different techniques were performed to precisely achieve a smooth and deep 45° slanted walls. One used an SU8 photoresist, but the SU8 walls were not straight and therefore not suitable for use as mirrors. Others were based on the wet etching to produce {110} plane of the crystallographic directions on Si(100) and Si(110) wafers. Different methods, including the use of different etchants, additives, hard mask layers and the use of pre-etched patterns to determine the crystal directions, were discussed and performed. In our experiment, 25% TMAH with 0.1% Triton X-100 was used stirring at 130 rpm and with a 180°C mixture temperature. A smooth 45° sidewall was attained with an etch rate of 0.43 µm/minutes.

However, given the large laser spot size, it was not enough to achieve the deep, wide mirrors required for laser alignment. As a result, an alternative approach was developed. This was underpinned by the fabricating structures that used etched vertical sidewalls with inclined patterns at 45° and -45°. Moreover, 45° etched walls were achieved by employing the 10 M KOH and 0.1 M *tert*-butanol mixture etching to produce vertical walls on that inclined 45° pattern. The advantage of this process is evident in the ability to achieve deep, smooth 45° micromirrors with high etch rates when compared to those fabricated using TMAH.

The structure of fabricated structures which created arrays of micromirrors that enable an optical beam to be reflected parallel back and forth from 45° and -45° tilted vertical structures were used in the polarimetry system. Only three passes could be achieved due to alignment issues. The optical rotation of the chiral molecules (glucose) was measured using this fabricated and integrated multi-reflection structure. The optical rotation was tripled. The structure enabled the use of a lower sample volume, with up to 20 times less microlitres. This method enables an increase in the path length in optofluidic devices where there is a need to increase the effective pathlength of a beam through a sample whilst keeping the device as small as possible.

Chapter 6 The Effect of pH and Temperature on the Microfluidic Polarimetry Measurements of Chiral Molecules

6.1 Introduction

pH is a well-established parameter influencing the optical rotations of chiral molecules [20, 118-123]. This phenomenon is linked with the protonation and electron arrangement around the asymmetric carbon centres of the chiral molecules [124]. Linthorst et al. [121] indicated that the protonation of the high acidity of hydroxyl acid, which happened at pH>3, results in a higher optical rotation. It happens when the hydroxyl (oH) ions open the chain of the chiral molecules and close it when interacting with the HCl or NaOH, which effects the chiral optical rotation. This is because the optical rotation depends on the handedness in the chiral molecules, which are changed by closed and opened chains [125].

It was found that in both glucose and BSA protein samples with a pH buffered solution, the optical rotation remains the same. BSA has a high molecular weight, which is an advantage in a polarimetry system as it increases the optical rotation even with low concentrations (up to nanomolar). Strong acids or alkalis, such as HCl and NaOH, change the optical activity for these chiral molecules [20]. The buffered solution does not protonate the hydroxyl groups of the chiral molecules and keeps the arrangement of the electrons around the chiral centres persistent; the optical rotation thereby remains the same.

In [20], depending on the previous results, the researchers used multiple wavelengths and light source polarimetry to measure the optical rotation of glucose and protein molecules. They realized that the rotation of glucose increases seven to eight times when using a blue laser and manages the pH to 7.6 at 26°C.

Here, an advantage has been added from incrementing the signal of the optical rotation by tuning the pH values. Compared to He-Ne pH=7.2, the specific rotation decreased by a factor of eight when using a blue laser with a solution of pH 6.4, compared to using a blue laser and pH=7.2 and a factor of 25. For glucose measurements, when using 11 reflection arrangements, the detection went down to 56 μM from 450 μM for pH=7.2 (normal) using the same laser and setup arrangement.

In addition, temperature also plays a role [20]. An increment in the optical rotation has been detected for every ten degrees in temperature increase and all are related to plane polarized interactions with a different arrangement of chiral molecule electrons [121].

In this chapter, the optical rotation of BSA has been studied along with the pH variations using the fabricated reflective device in Chapter 5. This enabled the system to detect 115 ng in a 2 μl sample via three reflections (9×10^{-7} μM).

6.2 Theory

6.2.1 Effect of pH and temperature on the optical rotation of chiral molecules

The pH of a solution is a measure of the concentration of hydrogen ions in a solution. The number of hydrogen ions is a direct measure of how acidic or how basic a solution is [126]. Chirality is known on the basis of asymmetric carbons in a molecule. These carbons are configurationally stable and have four different groups. The electric component of plane polarized light interacts with the electrons in molecules and ions. When the pH is low (pH < 2), the glucose molecule, as a chiral molecule, is electrically neutral and there is no net charge to be stabilized. Therefore, the glucose solution’s optical activity is stable. However, with its hydroxyl groups, glucose has enols that are deprotonated with increasing pH [127]. Apparently, the specific rotation is different for each ionized glucose molecule. However, the covalent bonds of asymmetric carbon centres remain intact. The number of electrons after deprotonation remain the same but the distribution of the electrons around the asymmetric centre varies, and thus the interaction of plane-polarized light with these altered electrons correspondingly changes [128], [121], [123]. In summary, the asymmetric carbon centres, which are responsible for the optical activity, are not the same for the ionized glucose molecule.

The effect of pH appears in wavelengths of less than 500 nm [20]. This is because the electrons are interacting and are active with the shorter wavelengths (higher energy) compared to those with longer wavelengths. This affects the distribution of the electrons around the asymmetric centres and consequently the optical activity.

When dealing with a sample with a small volume, the impact of temperature changes can be much more rapid compared to large samples. However, in the case of polarimetry, these specific rotation changes are minute and can be calculated using Equation (6.1).[20, 129].

$$\alpha_{\lambda}^{T} = \alpha_{\lambda}^{20°C}[1 + 0.0001(T - 20)] \tag{6.1}$$

Where, $\alpha_{\lambda}^{20°C}$ is the specific rotation at 20°C (constant), T is the temperature of the sample.

According to this equation, the influence of temperature on the optical rotation is minimal and is not affected by slight changes in the temperature. For example, the difference in the angle of rotation for 100 mM of glucose solution in 1 cm optical path cell is 0.000076° and 0.00038° when the temperature changed by ±10°C and ±50°C respectively. While 1 mM, α changed about 0.000007° and 0.000038° when the temperature changed by ±10°C and ±50°C respectively. From these results, the influence of temperature decreases as the glucose concentration decreases (illustrated in Figure 6.1).

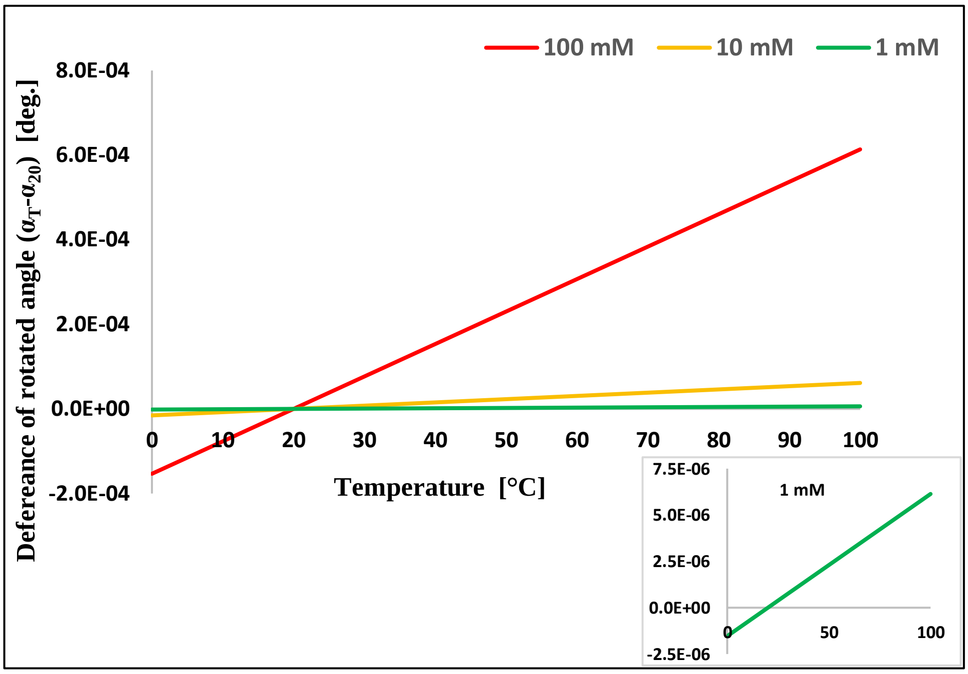

Figure 6.1 Influence of temperature change on the optical rotation of different glucose concentrations, 20 ml in 10 cm cell. Inset is for 1 mg/ml concentration.

For samples with high glucose concentrations, there is a significant influence on the angle of rotation resulting in a small difference in temperature. This impact will decline gradually at low concentrations.

6.2.2 Bovine serum albumin as chiral molecules

Proteins were the first molecules examined polarimetrically to determine the specific rotation from the measured optical rotation for use as a physical constant [130]. Then, with the development of optical activity theory, polarimetry has been used for the elucidation of protein structure.

Protein molecules are known to have very complex structures, both in the native and denatured states. It might be expected that some insight into their structures may be gained from an examination of their optical rotations [130].

6.3 Results and discussion

6.3.1 Buffered and non-buffered pH with glucose

A phosphate buffered pH solution of 6.4, 7.1 and 7.6 was prepared and mixed with appropriate weights of glucose powder to get 0.8 M and 5.5 mM. A He-Ne laser and a 403 nm diode laser measured the optical rotation for the same 0.8 M solutions, as illustrated in Figure 6.2. The 403 nm diode laser is then used for the rest of the measurement as the He-Ne laser had a negligible effect on the optical rotation when the pH changed [20].

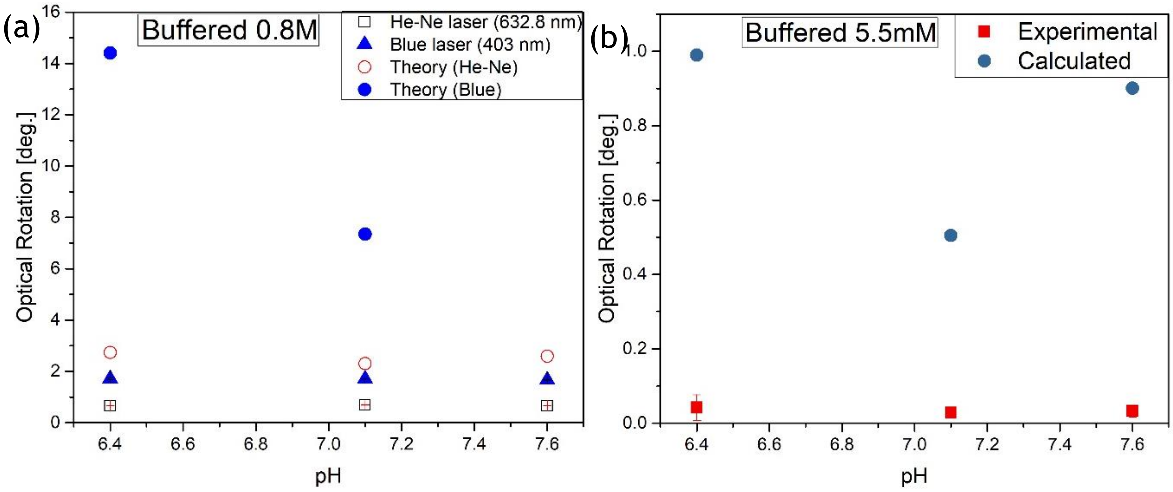

Figure 6.2 Optical rotation of a) 0.8 M, using both He-Ne laser and 403 nm laser and b) 5.5 mM glucose using only the 403 nm laser, respectively, with a pH of 6.4, 7.1, and 7.6 at room temperature (23°C). The vertical error bars show the standard deviation (n=3). The pH values selected depend on predictions of high optical rotation variations with these values [20].

The performance does not reach the theoretical limit, especially for the blue laser measurements, as the pH buffered solution does not interact with the chiral molecules and cause protonation. The measurements were tried for 0.4 M, but it shows that there is no detection of change with alterations to the pH. It is found that the pKa decreases with high concentrated glucose [131]. The deprotonation, therefore, becomes less, even for a high pH, and no optical activity change can sense highly concentrated glucose, as shown in the Henderson-Hasselbach equation (6.2) [132].

$$pH = pK_a + \log\frac{[A^-]}{[HA]} \qquad (6.2)$$

Where $[HA]$ is the molar concentration of the undissociated weak acid, $[A^-]$ is the molar concentration (molarity, M) of this acid's conjugate base, and pK_a is $-\log_{10} K_a$ where K_a is the acid dissociation constant.

A non-buffered solution of glucose was used. A glucose concentration was prepared with deionized water. Drops of 2 M HCl and NaOH were added to the glucose solution to tune the pH to the desired values. The optical rotations were thereby measured using the same pH and glucose concentration values (5.5 mM) demonstrated in [20], using 10 cm cell and 403 nm diode laser in the built setup (rig) and commercial polarimetry, as shown in Figure 6.3.

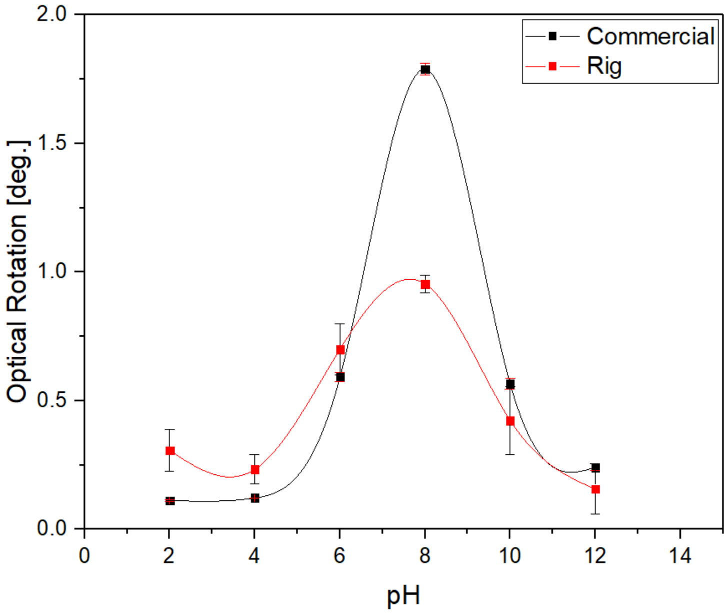

Figure 6.3 Optical rotation of 5.5 mM glucose with a different set of pH at room temperature (23 °C) using 10 cm pathlength, a 403 nm laser of built setup (rig) and commercial polarimetry. The vertical error bars show the standard deviation (n=3). The theoretical optical rotation of neutral pH 5.5 mM glucose is 0.118° [20]. Some of the error bars are large compared to others due to the additives of acids and alkali to vary the pH of the mixture.

The curve goes downwards after pH = 10 due to the dilution of the glucose with high amounts of NaOH to reach the high pH values. To tackle this, highly concentrated HCl and NaOH of 4 M were prepared to manage the pH without dilution in case of pH = 10 and 12. It proves that it has a high optical rotation of pH=8 (shown in Figure 6.4 Optical rotation of 5.5 mM glucose with a different set of pH at room temperature (23 °C) using 10 cm pathlength and 403 nm laser. The theoretical optical rotation of normal pH 5.5 mM glucose is 0.118° [4].

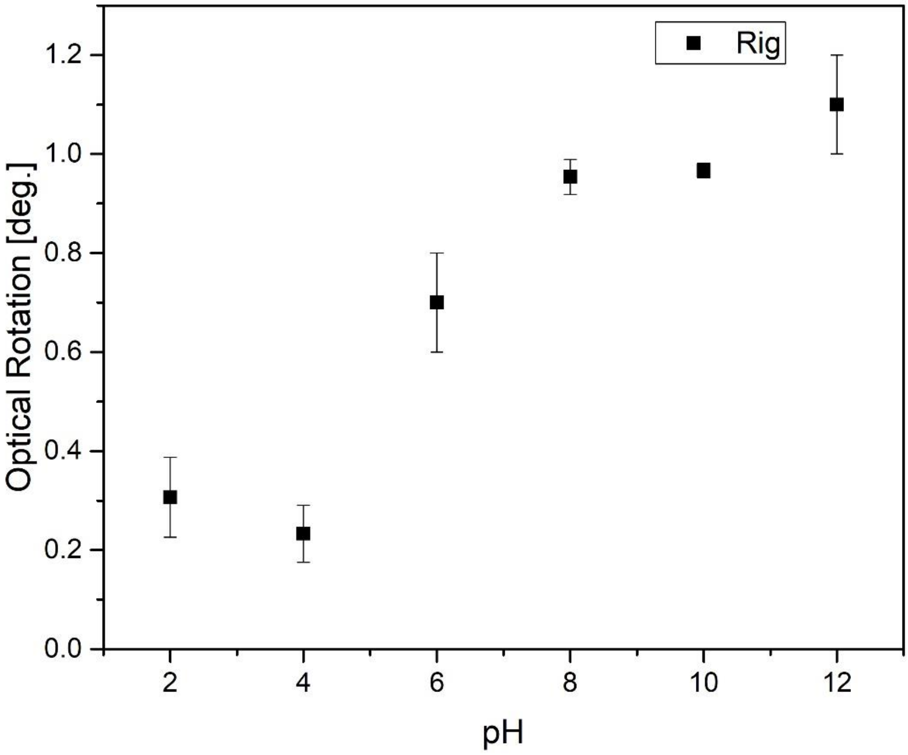

Figure 6.4 Optical rotation of 5.5 mM glucose with a different set of pH at room temperature (23 °C) using 10 cm pathlength and 403 nm laser. The theoretical optical rotation of normal pH 5.5 mM glucose is 0.118° [4]. Some of the error bars are large compared to others due to the additives of acids and alkali to vary the pH of the mixture.

The measurements were repeated many times, as the pH of the non-buffered solution was not stable; it looked like it decreased one digit every 20 minutes. Therefore, the measurements were implemented at approximately 2-3 minutes (for the sample and its reference) to avoid the varying pH and to ensure accurate results.

6.3.2 Effect of temperature with pH

Measuring optical activity in sub-microlitre volumes in a chip dimension is associated with a high probability ratio of changes in the sample temperature during exposure to the laser. In this case, the laser's power should be carefully selected and modified to avoid temperature variations. The timing of the measurements is critical; too much exposure of the sample to the laser, especially at high power and taking ten readings for each angle, will lead to different effects. One such effect is the change in sample temperatures between the first (low T) and the last (high T) angle through one scan. Another effect is the change in the sample's concentration between the first (low C) and the last (high C) angle through one scan, where the high power will evaporate some water leading to a higher glucose ratio in greater angles compared to the first angle.

The effect of the temperature on the optical rotation was measured in the commercial polarimetry, for 5.5 mM and pH=7.6 for 22,23,26°C, but there was no accountable difference. However, there are apparent variations in optical rotation with a higher difference in the temperature, such as 10°C difference (see Figure 6.5).

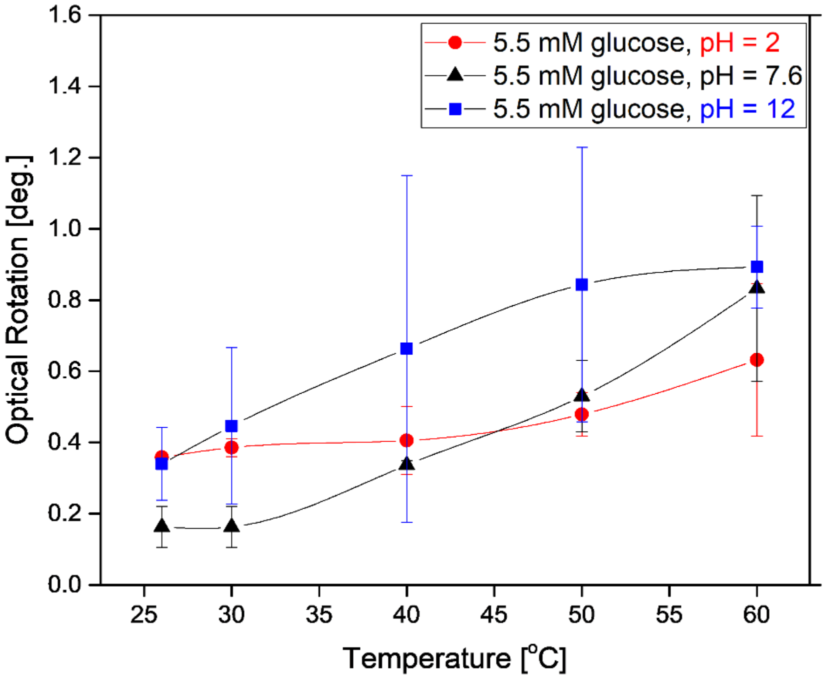

Figure 6.5 Optical rotation of 5.5 mM glucose with the variation of a sample temperature and pH. The vertical error bars show the standard deviation (n=3).

In addition to the contribution of both the pH and temperature to the optical rotation, the pH has a vital role along with temperature variation. The temperature trend is almost increased, but this is higher when the pH increases, especially with pH=12. For example, the optical rotation at 30°C surges from

0.16333 to 0.44667 when the pH increases from 7.6 to 12, respectively (see Figure 6.5).

6.3.3 Application

6.3.3.1 Bovine Serum Albumin (BSA)

The optical activity of proteins, such as the amino acids from which they are built, depends on the pH of the solution, and this outcome deserves special consideration in a study of protein structure based on polarimetric measurements [130]. A study of this effect can throw some light on certain functional groups in the molecule. With the aim of obtaining evidence on the combination mode of proteins with acids and bases, BSA was chosen as the prototype protein in this study and showed the functionality of the built-in system with the fabricated arrangement.

6.3.3.2 Results

The optical rotation has been measured for a different set of protein concentrations using our built-up polarimetry. Thus, 10 cm and 1 cm pathlength cells were initially used to test the system and verify whether it could detect the optical rotation of the protein. The maximum concentration measured was 0.1 mM as it is difficult to prepare (dissolve in water or PBS) this high concentrated BSA (BSA has a high molecular weight). In addition, the goal of the measurement is to study the lowest concentration and volume that the polarimetry can detect and realize the system limit of the detection by using this type of chiral molecule (Albumin from Bovine serum).

After testing the protein, a set of concentrations were measured with pH=7.5 using 403 nm laser, 1 cm cell, and a one pass setup at room temperature (see Figure 6.6).

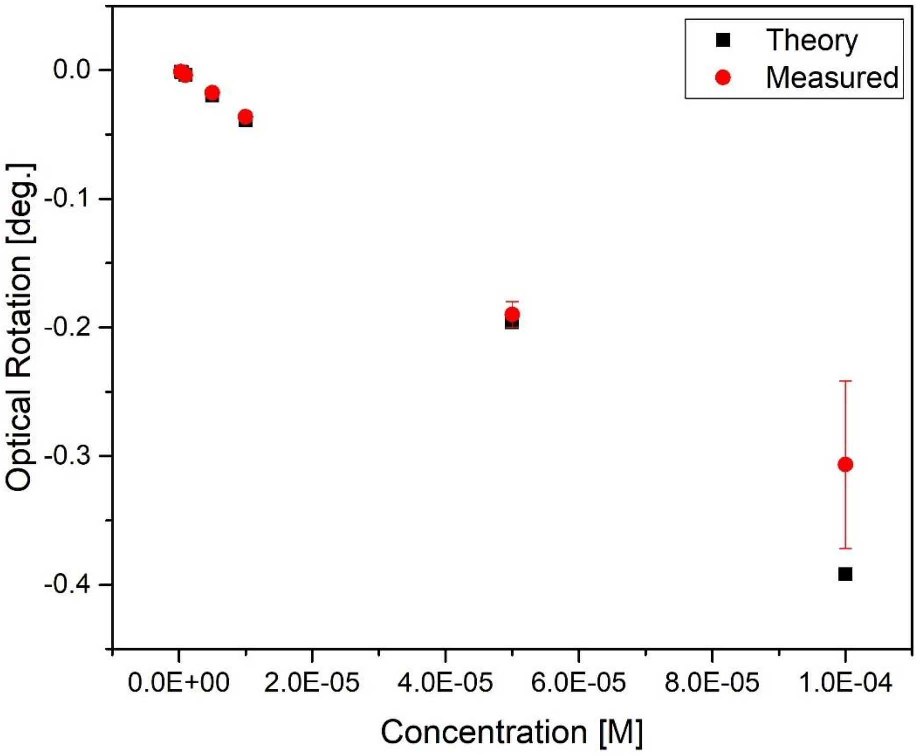

Figure 6.6 Optical rotation of the different set of protein concentrations using a one-pass system, a 403 nm laser, and 1 cm path length. The limit of detection (LOD) in this case is 3E-7 M (300 nM). The vertical error bars show the standard deviation (n=3).

The lowest concentration that the polarimetry can detect is 300 nM. The high variance that can be seen in the measurement of 0.1 mM is due to the scattering of the laser resulting from a high quantity of molecules in the sample of this highly concentrated, high molecular weight BSA.

6.3.3.3 pH with the protein:

With the aim of decreasing the sample's volume and concentration, the pH has been changed for the protein samples. The measurement of optical rotation in the polarimetry system was first done using PBS. However, no optical rotation change has been detected due to the fact that the PBS is a buffered solution and does not impact on the arrangement of the molecules around the chiral centre; consequently, no optical rotation alteration is obvious.

pH values were managed to the protein concentration of 0.1 mM by using the same glucose pH management protocol (NaOH and HCl) for 2,4,6.4,7.5,10, and 12 (via the pH meter). The optical rotation was then measured using a 403 nm diode laser, 1 cm cell, and a one pass setup, at room temperature, as illustrated in Figure 6.7.

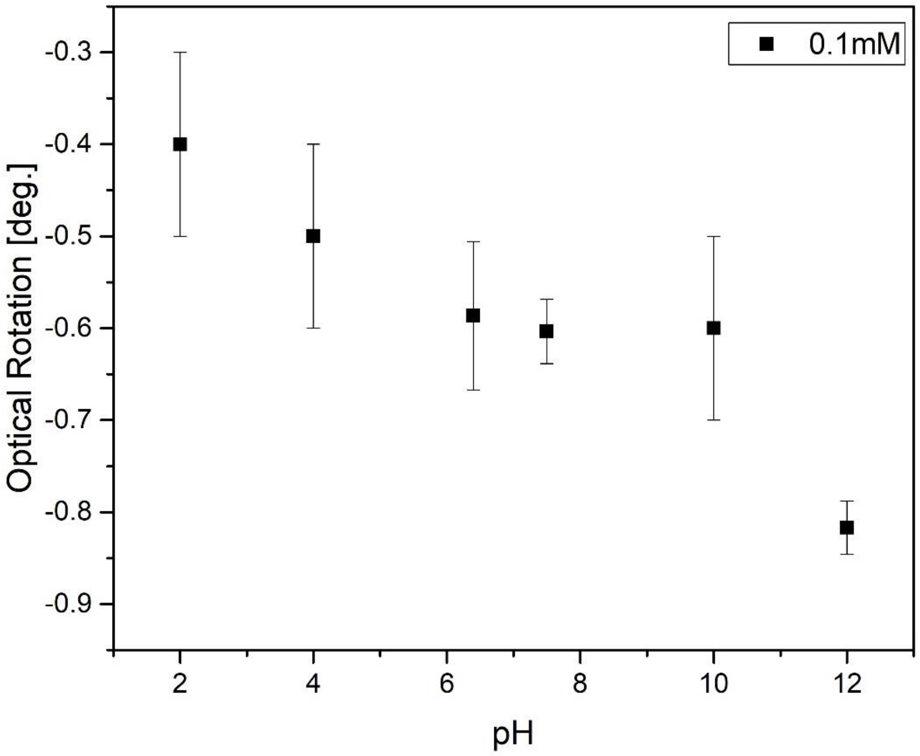

Figure 6.7 Optical rotation of the different set of 0.1 mM BSA for different pH values using a one-pass system, a 403 nm laser, and 1cm path length cell. The vertical error bars show the standard deviation (n=3).

Figure 6.7 shows that the same glucose trend as the optical rotation is increased when the pH values drive to the higher base range. For the protein results taken from 2 to 6.4, a rise in the absolute value of the optical rotation is seen. With a pH change of 6.4, 7.5, to 10, the optical rotation was stable. Thus, a pH of 12 was tested and subsequently, a rise in the optical rotation was observed. The observed change in the optical rotation with the increasing pH needs further confirmation by more pH values, but this effect has been reported in the literature for other chemical constituents [20]. Overall, the results show a substantial swing change in the optical rotation (high standard deviation) for 0.1 mM due to this highly concentrated BSA; this is because it has a high molecular weight that induces the scattering of the laser in the sample.

In the multi-reflections measurement scheme, a built-in reflections device has been used to increase the optical pathlength in the polarimetry system. The optical rotation for different BSA values was measured but using three reflections via the micromirror device - a 1 mm path length capillary rectangular tube, with 403 nm laser, as shown in Figure 6.8.

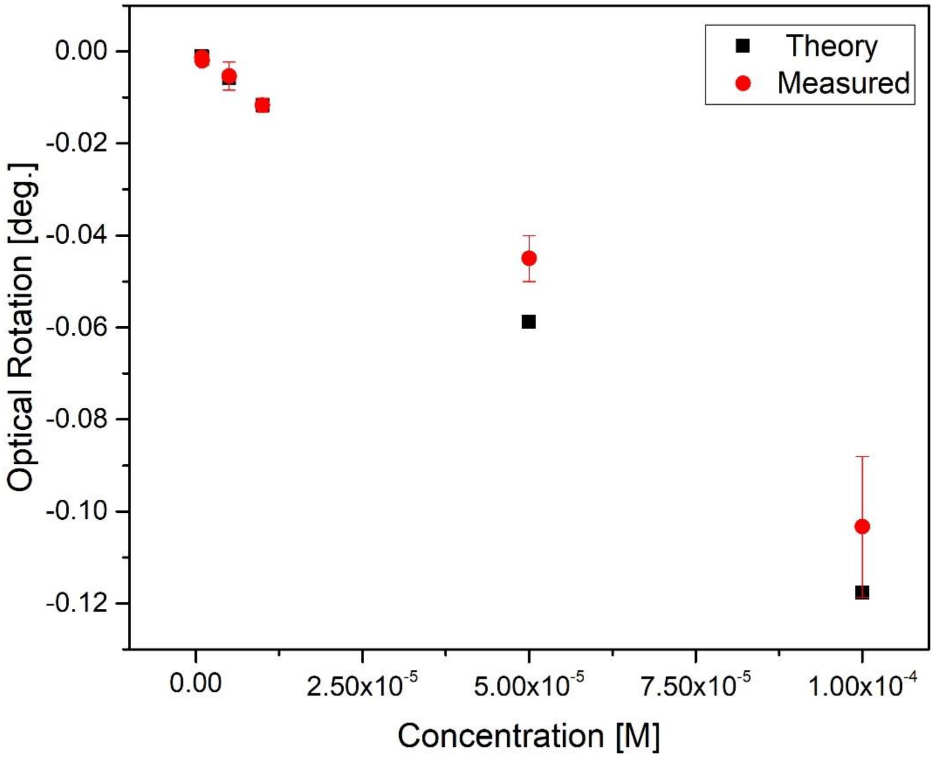

Figure 6.8 Optical rotation of a different set of BSA concentrations using a three pass system with a reflection device, a 403 nm laser, and 1 mm path length. The limit of detection (LOD) in this case is 9E-7 M (900 nM). The vertical error bars show the standard deviation (n=3).

The limit of detection in the three pass scheme and the 1 mm path length is three times more than the one pass system using a 1 cm pathlength (300 nM). However, it is still in the nano molecular (concentration) range and has a lower volume and shorter optical path length. On the other hand, if the measurement is implemented for one pass and at the same optical path length (1 mm), 5E-6 M might be the limit of detection, which is five times more than the LOD of the three reflections scheme. The optical rotation is then measured to 9×10^{-4} mM (the concentration used in the previous work [20]) of BSA for different pH values, a 1 mm path length, blue, using the reflective device (three passes) – see Figure 6.9.

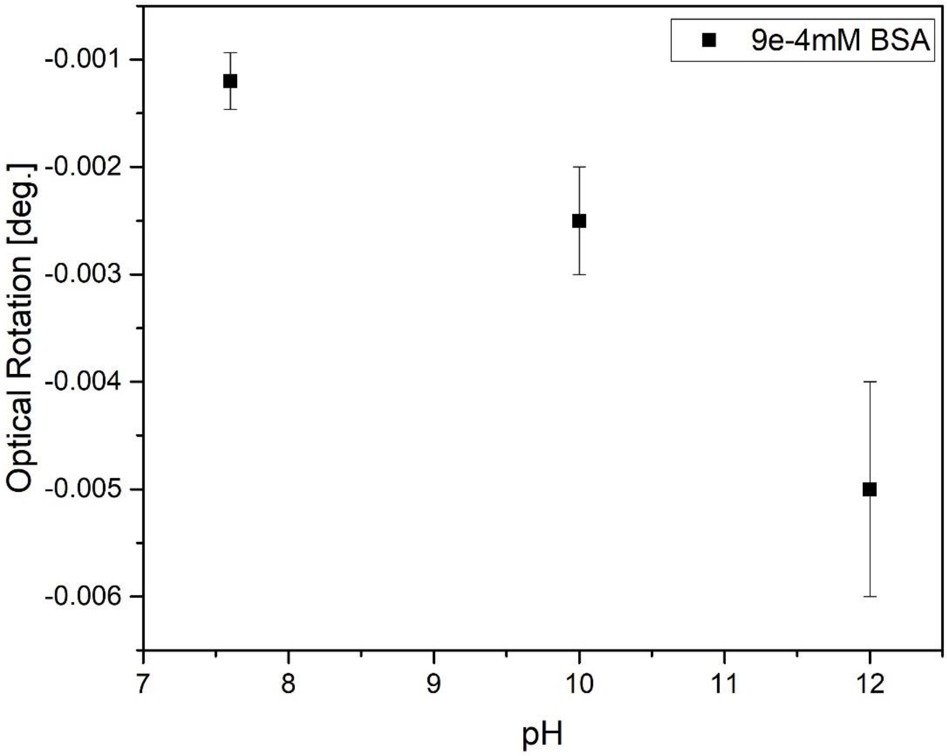

Figure 6.9 Optical rotation of the different set of 9×10^{-4} mM BSA for different pH values using a three pass reflective device, a 403 nm laser, and a 1 mm path length. The vertical error bars show the standard deviation (n=3). The linear correlation is $R^2>0.99$.

Figure 6.9 shows that the optical rotation cannot be measured for this concentration (9×10^{-4} mM) when the pH values are from 2.0 to 6.4, as they are under the limit of the detection for the system. However, it follows the same trend where the optical rotation increases with increasing pH.

6.4 Conclusions

The extra amount of chiral molecule optical rotation required to achieve a greater sensitivity can be added by varying the chiral molecules' pH and temperature.

Several points have to be considered; Phosphate buffered preparations were tried, but it was discovered that the buffer has a great capacity to contract pH effects. Therefore, the effects studied were based on de-ionized water preparations.

It can be concluded that, in both polarimetries (Rig and commercial), the optical rotation of the glucose increased from 0.118° to 0.954° and 1.789° respectively when the pH was changed to 8. Therefore, the specific rotation (and the optical rotation) increased by a factor of 8 when using a 403 nm laser and pH = 8, (specific rotation = 942.64 °/(dl.g/ml), which proves the same specific rotation of the work reported [20]), compared with the same laser wavelength and normal pH (specific rotation = 120.08 °/(dl.g/ml)). In addition, it improved by a factor of 22 compared with the use of a He-Ne laser and a normal pH (42.6°/(dl.g/ml)).

Consequently, the system can detect a glucose concentration down to 56 µM with 11 reflections in 20 µL, which is about 28 times higher than the limit of the best commercial instrument,[31], but was accomplished in three times smaller volume capillary using the blue laser, and increases the pH to around 8.

Regarding the BSA molecules, in the 0.1 mM measurement, and as a test, the LOD was doubled when the pH increased from natural to 12, as the optical rotations increased from 0.4 ° to 0.8 ° respectively.

Temperature can have an effect on the interaction between the chiral substance and light; in most common solutions at room temperatures (20°C) there will not be a noticeable change in the specific rotation. The influence of temperature on the specific rotation value also depends on the wavelength; it can have a drastic effect on the specific rotation of the substance as the wavelength decreases toward the UV range and the trend differs for each chiral substance. In addition, there is a temperature limit for each material, and when exceeding it, the molecular structure will change and the molecule may lose its properties.

Overall, the results show a change in the optical rotation for large swings in temperature and pH. However, there is a considerable optical rotation alteration with every 10°C period temperature variation. The optical rotation increased five times when the temperature increased from room temperature to 60°C. Nevertheless, for the He-Ne laser measurement, the effect is negligible; less than a few temperature degrees and tenths of pH unit variations. The absolute value of the optical rotation rises substantially with temperature and pH, particularly at shorter wavelengths.

Regarding another chiral biomolecule, protein, the system could not measure the 9×10^{-4} mM BSA optical rotation. This was because, when using 1 mm path length and a blue laser, the rotation was lower than the resolution limit (less than 0.001°). However, a reflections device was used to make three reflections to measure the same concentration with the same optical path length and environment. This enabled the system to reach the LOD of the device as the optical rotation increased with the increased optical path length (triplite). This is an addition to less volume (2 µl) and a shorter optical path length (1 mm) than used in other work [20]. In other work, they used 1 cm path length and the specific rotation of BSA, 590°/(dl.g/ml).

In summary, the LOD of our system using a BSA sample is 0.9 µM (115 ng) in a 2 µl microchannel via a reflective device (three reflections). This is about two times less than the limit of the best commercial instrument, [31], and was accomplished in 27 times smaller volume.

Chapter 7 Conclusions and Future Work

7.1 Conclusions

In this work, we have overcome the problems associated with short optical path lengths, inherent in microfluidic systems, by using micromirrors to create multiple reflections across a capillary channel. By using an external configuration of mirrors that gave *two* reflections before passing through the sample, we negated the 180° flipping of the polarization that normally occurs following single reflections. We demonstrate that, for a He-Ne laser, we can enhance the detection limit of D-(+)-glucose by ~30 times after only 11 passes. We also demonstrated that, by using shorter wavelength sources, we could further reduce the limit of detection. Further studies using an intense, collimated beam need to be realized before further advantages can be identified using multiple reflected light for the measurement of optical activity.

Multi-reflection polarimetry enables the use of small volumes (2 μL) compared with commercial polarimetry (ml), so microfluidics becomes available with acceptable accuracy for this microvolume. Therefore, expensive and precious chiral samples could be used like heterometallic complex [133] and zinc borate [134].

In the micro-mirrors fabrication, we show results demonstrating the development of high quality wet etch fabricated sidewalls in monocrystalline silicon. High quality 45° and 90° sidewalls have been achieved by varying the etch chemistry while using the same mask. The surface tension has an adverse effect on the 45° slanted wall while it is preferable to attain the vertical etched wall from the same window direction. Surfactant and alcohol are crucial in achieving smooth sidewalls. KOH has a high etch rate which is suitable for high throughput micromirror device applications. Using this fabrication technology, we have created a platform which can find a range of opto-microfluidic applications in the future, enabling multiple reflections to increase the optical path length. It is anticipated that this type of device could enable low cost, scalable optofluidic technologies in spectroscopic measurements within clinical, biomedical and environmental sciences.

Using this fabricated reflection device in the polarimetry system, the limit of detection for three passes was 1.8 mM, which is a threefold improvement compared to the one pass arrangement results. This is approximately the same comparison for the 2 mm cube mirror results for three passes but exhibits up to 10 times less sample volume (20 µL in a capillary tube when using cube mirrors and 2 µL when using the fabricated multi-reflections device).

Regarding the pH effect, it can be concluded that, in both polarimetries (Constructed and commercial), the optical rotation increased from 0.118° (theoretical) to 0.954° and 1.789° respectively, when the pH was changed from neutral to 8. Therefore, the specific (and optical) rotations increased by a factor of eight when using a 403 nm laser and pH = 8 compared with the same wavelength laser and normal pH (specific rotation= 120.08°/(dl.g/ml)). Also, it improved by a factor of 22 compared to the He-Ne laser and neutral pH (42.6°/(dl.g/ml)). So we can detect a concentration down to ~ 56 µM with 11 reflections in a 20 µL capillary using the blue laser, and an increased pH at around 8; however, it went down to 115 ng in a 2 µl sample via three reflections (9 µM) using the fabricated multi-reflection mirror device.

7.2 Future work

Building on this work, it was found that using a cavity ring, the optical path length could be much longer [45]. However, this, in turn, required a more stringent measuring procedure to determine the optical rotation via the frequency shift of each signal. Using this, it was demonstrated in a preliminary study, that by introducing an analysis system with different photodetectors, like the balanced detector, we could potentially simplify the measurement, [135], [136], of the optical rotation. It is proposed to use a loop mirror as an interferometer via a fibre loop, leaving the other intracavity components dependant on the preferable optical path length. The optical-rotation symmetry is broken by the presence of both chiral and Faraday birefringence, giving rise to signal reversals which allow rapid background subtractions.

If we suppose that the Faraday rotates 3°, and the chiral molecules rotates 1° (For a specific molecules and optical path length), the operation of this system will be like:

$\Theta cw=3+1=4^{\circ}$ (Counter wise)
$\Theta ccw=3-1=2^{\circ}$ (Counter clockwise)

$\Theta final=4-2=2$ (which is supposed to be for two passes through the chiral molecules, and there is no cancelation here)

So, in general:
$(\Theta f+ \Theta c)\, n = A$ (Counter wise)
$(\Theta f- \Theta c)\, n = B$ (Counter clockwise)

Where n is the number of passes, Θf is the Faraday rotation angle, chiral optical angle (rotation).

$SUB=A-B= \Theta f\, n+ \Theta c\, n- \Theta f\, n+ \Theta c\, n=2\, \Theta c\, n$
So,

$$\Theta c = \frac{SUB}{2n}$$

Measuring the sensitivity of optical rotation on fringe supports has been demonstrated [31]. However, this method utilised a He-Ne laser and only one reflection. Therefore, following the fabricated multi-reflection structure on the microchip support, the structural micromirrors' integrity in polarimetry with more than one reflection can be detected using a fringes approach. This would enable better-anticipated enhancements to the polarimetry system by utilising a smaller volume and detection of lower concentrations.

Furthermore, detailed lock-in amplifier scans of the input signals were provided following amplification, and weak signal detection on the output signal [137]. A preliminary study carried out in this work showed that the lock-in amplifier could detect the weak signals among lots of signals and noises [68]. This work has the potential for the design of platforms that can allow the use of nanomolar chiral molecules to support weak signal detection via this amplifier.

It was also analytically apparent that the more the reflections from a mirror's surface, the better the optical rotation length. As such, more work needs to be carried out to determine how closed mirror fabrication can be accomplished, and to explore possible ways to stabilise the structures following their alignment onto narrower zigzag micromirrors. In addition, improving the surface morphology by optimising the wet etching process will result in highly reflective mirrors [76]. These, in turn, will provide less distortion, as the beams will be close to each other and consequently also address the misalignment and low reflectivity issues.

Another future suggestion building on this cavity is the use of anisotropic material, such as lithium niobate ($LiNbO_3$) crystal, as a material [138] to amplify the polarisation rotation. This would help to overcome the small optical rotation inherited by a low concentration and/or the short optical path length in the microfluidic optical sensor.

Appendices

Appendix A Programming Enhancements

A.1 Modify the LabVIEW Code

A.1.1 Programming (real time)

LabVIEW code was improved to control both the motorised stage mount of the analyser and the power meter, see Figure A.1, to fit with the polarimetry setup measurements. The code was able to synchronise their operation and achieve accurate results. Even a small fraction of a second of timing running delay between them leads to a significant error in the results. This was resolved using LabVIEW as shown in the following developments:

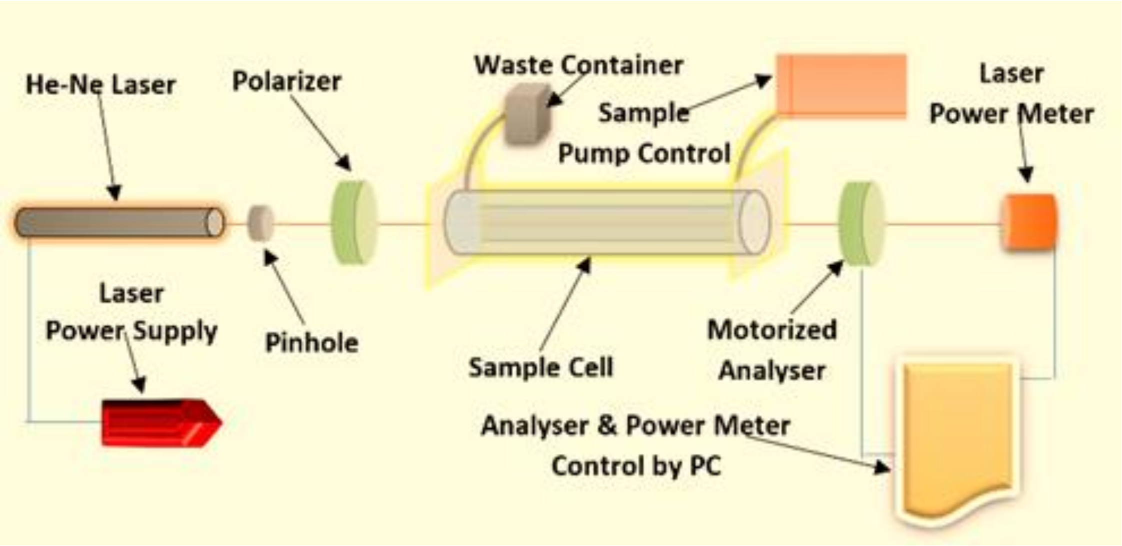

Figure A.1 Block diagram of polarimetry setup components.

A.1.1.1 Running the powermeter code:

This code demonstrates the ability to connect, acquire data and disconnect from the power meter via the LabVIEW program. Three VI's were used to apply these operations as shown in the flowchart – see Figure A.2.

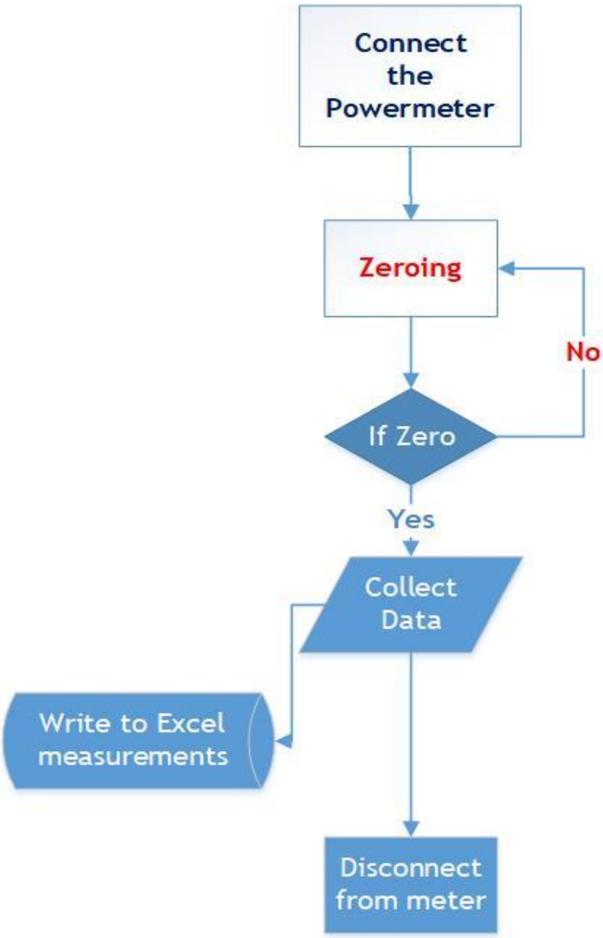

Figure A.2 Block diagram of main processes in the powermeter LabVIEW code

A.1.1.2 Running the Motorized Stage of Analyser Code:

The motorized stage was initialized using it’s original software to initialize the motorized stage and then using its LabVIEW code, as shown in flowchart – see Figure A.3.

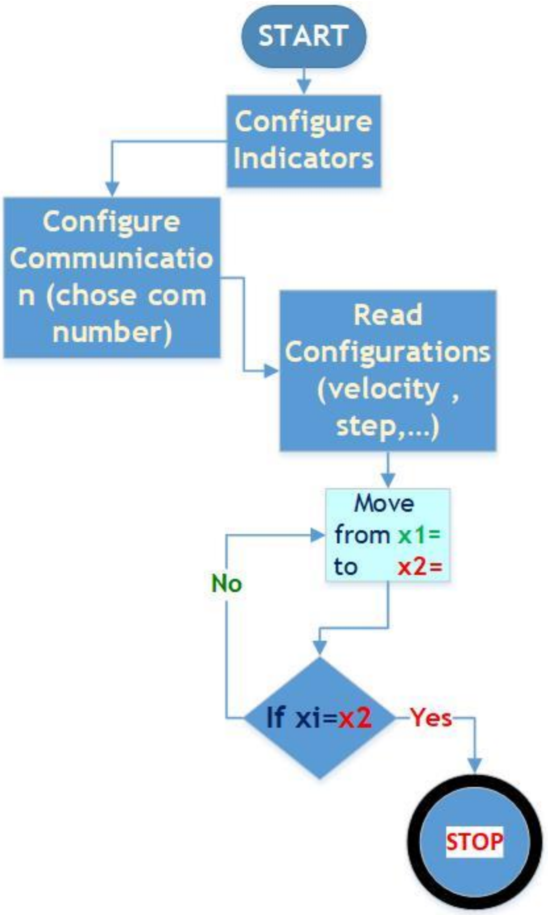

Figure A.3 Block diagram of main processes in motorized mount code.

A.1.1.3 Programming Both the Motorized Analyzer Mount Code and the Powermeter Code to Run them at the Same Time:

One code was designed to synchronize the running operations of the motorized mount of the analyzer with the power meter. First of all, a loop was created in the powermeter code to read several times (such as five and ten readings) for each step of the motorized stage. A Write to Excel Measurement and Appended Array commands were also utilised in this code to obtain and observe the measured power data as shown in Figure A.4.

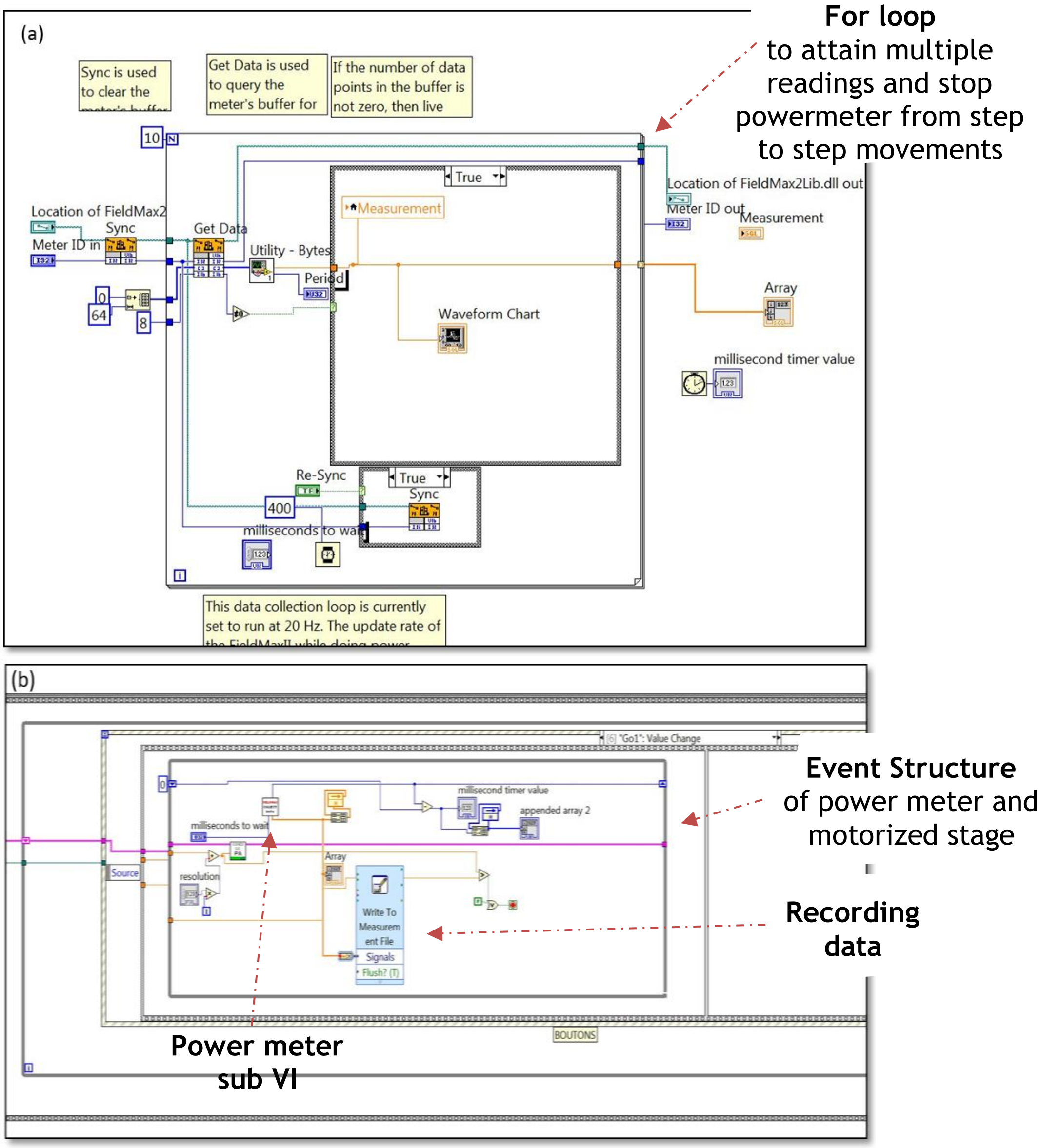

Figure A.4 Block diagrams of a) Powermeter code enhancements, b) Synchronization of the power meter and motorized codes in addition to the resolution of movement.

Secondly, the code of power meter was introduced inside the motorised stage code, exactly in the step movement event structure. This step allowed measuring the power for a specific step movement in real time as shown in Figure A.4 and flow chart in Figure A.5. The third step was the introduction of the Connect the Powermeter and Zeroing VIs, as sub VIs, in the motorized stage code by creating them in the new event structures in the motorized stage code and presenting them as buttons in the main front panel, as shown in Figure A.5.

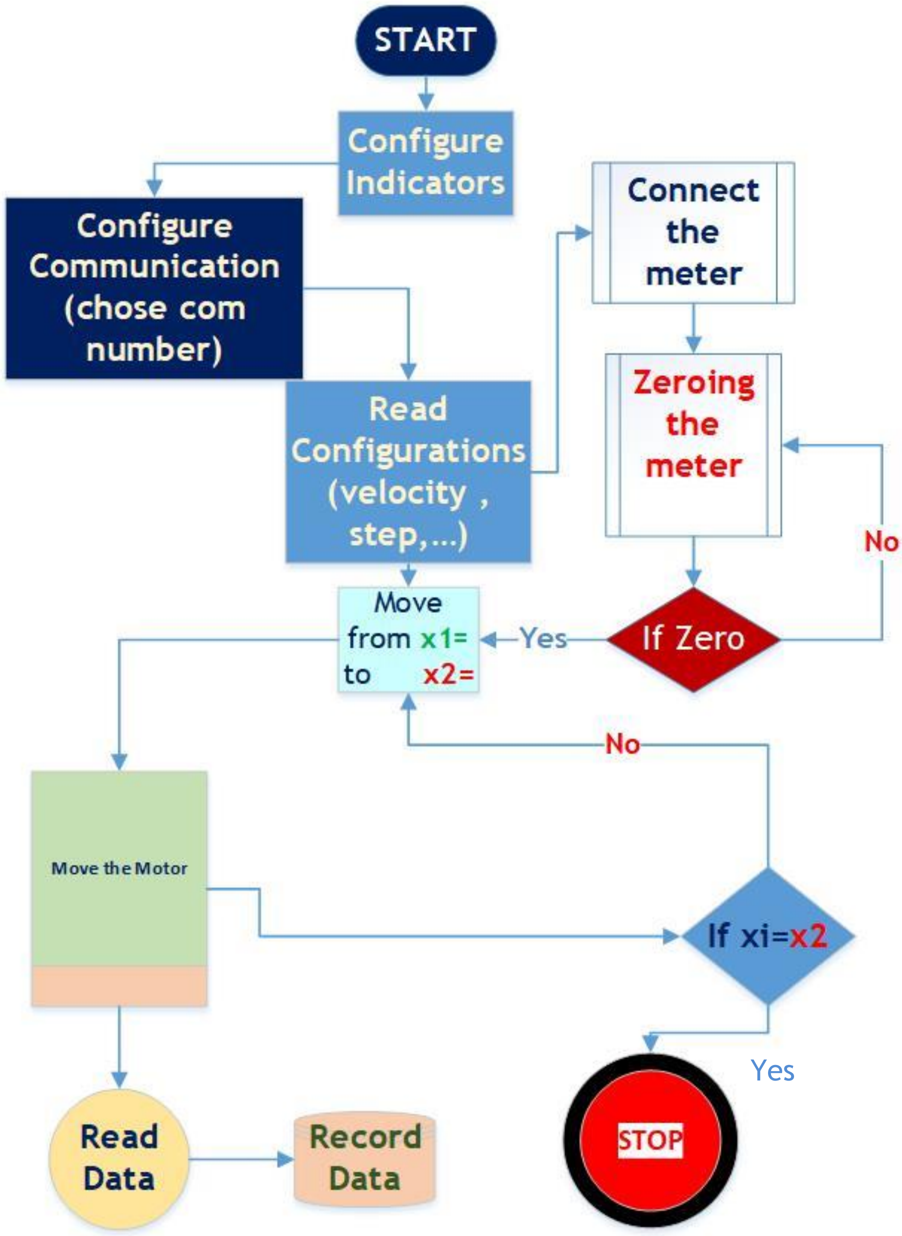

Figure A.5 Block diagram of LabVIEW code of synchronized running the power meter with the motorized mount of the analyzer.

A.1.1.4 Multiple readings in one movement and resolution Labview code modifications

In order to reduce the influence of laser fluctuation on the results, LabVIEW code was altered to be able to measure a different number of readings for each angle of analyzer mount and then take the mean for each set of specific readings. This was done by using a For Loop command in the power meter sub VI as shown in flow chart – see Figure A.6, then data analysis code was written using Matlab software to average these recorded data at each step before fitting them, as shown in sections A.4-7.

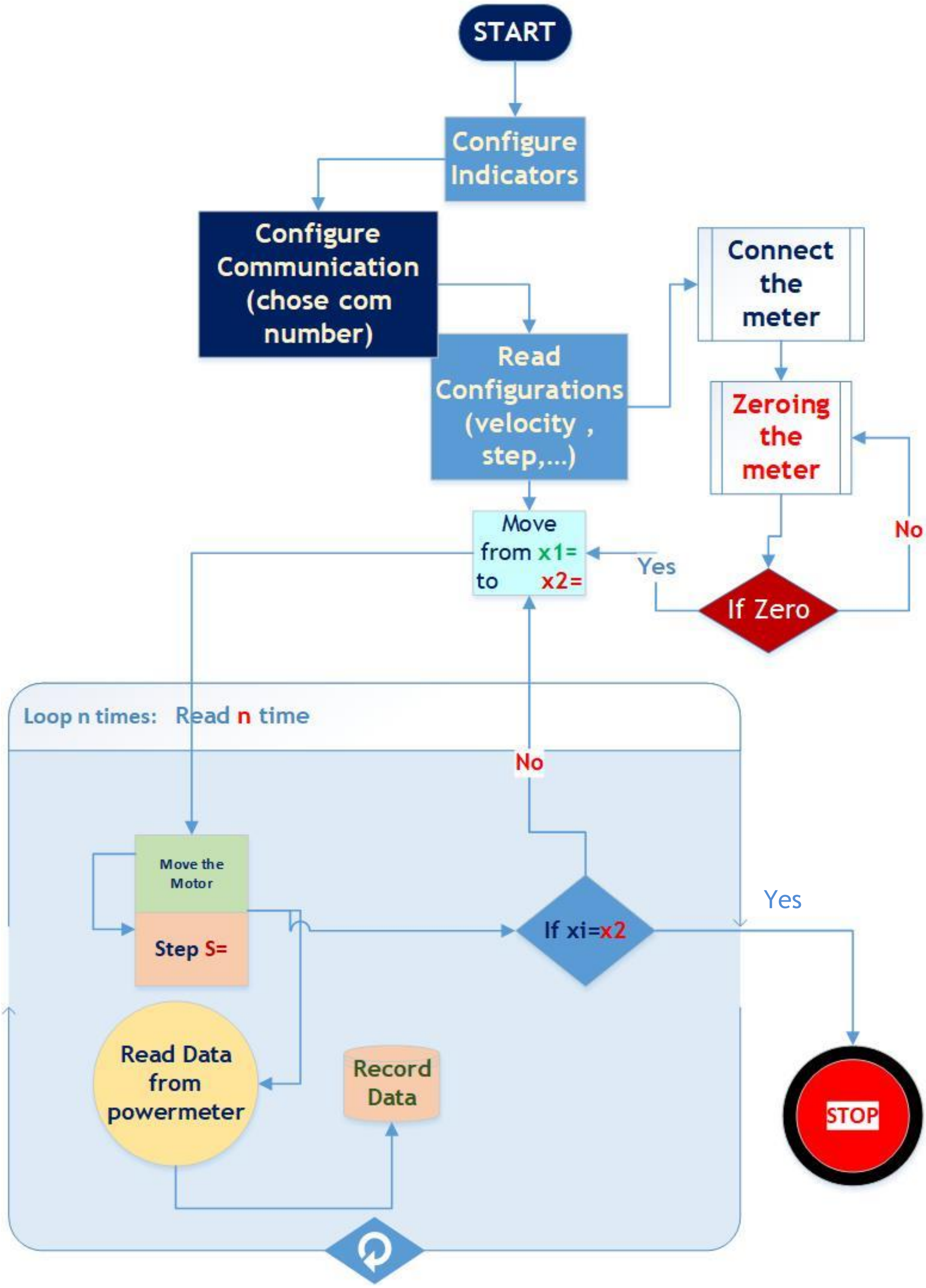

Figure A.6 Block diagram of Labview code of synchronized running of the powermeter with the motorized mount of the analyzer. Acquiring a different number of readings and controlling the resolution of the movements are also shown in this flowchart.

Low concentrations detection (in μM), require a small movement step size of the analyzer mount, which was achieved by manipulating the motorized mount code of the analyzer and introducing the resolution button in the same moving and reading loop to allow scanning very small step size (up to 1 millidegree) which is crucial in microfluidic measurements, as shown in Figure A.4 and Figure A.7.

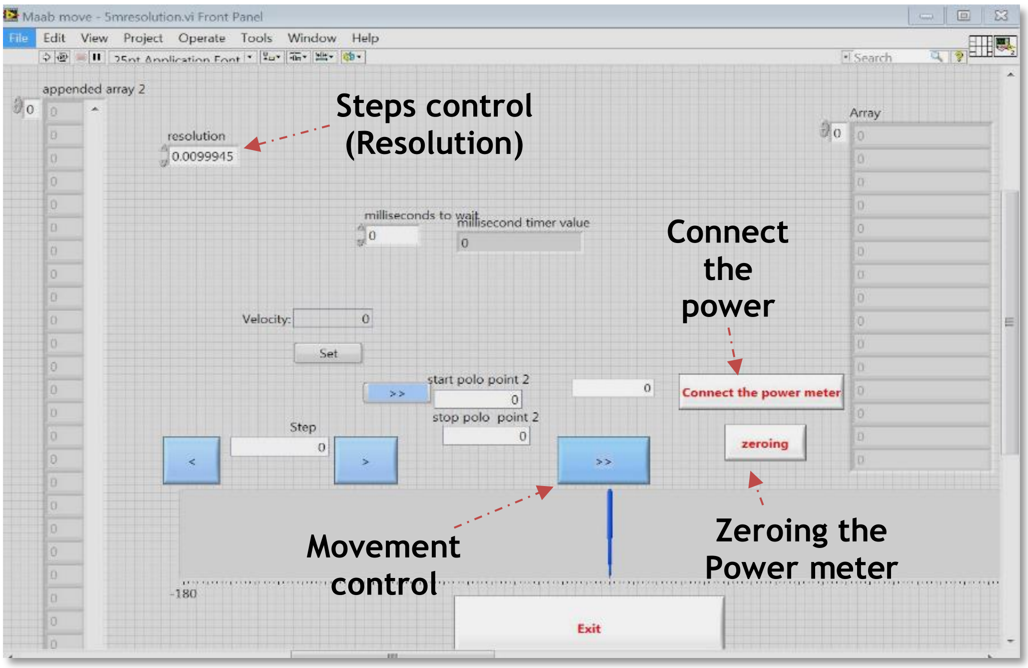

Figure A.7 LabVIEW front panel of synchronization the power meter with motorized stage codes in addition to the resolution of movement.

A.1.2 Increasing the speed of LabVIEW code

LabVIEW code required 10 seconds to move one step (10 recorded readings). This was required a long time to implement the full scan of the analyzer. It depends on the step size as well as the number of readings for each step, as shown in Table A.1.

Table A.1 Timing of measurements for different angle steps and a number of readings for each angle. The time for each scan depends on the specifications of both power meter and the motorized mount of the analyzer. While the required real time is longer than these values. Depending on several parameters; LabVIEW read and write process, motorized mount moving time, and step size.

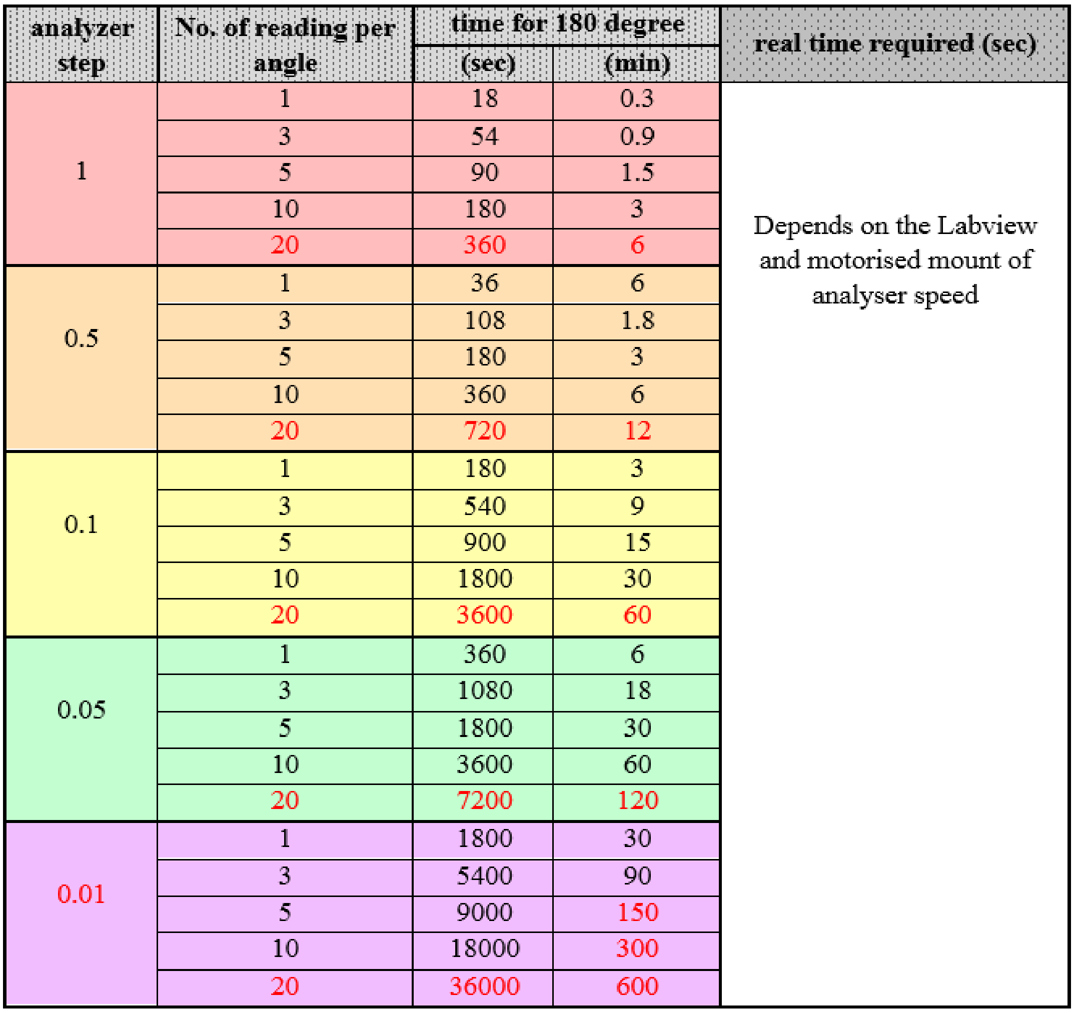

analyzer step	No. of reading per angle	time for 180 degree (sec)	time for 180 degree (min)	real time required (sec)
1	1	18	0.3	Depends on the Labview and motorised mount of analyser speed
	3	54	0.9	
	5	90	1.5	
	10	180	3	
	20	360	6	
0.5	1	36	6	
	3	108	1.8	
	5	180	3	
	10	360	6	
	20	720	12	
0.1	1	180	3	
	3	540	9	
	5	900	15	
	10	1800	30	
	20	3600	60	
0.05	1	360	6	
	3	1080	18	
	5	1800	30	
	10	3600	60	
	20	7200	120	
0.01	1	1800	30	
	3	5400	90	
	5	9000	150	
	10	18000	300	
	20	36000	600	

This has an adverse effect on the measurements in two aspects. Firstly, it is time consuming as it takes about 35 minutes for whole analyzer stage rotation, if the increment of analyzer rotation is 1°, for one sample measurements (half rotated scan; 180°). Secondly, an error in the measurements of the polarization angle is possible as it depends on the power; the power drift of the He-Ne laser is 5% per eight hours as in the He-Ne laser specifications. Thus, a shift for the third sample might not be accurate (real) as it underwent this drift in power (0.345 mW). For a diode laser (403 nm) the drift is <0.5% over 48 hours, but it has fluctuation that makes the measurement not accurate for long period measurements. Specifically, in He-Ne laser, the drift power appears early (before the supposed time in the laser specifications), as shown in Appendix C.

To tackle this, Labview was modified to take about 12 minutes for the whole analyser stage rotation (four seconds per step). The second approach to reduce the noise influence was by scanning a few ranges of angles around the trough, to determine a shift of the specific concentration. This will decrease the consumed time dramatically. For example, scanning 30 steps as 15 angles before and after the minimum power (trough) will consume two minutes only and will not affect the fitting of the curve. In addition, the scan of a few angles appeared to provide more accurate results than a full scan – see figure (1-4). The error was reduced down to 8%, as by the measurements which were implemented for the same concentrations but using the two approaches.

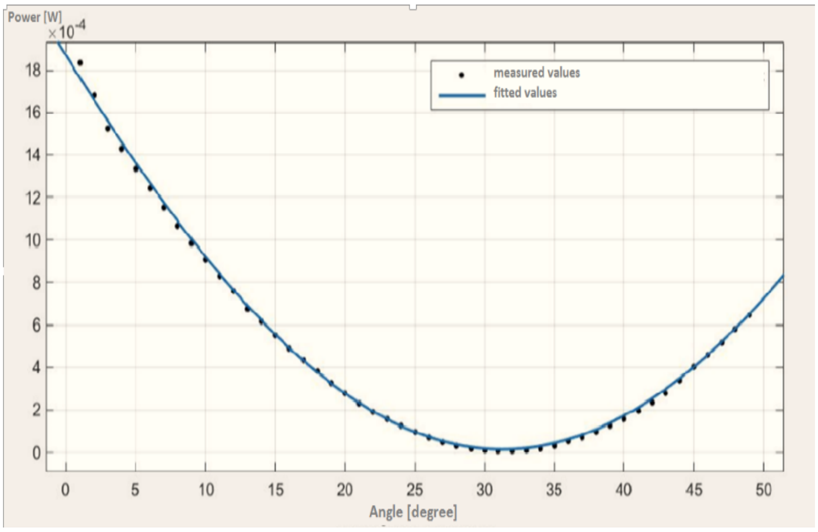

Figure A.8 Curve fitting of polarimetry output power for a few angles scan around the trough.

A.2 Enhancement of the Curve Fitting using Matlab Code

Matlab code was established to acquire the data from LabVIEW and make averaging for different readings. The most essential step in this Matlab code was the use of the curve fitting tool and calculating the phase shift for each sample (optical rotation).

The Curve Fitting tool is vital to reduce the errors in readings and calculate the rotation angle for each concentration related to the reference (water). The power meter records the variation of laser power corresponding to analyzer rotation in specific selected step size. In theory, for a linear polarizer, the ratio of light intensity from the analyzer to the input intensity should obey a square cosine function of the analyser angle (Malus's law). This allows data to be fitted with a Matlab curve fitting tool, as shown in equation (A.1) and Figure A.9.

$$y = a * \cos(\frac{\pi * (x + c)}{90}) + d \tag{A.1}$$

Where: y : power [W], a : amplitude [W], x : angle [degree], c : angle shift (rotated angle) [degree], d : vertical offset [W].

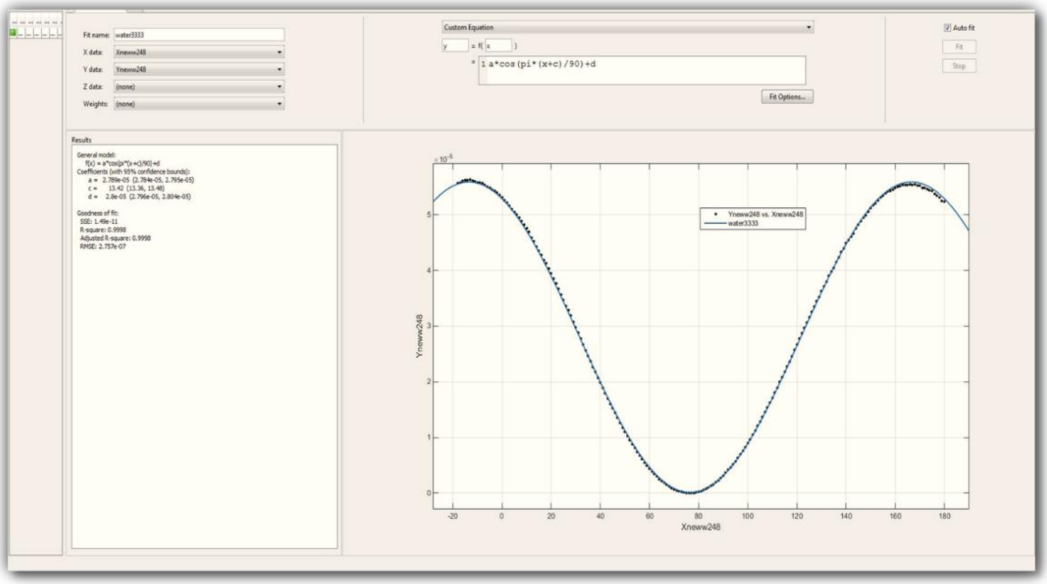

Fit name: water3333
X data: Xneww248
Y data: Yneww248
Z data: (none)
Weights: (none)

Custom Equation
y = f(x)
= 1 a*cos(pi*(x+c)/90)+d

☑ Auto fit

Results

```
General model:
  f(x) = a*cos(pi*(x+c)/90)+d
Coefficients (with 95% confidence bounds):
    a =  2.789e-05  (2.784e-05, 2.795e-05)
    c =      13.42  (13.36, 13.48)
    d =    2.8e-05  (2.796e-05, 2.804e-05)

Goodness of fit:
  SSE: 1.49e-11
  R-square: 0.9998
  Adjusted R-square: 0.9998
  RMSE: 2.757e-07
```

Figure A.9 Curve fitting tool in Matlab.

A.3 Data Acquisition Matlab code

Data averaging, calculating the rotation angle, and noise generation

```
clc;
clear;
close all;
DD=xlsread('C:\Users\2144019A\Desktop\matlab new final\theory waterr and 10mM
(1)');
df=1810          % degree of freedom(no. of readings)
ave=10           % No. of average
nl=0             % noise level
Yw=DD(1:df,7);   % power values of water
Xw=DD(1:181,1);  % angle of analyzer for water
Yg=DD(1:df,3);   % power values of glucose
Xg=DD(1:df,1);   % angle of analyzer for water
```

```
num_p=df/ave;    % numper of scan angles
l_noise=nl/100; % percentage value of noise level
v_noise=l_noise*max(Yw);  % percentage value of noise level according to maxixmum
power

for i=1:num_p
    k=i-1;
    Ynw(i)=mean(Yw(k*ave+1:i*ave));  % Water average power values ( power / ave)

    Yng(i)=mean(Yg(k*ave+1:i*ave));  % Glucose average power values ( power /
ave)
end
%Xnw=linspace(0,pi,num_p);
Xnw=Xw'*pi/180;     % analyzer angle for water in radain

for j=1:1
    yw_noise=rand(1,num_p)*v_noise; % generated randum noise in water case
    Ynnw=(Ynw+yw_noise)-v_noise/2;  % water power with noise

    [fitresult, gof] = createFit1(Xnw, Ynnw); % call fit cod for water
    A1=coeffvalues(fitresult);
    aw(j)=A1(1);
    bw(j)=A1(2);
    cw(j)=A1(3);
B1= struct2cell(gof);
B2=cell2mat(B1);
SSEw(j)=B2(1);
R_squarew(j)=B2(2);
  RMSEw(j)=B2(5);
end
Xng=Xg'*pi/180;   % analyzer angle for glucose in radain
for j=1:1
    yg_noise=rand(1,num_p)*v_noise; % generated randum noise in glucose case
    Ynng=(Yng+yg_noise)-v_noise/2;  % Glucose power with noise

    [fitresult, gof] = createFit2(Xnw, Ynng); % call fit cod for glucose
    A1=coeffvalues(fitresult);

    ag(j)=A1(1);
    bg(j)=A1(2);
    cg(j)=A1(3);
B1= struct2cell(gof);
B2=cell2mat(B1);
SSEg(j)=B2(1);
R_squareg(j)=B2(2);
  RMSEg(j)=B2(5);
  SSEg(j)=B2(1);
end
% results and statistical values
SSEmaxw=max(SSEw)
R_squareminw=min(R_squarew)
bminw=min(bw)
bmaxw=max(bw)
rmsemaxw=max(RMSEw)
brangew=max(bw)-min(bw)
noisemaxmw=max(yw_noise)
SSEmaxg=max(SSEg)
R_squareming=min(R_squareg)
bming=min(bg)
bmaxg=max(bg)
rmsemaxg=max(RMSEg)
brangeg=max(bg)-min(bg)
noisemaxmg=max(yg_noise)
           %fluc.[mW]  RMSE         R^2     SEE   b  [rad]     dltab]
resultw= [noisemaxmw rmsemaxw R_squareminw  SSEmaxw  bmaxw bminw brangew ]
resultg= [noisemaxmg rmsemaxg R_squareming  SSEmaxg  bmaxg bming brangeg ]
rotation= [(bmaxw-bming)*180/pi]    % angle of rotation in degree
```

```
ycc=Ynnw';
plot(Xnw,Ynnw,'r',Xnw,Ynnw,'--b')
%plot (Xw,Yw,'r',Xw,Yg,':')
```

A.4 Optical Rotation Calculation Matlab Code

A.4.1 Create fit for water

```
function [fitresult, gof] = createFit(Xw, Yw)
%CREATEFIT(Xw,Yw)
%  Create a fit.
%
%  Data for 'untitled fit 1' fit:
%      Xw Input : Xw
%      Yw Output: Yw
%  Output:
%      fitresult : a fit object representing the fit.
%      gof : structure with goodness-of fit info.
%
%  See also FIT, CFIT, SFIT.

%  Auto-generated by MATLAB on 03-Apr-2016 17:58:33


%% Fit: 'untitled fit 1'.
[xwData, ywData] = prepareCurveData( Xw, Yw );

% Set up fittype and options.
ft = fittype( 'aw*cos(xw+bw)*cos(xw+bw)+cw', 'independent', 'xw', 'dependent',
'yw' );
opts = fitoptions( 'Method', 'NonlinearLeastSquares' );
opts.Display = 'Off';
opts.Lower = [0 -Inf -Inf];
opts.StartPoint = [0.290791905469756 0.209161556210855 0.694828622975817];

% Fit model to data.
[fitresult, gof] = fit( xwData, ywData, ft, opts );
```

A.4.2 Create fit for glucose

```
function [fitresult, gof] = createFit(Xg, Yg)
%CREATEFIT(Xg,Yg)
%  Create a fit.
%
%  Data for 'untitled fit 1' fit:
%      Xg Input : Xg
%      Yg Output: Yg
%  Output:
%      fitresult : a fit object representing the fit.
%      gof : structure with goodness-of fit info.
%
%  See also FIT, CFIT, SFIT.

%  Auto-generated by MATLAB on 03-Apr-2016 17:58:33


%% Fit: 'untitled fit 1'.
[xgData, ygData] = prepareCurveData( Xg, Yg );

% Set up fittype and options.
ft = fittype( 'ag*cos(xg+bg)*cos(xg+bg)+cg', 'independent', 'xg', 'dependent',
'yg' );
opts = fitoptions( 'Method', 'NonlinearLeastSquares' );
opts.Display = 'Off';
opts.Lower = [0 -Inf -Inf];
opts.StartPoint = [0.290791905469756 0.209161556210855 0.694828622975817];

% Fit model to data.
[fitresult, gof] = fit( xgData, ygData, ft, opts );
```

A.5 Matlab code of output polarization for multi-reflections polarimetry setup

A.5.1 Matlab code for polarimetry system using Metal mirrors:

```
clc;
clear all;
%refractive index and extinction coefficient of the metal mirror (silver)
n=0.2;
k=3.4;
%incident angle
thi=5*pi/180;
%Imaginary refractive index(metal)
h=(((n+1i*k)^2)-((sin(thi))^2))^0.5;
%Refiactivity of s and p components
rs =(cos(thi)-h)/(cos(thi)+h)
rp =(h-(((n+1i*k)^2)*cos(thi)))/(h+(((n+1i*k)^2)*cos(thi)))
%Path length, specific rotation and concentration
 l= 1;
 alfa_c=42.6*pi/180;
 C= 0.18;
%Polarization angle of light, polarizer, and analyzer
 thetalight= 90*pi/180;
 thetapol=90*pi/180;
 thetaanal=(90-7.66)*pi/180;
 %Jon Matrix polarization of the input light
 L=[cos(thetalight);sin(thetalight)]
%Jon Matrix polarization of the polarizer
 P=[cos(thetapol)*cos(thetapol)
cos(thetapol)*sin(thetapol);cos(thetapol)*sin(thetapol)
sin(thetapol)*sin(thetapol)]
%Jon Matrix polarization of the chiral molecules
 Rot=[cos(alfa_c*l*C) sin(alfa_c*l*C);-sin(alfa_c*l*C) cos(alfa_c*l*C)]
 Jon Matrix representations of the s and p component
 R=[-rp 0;0 rs]
%Jon Matrix polarization of the analyzer
 A=[cos(thetaanal)*cos(thetaanal)
cos(thetaanal)*sin(thetaanal);cos(thetaanal)*sin(thetaanal)
sin(thetaanal)*sin(thetaanal)]
 %Jon Matrix polarization of the output light
 S=A*Rot*R*R*Rot*R*R*Rot*P*L
%Absolute rotation
 v=abs(S)
%phase shift
 qqs=atan(imag(S)./real(S))
```

A.5.2 Matlab code for polarimetry system using Dielectric mirrors:

Matlab code of polarimetry using metal mirror in A 3.1 was developed to measure polarization rotation of the same polarimetry setup but using dielectric mirror.

```
clc;
clear all;
%refractive index and extinction coefficient of the dielectric mirror
n=1.46;
```

```
k=3.4;
thi=45*pi/180;
h=(((n)^2)-((sin(thi))^2))^0.5;
rs =(cos(thi)-h)/(cos(thi)+h)
rp =(h-(((n)^2)*cos(thi)))/(h+(((n)^2)*cos(thi)))

 l= 1;
 alfa_c=42.6*pi/180;
 C= 0.18;
 thetalight= 45*pi/180;
 thetapol=90*pi/180;
 thetaanal=90*pi/180;

 L=[cos(thetalight);sin(thetalight)]
 P=[cos(thetapol)*cos(thetapol)
cos(thetapol)*sin(thetapol);cos(thetapol)*sin(thetapol)
sin(thetapol)*sin(thetapol)]
 Rot=[cos(alfa_c*l*C) sin(alfa_c*l*C);-sin(alfa_c*l*C) cos(alfa_c*l*C)]

 R=[-rp 0;0 rs]
 A=[cos(thetaanal)*cos(thetaanal)
cos(thetaanal)*sin(thetaanal);cos(thetaanal)*sin(thetaanal)
sin(thetaanal)*sin(thetaanal)]

 S=R*R*R*R*P*L
```

A.6 Matlab code to calculate the polarization rotation in sensitive region of rotation

```
lvwf=xlsread('C:\Users\bg7\Documents\LabVIEW Data\2ml1M+500ml10-4RB old setup2
10-1-17');
m1=lvwf(1:182,1);
N=182-1;
T=1;
M=1000;
s1=data238;
s2=data236;
lvwf2=xlsread('C:\Users\bg7\Documents\LabVIEW Data\water old setup 10-1-17');
m2=lvwf2(1:182,1);
X=fft([s1(2:end)'-mean(s1(2:end));zeros(N,1)]);Y=fft([s2(2:end)'-
mean(s2(2:end));zeros(N,1)]);
Cyx=Y.*conj(X);
Cyx_anal=[Cyx(1);2*Cyx(2:N);Cyx(N+1);zeros(2*M*N-N-1,1)];
cyx_anal=fftshift(ifft(Cyx_anal))*M*T;
[peak,m]=max(abs(cyx_anal));
t_g=(m-M*N-1)*T/M
function tg=time_delay(s1,s2,M,T)
N=numel(s1);
X=fft([s1;zeros(N,1)]);Y=fft([s2;zeros(N,1)]);
Cyx=Y.*conj(X);
Cyx_anal=[Cyx(1);2*Cyx(2:N);Cyx(N+1);zeros(2*M*N-N-1,1)];
cyx_anal=fftshift(ifft(Cyx_anal))*M*T;
[peak,m]=max(abs(cyx_anal));
tg=(m-M*N-1)*T/M;
```

A.7 Auto-scale Error Compensation Matlab code

Matlab code was created to alter and compensate the voltage output fluctuation due to auto-scale error, as shown in .

```
%assumes data is in an array called data1
%need to change the values in the scale array below to correspond to the
%values measured using the static/constant power measurements
lbvd=xlsread('C:\Users\2144019A\Documents\LabVIEW Data\polarimetry vol 01M5 9-11-16');
data1=lbvd(1:360,1);

scale(1)=1; scale(2)=0.1; scale(3)=0.01; scale(4)=0.001;
scale(5)=0.0001; scale(6)=0.00001; scale(7)=0.000001;
jumpfactor=2.5;
j=2;
for i=1:length(data1)-1
    if data1(i+1,1)>jumpfactor*10*data1(i,1); %autoscale jumps two ranges
        j=j+2;
    elseif data1(i+1,1)>jumpfactor*data1(i,1); %autoscale jumps one range
        j=j+1;
    elseif data1(i+1,1)<data1(i,1)/(jumpfactor*10); %autoscale jumps two ranges
        j=j-2;
    elseif data1(i+1,1)<data1(i,1)/jumpfactor; %autoscale jumps one range
        j=j-1;
    end
    data2(i+1)=data1(i+1,1)*scale(j); %make data2 equal to data1 x the correct scale

    data1(i+1,2)=scale(j); %put the value of the scale used in a column next to the data for checking
end
 plot(data1);
figure;
plot(data2);
```

For example, the following figure:

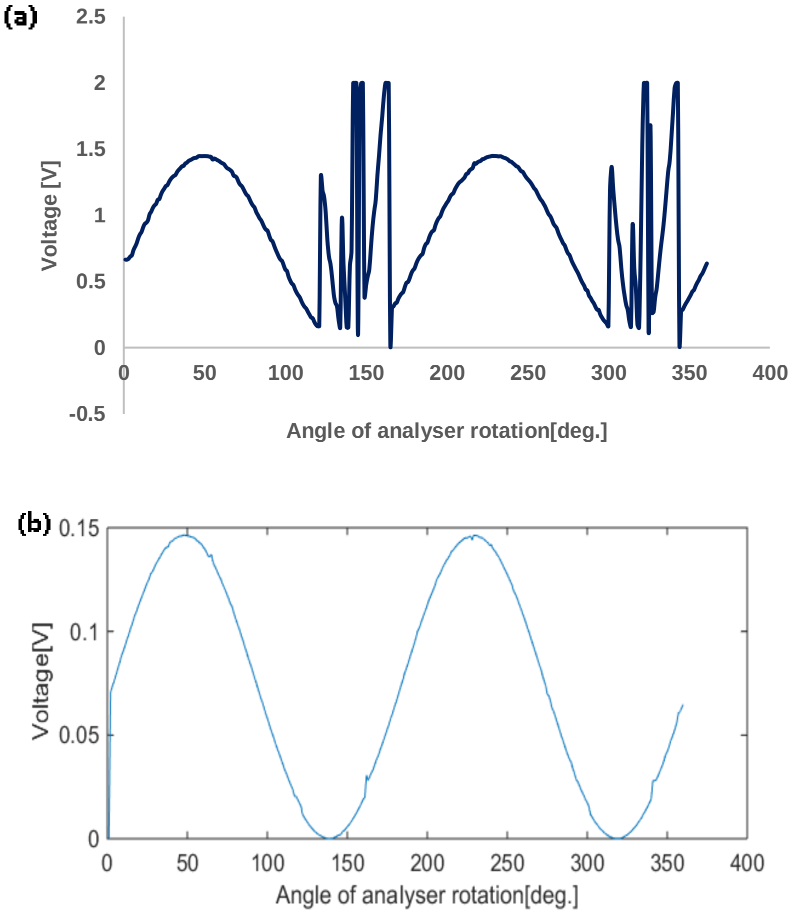

Figure A. 10 Fluctuation of output analogue voltage in the trough due to auto-scale fluctuation of powermeter, b) Output voltage after compensation of the fluctuated voltage.

Appendix B Effect of Different Parameters on the Polarimetry Measurements and Noise

B.1 Introduction

With the aim of decreasing the size of the system to micro-scale, various factors should be taken into account, including temperature changes, containing the noise of the powermeter and reducing the beam diameter and power.

Measuring optical activity in sub-microlitre volumes in chip dimension is associated with a high probability ratio of changes in the sample temperature during exposure to the laser. In this case, the laser power should be carefully selected and modified to avoid temperature variation. Time of the measurements is very important; too much exposure of the sample by the laser, especially at high power and when taking 10 readings for each angle, will lead to different effects. One such effect is the change in sample temperature between the first (low T) and the last (high T) angle through one scan. Another effect would be a change in the sample concentration between the first (low C) and the last (high C) angle through one scan, where high power will evaporate some water leading to the glucose ratio being higher in later angles than at the first angle.

B.2 Influence of different parameters on the sensitivity of the measurement

B.2.1 Influence of Low Signals Detection on the Sensitivity of the Measurements

In order to apply our set-up in a microfluidic scheme, small beam diameter (in micron rage) is required. For this purpose, different pinhole sizes were used and the measurements were taken for several samples with a reduced beam size (by using 400 and 100 µm pinholes in front of the laser). The results were close to the large spot beam as shown in Figure B.1.

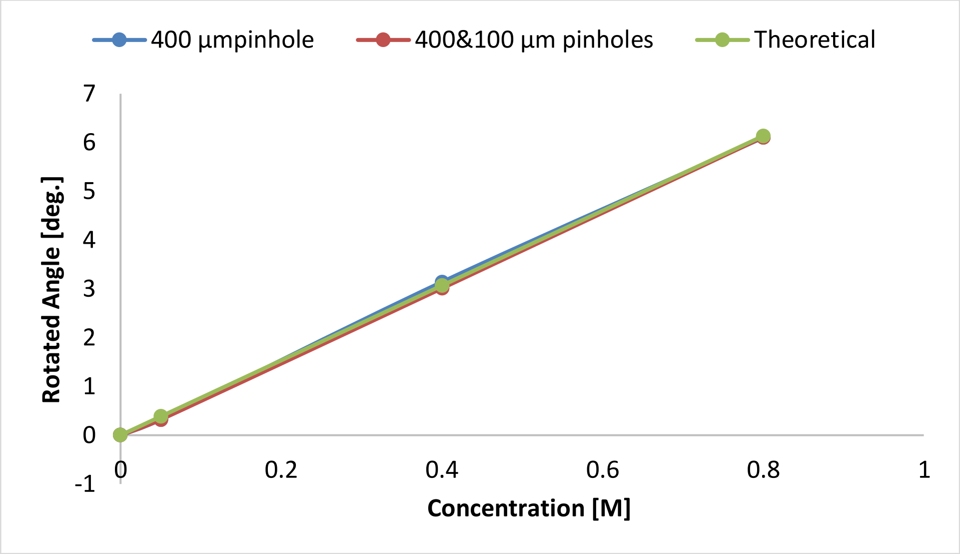

Figure B.1 Effect of reducing the laser beam size on the measurements of polarization.

It can be concluded that the powermeter detection of the small spot size was somewhat satisfactory in comparison to large laser beam detection. This is essential to the small sample measurements.

B.2.2 Noise in Power Measurements

Due to the small size of the pinhole (100 and 25 µm), the power decreases causing noise, and leading to inaccurate measurements. The error involved was calculated from the peak and the trough of the power curve measurements for different pinhole sizes i.e. 400, 100, and 25µm as shown in Figure B.2, Figure B.3, and Figure B.4.

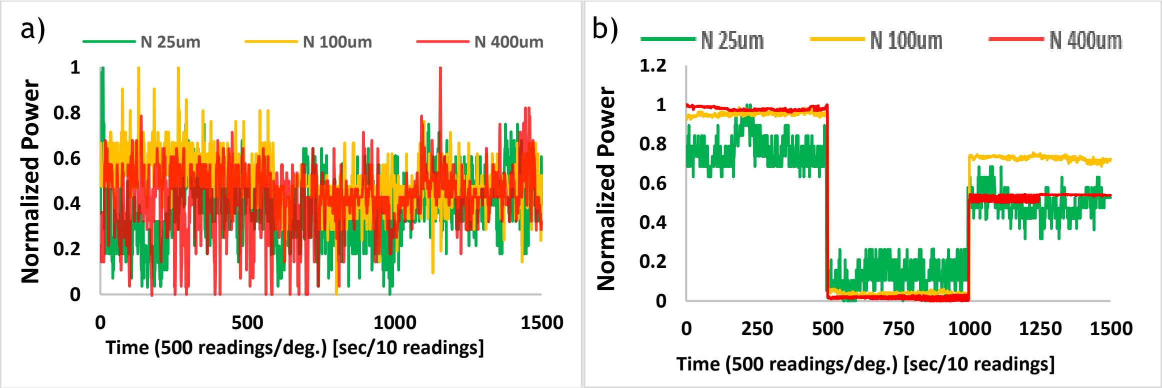

Figure B.2 Normalized power value for 3 different pinholes sizes at a) peak, b) trough value, N denotes to normalized.

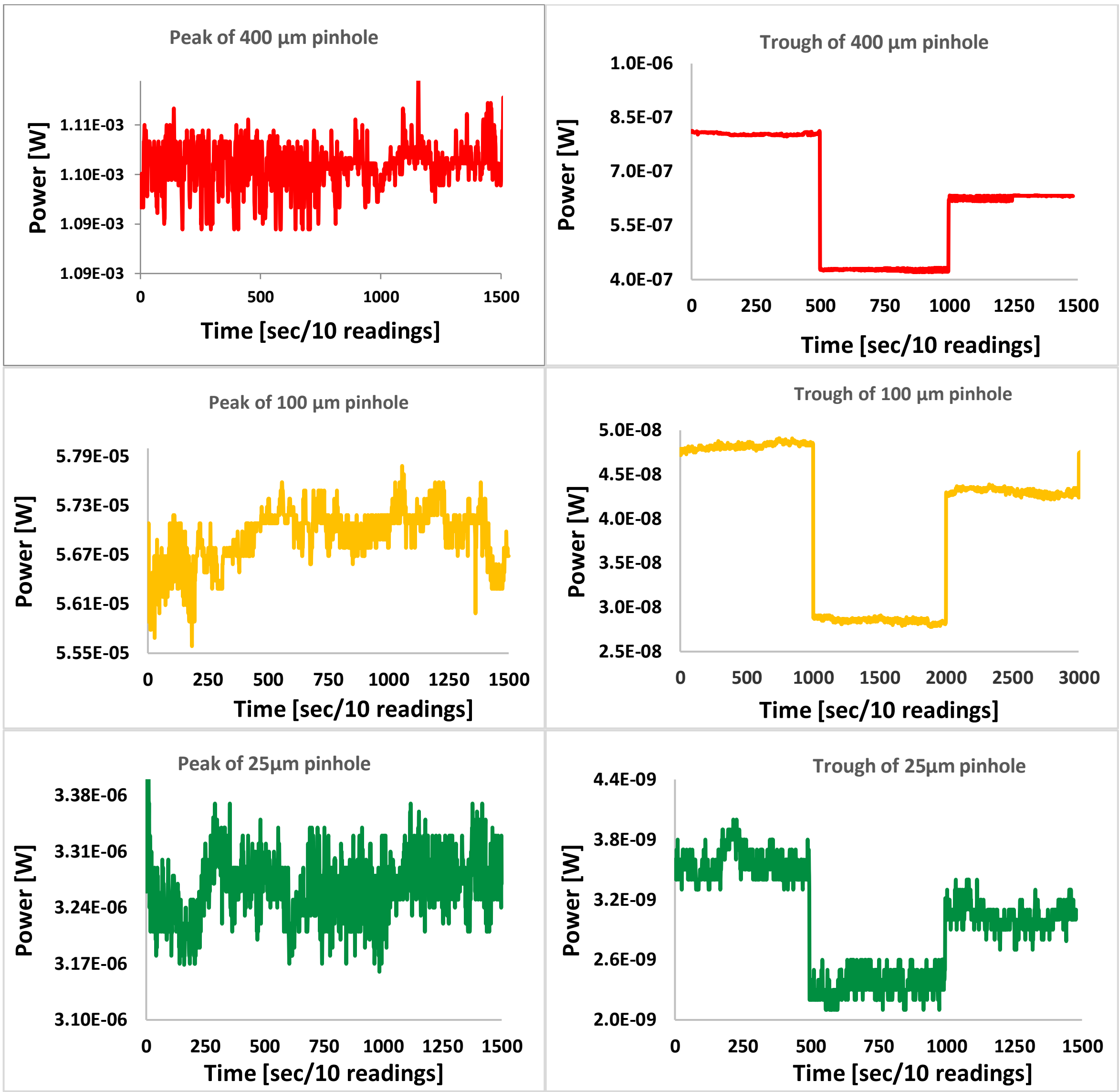

Figure B.3 Fluctuation of laser power for different pinhole sizes (25, 100, and 400 µm) at peak (left) and trough (right).

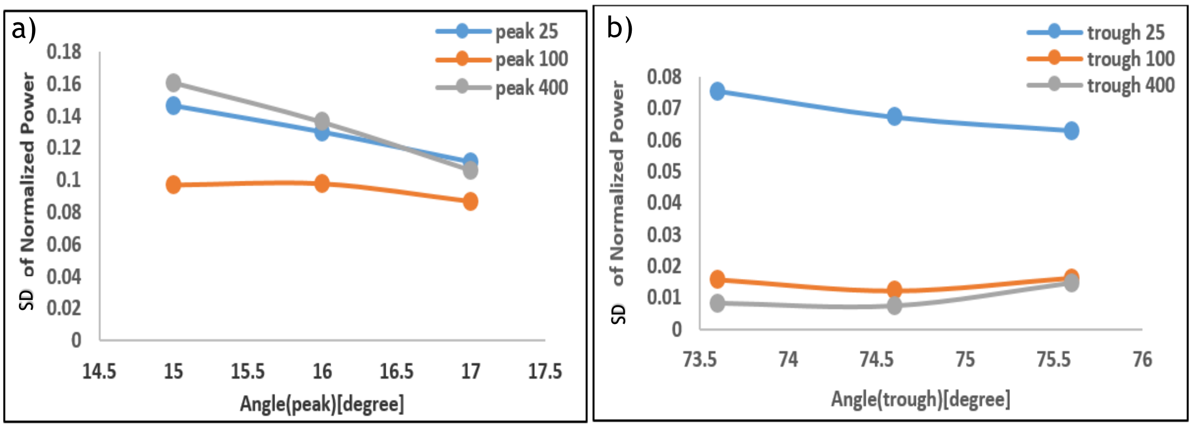

Figure B.4 Standard deviation values of 25, 100, and 400 µm pinholes at (a) peak (maximum power) and (b) trough (minimum power).

The obtained results showed that for the three different pinhole sizes of theses pinholes, the error values at the peak were larger than at the trough, as the oscillation output power at the peak corresponded to their values which were larger than these at the trough. Hence, at the peak, detecting and recognizing the phase shift wes very difficult between the three angles scan, while at the trough they were very clear and easy to detect.

B.3 Pinhole Effect

A comparison was made to recognise the effect of the pinhole on the optical rotation measurement in the polarimetry system. It was done by measure a different set of glucose concentration with and without using pinhole, as shown in Figure B.5 (a and b).

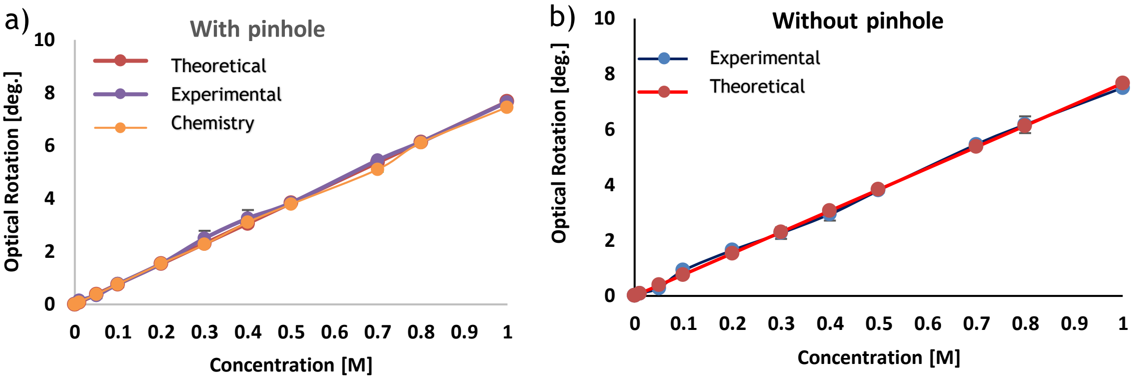

Figure B.5 Rotated angles for polarisation measurements with their theoretical values for different glucose concentrations (a) with, and (b) without using the pinhole (10 cm sample cell).

The results showed that there was no significant change when pinhole used. Therefore, minimizing the laser spot size, which is necessary in chip scheme, not affected the noise.

Appendix C Effect Detection and diagnosing source of the system error

C.1 Introduction

This appendix focuses on diagnosing a noise that influences the accuracy of experimental results. No measurement made is infinitely precise. The precision (number of significant figures) and accuracy (correctness) of a measurement are at all times limited by the degree of sensitivity of the apparatus used according to the data sheet [139].

The laser source represents the core of the system, so the majority of this section focuses on observed the stability of laser output intensity. The selection of laser within certain specifications directly correlates with the amount of precision obtained. So, the source of noise in polarimetry can be classified according to influential factors for each part in the setup.

Finally, Matlab code was written to show the influence of noise level on rotation value by adding a different generated random noise level to the pure signal.

C.2 Results and discussions

Optical rotation for different concentrations of glucose were measured using different arrangements, the average percentage error from the mean for each one is shown in Figure C.1. The minimum error observed was when using the Glan Thompson polarizer (3.45%) which increases the polarisation ratio (10000:1).

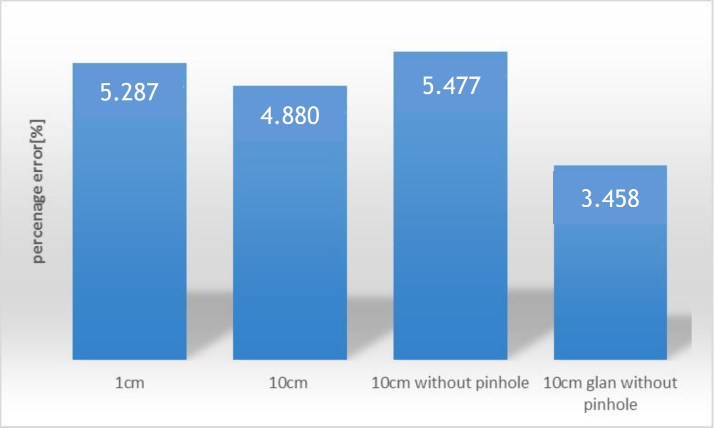

Figure C.1 Averaged percentage error for different glucose concentrations in different setup and sample sizes.

7.2.1 Investigation of the error in He-Ne Laser with and without optical elements

7.2.1.1 Laser only

The laser output power stability (fluctuation) at different time period were measured for 15 hours, with the average of 3, 5, 10 readings of recorded power, as shown in Figure C.2, Figure C.3 and Table C.1.

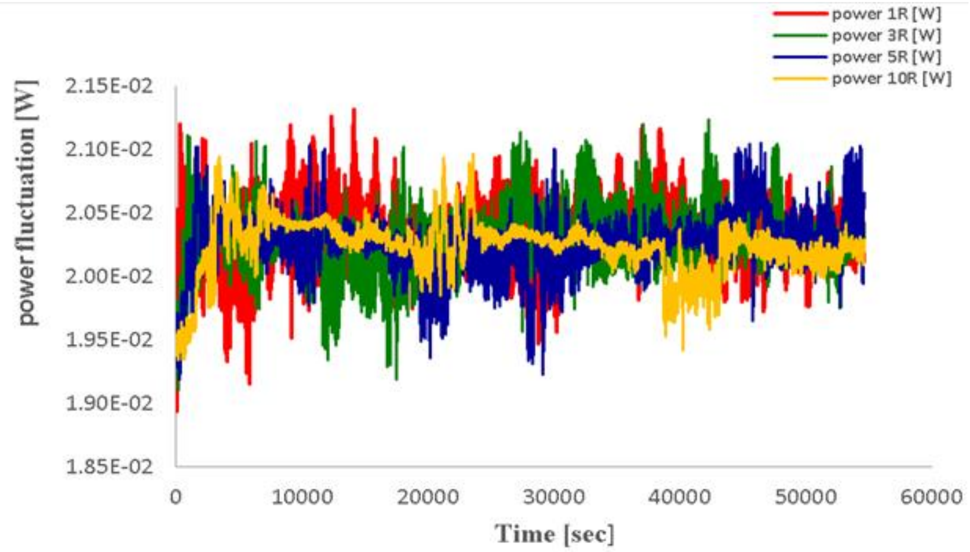

Figure C.2 Fluctuation of laser power for different number of readings versus time for 15 hours.

The fluctuation of laser declined enormously by taking the average for several readings of power for a specific point. For example, it was lessened from 2.37 to

0.1619 mW when the average was made for each 10 readings in 15 hours, as shown in Table C.1.

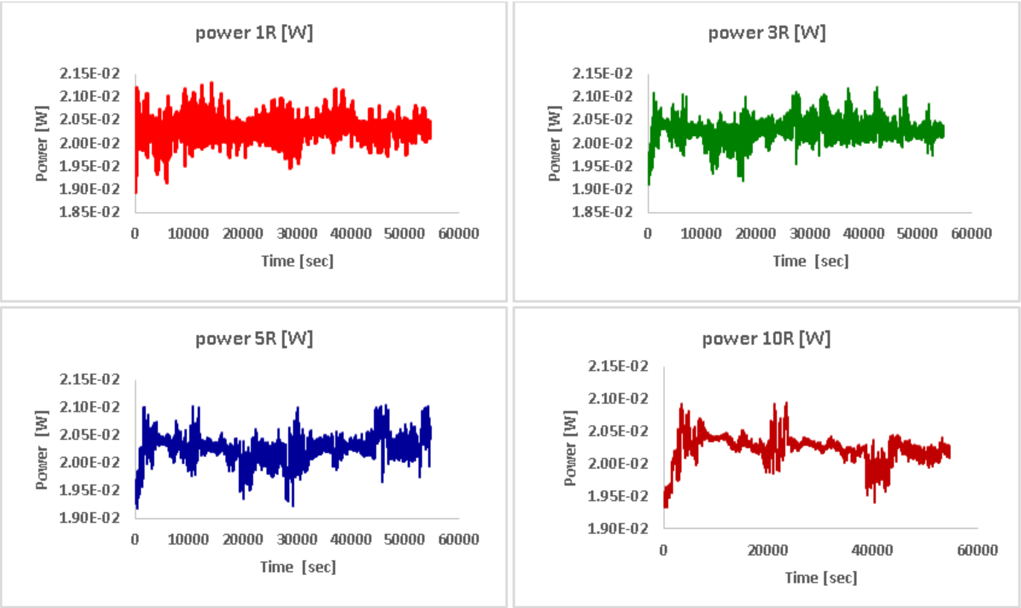

Figure C.3 Fluctuation of laser power for different number of averaged readings for each point (1, 3, 5, 10 readings) versus time for 15 hours.

Table C.1 Mean, SD, and fluctuation values of laser power versus number of averaged readings (15h).

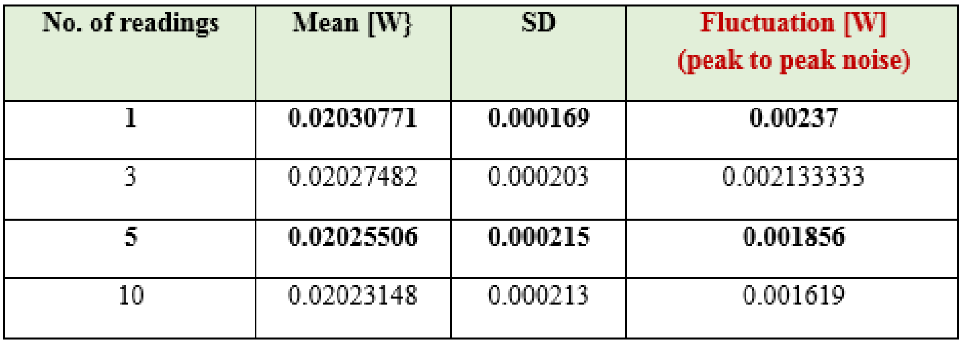

No. of readings	Mean [W}	SD	Fluctuation [W] (peak to peak noise)
1	**0.02030771**	**0.000169**	**0.00237**
3	0.02027482	0.000203	0.002133333
5	**0.02025506**	**0.000215**	**0.001856**
10	0.02023148	0.000213	0.001619

Figure C.4 illustrates the mean and fluctuation with different number of averaged readings for each point.

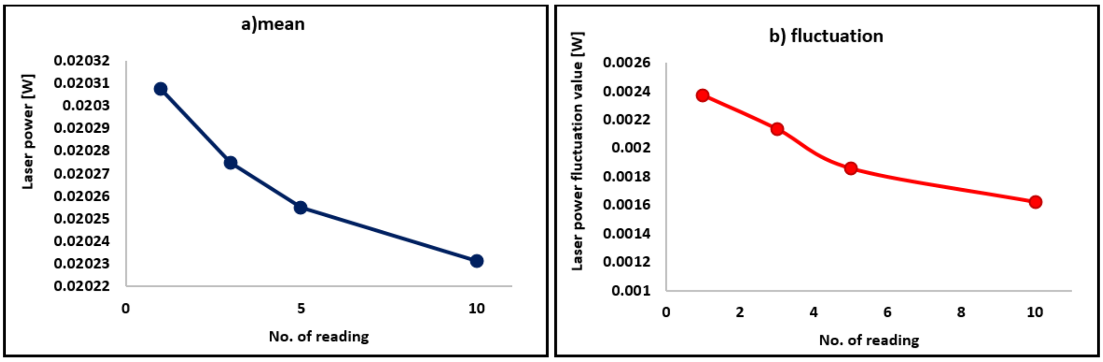

Figure C.4 (a) Laser power mean, and (b) Fluctuation of laser power versus number of averaged readings (15h).

The fluctuation results are shown in Figure C.5, the average of 10 readings showed the lowest fluctuation.

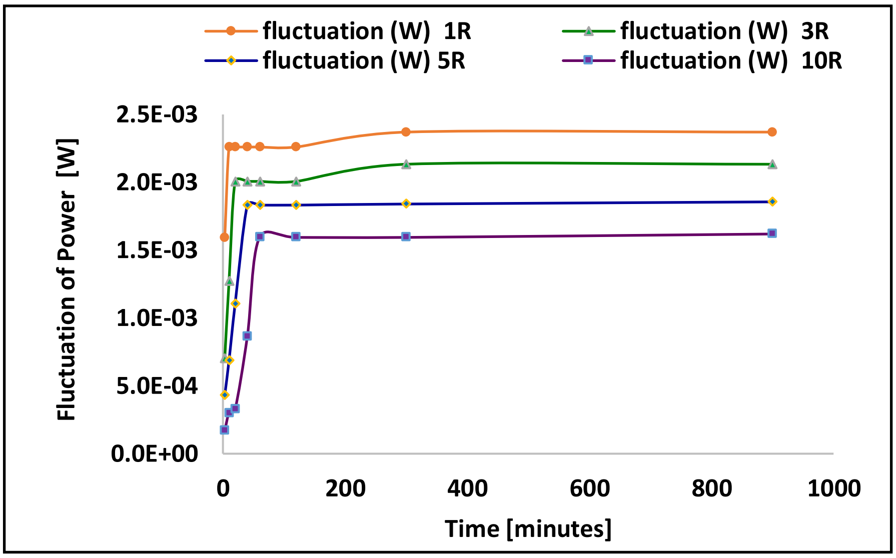

Figure C.5 Fluctuation of laser power with time for different numbers of averaged readings.

The same trend appeared for different time measurements (for 25 minutes), as shown in Figure C.6 (a). The fluctuation (10 averaged power readings) was roughly satisfactory (fluctuation: 0.07 mW) after 5 minutes for 30 second (minimum fluctuation for the whole scan) and it was then upsurged in next 5 minutes to reach (0.25 mW) within 30 seconds, as shown in Figure C.6 (b and c). In spite of low noise ratio in case of 10 readings averaged, the averaged 10 averaged readings power had different values in different period of time. The difference was about 0.07 mW within 5 minutes – Figure C.6 (b and c).

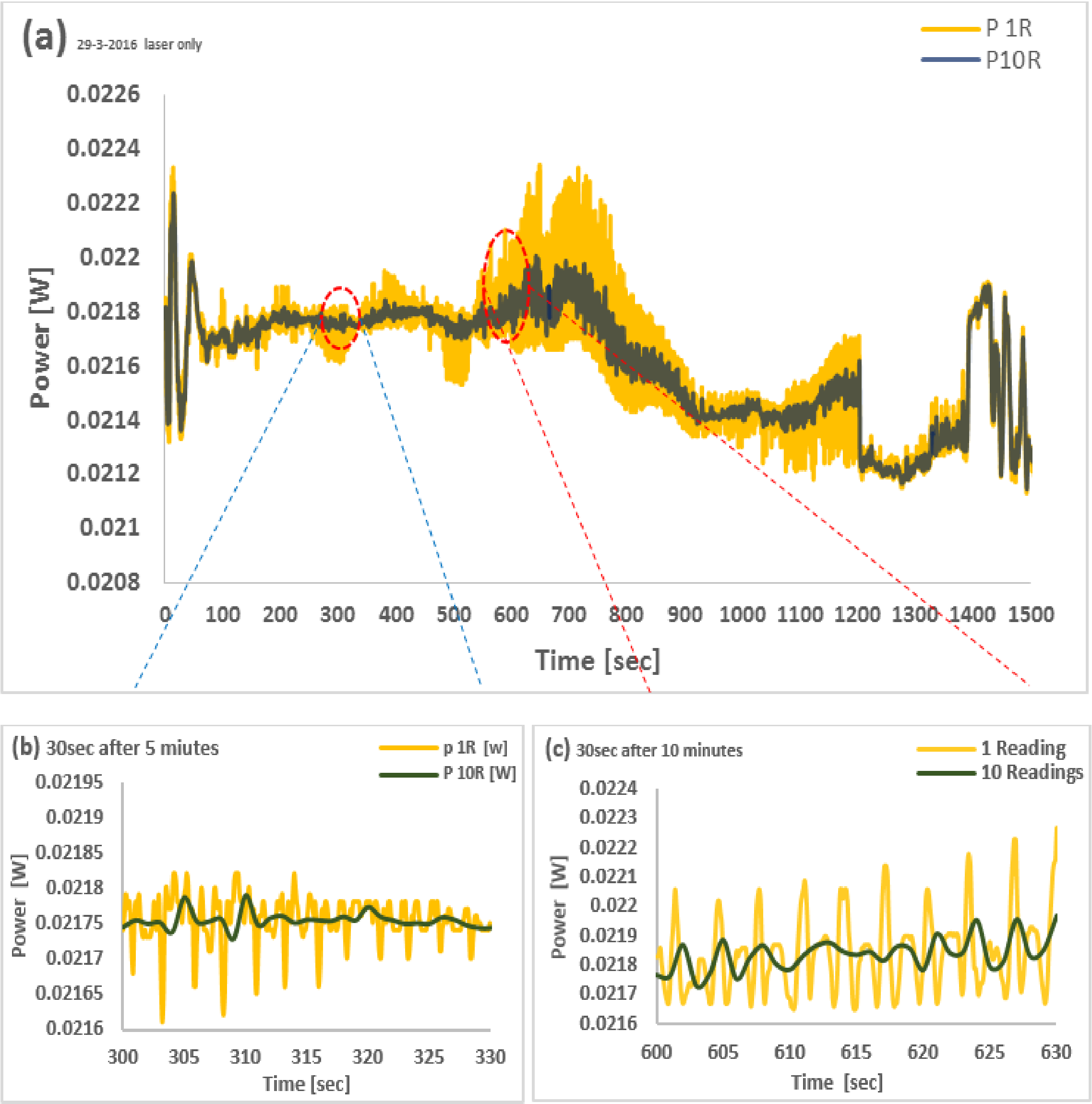

Figure C.6 1 and 10 averaged readings of laser power versus time for a) 25 minutes , b) 30 sec after 5 minutes, c) 30 sec after 10 minutes.

It can be concluded, despite of taking an average for each 10 readings of the power, the fluctuation value of laser power remains somewhat high (~ 1 mW within 25 minutes). Accordingly, the ability of laser to perform polarimetry measurements with the accuracy required (to detect in µM) is typically limited by a fluctuation of laser power.

7.2.1.2 Laser with different pinhole sizes

The laser power which passed through varying pinhole sizes (400, 100, 50, 25 µm) was measured and compared with the laser without a pinhole, as shown in Figure

C.7, Figure C.8, and Table C.2 Mean, fluctuation, SD, RIN, and noise of laser power for laser with and without different pinhole sizes. Table C.2.

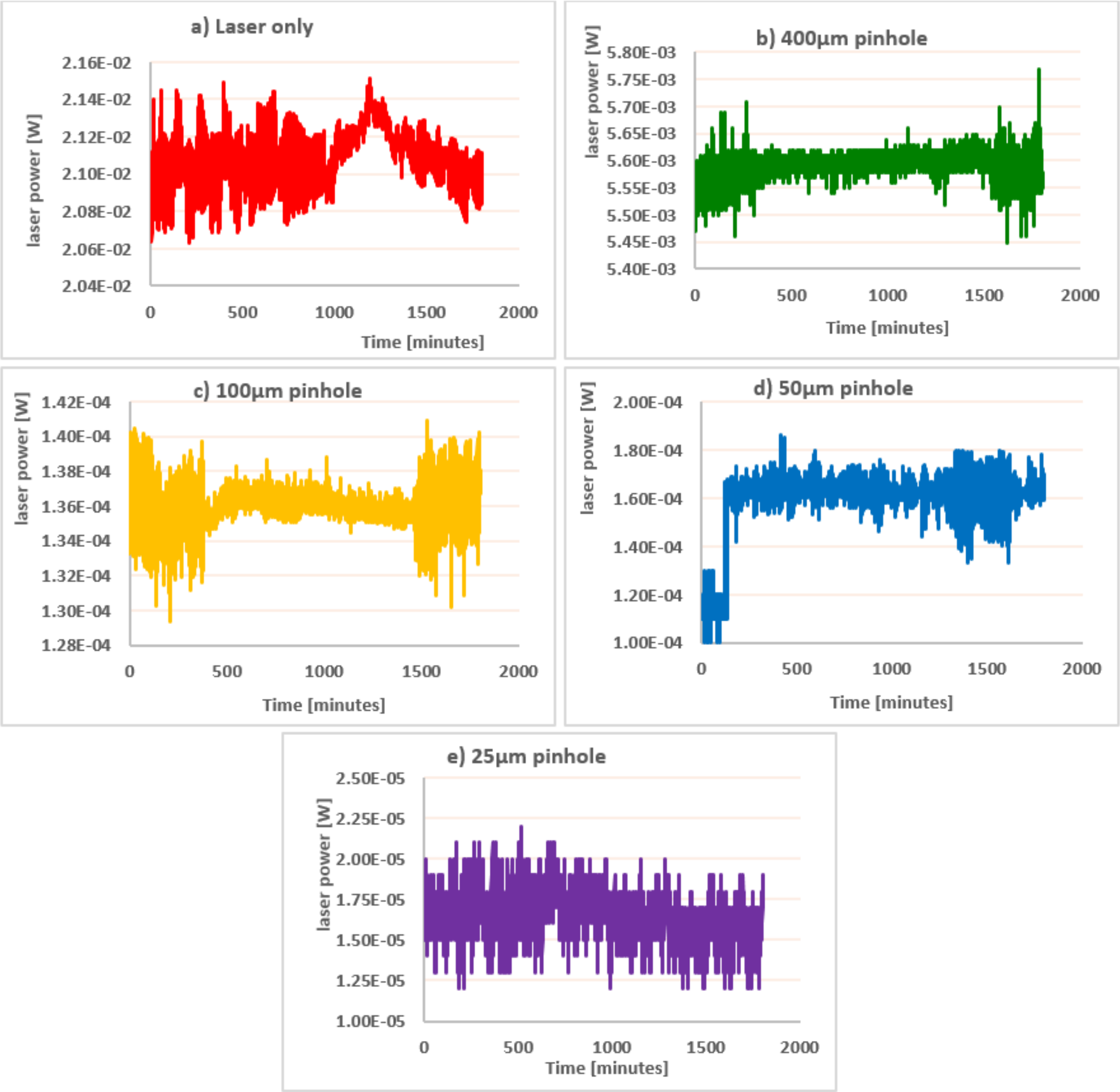

Figure C.7 Output power for laser and different pinhole sizes, a) laser only, b) 400 µm, c) 100 µm, d) 50 µm, e) 25 µm.

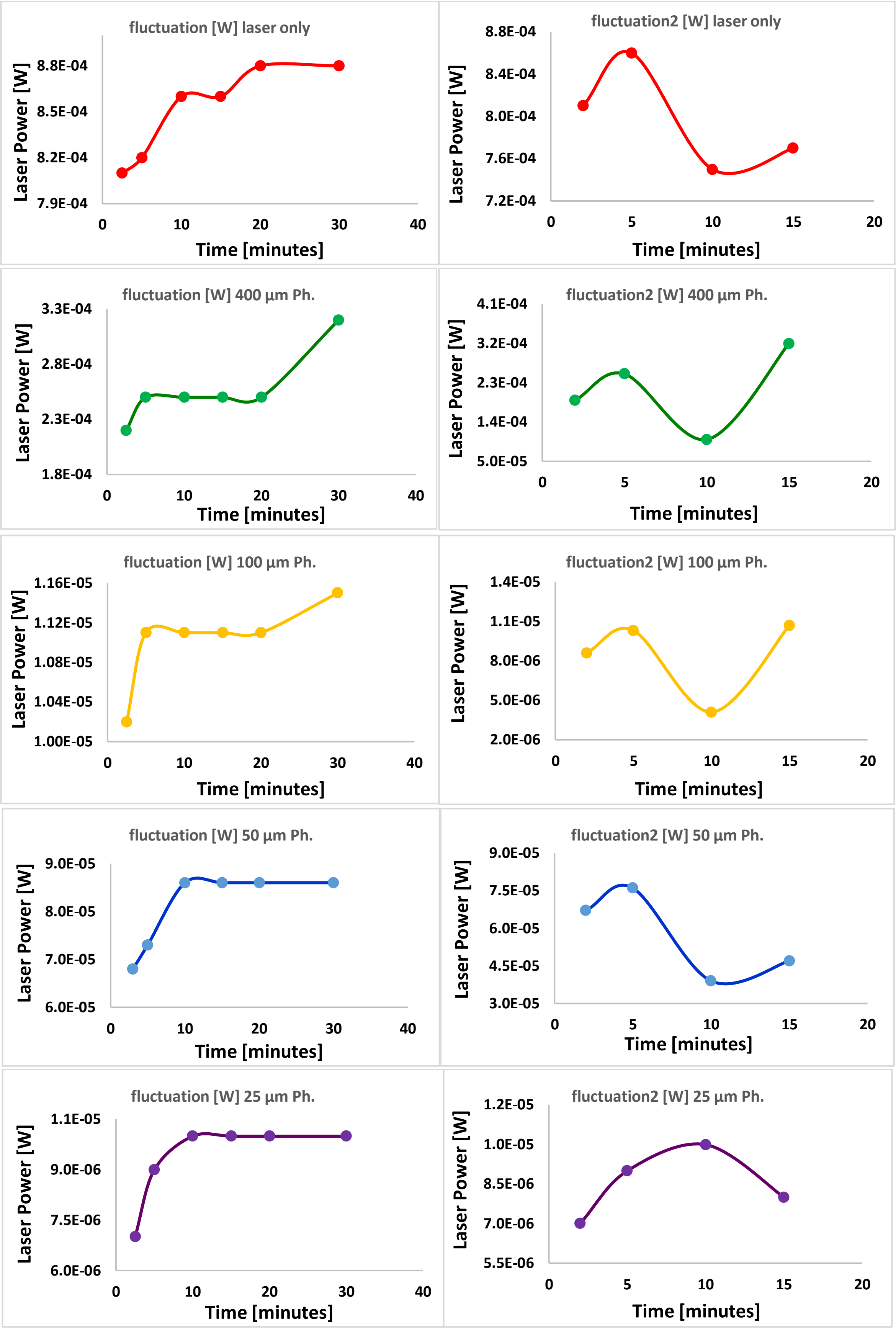

Figure C.8 Fluctuations of laser power within a period of 30 minutes with and without different pinholes for different time intervals (on the right for continuous measurement, and the left for stepwise).

Table C.2 Mean, fluctuation, SD, RIN, and noise of laser power for laser with and without different pinhole sizes.

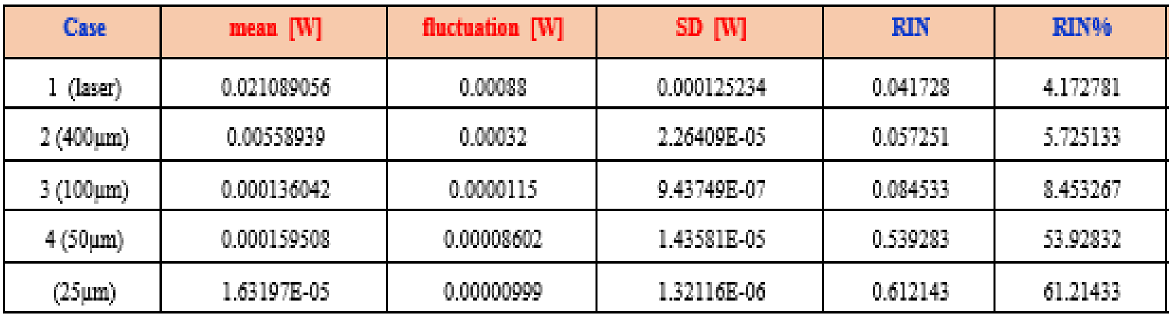

Case	mean [W]	fluctuation [W]	SD [W]	RIN	RIN%
1 (laser)	0.021089056	0.00088	0.000125234	0.041728	4.172781
2 (400µm)	0.00558939	0.00032	2.26409E-05	0.057251	5.725133
3 (100µm)	0.000136042	0.0000115	9.43749E-07	0.084533	8.453267
4 (50µm)	0.000159508	0.00008602	1.43581E-05	0.539283	53.92832
(25µm)	1.63197E-05	0.00000999	1.32116E-06	0.612143	61.21433

Relative intensity noise shows that 400 and 100 µm pinholes have approximately the same noise, at around 5%, while an a lot of noise occurred when using 50 and 25 µm pinhole sizes reaching 61% because the low power of the signal compared with noise ,as shown in Figure C.9.

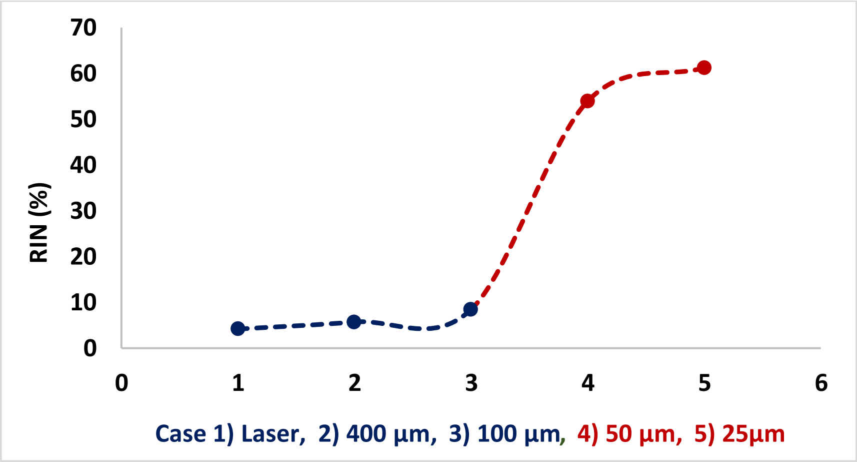

Figure C.9 RIN of laser power fluctuation with and without different pinhole sizes.

7.2.1.3 Laser with polarizer (power fluctuation analysis).

In this stage, the polarizer with respect to laser at three different angles (0˚,45˚,90˚) were established:

1- In case of laser with polarizer

A- At 90° (maximum power):

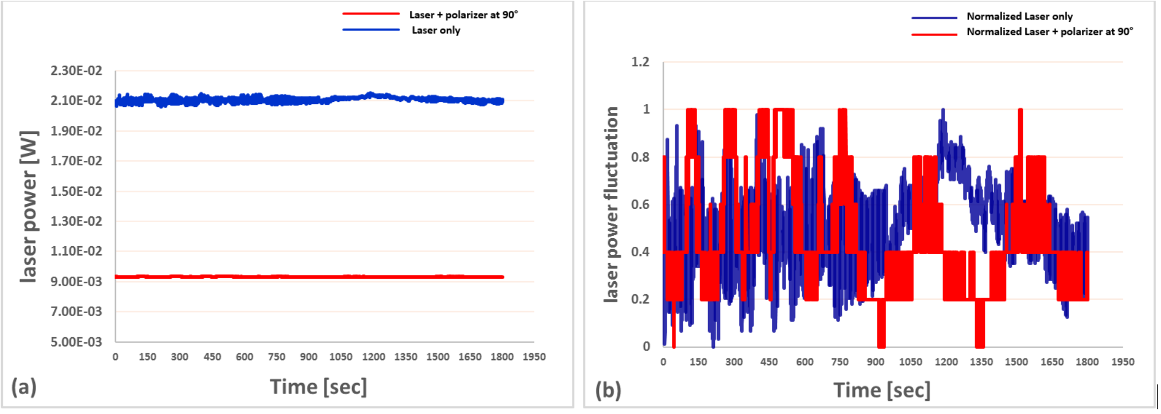

Figure C.10 Fluctuation of laser power output with and without polarizer. a) Real scale power values, b) Normalized power values.

It is clear from the comparison between two cases (with and without the polarizer), that the fluctuation of laser decreased to 0.05 mW from 9.35 mW, while the fluctuation was reduced to0.88 mW from 21.5 mW. However, the fluctuation behaviour with respect to polarizer had uniform fluctuation (every 30-60 sec) which approached a sinusoidal wave. This indicated that the polarization of the laser was not stable and fluctuated within 0.05 mW every (30-60) sec (as shown in Figure C.11) for every 5 minutes. The same behaviour using 400 μm pinhole is shown in Figure C.13 and Figure C.16.

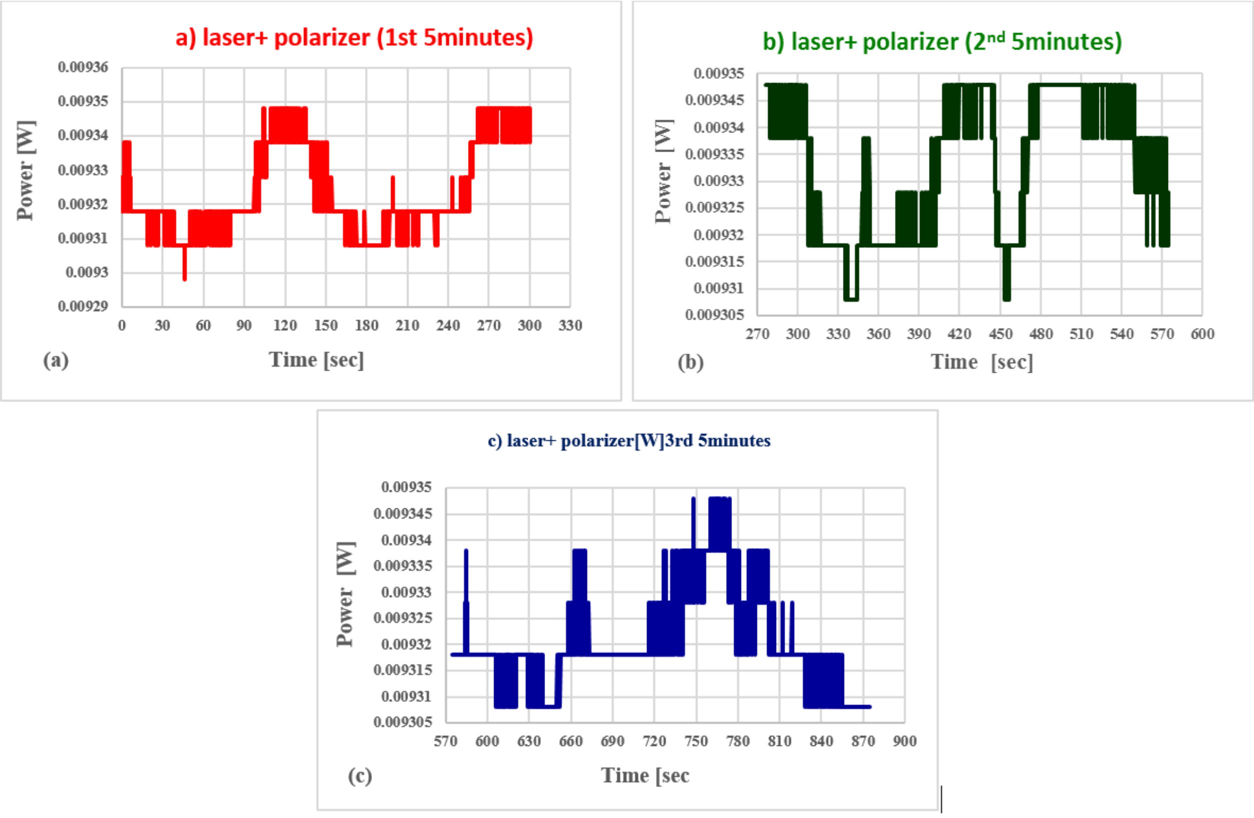

Figure C.11 Laser power output fluctuation with polarizer. a) First 5 minutes, b) Second 5 minutes, c) Third 5 minutes.

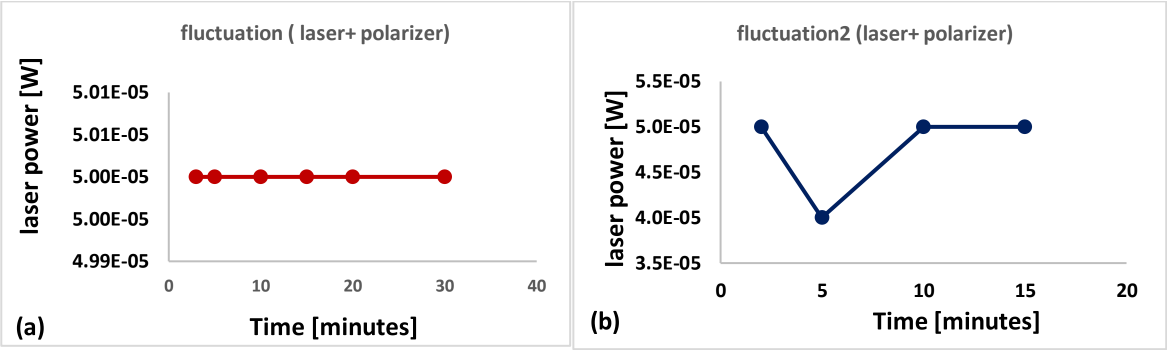

Figure C.12 Fluctuation of laser power output with polarizer for different periods (a) continuous, (b) stepwise.

B- In case of the laser with a polarizer at different positions (minimum to maximum) 0°, 45°, and 90° as shown in Figure C.13.

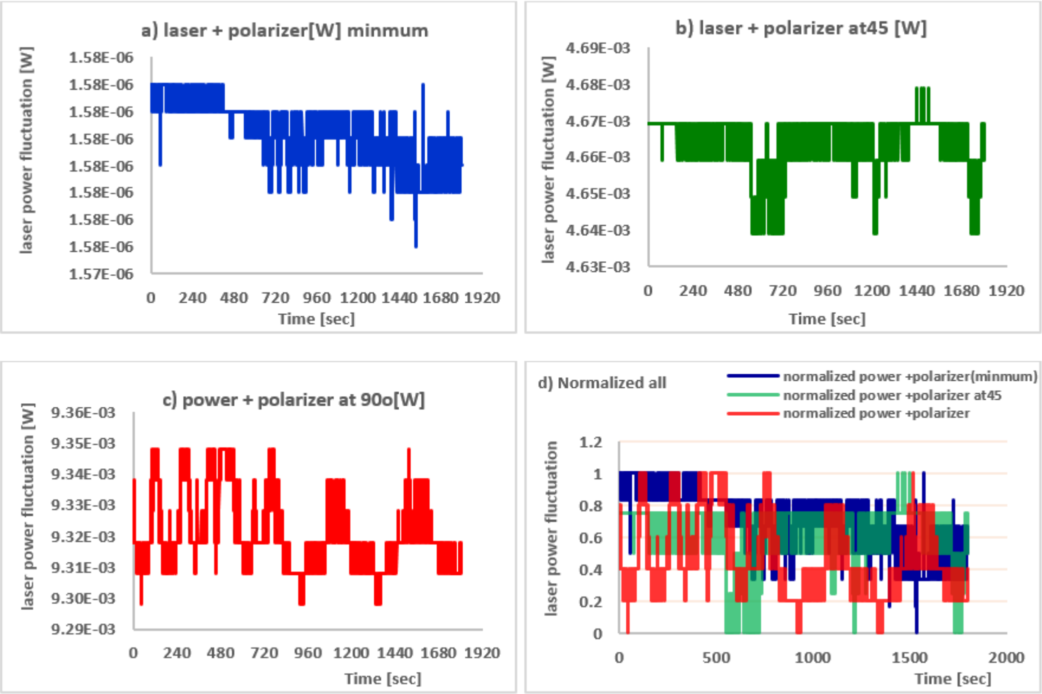

Figure C.13 laser with polarizer at different positions (minimum to maximum) a) 0°, b) 45°, c) 90°, and d) normalized all.

The fluctuation values at three different analyser angles (minimum, 45°, and maximum) were calculated with the corresponding power at each angle, as shown in Figure C.14. The noise values were (0.53%, 0.84%, and 0.38%) at angles (90°, 45°, and 0°) respectively. The plane of polarized light is parallel to the perpendicular case of laser power passing through the polarizer was calculated for 30 minutes as shown in Figure C.15.

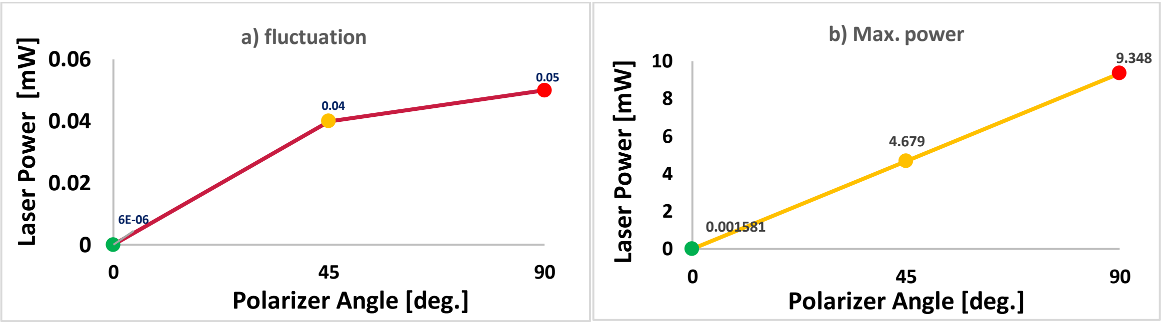

Figure C.14 (a) Fluctuation of laser power at different angles of polarizer, (b) power values at each angle.

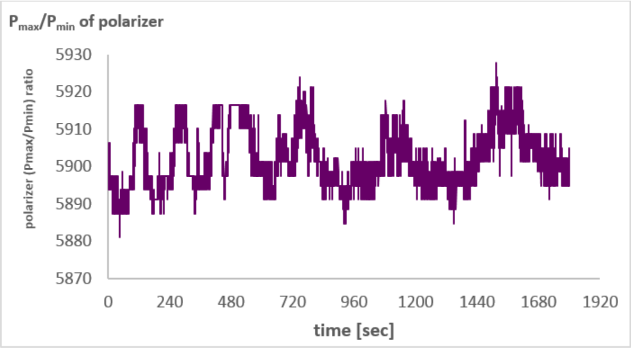

Figure C.15 The ratio of maximum to minimum power output from polarizer when the polarizer angle is 90° to 0°.

2- In case of using 400 μm pinhole with polarizer:

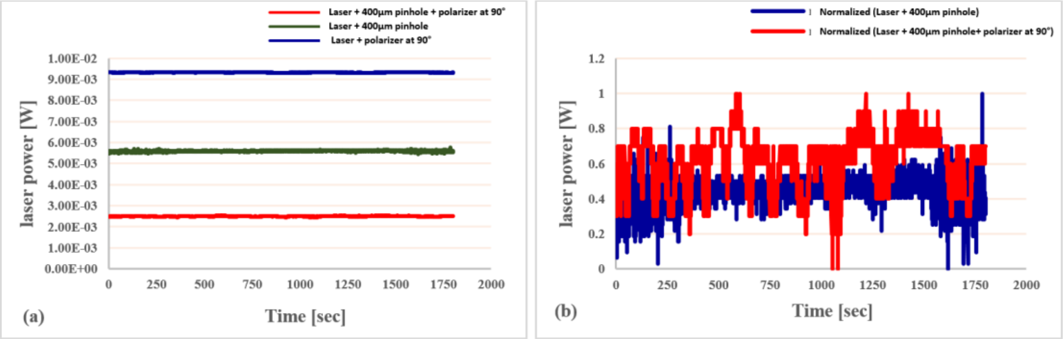

Figure C.16 Fluctuation of laser power output with and without polarizer with 400 μm pinhole.

In this case, the fluctuation value was reduced to 0.1 mW from 2.5 mW output power when using the pinhole. This had compared with the previous case (without a pinhole) where the fluctuation value was decreased to 0.05 mW from 9.35 mW output power. Figure C.18 illustrates the fluctuation of laser power from polarizer at different time periods.

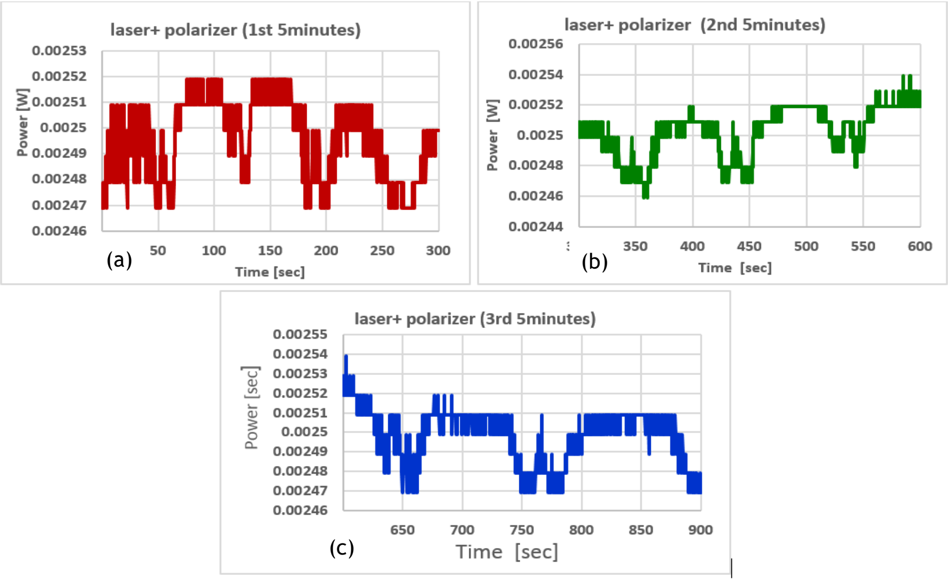

Figure C.17 Fluctuation of laser power output with polarizer and 400μm pinhole. a) First 5 minutes, b) Second 5 minutes, c) Third 5 minutes. (Power [W] versus time [sec]).

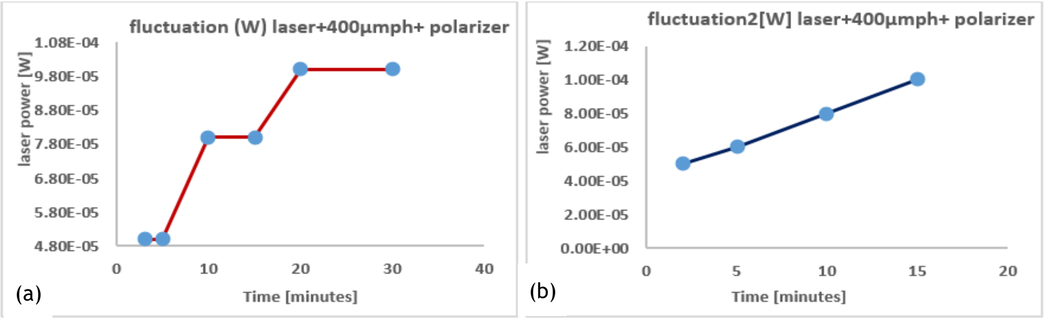

Figure C.18 Fluctuation of laser power output from polarizer in different period using 400 μm pinhole (a) continuous (b) stepwise.

3-In case of using Glan-Thompson polarizer (GTP)

In this case, the fluctuation was 0.16 mW from the 23 mW maximum power. It can be seen that there was no losses (attenuation) in laser power value. Figure C.19 (a) shows the laser power stability at the maximum for 30 minutes. The comparison between the normalized power value for both Glan and normal polarizer was made which showed the same sinusoidal behaviour as shown in Figure C.19(b). The fluctuation of output power oscillations in GTP increased with different periods of time, as shown in Figure C.20.

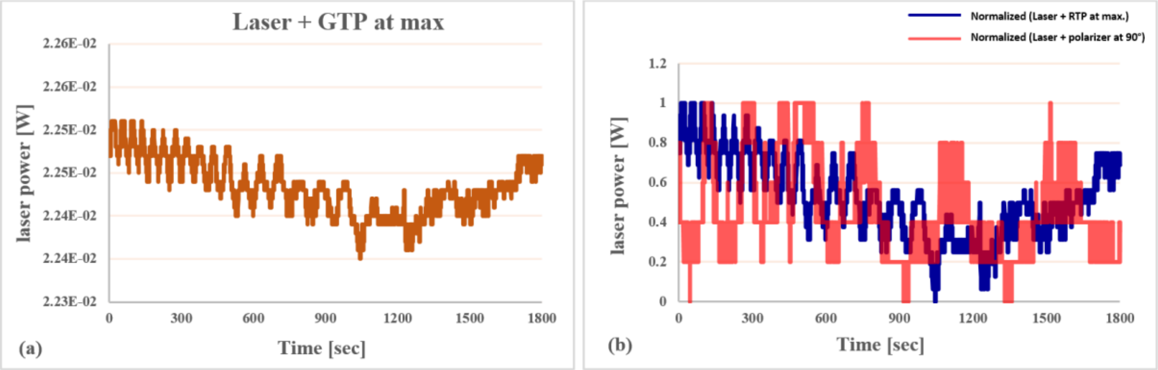

Figure C.19 (a) Fluctuation of laser power using Glan Thompson polarizer for 30 minutes at maximum state angle, (b) comparison between Glan and normal polarizer (normalized value).

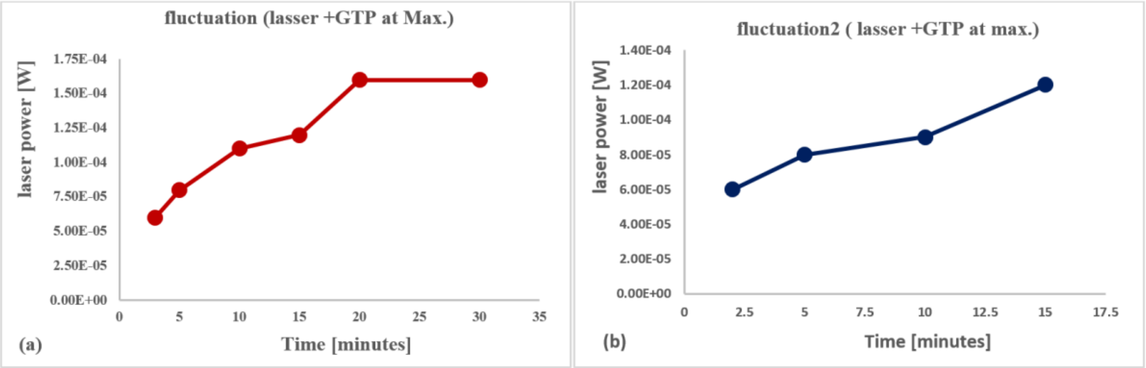

Figure C.20 Laser power fluctuation using Glan-Thompson polarizer for different time periods. a) continuous, b) step by step.

The behaviour of power oscillations in GTP appeared periodic and had a uniform shape. While this behaviour did not appear with the laser alone, as shown in Figure C.21 (a-d). It can be concluded that, the GTP works as a filter and it’s use reduces the noise value.

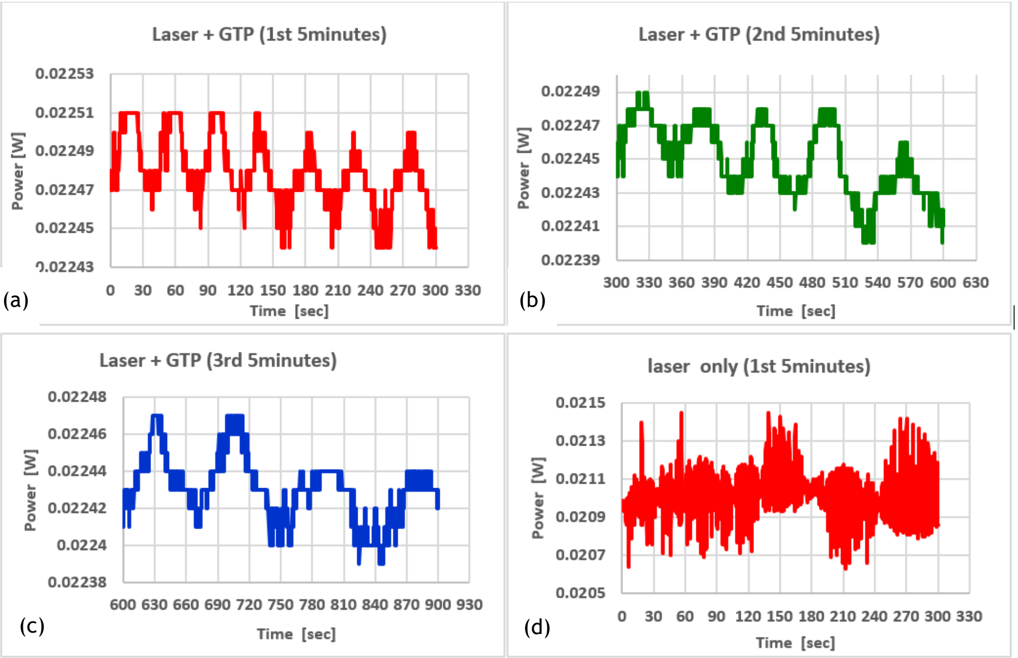

Figure C.21 Fluctuation of laser power output with Glan polarizer. (a) First 5 minutes (b) Second 5 minutes, (c) Third 5 minutes, (d) first 5 minutes for laser only.

For the initial 5minutes the fluctuation value was 0.07 mW, while it was 0.8 mW for laser.

According to these results, the observed noise in the presence of both GTP and normal polarizer realized a semiperiodic change in its state of polarization (SOP) which depends on the stability of polarization of laser source.

C.2.1.1 Laser with polarizer and analyzer

In one of the measurements of glucose concentration, the polarisation scan curve of the polarimetry when using two pinholes (400 and 100 µm), is shown in Figure C.22. Some analysis was done by dividing the curve into three regions (peak, trough, and between them) and the region that had a minimum noise was investigated to take into account a method to measure the rotation within this area.

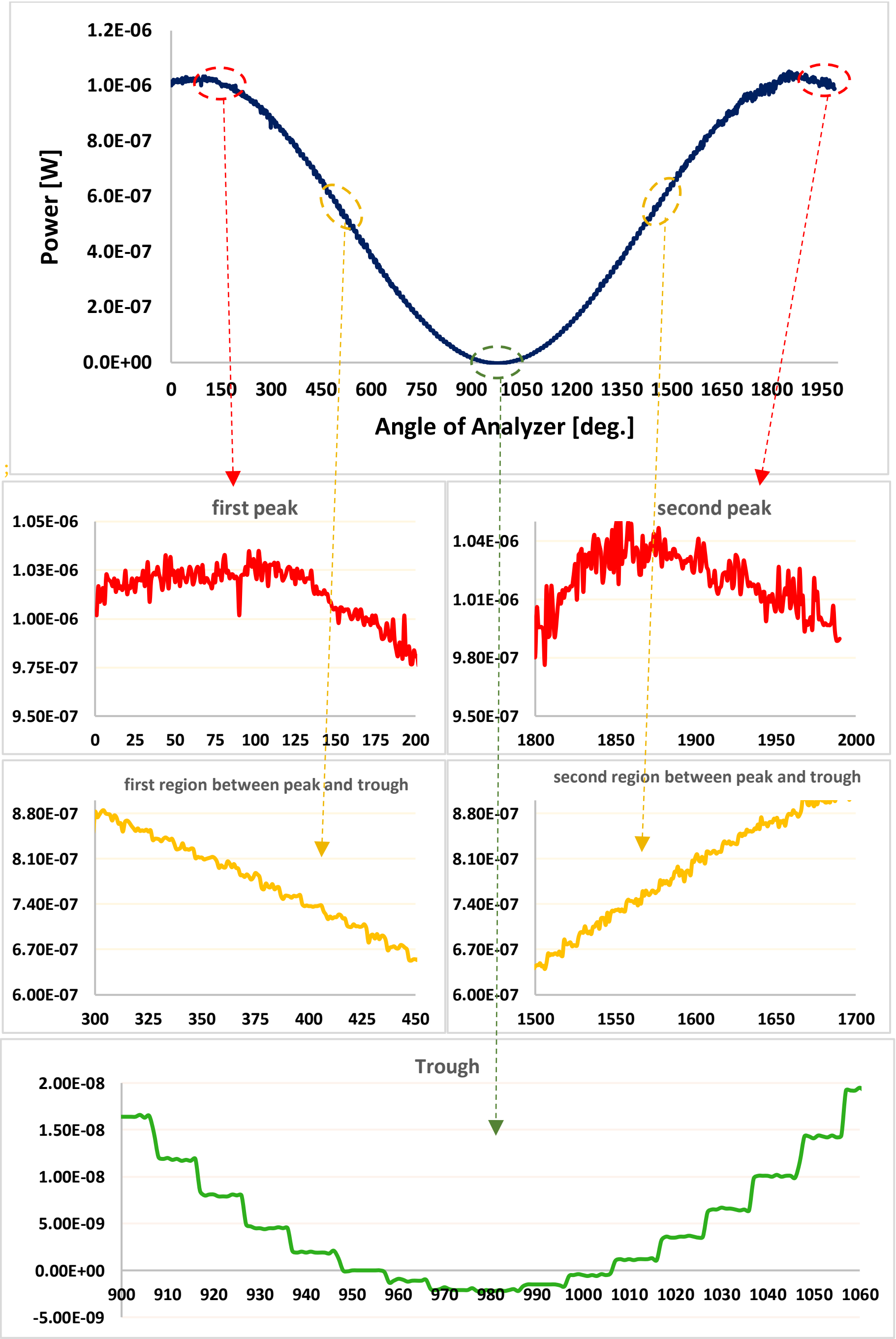

Figure C.22 Different regions of full scan analyzer output power (two pinholes).

The trough region appeared to have more stability than the other two regions; the fluctuation in peak is 0.03 μW (maximum power is 1μW) and in between is 0.01 μW while in trough is 1 nW.

C.2.2 All system components noise diagnosis

Different concentrations were measured in the polarimetry system using 1 cm cell. The results showed some fluctuations (0.46 mW) which was clear in the output power sine waves when repeating the measurements for the same sample as shown in Figure C.23. Table C.3 shows the amount of difference in the rotation angle when repeating the water measurements three times under the same conditions.

Table C.3 Differences in the angle of rotation due to repeating the water and glucose measurements several times under the same conditions.

Glucose concentration	α [degree] 1st time	α [degree] 2nd time	α [degree] 3rd time	Theoretical value
0.1 M with 1st time water	0.07281034	0.32166814	0.9152710724	0.07668°
0.1 M with 2nd time water	0.97764021	1.22182347	0.0075868891	
0.1 M with 3rd time water	1.23537605	1.47950443	0.250029184	

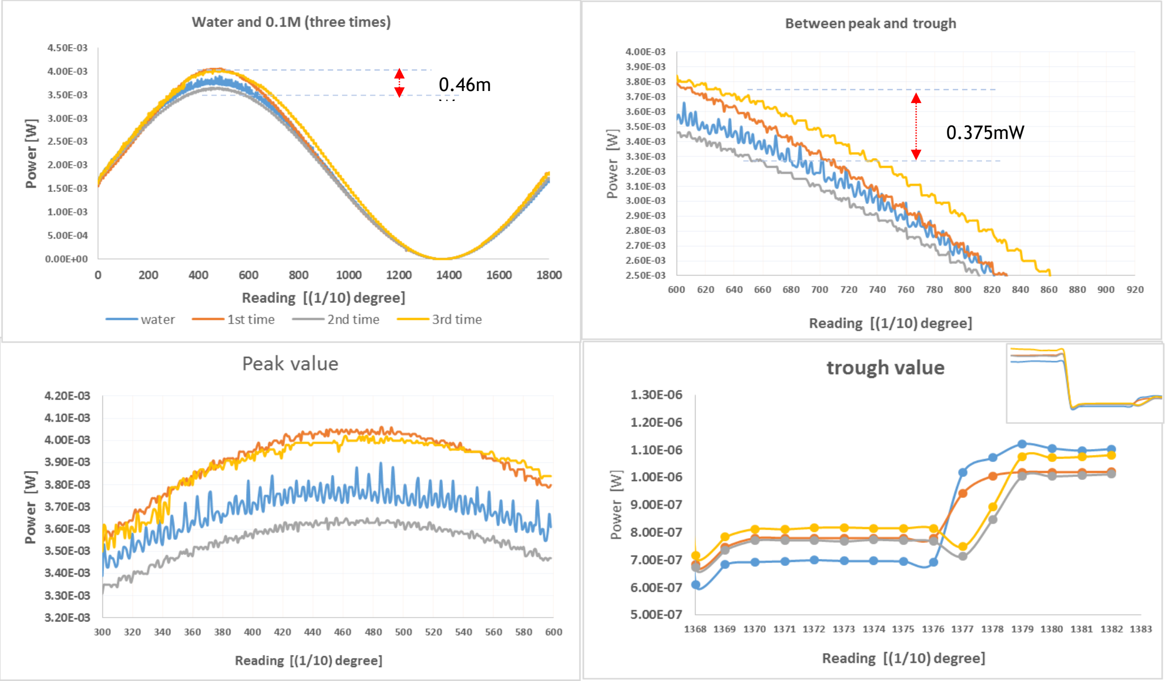

Figure C.23 Output power of 0.1 M glucose (three times) with respect to water (1° analyzer step).

Despite the acceptable ratio of fluctuation in case of using polarizer in section (B.2.1.3), the fast non-random fluctuations was still a major source of inaccurate result. Figure C.24 is the best example of this fluctuation, when just a measurement of polarisation for sample of water was repeated three times at the same conditions.

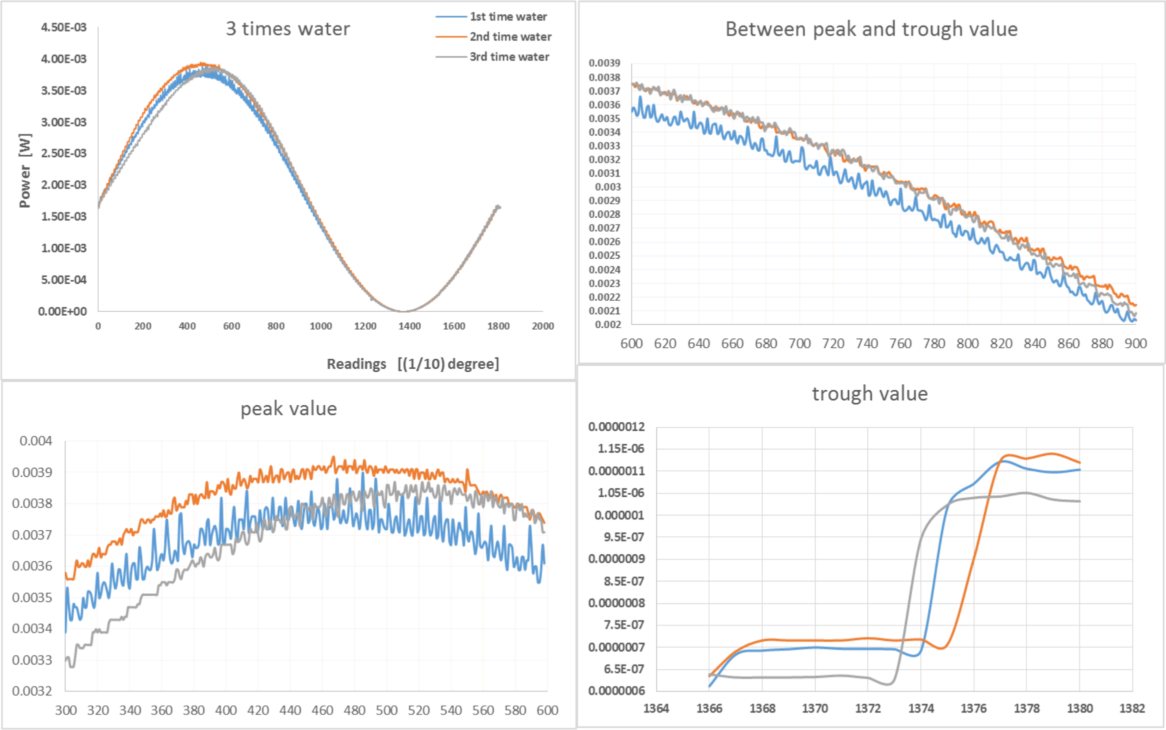

Figure C.24 Three times water scan within 1 hour at the same conditions (1° analyzer step).

C.3 Theoretical calculation of the shift error in the polarization angle for different noise levels using Matlab program

The source of noise in the polarimetry setup measurements were aimed at obtaining reference cases for comparison with the experimental results. For this purpose, Matlab code was written to simulate the ideal state, which corresponds to the experimental results depending on main equations (as shown in appendix A). At the same time, the code can generate any level of noise to combine it with the ideal signal and then estimate the amount of error which corresponds to the level of noise. The code includes the same fitting process that modify as a two sub-codes for the water and sample fitting respectively.

One of the advantages of this cod is the possibility to use it for the achieved experimental data as well as view the amount of rotation of the sample with all statistical results in one run.

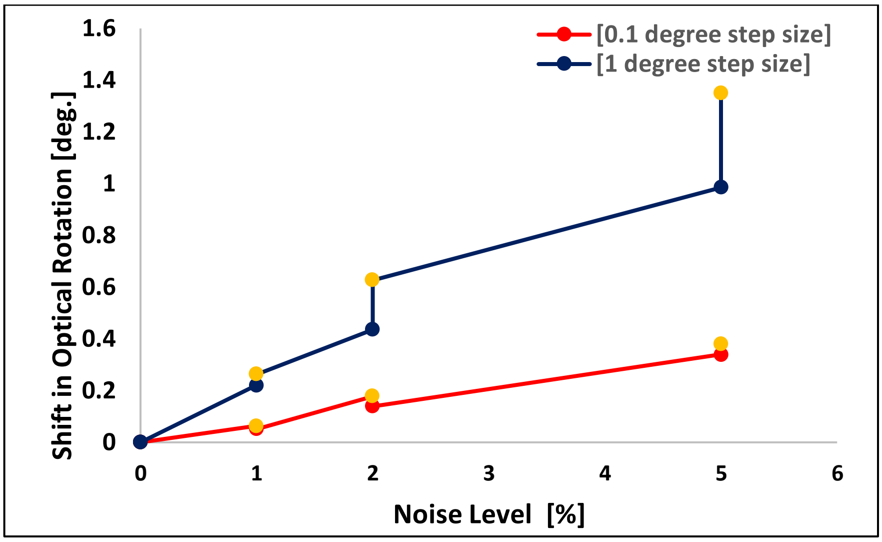

Figure C.25 Error values generated in rotation angles in 0.1 and 1 degree step depend on the generated noise level using Matlab code.

C.4 Conclusions

A polarimetry system has different components and various parameters which could have extreme effects on the results. One of the primary sources which influences all components is the laser as it passes through all components and ultimately the results depend on its power. He-Ne laser shows a power fluctuation of about 2.37 mW (for 15 hours). This measured fluctuation varies, and 1.61 mW was obtained after averaging ten readings, while at another time the fluctuation recorded was 1.2 mW within 40 minutes, which is more than its specification (1.15 mW, 5% drift after 8 hours). Several techniques can be helpful to reduce laser errors, such as increasing the number of measurements, decreasing the time taken to implement the measurements and enhancing the fitting of the power values when calculating the results (rotation angle). Polarizer, pinhole, and even the sample cell incorporates some error, but not as much as the laser noise, and it can be overcome by ensuring accurate alignment and identical condition to all of the samples and the reference (water). In the case of different pinholes sizes used, the laser output power drops after passing through the pinhole. The amount that power drops is directly proportional to the reduction in pinhole diameter, and the results show that the 100 μm pinhole causes a smaller error value compared to 400 and 25 μm. The highest error value is in the case of 25 μm especially at the trough, because of the very low S/N ratio in this case (signal is

3.8 nW). In other words, the signal power is very weak (μW) and the ability of the detector to recognize it from the noise signal is low.

References

1. Blout, E. and C. Djerassi, *Optical Rotatory Dispersion*. by Djerassi C., MacGraw-Hill Book Company, New York, NY, 1960: p. 238.
2. McNichols, R.J. and G.L. Cote, *Optical glucose sensing in biological fluids: an overview*. Journal of biomedical optics, 2000. **5**(1): p. 5-16.
3. Rouhi, A.M., *Chiral roundup - As pharmaceutical companies face bleak prospects, their suppliers diligently tend the fertile fields of chiral chemistry in varied ways*. Chemical & Engineering News, 2002. **80**(23): p. 43-+.
4. Korbel, G.A., G. Lalic, and M.D. Shair, *Reaction microarrays: a method for rapidly determining the enantiomeric excess of thousands of samples*. Journal of the American Chemical Society, 2001. **123**(2): p. 361-2.
5. May, O., P.T. Nguyen, and F.H. Arnold, *Inverting enantioselectivity by directed evolution of hydantoinase for improved production of L-methionine*. Nature biotechnology, 2000. **18**(3): p. 317-20.
6. Fathima, A., M. Sharma B.S, and N. Sujatha, *Selective sensitivity of Mueller imaging for tissue scattering over absorption changes in cancer mimicking phantoms*. Optics and Lasers in Engineering, 2018. **102**: p. 112-118.
7. Demos, S.G., H.B. Radousky, and R.R. Alfano, *Deep subsurface imaging in tissues using spectral and polarization filtering*. Optics Express, 2000. **7**(1): p. 23-28.
8. Woltman, S.J., G.P. Crawford, and G.D. Jay, *Liquid Crystals: Frontiers in Biomedical Applications*. 2007: World Scientific, ISBN (9789812705457).
9. Lima, J.J., et al., *Enantiomeric fraction of styrene glycol as a biomarker of occupational risk exposure to styrene*. Chemosphere, 2017. **168**: p. 903-907.
10. Zhou, G.X., J.M. Schmitt, and C.E. Ellicott, *Sensitive detection of optical rotation in liquids by reflection polarimetry*. Review of Scientific Instruments, 1993. **64**(10): p. 2801-2807.
11. MEHTA, N., *Textbook of Engineering Physics*. 2008: PHI Learning, ISBN (9788120333611).
12. Frankel, E., *Corpuscular Optics and the Wave Theory of Light: The Science and Politics of a Revolution in Physics*. Social Studies of Science, 1976. **6**(2): p. 141-184.
13. Sassen, K., *Polarization and Brewster angle properties of light pillars*. Journal of the Optical Society of America A, 1987. **4**(3): p. 570-580.
14. Hull, G.F., *Essentials of Physics for College Students*. Science, 1913. **37**(944): p. 184-185.
15. BARUS, C., *The Mathematician in Modren Physics*. Science, 1914. **40**(1038): p. 721-727.
16. Malik, B.H. and G.L. Coté, *Real-time, closed-loop dual-wavelength optical polarimetry for glucose monitoring*. Journal of Biomedical Optics, 2010. **15**(1): p. 017002-017002-6.
17. Bornhop, D.J. and J. Hankins, *Polarimetry in Capillary Dimensions*. Analytical Chemistry, 1996. **68**(10): p. 1677-1684.

18. Cameron, B.D., et al., *The use of polarized laser light through the eye for noninvasive glucose monitoring*. Diabetes Technol Ther, 1999. **1**(2): p. 135-43.
19. Brent D. Cameron, J.S.B., and Gerard L. Coté., *Measurement of the Glucose Transport Time Delay Between the Blood and Aqueous Humor of the Eye for the Eventual Development of a Noninvasive Glucose Sensor*. Diabetes Technology & Therapeutics, 2001. **3**(2): p. 7.
20. Baba, J.S., et al., *Effect of temperature, pH, and corneal birefringence on polarimetric glucose monitoring in the eye*. Journal of biomedical optics, 2002. **7**(3): p. 321-8.
21. Wan, Q., G.L. Cote´, and J.B. Dixon, *Dual-wavelength polarimetry for monitoring glucose in the presence of varying birefringence*. Journal of Biomedical Optics, 2005. **10**(2): p. 024029-0240298.
22. Cameron, B.D. and H. Anumula, *Development of a real-time corneal birefringence compensated glucose sensing polarimeter*. Diabetes Technol Ther, 2006. **8**(2): p. 156-64.
23. Purvinis, G., B.D. Cameron, and D.M. Altrogge, *Noninvasive polarimetric-based glucose monitoring: an in vivo study*. J Diabetes Sci Technol, 2011. **5**(2): p. 380-7.
24. Ansari, R.R., S. Bockle, and L. Rovati, *New optical scheme for a polarimetric-based glucose sensor*. Journal of biomedical optics, 2004. **9**(1): p. 103-15.
25. Cameron, B.D. and Y. Li, *Polarization-Based Diffuse Reflectance Imaging for Noninvasive Measurement of Glucose*. Journal of diabetes science and technology (Online), 2007. **1**(6): p. 873-878.
26. Markowicz, P.P., et al., *Phase-sensitive time-modulated surface plasmon resonance polarimetry for wide dynamic range biosensing*. Optics Express, 2007. **15**(4): p. 1745-1754.
27. Patskovsky, S., et al., *Phase-sensitive spatially-modulated surface plasmon resonance polarimetry for detection of biomolecular interactions*. Sensors and Actuators B: Chemical, 2008. **133**(2): p. 628-631.
28. So, C.-F., et al., *Recent advances in noninvasive glucose monitoring*. Medical devices (Auckland, N.Z.), 2012. **5**: p. 45-52.
29. Bornhop, D.J. and S. Dotson, *CHAPTER 11 - Micro-scale polarimetry*, in *Chiral Analysis*. 2006, Elsevier: Amsterdam. p. 343-361.
30. Gibbs, P.R., et al., *Imaging Polarimetry for High Throughput Chiral Screening*. Biotechnology Progress, 2003. **19**(4): p. 1329-1334.
31. Bornhop, D.J., S. Dotson, and B.O. Bachmann, *On-chip polarimetry for high-throughput screening of nanoliter and smaller sample volumes*. 2012, Google Patents (No. US8134707B2).
32. Ghosh, A. and P. Fischer, *Chiral Molecules Split Light: Reflection and Refraction in a Chiral Liquid*. Physical Review Letters, 2006. **97**(17): p. 173002.
33. R. P. Rajan, A.G., *Demonstration of a microfluidic polarimeter*, in *Frontiers in Biological Detection:From Nanosensors to Systems IV*. 2012, BiOS SPIE Photonics West: Indian Institute of Science (India). p. 121.
34. Papukutty Rajan, R. and A. Ghosh, *Enhancement of circular differential deflection of light in an optically active medium*. Optics Letters, 2012. **37**(7): p. 1232-1234.

35. Yeung, E.S., et al., *Detector based on optical activity for high performance liquid chromatographic detection of trace organics*. Anal Chem, 1980. **52**(9): p. 1399-402.
36. Maystre, F., et al., *Enhanced Polarimetric Detection in HPLC Using a Refractive Index Equalizer*. Analytical Chemistry, 1994. **66**(18): p. 2882-2887.
37. Bobbitt, D.R. and E.S. Yeung, *Direct and indirect polarimetry for detection in microbore liquid chromatography* Anal. Chem., 1984. **56**: p. 1577-1581.
38. Lloyd, D.K., D.M. Goodall, and H. Scrivener, *Diode-laser-based optical rotation detector for high-performance liquid chromatography and on-line polarimetric analysis*. Analytical Chemistry, 1989. **61**(11): p. 1238-1243.
39. Bornhop, D.J., *Microvolume index of refraction determinations by interferometric backscatter*. Applied Optics, 1995. **34**(18): p. 3234-3239.
40. Swinney, K., J. Nodorft, and D. Bornhop, *Nanoliter Volume Polarimetry*. Vol. 56. 2002. 134-138.
41. Swinney, K., J. Nodorft, and D.J. Bornhop, *Capillary-scale polarimetry for flowing streams*. Analyst, 2001. **126**(5): p. 673-675.
42. Markov, D.A., et al., *A Fourier analysis approach for capillary polarimetry*. Electrophoresis, 2002. **23**(5): p. 809-812.
43. Bougas, L., et al., *Chiral cavity ring down polarimetry: Chirality and magnetometry measurements using signal reversals*. The Journal of Chemical Physics, 2015. **143**(10): p. 104202.
44. Bougas, L., et al., *Fundamentals of cavity-enhanced polarimetry for parity-nonconserving optical rotation measurements: Application to Xe, Hg, and I*. Physical Review A, 2014. **89**(5): p. 052127.
45. Sofikitis, D., et al., *Evanescent-wave and ambient chiral sensing by signal-reversing cavity ringdown polarimetry*. Nature, 2014. **514**(7520): p. 76-79.
46. Sofikitis, D., et al., *Cavity-based Chiral Polarimetry*. 2018. p. 649-678.
47. Müller, T., et al., *Cavity ring-down polarimetry (CRDP): theoretical and experimental characterization*. Journal of the Optical Society of America B, 2002. **19**(1): p. 125-141.
48. Protasov, E.A., D.E. Protasov, and A.V. Ryzhkova, *Laser Polarimeter for Measurement of Optical Activity of Biological Objects*. Physics Procedia, 2015. **71**: p. 261-266.
49. A. Vardanyan, G., et al., *Polarization plane's weak rotation amplifiers and polarization azimuth stabiliziers*. Vol. 5758. 2005. 345-355.
50. Goldstein, D., *The Jones Matrix Calculus*, in *Polarized Light, Revised and Expanded*. 2003, CRC Press, ISBN (978-0-8247-4053-5).
51. Silveira, G., https://www.slideshare.net/gustavopsilveira/aula-11-13-estereoqumica

2013.

52. Bass, M. and O.S.o. America, *Handbook of Optics: Fundamentals, techniques, and design*. 1994: McGraw-Hill, ISBN (9780070477407).
53. Hodgson, N., Weber, Horst, *Laser Resonators and Beam Propagation* 2ed. Springer Series in Optical Sciences, ed. 2. 2005: Springer-Verlag Berlin Heidelberg.

54. Hecht, E., *Optics*. 2012: Pearson Education, ISBN (9788131718070).
55. Nikolova, L. and P.S. Ramanujam, *Polarization Holography*. 2009, Cambridge: Cambridge University Press.
56. Bruice, P.Y., J. Jones, and P.Y. Bruice, *Study guide and solutions manual [for] Organic chemistry*. 2014.
57. Schäferling, M., *Chirality in Nature and Science*, in *Chiral Nanophotonics: Chiral Optical Properties of Plasmonic Systems*. 2017, Springer International Publishing: Cham. p. 5-42.
58. Lakhtakia, A., *Selected Papers on Natural Optical Activity*. 1990: SPIE Optical Engineering Press.
59. Justin Peatross, M.W., *Physics of Light and Optics*. 2015: Brigham Young University.
60. Azzam, R.M.A., *The intertwined history of polarimetry and ellipsometry*. Thin Solid Films, 2011. **519**(9): p. 2584-2588.
61. Fujiwara, H., *Principles of Optics*, in *Spectroscopic Ellipsometry*. 2007, John Wiley & Sons, Ltd. p. 13-48.
62. Li, Y., et al., *Elliptical polarization of near-resonant linearly polarized probe light in optically pumped alkali metal vapor*. Scientific Reports, 2017. **7**: p. 43066.
63. Boyes, W., *Instrumentation Reference Book*. 2002: Elsevier Science.
64. Max Born , E.W., *Principles of Optics*, ed. forth. 1970, City of Liverpool: Pergamon Press.
65. Cameron, B.D. and G.L. Cote, *Noninvasive glucose sensing utilizing a digital closed-loop polarimetric approach*. IEEE Transactions on Biomedical Engineering, 1997. **44**(12): p. 1221-1227.
66. Malacara, D., *Physical Optics and Light Measurements*. 1989: Elsevier Science.
67. Bobbitt, D.R. and E.S. Yeung, *Direct and indirect polarimetry for detection in microbore liquid chromatography*. Analytical Chemistry, 1984. **56**(9): p. 1577-1581.
68. Baba, J.S., et al., *Effect of temperature, pH, and corneal birefringence on polarimetric glucose monitoring in the eye*. Journal of Biomedical Optics, 2002. **7**(3): p. 321-328.
69. Levinson, H., *Principles of lithography: Third edition*. 2011. 1-505.
70. Mohd Said, N.A., V. Ogurtsov, and G. Herzog, *Electrochemical biosensor based on microfabricated electrode arrays for life sciences applications*. 2014.
71. *Scanning Electron Microscopy for the Life Sciences*. Advances in Microscopy and Microanalysis. 2012, Cambridge: Cambridge University Press, ISBN (9780521195997).
72. Northrop, R.B., *Introduction to Instrumentation and Measurements*. 2005: Taylor & Francis, ISBN (9780849337734).
73. Rola, K.P., et al., *Silicon 45° micromirrors fabricated by etching in alkaline solutions with organic additives*. Microsystem Technologies, 2014. **20**(2): p. 221-226.
74. Drago, R., et al., *The role of Triton surfactant in anisotropic etching of {1 1 0} reflective planes on (1 0 0) silicon*. Journal of Micromechanics and Microengineering, 2005. **15**(6): p. 1174.
75. Sangwoo, L., P. Sangjun, and D.I. Cho, *The surface/bulk micromachining (SBM) process: a new method for fabricating released MEMS in single*

crystal silicon. Journal of Microelectromechanical Systems, 1999. **8**(4): p. 409-416.

76. Xu, Y.W., A. Michael, and C.Y. Kwok, *Formation of ultra-smooth 45° micromirror on (100) silicon with low concentration TMAH and surfactant: Techniques for enlarging the truly 45° portion*. Sensors and Actuators A: Physical, 2011. **166**(1): p. 164-171.
77. Prem, P. and S. Kazuo, *Complex three-dimensional structures in Si{1 0 0} using wet bulk micromachining*. Journal of Micromechanics and Microengineering, 2009. **19**(10): p. 105008.
78. Zubel, I. and M. Kramkowska, *Possibilities of extension of 3D shapes by bulk micromachining of different Si (h k l) substrates*. Journal of Micromechanics and Microengineering, 2005. **15**(3): p. 485.
79. Yang, E.H., et al., *Fabrication and dynamic testing of electrostatic actuators with p+ silicon diaphragms*. Sensors and Actuators A: Physical, 1995. **50**(1): p. 151-156.
80. Ciarlo, D.R., *A latching accelerometer fabricated by the anisotropic etching of (110) oriented silicon wafers*. Journal of Micromechanics and Microengineering, 1992. **2**(1): p. 10.
81. Uenishi, Y., M. Tsugai, and M. Mehregany, *Micro-opto-mechanical devices fabricated by anisotropic etching of (110) silicon*. Journal of Micromechanics and Microengineering, 1995. **5**(4): p. 305.
82. Ammar, E.S. and T.J. Rodgers, *UMOS transistors on*. IEEE Transactions on Electron Devices, 1980. **27**(5): p. 907-914.
83. Seong-Hyok, K., et al. *(110) silicon etching for high aspect ratio comb structures*. in *Emerging Technologies and Factory Automation Proceedings, 1997. ETFA '97., 1997 6th International Conference on*. 1997.
84. Dutta, S., et al., *Comparison of etch characteristics of KOH, TMAH and EDP for bulk micromachining of silicon (110)*. Microsystem Technologies, 2011. **17**(10): p. 1621.
85. Sato, K., et al., *Characterization of orientation-dependent etching properties of single-crystal silicon: effects of KOH concentration*. Sensors and Actuators A: Physical, 1998. **64**(1): p. 87-93.
86. Prem, P., A.G. Miguel, and S. Kazuo, *Silicon Micromachining Based on Surfactant-Added Tetramethyl Ammonium Hydroxide: Etching Mechanism and Advanced Applications*. Japanese Journal of Applied Physics, 2010. **49**(5R): p. 056702.
87. Agarwal, R., S. Samson, and S. Bhansali, *Fabrication of vertical mirrors using plasma etch and KOH:IPA polishing*. Journal of Micromechanics and Microengineering, 2007. **17**(1): p. 26.
88. Rao, A.V.N., V. Swarnalatha, and P. Pal, *Etching characteristics of Si{110} in 20 wt% KOH with addition of hydroxylamine for the fabrication of bulk micromachined MEMS*. Micro and Nano Systems Letters, 2017. **5**(1): p. 23.
89. Ashok, A. and P. Pal, *Silicon micromachining in 25 wt% TMAH without and with surfactant concentrations ranging from ppb to ppm*. Microsystem Technologies, 2017. **23**(1): p. 47-54.
90. Prem, P., et al., *Fabrication of novel microstructures based on orientation-dependent adsorption of surfactant molecules in a TMAH solution*. Journal of Micromechanics and Microengineering, 2011. **21**(1): p. 015008.

91. Cheng, D., et al., *Improvement in smoothness of anisotropically etched silicon surfaces: Effects of surfactant and TMAH concentrations*. Sensors and Actuators A: Physical, 2006. **125**(2): p. 415-421.
92. Zubel, I. and M. Kramkowska, *The effect of alcohol additives on etching characteristics in KOH solutions*. Sensors and Actuators A: Physical, 2002. **101**(3): p. 255-261.
93. Merlos, A., et al., *TMAH/IPA anisotropic etching characteristics*. Sensors and Actuators A: Physical, 1993. **37-38**: p. 737-743.
94. Oliver, P. and H.B. Harrison, *Anisotropic etching of {100} and {110} planes in (100) silicon*. Journal of Micromechanics and Microengineering, 2001. **11**(3): p. 217.
95. Kendall, D.L., *Vertical Etching of Silicon at very High Aspect Ratios*. Annual Review of Materials Science, 1979. **9**(1): p. 373-403.
96. Singh, S.S., et al., *Precise identification of directions on Si{0 0 1} wafer using a novel self-aligning pre-etched technique*. Journal of Micromechanics and Microengineering, 2016. **26**(2): p. 025012.
97. Hiroyuki, Y., et al., *Forty-Five Degree Micromirror Fabrication Using Silicon Anisotropic Etching with Surfactant-Added Tetramethylammonium Hydroxide Solution*. Japanese Journal of Applied Physics, 2010. **49**(9R): p. 096503.
98. *Silicon anisotropic etching in TMAH solutions containing alcohol and surfactant additives*. Sensors and Actuators A: Physical, 2012. **178**: p. 126.
99. Gosálvez, M.A., et al., *Orientation- and concentration-dependent surfactant adsorption on silicon in aqueous alkaline solutions: explaining the changes in the etch rate, roughness and undercutting for MEMS applications*. Journal of Micromechanics and Microengineering, 2009. **19**(12): p. 125011.
100. *Atomistic mechanism for the macroscopic effects induced by small additions of surfactants to alkaline etching solutions*. Sensors and Actuators A Physical, 2010. **157**(1): p. 91.
101. *Ellipsometry study of the adsorbed surfactant thickness on Si{110} and Si{100} and the effect of pre-adsorbed surfactant layer on etching characteristics in TMAH*. Sensors and Actuators A Physical, 2009. **156**(2): p. 334.
102. Pal, P., et al., *Surfactant Adsorption on Single-Crystal Silicon Surfaces in TMAH Solution: Orientation-Dependent Adsorption Detected by In Situ Infrared Spectroscopy*. Journal of Microelectromechanical Systems, 2009. **18**(6): p. 1345-1356.
103. Brockmeier, A., et al., *Surface tension and its role for vertical wet etching of silicon*. Journal of Micromechanics and Microengineering, 2012. **22**(12): p. 125012.
104. Hopcroft, M.A., W.D. Nix, and T.W. Kenny, *What is the Young's Modulus of Silicon?* Journal of Microelectromechanical Systems, 2010. **19**(2): p. 229-238.
105. Davies, J.H. *The Physics of Low-dimensional Semiconductors : an Introduction*. 1997; Available from: http://public.eblib.com/choice/publicfullrecord.aspx?p=3004820.
106. Eto, Y., S. Shibata, and M. Shikida. *Proposal of shear stress sensor based on optical detection*. in *2013 IEEE SENSORS*. 2013.

107. Zubel, I., *Anisotropic etching of silicon in solutions containing tensioactive compounds*. Electron Technology Conference ELTE 2016. Vol. 10175. 2016: SPIE.
108. Rola, K.P. and I. Zubel, *Impact of alcohol additives concentration on etch rate and surface morphology of (100) and (110) Si substrates etched in KOH solutions*. Microsystem Technologies, 2013. **19**(4): p. 635-643.
109. Rola, K. and I. Zubel, *Micromirrors inclined at 45° towards Si substrates fabricated by anisotropic etching*. Vol. 41. 2011. 423-430.
110. Rola, K., et al., *Characterization of 45° Micromirrors Fabricated by Silicon Anisotropic Etching in Solutions Containing Different Organic Additives*. Procedia Engineering, 2012. **47**: p. 510-513.
111. Zubel, I., M. Kramkowska, and K. Rola, *Silicon anisotropic etching in TMAH solutions containing alcohol and surfactant additives*. Sensors and Actuators A: Physical, 2012. **178**: p. 126-135.
112. Chen, P.-H., et al., *The characteristic behavior of TMAH water solution for anisotropic etching on both Silicon substrate and SiO2 layer*. Sensors and Actuators A: Physical, 2001. **93**(2): p. 132-137.
113. *Anisotropic etching of silicon in KOH + Triton X-100 for 45° micromirror applications*. Microsystem Technologies, 2017. **23**(5): p. 1463.
114. *Determination of precise crystallographic directions for mask alignment in wet bulk micromachining for MEMS*. Micro and Nano Systems Letters, 2016. **4**(1).
115. Seidel, H., et al., *Anisotropic Etching of Crystalline Silicon in Alkaline Solutions I. Orientation Dependence and Behavior of Passivation Layers*. Vol. 137. 1990. 3612-3626.
116. Ensell, G., *Alignment of mask patterns to crystal orientation*. Sensors and Actuators A: Physical, 1996. **53**(1): p. 345-348.
117. Tetzlaff, D., et al., *Introducing pinhole magnification by selective etching: application to poly-Si on ultra-thin silicon oxide films*. Vol. 124. 2017. 435-440.
118. Horace S. Isbell, J.F.B., Nancy B. Holt, and Harriet L. Frush *Behavior of Certain Sugars and Sugar Alcohols in the Presence of Tetraborates-Correlation of Optical Rotation and Compound Formation*. 1948. **40**(U. S. Department of Commerce National Bureau of Standards): p. 129-149.
119. Rossi, S., et al., *Specific Anion Effects on the Optical Rotation of a-Amino Acids*. The Journal of Physical Chemistry B, 2007. **111**(35): p. 10510-10519.
120. Jirgensons, B., *Optical rotation and viscosity of native and denatured proteins. I. Influence of pH, and the stability of various proteins toward several denaturing reagents*. Arch Biochem Biophys, 1952. **39**(2): p. 261-70.
121. Linthorst, J.A. and d.W.-V. Johanna van, *Polarimetry and stereochemistry: the optical rotation of Vitamin C as a function of pH*. Educación Química, 2014. **25**(2): p. 135-138.
122. Jirgensons, B. and S. Sirotzky, *The Optical Rotation of Human Serum Albumin and γ-Globulin1*. Journal of the American Chemical Society, 1954. **76**(5): p. 1367-1370.
123. Toome, V. and G. Reymond, *Solvent and pH Effects on the Sign of the ORD Spectrum of N-Methyl-4-phenyl-7-methoxy-1,2,3,4-*

tetrahydroisoquinoline in the Visible Spectral Range. Spectroscopy Letters, 1975. **8**(8): p. 595-598.

124. Vollhardt, K.P.C., *Organic chemistry : structure and function* 1999, USA: W. H. Freeman; Third (3rd) Edition edition (1999).
125. Katritzky, A.R., *Advances in Heterocyclic Chemistry*. 1995: Elsevier Science.
126. P. Buck, R., et al., *Measurement of pH. Definition, Standards, and Procedures*. Vol. 74. 2002.
127. Haynes, W.M., *CRC Handbook of Chemistry and Physics, 93rd Edition*. 2012: Taylor & Francis.
128. Feng, S., C. Bagia, and G. Mpourmpakis, *Determination of Proton Affinities and Acidity Constants of Sugars*. The Journal of Physical Chemistry A, 2013. **117**(24): p. 5211-5219.
129. Pomeranz, Y., *Food Analysis: Theory and Practice*. 2013: Springer US.
130. Golub, M.A. and E.E. Pickett, *Effect of temperature and pH on the optical rotation of proteins*. Journal of Polymer Science, 1954. **13**(71): p. 427-440.
131. Alexeev, V.L., et al., *Photonic crystal glucose-sensing material for noninvasive monitoring of glucose in tear fluid*. Clin Chem, 2004. **50**(12): p. 2353-60.
132. Po, H.N. and N.M. Senozan, *The Henderson-Hasselbalch Equation: Its History and Limitations*. Journal of Chemical Education, 2001. **78**(11): p. 1499.
133. Zhang, S.-S., et al., *A Rare Chiral Self-Catenated Network Formed by Two Cationic and One Anionic Frameworks*. Inorganic Chemistry, 2007. **46**(11): p. 4365-4367.
134. Pan, C.-Y., et al., *Zn(1,3-DAP)[B4O7]: A rare chiral zeolitic framework constructed of four-connected [B4O9] clusters with a single-stranded helical channel*. Vol. 51. 2014.
135. Haller, K.L. and P.C.D. Hobbs, *Double-beam laser absorption spectroscopy: shot noise-limited performance at baseband with a novel electronic noise canceler*. Optics, Electro-Optics, and Laser Applications in Science and Engineering. Vol. 1435. 1991: SPIE.
136. Houser, G.D. and E. Garmire, *Balanced detection technique to measure small changes in transmission*. Applied Optics, 1994. **33**(6): p. 1059-1062.
137. R Silva, C., et al., *Assembly of a Faraday modulator for polarimetric measurements*. Vol. 575. 2015. 012019.
138. Gevorgyan, A., et al., *Polarization plane's weak rotation amplifiers and polarization azimuth stabilizers*. Vol. 117. 2006. 309-316.
139. Lindberg, V. *Uncertainties and Error Propagation*. Part I of a manual on Uncertainties, Graphing, and the Vernier Caliper 2000; http://www.rit.edu/~w-uphysi/uncertainties/Uncertaintiespart1.html].